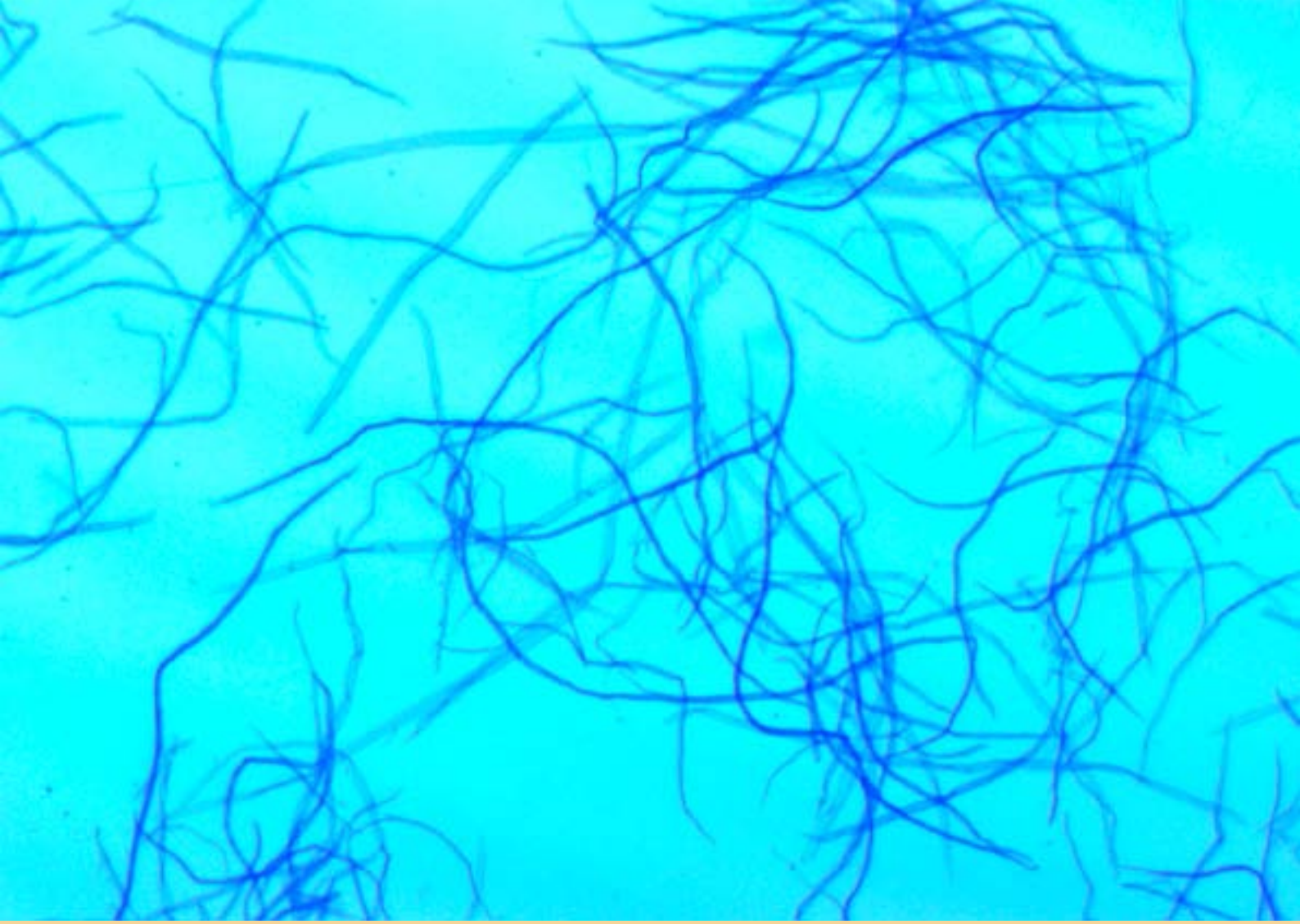

Carla Isabel Pires Cotas

MODELLING OF FIBER SUSPENSIONS FLOW IN PIPES

Simulação do Escoamento de Suspensões de Fibras em Condutas

PhD Thesis in Chemical Engineering, supervised by Professor Doctor Maria da Graça Bontempo Vaz Rasteiro and Professor Doctor Dariusz Asendrych and presented to the Department of Chemical Engineering, Faculty of Sciences and Technology of the University of Coimbra

October 2015

· U C ·

Universidade de Coimbra

Carla Isabel Pires Cotas

MODELLING OF FIBER SUSPENSIONS FLOW IN PIPES

Simulação do Escoamento de Suspensões de Fibras em Condutas

Doctoral Thesis in the scientific area of Chemical Engineering and submitted to the Department of Chemical Engineering

Faculty of Sciences and Technology, University of Coimbra

Supervisors:

Prof. Dr. Maria da Graça Bontempo Vaz Rasteiro

Prof. Dr. Dariusz Asendrych

Host institutions:

CIEPQPF - Research Centre for Chemical Processes Engineering and Forest Products, Department of Chemical Engineering,

Faculty of Sciences and Technology of the University of Coimbra

Coimbra
2015

• U C •

UNIVERSIDADE DE COIMBRA

The flow of paper pulp suspensions is non-trivial, both regarding measurements and simulations.

– David Hammarström

Acknowledgements

I would like to thanks to my supervisors for all the help and advices they gave me during these years, which helped me to be a better researcher, as well as a better person in life. To Professor Doctor Maria G. Rasteiro for her guidance, encouraging and fruitful comments on my work. Well, also for pulling my ears when I needed. The most important, I am grateful that she believed in my work, in my results and for her invaluable support. A huge thanks to Professor Doctor Dariusz Asendrych to help me regarding my two STSM in the Częstochowa University of Technology. I have no words to express my gratitude to him. I also want to thanks to him all the remote assistance and to teach me all that I needed to develop the numerical model and perform my simulations. Also, a sincere gratitude for all the important feedback regarding the revisions of my manuscripts. A special thanks to both supervisors to comprehend my limited time to submit this thesis.

A special and sincere thanks to Professor Doctor António Gameiro, for his good advices and helpful comments on my Thesis Project defense, as a jury member. I hope not to have disappointed him with the work developed.

I also acknowledge the professors from the Department of Mechanical Engineering, University of Coimbra, who taught me great part of my knowledge regarding Computational Fluid Dynamics.

Thank you Sara, Professor Almerindo, Professor Gameiro, Pedro and Cátia for all the support during my initial time in this work. Also, thank you for all the lunches, dinners and coffees to make a break from the work. Thank you Telma, Ana Maia, Ana Isabel, Danieli and Véronique for all the friendship, good advices, thank you for everything. Thank to my lunch friends, Ana Paula, Ana Sofia and Ana Filipa to all the encouragement words and for the break time. Thank to whom directly or indirectly contributed with something during this work.

À minha mãe, ao meu pai e ao meu irmão quero expressar a minha imensa gratidão por tudo, todo o apoio e ajuda. A invasão dos papéis está a acabar!

Thank you!

ABSTRACT

In this thesis the flow behaviour of pulp fiber suspensions is investigated. A central issue in pulp and paper mills is related to high energy costs, some of them due to not proper equipment design. One of the main source is related to the pulp transport systems and the main reason for that is the use of empirical correlations out of their range of applicability. Additionally, different grades of pulp consistency as well as mean flow velocity are present during the industrial process. Even if the process stages are based on the same principles, the final product can have different properties depending on process conditions. Therefore, experimental and numerical methods in the area of flow monitoring of pulp fibre suspensions are increasingly important. Aiming to gain more knowledge concerning flow of pulp suspensions, the applicability of Computational Fluid Dynamics (CFD) strategies to predict pulp's flow was the main motivation for this work.

In this context, a Newtonian homogeneous single-phase model was chosen as start point. Additionally, a pseudo-homogeneous strategy was followed since high consistency range is of interest. In general, two main factors contribute for the complex behaviour of pulp suspensions in relation to other multiphase systems: fiber suspensions behave as non-Newtonian fluids and the presence of fibers in the flow induces a *drag reduction* effect.

As a first approach, the non-Newtonian behaviour of pulp suspensions was implemented by relating viscosity to shear rate as a power-law. A very thin pure water annulus surrounding the flow core region was considered. Also, the CFD model took into account new logarithmic wall functions for the standard high Reynolds k-ε turbulence model. Several computational runs were performed in order to optimize different parameters on the wall functions, related to the S-shaped profile of dimensionless velocity presented in the literature for the flow conditions of pulp suspension under analysis. CFD model predictions were validated with pressure drop measurements.

By combining a new viscosity model with low-Reynolds-number k-ε turbulence models, turbulent flow of pulp suspensions was also investigated. It was found that a new viscosity expression could be applied to describe the non-Newtonian behaviour of pulp suspensions.

The influence of pulp consistency as well as shear rate could be included in the viscosity expression. In this way, the presence of a pure water annulus or a lubrication layer was tested. The presence of a few number of fibers in the lubrication layer was taken into account by considering consistency in that region as a function of the distance to the pipe wall. The attenuation of turbulence, by modifying the turbulence model, considering new damping functions of turbulent viscosity was investigated. The influence of damping functions applied successfully by other authors to deal with the flow of power-law fluids as well as particles was tested. Whereas the implementation considering the standard version of those functions were not leading to good enough predictions, improvements on numerical results were observed when testing new constant values on those functions. The CFD predictions were found to fit well with experimental data, when an additional term related to fiber aspect-ratio was included on the damping function adapted from literature to deal with the flow of particles.

It was also investigated the applicability of an experimental visualization technique, electrical Impedance Tomography - EIT system, to evaluate the flow regimes of pulp suspensions. Conductivity images were reconstructed which allowed one to conclude about plug evolution and fibers radial distribution. Moreover, pressure drop measurements together with EIT images gave information about pulp flow regime. The efficiency of the CFD pseudo-homogeneous model developed on the simulation of the experimental data obtained for the two higher mean pulp flow velocity attained experimentally was evaluated.

The different stages on the CFD model development were validated for different pulp consistencies, dilute and high concentration range, flow velocities and two types of fibers, short and long fibers (*Eucalyptus* and *Pine* pulp fibers). Additionally, the applicability of the final model developed was tested for the prediction of pulp flow data corresponding to a different pulp flow regime. CFD can represent a powerful tool to obtain flow characteristics of pulp suspensions, in order to give useful information to optimize pulp and paper industrial processes.

Keywords: Computational Fluid Dynamics, fiber suspensions, flow, modelling, rheology

RESUMO

O estudo desenvolvido no âmbito desta tese foi realizado com o intuito de investigar o escoamento de suspensões fibrosas. Os custos energéticos no processo de produção de pasta e papel são sempre muito elevados. Uma parte significativa destes custos tem a ver com os sitemas de transporte/admissão da pasta e o seu valor é mais elevado em parte devido ao incorrecto dimensionamento dos equipamentos industriais, como seja o caso de sistemas de transporte das suspensões fibrosas. A aplicação de correlacções empíricas para condições operatórias que se situam fora da gama de aplicabilidade para as quais estas foram desenvolvidas resulta, geralmente, no sobredimensionamento das unidades de transporte. As características do produto final dependem das condições processuais, e as condições operatórias são seleccionadas de acordo com a aplicação do produto final. O correcto e completo conhecimento das características do escoamento das suspensões fibrosas é importante quer ao nível das propriedades do produto final quer ao nível da selecção das melhores condições operatórias e dimensionamento das unidades. Este conhecimento pode ser conseguido tanto através de estratégias experimentais como de estratégias computacionais. Assim, com este trabalho pretende-se contribuir para um melhor conhecimento do escoamento de suspensões de fibras celulósicas recorrendo a ferramentas computacionais baseadas na utilização da dinâmica de fluidos computacional (CFD).

Neste trabalho foram testadas diferentes estratégias tendo como ponto de partida o modelo Newtoniano e homogéneo. Esta estratégia foi aplicada uma vez que se pretendia estudar o escoamento de suspensões fibrosas para diferentes gamas de consistência, suspensões diluídas e concentradas, em condutas de secção circular. Apesar das suspensões fibrosas serem classificadas como sistemas multifásicos, o comportamento não-Newtoniano e a atenuação de turbulência verificada durante o escoamento, tornam estes sistemas complexos e diferentes dos outros sistemas multifásicos.

Numa primeira etapa, duas modificações foram introduzidas ao modelo de turbulência k-ε para elevados números de Reynolds. O comportamento não-Newtoniano das suspensões fibrosas foi implementado através da expressão da dependência da viscosidade em ordem à

velocidade de corte. Assumindo, que os dados reológicos podem ser ajustados por uma lei de potência, uma expressão para a viscosidade em função da velocidade de corte foi obtida para cada consistência estudada. Uma camada constituída apenas por água, com a espessura igual ao comprimento médio das fibras, foi considerada junto da parede, rodeando a zona central do escoamento. Adicionalmente, as funções de parede para a região turbulenta, lei logarítmica, foram modificadas tendo em conta uma expressão proposta na literatura. Esta expressão traduz matematicamente os perfis de velocidade adimensional, cujo comportamento peculiar em forma de S foi descrito na literatura. Foram realizadas diferentes simulações com vista a optimizar os diferentes parâmetros possíveis de serem relacionados para o escoamento em estudo. Dados experimentais de queda de pressão foram utilizados na validação do modelo desenvolvido.

De seguida, um novo modelo foi testado. Uma nova expressão para a viscosidade da suspensão fibrosa foi proposta. Este novo modelo incluiu a dependência da viscosidade em ordem à velocidade de corte, bem como com a consistência da suspensão. Adicionalmente, a influência da inclusão de fibras numa camada de espessura igual ao comprimento médio das fibras junto da parede, *lubrication layer*, foi testada. Como reportado na literatura para casos em que o escoamento envolve a atenuação de turbulência, foram considerados modelos de turbulência k-ε para baixos números de Reynolds. Adicionalmente, a função de amortecimento da viscosidade turbulenta foi modificada de acordo com informação da literatura em que a atenuação da turbulência foi correctamente representada numericamente. Estes casos incluíram o escoamento de partículas e fluidos em que a reologia é traduzida por uma lei de potência. Contudo, verificou-se que alterar o modelo base de baixo Reynolds com as novas funções de amortecimento para fluidos não-Newtonianos não conduzia resultados suficientemente bons. Porém, melhorias significativas foram observadas quando novas simulações foram realizadas com novos valores para as constantes nas funções de amortecimento. Melhorias significativas, tanto para a suspensão mais diluída como concentrada, foram verificadas quando a função de amortecimento base seleccionada foi a desenvolvida por outro autor para lidar com o escoamento de partículas, a qual foi modificada neste trabalho com um termo adicional relacionado com as características das fibras, a relação comprimento/diâmetro da fibra (*aspect-ratio*).

Numa última etapa, previsões numéricas com o modelo de CFD desenvolvido foram comparadas com dados experimentais obtidos numa instalação piloto, cuja secção de teste está equipada com um sistema de tomografia de impedância eléctrica (EIT) desenvolvido internamente. Os dados recolhidos experimentalmente serviram para validar o modelo

numérico através dos valores de queda de pressão, assim como foram utilizados para validar o tipo de escoamento. Adicionalmente, as imagens reconstruídas da distribuição radial de conductividade eléctrica permitiram inferir acerca da distribuição radial das fibras e sobre a evolução do *plug* de fibras.

As diferentes modificações ao modelo inicial, modelo Newtoniano e homogéneo, testadas e apresentadas neste trabalho foram validadas quantitativamente por comparação dos valores numéricos e experimentais da queda de pressão. Os perfis de velocidade e velocidade adimensional foram comparados qualitativamente com dados reportados na literatura. De um ponto de vista geral, boas previsões foram obtidas com o modelo proposto neste trabalho para dois tipos de suspensões de fibras, fibras longas e fibras curtas, pinho e eucalipto respectivamente, quando se aplicou o modelo para diferentes consistências e diferentes velocidades médias de escoamento. Adicionalmente, o modelo mostrou previsões coerentes quando aplicado na simulação de dados experimentais obtidos numa conduta de maior diâmetro e regimes de escoamento diferentes do regime para o qual foi desenvolvido. Em resumo, o modelo CFD desenvolvido pode ser aplicado na previsão do escoamento de suspensões fibrosas permitindo obter informação ainda não disponível experimentalmente.

Palavras-chave: Dinâmica de Fluidos Computacional, suspensões de fibras, escoamento, modelização, reologia

LIST OF CONTENTS

LIST OF TABLES

LIST OF FIGURES

NOMENCLATURE

A	Area, m^2
A_S	Constant of Bartosik II damping function (Equation (IV.10))
a	Linearized coefficients in the cell and neighbour cells in the discretized equations (Equation (III.12))
B	Empirical constant (=5.5, Equation (III.58))
b	Source-term in the discretized equations (Equation (III.12))
C	Moisture-free consistency (Equation (II.1)), %
C	Consistency of pulp suspension (Equation (II.2)), %
C_{B1}, C_{B2}	Constants of modified Bartosik II damping function (Bartosik II constants, Equation (IV.11))
C_{M1}, C_{M2}, C_{M3}	Constants of modified Malin damping function (Malin constants, Equation (IV.6))
$C_{\varepsilon 1}$, $C_{\varepsilon 2}$	Constants of turbulence model (Equations (III.8) and (IV.4))
C_μ	Constant of turbulence model (Equations (III.6) and (IV.3))
c, c	Consistency of pulp suspension, %
$\bar{c}$	Mean consistency of pulp suspension, %
c_v	Volumetric concentration of solids and consistency of pulp suspension on the Bartosik II damping function (Equation (IV.10)), %
D	Internal pipe diameter, m
d	Average particles diameter and average fiber diameter on the Bartosik II damping function (Equation (IV.10))
d_{fiber}	Average fiber diameter, m
E	Empirical constant (=9.793, Equation (III.52))
f_1, f_2, f_μ	Damping functions of low-Reynolds-number k-ε turbulence models (Tables IV.4 and IV.9)
J	Mass flux, kg m^{-2} s^{-1}

K	Numerical coefficient (Equation (II.1))
K	Numerical coefficient (Equation (II.2))
K	Consistency coefficient (Chapters III and IV), Pa s^n
K'	Constant of viscosity expression (Equation IV.1 and Table IV.1), Pa $s^{1+\beta}$
k	Turbulent kinetic energy, m^2 s^{-2}
k	Constant of yield stress expression (Equation (IV.9)), N m^{-2}
k_w	Wall boundary condition for k, N m^{-2}
L	Pipe length, m
L_{fiber}	Average fiber length, m
l_i	Length interval i (Equation (IV.14)), m
$\dot{m}_b$	Mass flow rate, kg s^{-1}
N	Crowding factor
n	Flow behaviour index (Chapters III and IV)
n	Local radial coordinate of the adjacent cells to the wall (Equation (III.55)), m
n	Total number of electrodes (Chapter V)
P_k	Rate of shear production of turbulent kinetic energy (Equation (III.9)), Pa s^{-1}
p	Pressure, Pa
Q_b	Volumetric flow rate, m^3 s^{-1}
R	Pipe radius, m
R	Interval length ratio (Equation (IV.14))
R^+	Dimensionless distance of the upper limit of the *core* region
Re_k, Re_t	Turbulent Reynolds number (Table IV.4)
Re_ε	Reynolds number based on Kolmogorov velocity scale $u_\varepsilon=(\mu\varepsilon/\rho)^{1/4}$ (Table IV.4)
r	Radial coordinate, m
r	Fiber aspect-ratio in the new Bartosik I and Bartosik II damping functions (Equations (IV.12) and (IV.13))
S_C	Constant part in the source-term (Equation (III.11))
S_P	Coefficient of ϕ in the source-term (Equation (III.11))
ºSR	Schopper-Riegler Freeness

S_ϕ	Source-term in the general differential equation (Equation (III.10))
U_b, Ub	Mean flow velocity, m s^{-1}
u	Mean velocity component in the *x*-direction, m s^{-1}
u^*	Dimensionless velocity (Equation (III.47))
u^+	Dimensionless velocity (Equation (III.49))
u_{RMS}	Root mean square velocity, m s^{-1}
u_τ	Friction velocity (Equation (III.50))
V	Bulk velocity, m s^{-1}
V_m	Velocity at the maximum of head loss on the plug flow regime, m s^{-1}
V_W	Velocity at the onset of the *drag reduction* effect, m s^{-1}
V_{red}	Velocity at the maximum of drag reduction, m s^{-1}
v	Mean velocity component in the *r*-direction, m s^{-1}
y	Distance from the wall surface, m
y^*	Nondimensional length from wall surface (Equation (III.46))
y^+	Nondimensional length from wall surface (Equation (III.48))
y_C^+	Dimensionless distance of the border of the *yield* region with the *near wall* region
y_L^+	Dimensionless distance of the border of the *yield* region with the *core* region
y_v^+	Dimensionless thickness of the viscous sublayer
y_n	Distance to the wall from the interface between cell P and neighbour cell, m
y_P	Distance to the wall from cell P, m
y_v	Border of viscous sublayer, m
x	Longitudinal coordinate, m

Greek letters

Γ_ϕ	Turbulent diffusion coefficient (Equation (III.10))
$\Delta H/L$	Head loss, Pa m^{-1}
$\Delta p/L$	Pressure drop, Pa m^{-1}

$\Delta p/L_{\text{built-in}}$	Predicted pressure drop for the pulp suspensions flow with the built-in models of ANSYS Fluent, Pa m^{-1}
$\Delta p/L_{\text{exp}}$, $\Delta p/L_{\text{pulp}}$	Experimental pressure drop for the flow of pulp suspensions, Pa m^{-1}
$\Delta p/L_{\text{num}}$	Predicted pressure drop for the flow of pulp suspensions, Pa m^{-1}
$\Delta p/L_{\text{standard } k\text{-}\varepsilon}$	Predicted pressure drop for the pulp suspensions flow with the standard high Reynolds k-ε turbulence model considering the non-Newtonian behaviour of pulp suspension (Chapter III, Section III.4.1), Pa m^{-1}
$\Delta p/L_{\text{water}}$	Pressure drop for the water flow in the same test rig, Pa m^{-1}
$\Delta p/L_{\text{UDF}}$	Predicted pressure drop for the pulp suspensions flow with the models implemented by User-Defined Functions, Pa m^{-1}
Δu^{+}	Function in the dimensionless velocity profile based on the standard logarithmic law (Equation (III.58))
ΔV	Volume of the control volume, m^3
α	Exponent (Equation (II.2))
α	Under-relaxation parameter (Equations (III.34), (III.35) and (III.36))
α	Adjustable parameter related to the slope of the dimensionless velocity profile in the *yield* region (Chapter III)
α	Constant of yield stress expression (Equation (IV.9))
α, β, γ	Indices (Equation (II.1))
α, β	Constants of viscosity expression (Equation IV.1 and Table IV.1)
β	Adjustable parameter related to the slope of the dimensionless velocity profile in the *core* region (Chapter III)
$\dot{\gamma}$	Shear rate, s^{-1}
δ	Relative error (=($\Delta p/L_{\text{exp}}$ - $\Delta p/L_{\text{num}}$)/ $\Delta p/L_{\text{exp}}$ × 100), %
ε	Dissipation rate of turbulent kinetic energy, $m^2\ s^{-3}$
ε_{w}	Wall boundary condition for ε, $m^2\ s^{-3}$
κ	von Kármán constant (=0.4187, Equation (III.52))
μ	Dynamic viscosity, Pa s
μ_{app}	Apparent viscosity of pulp suspension, Pa s
μ_{eff}	Effective viscosity, Pa s
μ_{t}	Turbulent viscosity, Pa s
μ_{w}	Mean wall viscosity, Pa s

ν	Kinematic viscosity, $m^2\ s^{-1}$
ρ	Density, $kg\ m^{-3}$
σ	Conductivity, $S\ m^{-1}$
σ_k, σ_ε	Turbulent Prandtl numbers for diffusion terms of k and ε
τ	Shear stress, $N\ m^{-2}$
τ_d	Shear stress needed to complete the plug disruption, $N\ m^{-2}$
τ_y	Yield stress, $N\ m^{-2}$
τ_w	Wall shear stress, $N\ m^{-2}$
ϕ	Generic variable (Equation (III.10))

Subscripts

0	Initial field
app	Apparent
b	Bulk
cal	Calculated
E	Neighbour cell located at east of cell P (Figure III.4)
eff	Effective
exp	Experimental
f	Interface
N	Neighbour cell located at north of cell P (Figure III.4)
nb	Neighbour cells (Figure III.4)
num	Numerical
P	Cell P (Figure III.4)
S	Neighbour cell located at south of cell P (Figure III.4)
t	Turbulent
W	Neighbour cell located at weast of cell P (Figure III.4)
w	Wall

Abbreviations

AB	Abid
ABI	Abe-Kondoh-Nagano Bartosik I
ABII	Abe-Kondoh-Nagano Bartosik II

AKN	Abe-Kondoh-Nagano
AM	Abe-Kondoh-Nagano Malin
AMG	Algebraic multigrid method
CBI	Chang-Hsieh-Chen Bartosik I
CBI.1	*new* Chang-Hsieh-Chen Bartosik I
CBII	Chang-Hsieh-Chen Bartosik II
CBII.1	*new* Chang-Hsieh-Chen Bartosik II
CEM	Complete Electrode Model
CEPI	Confederation of European Paper Industries
CFD	Computational Fluid Dynamics
CHC	Chang-Hsieh-Chen
CM	Chang-Hsieh-Chen Malin
DEM	Discrete element models
DES	Detached eddy simulations
DNS	Direct numerical simulations
EIDORS	Electrical Impedance and Diffuse Optical Reconstruction Software
EIT	Electrical Impedance Tomography
ERT	Electrical Resistance Tomography
FEM	Finite element method
LB	Lam-Bremhorst
LDA	Laser Doppler Anemometry
LES	Large eddy simulation
LRN	Low-Reynolds-number
LS	Launder-Sharma
MFC	Microfibrillated cellulose
MRI	Magnetic Resonance Imaging
NBSK	Northern bleached softwood *kraft*
NMRI	Nuclear Magnetic Resonance Imaging
OCT	Optical Coherence Tomography
PD	Pressure drop
PIV	Particle Image Velocimetry
PVC	Polyvinyl chloride
RANS	Reynolds-averaged Navier-Stokes
RMS	Root Mean Square

SIMPLE	Semi-Implicit Method for Pressure-Linked Equations
UDFs	User-Defined Functions
UDM	User-Defined Memory
UDP	Ultrasonic Doppler Profiling
UDS	User Defined Scalar
UDV	Ultrasonic Doppler Velocimetry
UPDV	Ultrasonic Pulsed Doppler Velocimetry
UVP	Ultrasound Velocity Profiling
YS	Yang-Shih

PART A. THESIS SCOPE AND OUTLINE

The first part of this thesis supplies a brief description of the pulp and paper manufacturing process. This kind of industry requires a large consumption of energy, which is in part due to the incorrect design of industrial equipment, including piping and pumping systems. Particular attention is given to the pulp suspension flow. Aiming to improve the design of piping and pumping systems, despite the still current use of empirical correlations, the use of computational methods has been increasing. The advantages of Computational Fluid Dynamics tools, to predict the pulp suspension flows, are discussed in this section. A brief reference to single and multiphase models is addressed. At the end of the first chapter, motivation, scope and outline of the thesis is presented.

The second chapter of the thesis summarises the most relevant work presented in literature. Firstly, the rheological models are reviewed to characterise the non-Newtonian behaviour of pulp suspensions. Secondly, experimental techniques and methods adopted for fiber suspension flows characterization are presented. Finally, the numerical methodologies to predict the flow of fiber suspensions are addressed with special focus on pseudo-homogeneous models.

I – INTRODUCTION

The main motivation for the work developed on this thesis is to obtain a numerical model able to describe the turbulent flow of concentrated pulp suspensions. The first chapter of this thesis is directed to expose some important topics and concepts helpful to a better understanding of the topics covered in the present dissertation work. Thus, in this section will be addressed some general concepts with special emphasis to the pulp fiber flow, the main motivation and objectives will be presented, and, the section will be finished with the outline of the document.

I.1 – GENERAL CONCEPTS

The appearing of the first paper sheets into our society remounts more than 2000 years ago (Lundell *et al.*, 2011). Its production method was a result from wetting and beating fibers from plants into a fiber-water mixture. This mixture, currently known as stock or pulp suspension, was then passed into a sieve to separate the fibers from the water. The fibers which stayed into the sieve were let to dry, and, then, they were used to form the paper sheet. Nowadays, wood, a source of cellulose fibers, is the main raw material to produce paper.

The presence of paper products and its derivatives in our lives is of relevant importance. Its existence is present in the form of simple paper to communicate information as encountered in books, thesis, reports, newspapers and magazines. Also, it can be found as packing material for food and other items. Paper products are present as well in paper money, paper towels, facial tissue, paper cups, tickets, and, in a wide range of other paper products. The end product influences the process characteristics, which is designed to produce a homogeneous paper sheet by keeping the fibers and removing the higher possible amount of water.

The total amount of paper produced in the world was 400 million tonnes in 2012, and, 185 million tonnes of pulp (CEPI Sustainability Report, 2013). The recent increase of Information and Communication Technologies usage and the economic crisis in Europe beginning in 2008 and 2009, motivated the industry to focus its production in different paper

products to deal with the less demand for their traditional products. As referred in CEPI Sustainability Report (2013), in 2012, the paper consumption in Europe arrived to the same level as in 1998, approximately 84 million tonnes. The significant part of the costs involved in the paper and pulp industry come from the energy costs, representing almost 16 %, electricity and fuels (CEPI Sustainability Report, 2013). The process heat required to produce 1 tonne of paper is 5-17 GJ which depends on the paper type and, also, on the process technology involved (Szabó *et al.*, 2009). The continuous research for new improvements at the end product and, also, at the process level leads to challenges in the pulp and paper industry.

The manufacturing process principles are basically the same and are very well established despite the wide range of final applications of the end product which can be quite different. The technology used depends on the final product specifications. Chemistry, physics and fluid mechanics are disciplines of significant importance in the process. The raw material on the papermaking process is called pulp, which is a suspension composed of a mixture of wood fibers in water. Some mills just produce pulp, others buy pulp to produce the end product, and, the most complete mills operate from the raw material to the end product. There are different process steps involved on the pulp and paper production (see Figure I.1). The main steps in the papermaking process are the production of pulp from the carefully selected and prepared raw material, wood, by mechanical defibrillation or by wood cooking; then, the end product forming process which uses as raw material the pulp, including or not the bleaching step, and which occurs in the paper machine is usually preceded by a refining step.

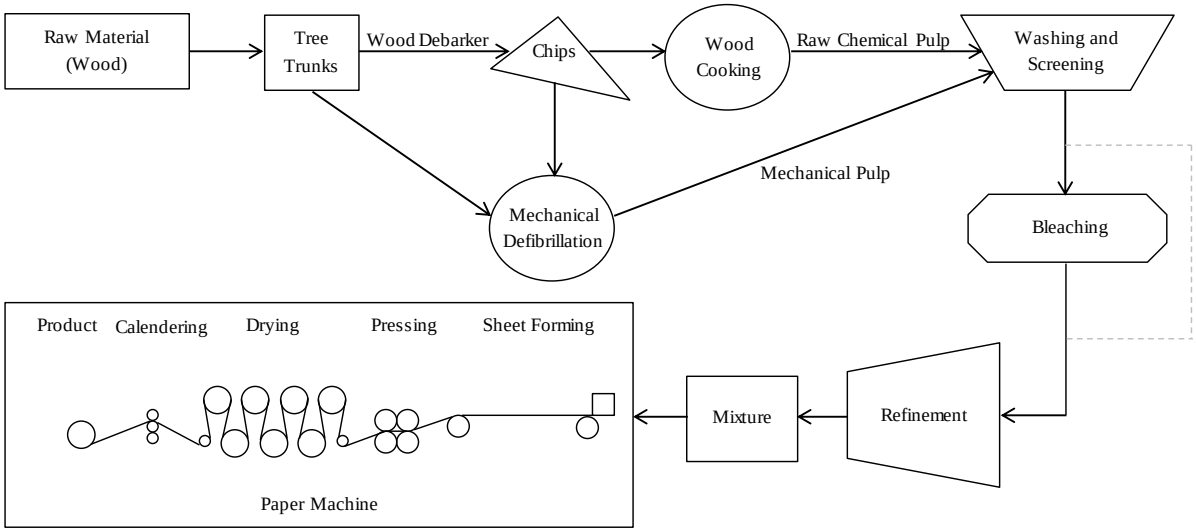

Figure I.1 – Papermaking process and steps involved starting from the wood raw material (adapted from Carvalho (1999) and Lundell *et al.* (2011)).

The pulp production process begins with obtaining tree trunks of the raw material, wood. Different types of wood can be used giving different morphological properties, fiber length and diameter, to the pulp. *Softwood* trees such as *Pine*, *Spruce*, *Fir* and *Larch* are usually used to produce products where high strength is required (paperboard used for packaging) because those species have longer fibers. *Hardwood* trees such as *Eucalyptus*, *Birch* and *Aspen* are used to produce writing papers and printing papers. The type of pulp produced can be chemical pulp or mechanical pulp, depending, if there is wood cooking to remove lignin or if the tree trunks and chips are ground to separate the fibers, respectively. The raw chemical pulp is obtained from a process that occurs in a digester, wood cooking, where the chips resulting from the wood debarking of the tree trunks are fed. The mechanical pulp results from the mechanical defibrillation of the woodchips and tree trunks. In both cases, the pulp is then washed to remove residual products, organic and inorganic, resulting from the cooking or mechanical processes and screened to remove undesired particles and other impurities. At this stage, the product resulting from the process is the unbleached pulp. This kind of pulp presents a brown colour due to the presence of residual lignin and is used mostly in the production of brown paper shopping bags. The bleaching step is necessary when the whiteness level of the end product is important. In this stage, the unbleached pulp that feeds the bleaching plant still contains residual lignin which is gradually removed by chemical reactions with bleaching agents, such as hydrogen peroxide, oxygen and chlorine dioxide, resulting in a pulp that looks like a white bulk suspension. The pulp obtained in the process described so far, pulp production process, is not yet able to produce an end product of high quality. The next step is the refinement which is a mechanical treatment applied in a continuous process to make the fibers suitable for the production of the desired end product. By the end of the refining process, the final result is the fibrillation, hydration and shortening of fibers. The pulp suspension obtained in the refining process can be treated in various ways before the forming of the paper sheet, depending on the end product and, also, on the type of paper machine. The unbleached or bleached pulp has to be treated in a proper way on the papermaking process which begins with the blending of different types of pulps and the addition of various chemicals and inorganic fillers. The excessive fiber flocculation leads to a poor quality paper which can be avoided if the suspension that feeds the paper machine has a concentration which allows to minimize the flocculation effects. Before entering on the paper machine the pulp suspension is diluted to a concentration less than 1 % (Lundell *et al.*, 2011). On the paper machine, a nozzle or headbox, produces a planar fiber suspension jet which is impinged on a wire or forming fabric that is a moving endless permeable belt. The fibers are

retained on the forming fabric and the water is drained. This sheet forming process (invented by Nicholas Louis Robert in 1798 (Lundell *et al.*, 2011)), uses rotating rolls below and in touch with the forming fabric, which allows an effective drainage. In the beginning, this process didn't use rotating rolls instead, the drainage was solely by gravity corresponding to a slow separation process. During this process, it is formed the sheet structure and the fiber concentration from the headbox increases to 3-5 % (Lundell *et al.*, 2011). However, the water quantity after the sheet forming process is still more than 80 % by mass (Lundell *et al.*, 2011). Thereafter, the pressing step is conducted to remove as much water as possible by mechanical dewatering. The fiber network formed on the sheet forming process is compressed in a nip between two rolls with one or two supporting felts, and the water is pressed out from the fiber network. On the dryer section, the remaining water in the fiber network is removed by evaporation on steam heated cylinders. To get a homogeneous, well defined thickness and smooth sheet, the final fiber network from the dryer section passes through roll nips in a calender. The end product is then wound into a reel or cut into sheets.

In all the production lines, the paper machine is composed of a headbox, former, press and dryer. The design and layout of the paper machine depends on the paper type to be produced, and the machine speed and paper grade influences the quantity of water drained during the sheet forming process. The paper making process requires wood fibers, fillers and chemicals. At the end, the paper sheet is composed mainly by cellulose fibers.

As mentioned previously, the end product can be quite different despite of the papermaking process principles being basically the same. A global papermaking process was described; however, this process depends on the raw material and on the end product specifications. The different operations during the papermaking process will influence the end product properties; the two most important steps are the pulping and the paper finishing on the paper machine. The flow of fiber suspensions occurs between different equipment and unit operations during the papermaking process having an important relevance on the global process. The fiber suspension concentration differs in the different steps of the papermaking process, its characteristics influences the end product quality and plays an important role on the design of the industrial equipment, the pumping systems, screens, washers, mixers, and the energy costs associated to the process. The conservative and oversized design of industrial equipment is based on poor understanding of the pulp suspensions flow dynamics which usually results on expensively energy consumption. A better knowledge of the pulp suspensions flow should be achieved in order to enhance the design of industrial equipment on pulp and paper mills.

I.1.1 – PULP SUSPENSIONS FLOW

The pulp suspensions are composed mainly by a mixture of water and cellulose fibers derived from the disintegration of wood, despite of the presence of three phases on the flow interacting with each other, cellulose fibers, fillers and fines (solid phase), water (liquid phase) and air (gas phase). These fibers have a hollow core, lumen, they do not present a rigid form instead they are flexible and shaped as a cylinder. Due to its flexible form, the fibers' shape can be influenced by the flow and, also, by the interaction with other fibers on the surroundings. Also, complex interactions between the different pulp and paper components present on the flow exist, which turn pulp suspensions different from all the other solid-liquid systems. The pulp suspension components can develop suspension structures (floccettes, flocs and networks) which depend on suspension nature and influence the flow behaviour, mainly, due to the interparticle forces that can be generated at intermediate and high consistencies (Duffy, 2003, 2006; Ventura *et al.*, 2011). In the production line, from wood to the end product, the fibers are subject to a series of mechanical and chemical treatment which modify its properties mainly during the pulping process (mechanical defibrillation, wood cooking and bleaching) and refinement.

The flow behaviour of a pulp suspension is influenced by a large number of parameters related to the fiber type and flow characteristics, namely, the fiber flexibility, the surface properties of fiber, the fiber aspect-ratio, the suspension concentration, the viscosity of the suspension, the ratio between the density of the fibrous material and the fluid and the Reynolds number of the flow. The understanding of fiber suspensions flow behaviour, as much complete as possible, at the suspension level, fiber network and individual fiber represents an important step to get an efficient design methodology for any unit operation in the pulp and paper mill.

Regarding the flow and deformation characteristics, the rheology of pulp fiber suspensions presents a unique and complex behaviour, and, in some ways, it can be considered as a non-Newtonian fluid. A typical rheogram of a pulp fiber suspension is presented in Figure I.2. The pulp flow begins when the shear stress applied surpasses a minimum value denoted as yield stress, τ_y. A fluid-like behaviour can be present and the network structure can be absolutely disrupted when the shear tress exceeds the fluidization

point, τ_d. At this point, the pulp hydrodynamic properties are similar to those of water and the pulp suspensions starts to move in a fully dispersed flow.

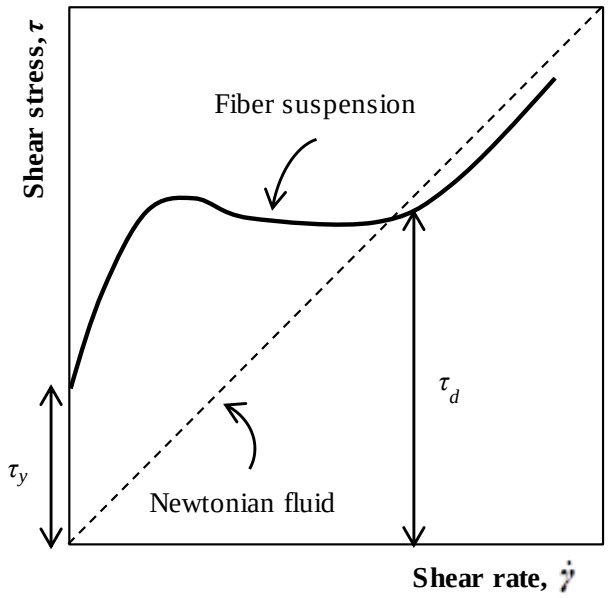

Figure I.2 – Typical rheogram for a fiber suspension (adapted from Gullichsen and Härkönen (1981)).

The flow of pulp suspensions differs from those of other solid-liquid systems revealing different flow regimes and pressure loss curves. The turbulent and laminar flows are the usual flow regimes of Newtonian fluids flows. However, the flow regimes for pulp suspensions flow are more complex. These flow regimes observed by visual inspection or by indirect measurements (Gullichsen and Härkönen, 1981; Duffy, 2006, Jäsberg, 2007; Nikbahkt, 2014), are basically three different regimes: the plug, transition and turbulent flow regimes (see Figures I.3 and I.4). However, in each regime there are sub-regimes characterised by well-defined shear mechanisms in which the principal difference occurs in the region close to the wall (Gullichsen and Härkönen, 1981; Ventura *et al.*, 2008b, 2011).

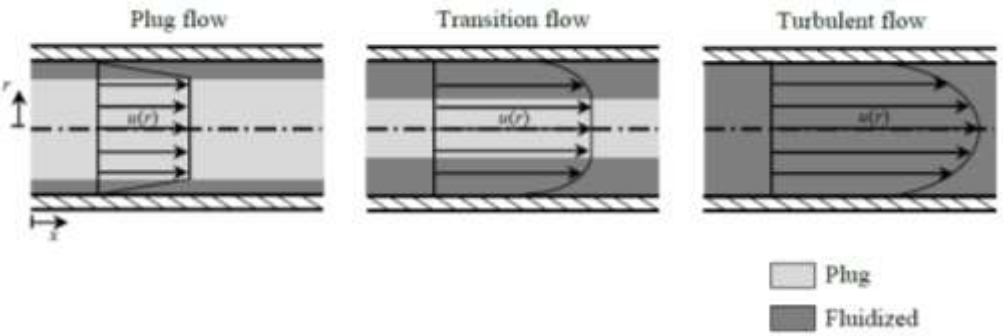

Figure I.3 – Schematic representation of the three different flow regimes of a pulp suspension flow in a pipe (adapted from Gullichsen and Härkönen (1981) and Lundell *et al.* (2011)).

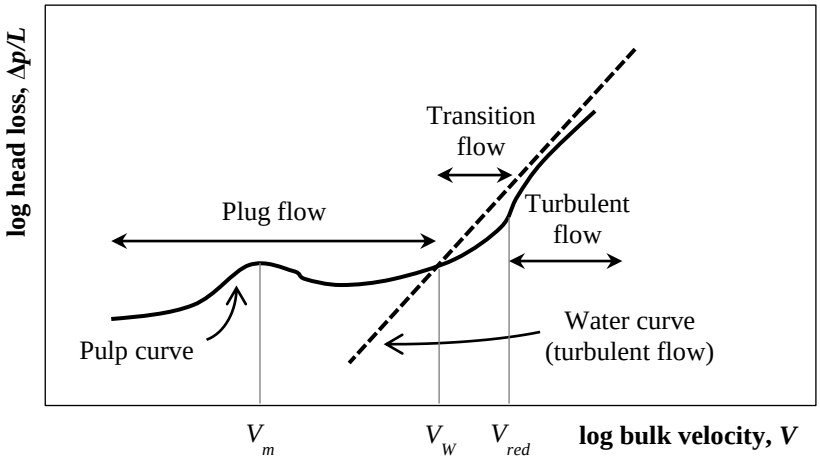

Figure I.4 – Characteristic pressure drop curve for pulp suspensions flow (adapted from Gullichsen and Härkönen (1981), Li *et al.* (2001b) and Lundell *et al.* (2011)).

According to the rheological behaviour of pulp suspensions, any movement of the pulp begins when the shear force imposed exceeds the yield stress distorting the plug. The different flows regimes are a direct consequence of the increase of flow velocity that will increase the shear force acting on the lubricating layer to values high enough to disrupt the suspension structure. At low velocities, the entire pulp suspension flows as a plug of fibers and water characterised by an almost uniform flow velocity in the core region, with strong velocity gradients in a very thin layer near the pipe wall, lubricating water layer, where the entire shear occurs. The plug flow regime is, also, characterised by head loss values larger than those of water flow considered for the same test rig and conditions (see Figure I.4). regarding head loss, the different regimes are represented by a not uniform increase of pressure drop with flow velocity. Instead, a decrease on the head loss is observed after the velocity corresponding to the maximum of head loss on the plug flow regime, V_m, is reached, as a consequence of the increase of the lubrication layer thickness. The plug structure starts to break with the increase of flow velocity and the pulp suspension flow begins to be more fluidized. The transition from plug flow to the transition flow happens at a specified flow velocity, V_W, which corresponds to the onset of the drag reduction effect. At intermediate velocities, transition flow, the head loss presents values lower than those of the turbulent flow of water. There are more fibers broken from the plug due to the increase of flow velocity which intensifies the turbulence, and the thickness of the plug decreases. For the velocity value corresponding to the maximum of drag reduction, V_{red}, the head loss curve for pulp suspension becomes parallel to that representing the turbulent water flow in the same test rig, having still lower values than those of water. After this point, all pulp suspension presents a turbulent fluid-like behaviour and the

consistency gradients almost disappear. The overall behaviour of the pulp flow is described by the usual pressure drop curve presented in Figure I.4 which is strongly influenced by the fiber concentration and the flow velocity (Cotas, 2012).

The piping systems play an important part on the design of the process since they are present in all production lines to transport the pulp between the different parts of the process. Better knowledge of the suspension dynamics represents an important step to get the complete understanding of the process and optimize the energy consumption. It can help on the correct design of the process and equipment, and, on process monitoring and decision support, as well as on a better prediction of the final product properties. According to Lundell *et al.* (2011), the fluid mechanics associated with the pulp and paper process can be divided into three groups, directly interlinked, with each group providing input to other: (*i*) the modelling of fiber suspension considering the orientation and concentration of fibers representing the physical meaning as most as possible, (*ii*) experimental methods providing the required data to validate the numerical codes, and to get a more complete knowledge regarding the pulp behaviour, and (*iii*) the rheological characterization of pulp suspension, namely, how the rheological behaviour of the suspension is associated with its characterization, e.g., fiber length, fiber aspect-ratio, and concentration. The better knowledge of the pulp and paper process dynamics involves important questions representing numerical and experimental challenges. These numerical and experimental tasks should, by the end, be able to provide data to explain the influence of the fiber type on the flow, the motion of fibers at different Reynolds numbers, the hydrodynamic interaction of fibers, the distribution and orientation of fibers in space, the knowledge about the flocculation and the behaviour of flocculated suspensions, and how the presence of fibers on the flow interferes with turbulence. The answer to these questions helps to optimize the process at the energy and products level.

Computational methods are applied successfully in many industrial and engineering cases. Still, due to its complexity, the study of the pulp suspensions flow using computational techniques still needs more development. Actually, the use of *Computational Fluid Dynamics* (CFD) tools is increasing its importance to study, at the numerical level, the pulp suspensions behaviour. This kind of tool is a scale neutral tool based on the fundamental laws of mass, momentum and energy, presenting scale-neutral information. The fundamental laws are mathematically described by differential equations that are solved numerically, and the solutions are interpreted for practical design. The continuous development and research for better and complete understanding of the physics involved on the pulp flow behaviour, the improvement on the experimental techniques to visualize and to infer the pulp flow, and the

high technology development observed on the past years allows a more complete study regarding the pulp flow with a more interconnection between the different fields involved. This improvement of knowledge results on a better understanding of idealized fiber suspension flows in less time, and also, in the future, on the understanding of flows with complex cellulose fibers (Cotas, 2012).

Over the years, different mathematical models have been proposed to describe the fiber suspension flows, with an increasing interest on numerical tools to describe this kind of flows. In the literature there are two strategies described to study the pulp flow, each differing in the complexity level and specific domain of application, the pseudo-homogeneous models and the multiphase models (Hämäläinen *et al.*, 2011b). The high computational efforts due to high level of complexity of the multiphase models turn these models appropriate for dilute systems. Contrarily, the pseudo-homogeneous models are appropriate for concentrated systems where the pulp rheological properties are used to characterise the fiber-fiber and fiber-fluid interactions.

In the present work, it is studied numerically the fully developed turbulent flow of concentrated *Eucalyptus* and *Pine* pulps in a pipe using CFD methods. Although this kind of flow presents an industrial interest its understanding still far from being complete. The Newtonian homogeneous single-phase fluid model is reformulated assuming the presence of fibers on the flow (modifications at the local fluid viscosity level) and its influence at the turbulence level is studied (modifications to the k-ε turbulence models). When dealing with pulp suspension flows, the most common measurements made are related to the head loss at various flow velocities and concentrations. The experimental information is used to validate the numerical results, and also, to tune the model parameters on the numerical model developed. The model developed is validated by comparing the pressure drop values with the experimental ones. Also, the behaviour of some variables is compared with the expected behaviour reported in the literature, such as the pulp flow velocity and turbulent quantities. Additionally, it is studied experimentally the flow of *Eucalyptus* pulps using Electrical Impedance Tomography (EIT).

I.2 – MOTIVATION AND SCOPE OF THE THESIS

CFD tools are powerful methodologies to reproduce, numerically, processes occurring at different scales and, in this way, can present an important step towards the improvement of processes and products. In particular, they are useful tools to predict the flow of non-Newtonian fluids, namely under turbulent conditions. These tools can contribute to develop better models describing the flow of fiber suspensions and in this way add information that can help on the design of the conveying systems in the different stages of the process, avoiding oversize of the pumping and piping systems resulting from the use of empirical correlations, and contributing for the energetic optimization of the processes. With the present thesis, the main purpose is to contribute to improve the knowledge related to pulp suspensions flow, taking advantage of the existing CFD studies from literature concerning the flow of non-Newtonian fluids.

The present work is motivated by the successful application of CFD models to simulate the flows of different materials/fluids in different kinds of industry. The work developed under this study is focused on some important facts: (*i*) the predictive models should, as much as possible, translate correctly the phenomena involved during the flow of pulp suspensions; (*ii*) CFD is based on the fundamental principles of conservation; (*iii*) there are only few studies reported in literature concerning the flow of concentrated pulp suspensions using pseudo-homogeneous models; (*iv*) there is a great interest on this subject and most of the published work is based on multiphase models. However, these models require a large quantity of data, the number of fibers in the suspensions has to be limited to avoid a too high simulation time, and thus only dilute systems can be handled due to the computational time and CPU requirements; (*v*) most of the studies reported in literature address separately the experimental, rheological and numerical strategies; (*vi*) in the pulp suspension flows there are different flow regimes and the raw material can have different characteristics, still the studies published in the literature usually take into account just one type of pulp suspension.

A pseudo-homogeneous approach will be applied to describe the flow of different pulp suspensions. Available CFD models will be modified taking into account literature cases for different flows involving the *drag reduction* effect and applied to non-Newtonian fluids. The experimental validation will be made by comparing calculated and propriety experimental

pressure drop data. With this pseudo-homogeneous approach, it is expected to contribute to the improvement of knowledge regarding the flow of concentrated pulp suspensions.

The numerical work present in Part B follows the previous experiments developed under the NODESZELOSS project, COOP-CT-2004-512117. It should be noted that the experimental data mentioned in Part B of this manuscript corresponds to the published (Blanco *et al.*, 2007;Ventura *et al.*, 2007, 2008a, 2008b, 2011) and unpublished data kindly provided by the NODESZELOSS project team. Experimental characterization of the pulp flow regimes using an EIT system, developed by the team of the project PTDC/EQU-EQU/112388/2009, is used in the validation of the CFD model in Part C of this manuscript. This work was developed under the project PTDC/EQU-EQU/112388/2009, financed by FCT/MCTES (PIDDAC) and co-financed by the European Regional Development Fund (ERDF) through the COMPETE program, and also in connection with COST Action FP1005, *Fiber suspension flow modelling: a key for innovation and competitiveness in the pulp & paper industry*.

I.3 – OUTLINE

This document is structured into five main chapters. The current chapter has an introductory character, written to contextualize the reader with the topic of the thesis, pulp suspensions flows and numerical strategy for their description, providing the general concepts concerning the research subject required to understand the other chapters, the main motivation and objectives of the present study. State of art is addressed in the second chapter presenting a summarised review of the scientific literature in the areas of rheology, experimental techniques and numerical methodologies to deal with the pulp suspension flows. Numerical strategies applied to study the flow of different systems with characteristics similar to those of pulp suspensions are presented, including the flow of fiber suspensions. The Part A of this manuscript is composed of these two first chapters.

Part B represents the main part of this document. This part is dedicated to the CFD studies of pulp suspension flows using a pseudo-homogeneous based approach. The Chapters III and IV are devoted to two different CFD approaches: in Chapter III a modified near wall treatment is applied to take into account the presence of fibers on the flow, and a rheological approach is introduced by considering the fluid viscosity not constant as mentioned in literature cases; Chapter IV represents the main and most representative work of this thesis

topic, aiming to analyse the applicability of low-Reynolds-number (LRN) k-ε turbulence models to simulate the flow of pulp suspensions. Different LRN k-ε turbulence models available in the commercial CFD software ANSYS Fluent® (built-in and own-developed) were applied. Additionally, the most suitable turbulence models are modified taking into account literature information for flows with the similar characteristics to the pulp suspension flow, namely, the existence of a *drag reduction* effect. Furthermore, a new rheological model is proposed in this chapter and, finally, the fibers distribution along the pipe radial position is included in the model by considering the pulp consistency as a function of the distance to the wall.

Part C is allocated to the experimental characterization of *Eucalyptus* pulp flow and flow simulation with the pseudo-homogeneous model developed in Chapter IV. EIT is used to distinguish the different flow regimes. Additionally, the CFD model developed in Part B is used to simulate the turbulent flow of *Eucalyptus* pulp characterised experimentally.

The most important conclusions and recommendations for future work are exposed in Part D, Chapter VI. Additional information is collected in Appendix A.

II – STATE OF ART

This chapter describes the existing literature in the flow of pulp fiber suspensions. The literature is reviewed for the different types of flow of pulp fiber suspensions with special emphasis to the pipe flow. Rheological models and some measurements techniques are identified. Different experimental techniques to evaluate the pulp suspension flow are presented. Finally, simulation approaches to describe the flow of pulp suspensions are systematised with special consideration to the pseudo-homogeneous models.

II.1 – RHEOLOGICAL STUDIES

The complete understanding and knowledge of pulp's rheology is necessary for the development of appropriate methods and models, for studying the fiber network deformation and pulp flow behaviour, which even today is not totally complete due to the complex properties and unique behaviour of pulp suspensions. Therefore, the development of suitable strategies to obtain rheological data and appropriate rheological models are of great interest. In fact, in spite of the great importance of establishing a rheological model suitable for pulp suspensions, there is no agreement concerning the model to be used (Blanco *et al.*, 2007; Ventura *et al.*, 2007).

Recently, the growing interest in the suspensions rheology leads to the increase of literature work devoted to the rheological behaviour of different types of suspensions, including pulp fiber. Table II.1 presents a chronological list of important works from the literature giving an insight of the existing literature on the rheology of suspensions. Theoretical and experimental rheological works about rigid particles and flexible fibers are included in the table. The revision studies presented in the literature concerning the rheological behaviour of suspensions are scarce and they are limited to specific type of suspensions. The first review fully dedicated to study the applicability of computer simulations to simulate suspension rheology was presented by Barnes *et al.* (1987).

Table II.1 – Papers that present a review on suspensions rheology.

Authors	Title
Jeffrey and Acrivos (1976)	The rheological properties of suspensions of rigid particles
Cheng and Richmond (1978)	Some observations on the rheological behaviour of dense suspensions
Ganani and Powell (1985)	Suspensions of rodlike particles: literature review and data correlations
Barnes *et al.* (1987)	Applications of computer simulations to dense suspension rheology
Powell (1991)	Rheology of suspensions of rodlike particles
Mewis (1996)	Flow behaviour of concentrated suspensions: predictions and measurements
Petrie (1999)	The rheology of fibre suspensions
Asokan *et al.* (2005)	Review of chaos in the dynamics and rheology of suspensions of orientable particles in simple shear flow subject to an external periodic force
Stickel and Powell (2005)	Fluid mechanics and rheology of dense suspensions
Huhtanen and Karvinen (2006)	Characterization of non-Newtonian fluid models for wood fibre suspensions in laminar and turbulent flows
Kerekes (2006)	Rheology of fibre suspensions in paper making: an overview of recent research
Bousfield (2008)	Rheological issues in the paper industry
Eberle *et al.* (2008)	Rheology of non-Newtonian fluids containing glass fibres: a review of experimental literature
Morris (2009)	A review of microstructure in concentrated suspensions and its implications for rheology and bulk flow
Mewis and Wagner (2009)	Current trends in suspensions rheology
Derakhshandeh *et al.* (2011)	Rheology of pulp fibre suspensions: A critical review
Denn and Morris (2014)	Rheology of non-Brownian suspensions
Haavisto *et al.* (2014)	New insight into rheology and flow properties of complex fluids with Doppler optical coherence tomography

Some studies dealt with the rheology of spherical particles in shear flow (Jeffrey and Acrivos, 1976) and rodlike particles in extensional flow, Newtonian and non-Newtonian fluids (Jeffrey and Acrivos, 1976; Ganani and Powell, 1985; Powell, 1991). Similarly, rheological work devoted to suspensions of rigid particles, long slender particles, was described by Petrie (1999) as well as the rheology of spheres, ellipsoids and rods. Cheng and Richmond (1978) and Stickel and Powell (2005) presented rheological experiments and simulation of the flow/deformation behaviour in mixtures in which the solid phase had high concentration (dense suspensions). The rheological data for red lead oxide slurry (mine tailing), cement grout and barley meal-water mixture were described by Cheng and Richmond (1978). A wide range of instruments was used to measure suspensions rheology and viscosity data. The works presented by Stickel and Powell (2005), Morris (2009) and Denn and Morris (2014) were dedicated to study the rheology of spherical particles; the work presented by Morris (2009) was focussed on the rheology and microstructure of spherical particles and the connection between them. Mewis (1996) and Mewis and Wagner (2009) reviewed literature studies concerning the rheology of spherical and non-spherical particles and, also, the rheology of suspensions when the suspending medium was viscoelastic (Mewis and Wagner, 2009). Eberle *et al.* (2008) gave special attention to rheological experiments used to measure rheological properties of glass fibers in non-Newtonian suspending media. Asokan *et al.*

(2005) analysed rheological work from literature regarding suspensions that could be composed of particles with electric or magnetic charges (dipolar particles).

Particular attention was given to the rheological properties of flexible fiber suspensions with a focus on pulp suspensions (Huhtanen and Karvinen, 2006; Kerekes, 2006; Bousfield, 2008; Derakhshandeh *et al.*, 2011). Huhtanen and Karvinen (2006) reviewed the rheological experiments of pulp fiber suspensions presented in literature (e.g., Möller (1972), Swerin (1995) and Huhtanen (2004)), concerning pipe flow measurements, measurements in a mixing tank near a rotating disk and in an oscillating plate-plate type rheometer. The work presented by Kerekes (2006) addressed the fiber suspension rheology from a papermaking point of view; it covered a wide range of topics, namely, how the pulp suspensions rheology is affected by the forces that could be present in the suspension and by the formation and dispersion of flocs. Also, the fiber network strength and yield stress were addressed. Moreover, this review included a summary of literature concerning the fiber suspensions rheology when chemical additives are present in the suspension. It is important to notice that the work presented by Kerekes (2006) included a section devoted to the applications of pulp suspension rheology and its importance in the papermaking process. Bousfield (2008) reviewed not only the rheology of pulp suspensions but, also, the rheology of paper coating suspensions. The most recent review work related to pulp suspensions is presented by Derakhshandeh *et al*. (2011). Important topics in the area of pulp rheology were discussed in that work, such as, the factors that contributed to the complex rheology of pulp suspensions, the apparent yield stress as well as the different techniques and measurement devices used to measure the viscosity of pulp suspensions. The connection between pulp suspension rheology and pulp flow in a pipe was also presented. The review presented by Haavisto *et al.* (2014) was focused on the rheology of microfibrillated cellulose (MFC); it was dedicated to the effectiveness of applying Optical Coherence Tomography (OCT) to measure rheological properties of complex fluids, and, to the application of this technique outside the medical field.

Section II.1.1 presents the most relevant works dealing with the rheology of pulp suspensions both measurement techniques and rheological modelling being addressed.

II.1.1 – PULP SUSPENSIONS

The rheological behaviour of pulp suspensions has been studied by several authors and new techniques have been proposed. Numerous studies have been developed concerning the applicability of experimental rheological strategies, standard and adapted to obtain rheological measurements data for multiphase systems as, for example, pulp suspensions. Thereafter, different rheological measurement techniques were proposed to obtain and characterise the rheology of pulp suspensions, namely, in-line and off-line techniques. The simultaneous measurement of pressure drop and flow rate during the flow of pulp allows obtaining in-line rheological data. Alternatively, the use of different rheometer configurations allows acquiring off-line rheological data. Simultaneously, the applicability of non-Newtonian rheological models developed for single-phase fluids to describe the rheology of pulp suspensions has been studied, and several strategies to model pulp suspensions rheology have been proposed.

II.1.1.1 – MEASURING TECHNIQUES

Rotational rheometers

One approach to measure the rheological properties of suspensions is by rotational viscometers or rheometers. Table II.2 summarises the literature studies using rotational rheometer to analyse the rheology of fiber suspensions with emphasis on pulp suspensions.

There are several studies for rheological data acquisition of suspensions with different characteristics from those of pulp fiber suspensions, as previously mentioned. Underwood (1976) developed a modified Brookfield viscometer able to measure viscosity data of slurry or suspension. This device was composed of a Brookfield viscometer with additional twelve "Tee-bar" spindles. Marti *et al.* (2005) characterised the flow behaviour of suspensions of pure glass fibers, pure glass spheres and the mixture of glass fibers and glass spheres. They used a strain-controlled rheometer with Couette geometry, and image analysis to investigate the time-dependent and shear-rate dependent flow behaviour. Saarikoski *et al.* (2012) combined different techniques to obtain rheological information of MFC suspensions prepared from never dried pre-refined *Birch* pulp. They measured the rheological properties in a rotational rheometer with concentric cylinders geometry combined with a visualization

Table II.2 – Summary of literature work on the pulp suspensions rheology – rotational devices.

References	Fiber suspension type	Rheological measurement method	Rheological models
Gullichsen and Härkönen (1981)	Bleached *Pine kraft* pulp suspension	Rotary shear tester with a concentric-cylinder geometry Measurement of torque and rotational speed High speed photographs	-
Bennington *et al.* (1991)	Semi-bleached *kraft* pulp suspension	Rotary shear tester with a concentric-cylinder geometry Rotor/housing combinations: wide-gap and narrow-gap Measurement of torque and rotational speed High speed photographs	-
Bennington and Kerekes (1996)	Semi-bleached *kraft* softwood pulp suspension	Rotary shear tester with a concentric-cylinder geometry Rotor/housing combinations: wide-gap Measurement of torque and rotational speed	-
Silveira *et al.* (2002, 2003a, 2003b)	*Eucalyptus* and *Pine* bleached *kraft* pulp suspensions	Brookfield digital viscometer (model DV-II)	Fitted expressions of viscosity data
Blanco *et al.* (2007)	Bleached hardwood *kraft* pulp suspension – *Eucalyptus globulus* fibers	Searle-type rotational device, three different internal rotors: cylinder, plates and bars Shear rate calculated from rotational speed of the rotor Shear stress calculated from the torque of the inner cylinder Apparent viscosity calculated from the torque and rotational speed	-
Ventura *et al.* (2007)	Long- and short-fiber bleached *kraft* pulp suspensions – *Eucalyptus* and *Pine* fibers	Plate rotational viscometer based on the Searle effect Measurement of shear in the rotor and in the vessel, quantification of the torque applied by the rotor and transmitted by the pulp to the vessel	Herschel-Bulkley model
Gomez *et al.* (2010)	Bleached softwood *kraft* pulp fiber suspensions Carbopol 940 powder dispersed in deionized water	Bohlin C-VOR rheometer, controlled stress mode Measurement of flow curves	Herschel-Bulkley model
Chaussy *et al.* (2011)	Bleached *kraft* softwood fibers	Semi industrial disk refiner Shear stress calculated from the net torque obtained from the net mechanical power Shear rate calculated from angular velocity	Modified Carreau-Yasuda model
Saarikoski *et al.* (2012)	Microfibrillated cellulose prepared from never-dried birch pulp	Rotational rheometer equipped with a camera and OCT Imaging the flow across the rheometer gap through a camera Calculation of shear stress and shear rate	-
Sorvari *et al.* (2013)	Microfibrillated cellulose prepared from never-dried bleached *kraft* birch pulp	Rotational rheometer equipped with a camera and OCT Imaging the flow across the rheometer gap through OCT and camera Calculation of shear stress and shear rate	-
Yu *et al.* (2015)	Unbleached wheat straw pulp	Novel device based on an oscillating torsional resonator Continuously-varying-frequency capability Measurement of frequency-dependent viscoelastic properties	Power-law model

technique where photographs were taken with a camera to see the modifications on floc structure when changing the shear conditions. Similarly, Sorvari *et al.* (2013) studied the rheology of MFC suspensions prepared from never dried bleached *kraft Birch* pulp, using the same strategy as described by Saarikoski *et al.* (2012). They combined a rotational rheometer with concentric cylinders geometry with a camera, also, they include an additional imaging technique, Optical Coherence Tomography. It is of interest to refer that the strategy presented by Sorvari *et al.* (2013) allows obtaining the rheograms for the MFC suspension, taking images to see the macroscopic floc structure and obtaining information about the pulp behaviour until very near the wall, through the rheometer gap.

Relevant work was presented in literature concerning the application of rotational devices to characterise the rheological behaviour of pulp fiber suspensions. There are some studies where it is applied commercial equipment, modified or not adapted, to obtain rheological and viscosity data of pulps. Gullichsen and Härkönen (1981) used a rotary device that they built, to measure the torque and rotational speed to characterise the flow of bleached pine *kraft* pulp suspensions. The device had a transparent wall to allow visualizing the flow and making ultra-rapid films to see the turbulent movement which is difficult to see by the operator just by eye visualization. Bennington *et al.* (1991) measured the torque vs. rotational speed of semi-bleached *kraft* (SBK) fiber suspensions in a rotary shear tester with concentric-cylinder geometry, a rotary device similar to that used by Gullichsen and Härkönen (1981). This device was constructed in such a way (housing with baffles) to avoid slippage between the rotor and the suspension interface, lugs in the rotor, and to inhibit slip at the outer wall. Two types of rotor/housing configurations were tested: wide-gap and narrow-gap. They found that the flow behaviour was dependent on the geometry of the mixing device, the shear rate, the air content in the suspensions, the fiber type and the properties of the suspending medium. Another study was presented by Bennington and Kerekes (1996) considering SBK pulp suspensions and using a similar device to the one developed in Bennington *et al.* (1991); however, this new study involved only the wide-gap rotor/housing configuration. Silveira *et al.* (2002, 2003a, 2003b) employed a Brookfield digital viscometer to study the influence of consistency, fiber length, temperature, mixture of different fibers, and pH, on the viscosity of *Eucalyptus* and *Pine* bleached *kraft* pulp suspensions. Silveira *et al.* (2002) fitted the viscosity results to obtain an expression for viscosity as a function of consistency and fiber length which correlated well with the viscosity data. Silveira *et al.* (2003a) proposed an expression to describe the dependency of viscosity on the temperature for *Eucalyptus* and *Pine* pulps, and, they also studied the dependency of the viscosity of mixtures of *Eucalyptus* and *Pine* pulp on

the mass fraction of each fiber type. Silveira *et al.* (2003b) developed an expression for pulp viscosity as a function of pH and pulp consistency which agreed well with the experimental data obtained in the Brookfield digital viscometer.

The development of a different geometry rheometer to deal with pulp suspensions was investigated by Blanco *et al.* (2007) and Ventura *et al.* (2007). Blanco *et al.* (2007) employed a Searle-type rotational device with three different rotor configurations: concentric cylinders, plates and bars. Furthermore, Ventura *et al.* (2007) analysed the rheological properties of pulp suspensions in a similar Searle-type rotational device, but considering a plate type configuration which was the best configuration described by Blanco *et al.* (2007) to deal with pulp fiber suspensions. This rheometer favoured the homogeneous distribution of the pulp suspension and made wall effects almost negligible due to the dimensions of the chambers. Two different types of pulp suspensions were used to test the new rheometer: *Eucalyptus* (Blanco *et al.*, 2007; Ventura *et al.*, 2007) and *Pine* (Ventura *et al.*, 2007) pulp suspensions. The rheograms were obtained by correlating the shear stress and shear rate with the measured torque and rotational speed of the rotor, respectively. From the rheograms data it could be calculated the apparent viscosity of pulp suspension. The work presented by Ventura *et al.* (2007) besides presenting data obtained with a similar device to that of Blanco *et al.* (2007) was focused on the study of the application of the rheological Herschel-Bulkley model, which, according to the authors could be used to describe the pulp suspensions rheology. Moreover, the influence of pulp consistency, fiber length and temperature on the rheological parameters important to describe the stress-shear rate curve for pulp suspensions was investigated and statistical models were produced which allowed predicting pulp suspensions viscosity.

One interesting idea was developed by Gomez *et al.* (2010). This idea was based on using another fluid with rheological behaviour similar to pulp fiber suspension (equivalent fluid) and, thus, avoid rheological tests with pulp fiber suspensions that are complex systems to analyse with the most common commercial equipment. They tested carbopol, crosslinked polyacrylate polymer solutions, as a similar fluid to study the mixing of pulp fiber suspensions. The tests were performed in a rheometer with a wide-gap cup and four-vane geometry, under controlled stress conditions.

Another study to characterise the rheology of pulp fiber suspensions was presented by Chaussy *et al.* (2011). Here the authors considered a semi-industrial disk refiner to obtain the rheological data for industrial bleached *kraft* softwood fibers. They considered the disk refiner as a plate rotational rheometer. The shear rate was obtained from the angular velocity of the

refining machine, and the shear stress at the periphery of the refiner from the net mechanical power and angular velocity.

Recently, Yu *et al.* (2015) proposed a new device based on oscillatory shear to measure the rheological properties of unbleached wheat straw pulp. The torsion resonator equipment developed allowed the variation of frequency continuously. The viscosity data were fitted with a power-law model considering viscosity as a function of frequency.

Ultrasound velocity profiling - pressure difference and ultrasonic Doppler velocimetry

Ultrasound velocity profiling (UVP) simultaneous with pressure drop (PD) measurement have been reported to characterise the rheology of different non-Newtonian fluids as, for example, yoghurt, cheese sauce, vegetable sauce, mayonnaise, mineral slurry, (Wiklung *et al.*, 2007; Wiklund and Stading, 2008), cellulose suspensions and microfibrillated cellulose suspensions (Haavisto *et al.*, 2010, 2011) and, also, pulp fiber suspensions (Wiklung *et al.*, 2006; Wiklund and Stading, 2008) (see Table II.3). Ultrasound velocity profiling simultaneously with pressure drop measurements is employed to obtain rheological information of a pulp suspension composed of a mixture of *Pine* and *Spruce* fibers (Wiklung *et al.*, 2006), cellulose pulp (Wiklund and Stading, 2008) and bleached *Birch* pulp (Haavisto *et al.*, 2010, 2011). A vertical pipe rheometer was used in the work of Haavisto *et al.* (2010, 2011) and, instead, a horizontal pipe rheometer was tested by Wiklung *et al.* (2006) and Wiklund and Stading (2008). The measurements performed by Wiklung *et al.* (2006) for plug flow regime showed that the plug radius could be obtained, with the UVP measurement technique, which was correlated to the yield stress and pressure drop. Additionally, Wiklung *et al.* (2006) compared the UVP technique and Laser Doppler Anemometry (LDA) for velocity data acquisition, and they had shown that LDA failed to detect the velocity gradients near the pipe wall. Wiklung *et al.* (2008) compared the apparent viscosity profiles of different non-Newtonian fluids, using Ultrasound Velocity Profiling and Pressure Difference (UVP-PD) method and conventional rheometers; however, no data was presented for cellulose pulp. Haavisto *et al.* (2010, 2011) determined the apparent viscosity of *Birch* pulp suspensions and MFC suspensions from the velocity profile measured by the UVP technique and pressure drop measurements. They compared the viscosity of MFC suspensions obtained in the pipe rheometer with that acquired in a conventional rheometer (stress controlled rotational rheometer with vane geometry). Both rheological techniques were able to measure the rheology of MFC with good agreement between those data. Also, the rheology of *Birch* pulp

was obtained from the pipe rheometer and it was found that the viscosity of *Birch* pulp is lower than that of MFC suspensions (Haavisto *et al.*, 2011).

Table II.3 – Summary of literature work on pulp suspensions rheology – ultrasound velocity profiling - pressure drop measurement and ultrasonic Doppler velocimetry.

References	Fiber suspensions type	Rheological measurement methods	Rheological models
Wiklung *et al.* (2006)	Bleached *kraft* pulp suspension: *Pine* and *Spruce*	Ultrasound velocimetry profiling equipment	Herschel-Bulkley model
Wiklund and Stading (2008)	Cellulose pulp	Ultrasound velocimetry profiling equipment; Conventional rheometers: controlled strain rheometer (Bohlin VOR) and controlled stress rheometer (Stresstech HR) concentric cylinder geometries	Power-law model
Derakhshandeh *et al.* (2010)	Bleached softwood *kraft* pulp Bleached hardwood *kraft* pulp Thermal-mechanical pulp Stone-ground wood pulp suspension	Stress-controlled Kinexus rotational rheometer Measurement of steady-state shear rates for constant shear stress values Haake RV12 viscometer coupled with ultrasonic Doppler velocimetry Measurement of local velocity and shear stress distributions across the gap Stress distribution calculated based on the torque imposed on the moving vane Local shear rate calculated from the velocity profile	Power-law model Herschel-Bulkley model
Haavisto *et al.* (2010, 2011)	Bleached *birch* pulp suspension	Ultrasound velocimetry profiling equipment	-
Derakhshandeh *et al.* (2012)	Stone-ground wood pulp suspension	Stress-controlled Kinexus rotational rheometer Shear rate calculated from the torque applied and vane rotational velocity Rate-controlled Haake RV12 viscometer coupled with pulsed ultrasonic Doppler velocimetry Stress distribution obtained from the torque imposed on the moving cylinder Local shear rate obtained from the velocity profile measured by ultrasonic Doppler velocimetry	Herschel-Bulkley model Kohlrausch-Williams-Watts function

Only a scarce number of studies have been reported in literature suggesting the use of ultrasonic Doppler velocimetry (UDV) coupled with conventional rheometry to study the rheological properties of pulp suspensions (see Table II.3). This measurement technique was reported by Derakhshandeh *et al.* (2010) and Derakhshandeh *et al.* (2012). They proposed to link together UDV with conventional rheometry (four-bladed vane geometry) to study the rheological properties of bleached softwood *kraft* (Derakhshandeh *et al.*, 2010), bleached hardwood *kraft* (Derakhshandeh *et al.*, 2010), thermal-mechanical (Derakhshandeh *et al.*, 2010) and stone-ground wood pulp (Derakhshandeh *et al.*, 2010, 2012). Ultrasonic Doppler

velocimetry combined with conventional rheometry provided information about the shear stress distribution across the rheometer gap by using the torque data and information about the local shear rate distribution obtained from the velocity profile given by the UDV method.

II.1.1.2 – RHEOLOGY MODELLING

Some studies have been developed towards the modelling of the rheological behaviour of suspensions. However, only a scarce number of studies are dedicated to modelling the rheological behaviour of pulp suspensions. The majority of the literature reviewed here is about modelling the rheology of non-spherical suspensions with emphasis on flexible fibers. Literature work on the numerical rheological behaviour of non-spherical suspensions is summarised in Table II.4.

Table II.4 – Summary of literature work modelling non-spherical suspensions rheology.

References	Fiber suspensions type	Rheological modelling strategy
Barbosa and Bibbó (2000)	Suspensions of cylindrical particles	Hydrodynamic approach
Switzer III and Klingenberg (2003)	Non-Brownian, flexible fiber suspensions	Particle-level model
Lin *et al.* (2006a)	Suspensions of cylindrical particles	Shear stress calculated based on the mean orientation distribution function of fibers
Chatterjee and Wu (2008)	Spherical polystyrene beads	Dissipative particle dynamics
Lindström and Uesaka (2009)	Monodispersed non-Brownian fiber suspensions	Particle-level model
Yamanoi and Maia (2010)	Suspensions of rigid fibers	Particle simulation method
Yamanoi *et al.* (2010)	Suspensions of flexible fibers	Particle simulation method

Barbosa and Bibbó (2000) investigated the rheology of suspensions composed of cylindrical particles, based on a hydrodynamic approach. They first studied the equations of motion for fibers which were specified in terms of spherical polar angles that characterise the orientation of fibers. The fiber orientation was specified as a function of shear rate and initial fiber orientation. The rheological study considered that the shear stress was related to both the contribution of stress from the solvent and stress from the fibers and took into account the fiber orientation distribution. The viscosity of the suspension was expressed taking into account the spherical polar angles that characterised the orientation of fiber and the number of fibers present in the domain.

A particle-level simulation was applied by Switzer III and Klingenberg (2003) to characterise the rheology of flexible fibers suspensions. They considered that the flexible fiber was represented by rigid cylinders with hemispherical end caps linked by ball and socket joints. This method was based on equations of motion for each fiber that took into account position and orientation over the time. The suspension stress was obtained considering

particle positions and orientations. Switzer III and Klingenberg (2003) analysed the effect of fiber shape and friction, aspect ratio and stiffness, and flocculation on the viscosity of fiber suspensions. Also, they predicted numerically the yield stress.

Lin *et al.* (2006a) studied the rheological properties of suspensions composed of rigid cylinders flowing in a channel. They analysed the shear stress, the first normal stress difference, and the relationship between them, orientation distribution function and shear rate. The mean equation for the orientation distribution function of fibers was derived based on the relation between the fluctuating orientation distribution function and angular velocities-correlated terms. Through the orientation distribution of fibers they concluded that the fiber orientation distribution in laminar channel flow differed greatly from that in turbulent regime flow.

Chatterjee and Wu (2008) considered a dissipative particle dynamics to simulate the rheological behaviour of non-dilute spherical polystyrene beads suspensions. In this approach, they considered two distinct types of particles: fluid particles representing the water, and solid particles representing the polystyrene. The validation of the numerical scheme was made through the comparison between the numerical viscosity values versus shear rate predicted, and experimental measurements performed in a shear rate controlled cone-plate viscometer.

Lindström and Uesaka (2009) investigated numerically the rheology of monodispersed non-Brownian fibers suspension through particle level simulation. The effect of fiber flexibility and ability to form fiber network on the rheology of the suspension was not taken into account. The model took into account the fluid phase and the solid phase, fibers, described separately, and fiber-fluid interactions as well as fiber-fiber interactions. Navier-Stokes equations were used to describe the motion of the fluid. The fibers were represented as chain of fiber segments with cylindrical geometry. The apparent viscosity of the suspension, dimensionless first normal stress difference and dimensionless second normal stress difference were related to the orientation distribution of the fibers. They investigated the effect of fiber aspect-ratio, concentration and interparticle friction coefficient on the apparent viscosity of the suspension, first and second normal stress difference. Also, they proposed an expression for each of the rheological properties (apparent viscosity of the suspension, dimensionless first normal stress difference and dimensionless second normal stress difference) as a function of fiber aspect-ratio, concentration and interparticle friction coefficient.

Yamanoi and Maia (2010) studied the rheology of suspensions composed of rigid fibers modelled as a series of connected beads. The strategy proposed was a direct fiber simulation.

They studied the rheology of fibers for different fiber concentrations and aspect-ratios. The same strategy, direct fiber simulation, was studied by Yamanoi *et al.* (2010); they simulated the rheology of suspensions composed of flexible fibers modelled as series of connected beads. The rheological properties studied were viscosity and the first and second normal stresses for different fiber suspension concentration and fiber aspect-ratios. The numerical model did not take into account the far-field hydrodynamic interactions, which must be the main reason given by Yamanoi *et al.* (2010) to explain why the predictions and literature data were not totally in agreement.

Noteworthy, the difficulties described above make the measurement of the rheological properties of pulp fiber suspensions very challenging. How to measure and how to express yield stress is one of the most important factors for which data is still scarce. The major reason is the difficulty and high uncertainly of data for very low values of shear rate. A high level of interest for the development of suitable rheological methods is observed presently.

In summary, fiber suspensions are complex multiphase systems and their rheological characterization is difficult to investigate, either with experimental or modelling techniques. Different strategies have been developed but still more detailed knowledge of the rheology of fiber suspensions, including pulp fiber suspensions, is necessary for the development of complete models and experimental techniques to characterise this type of mechanical systems. The development of an appropriate rheological model as well as rheological measurements needed to characterise pulp's rheology will be discussed in the next chapters of this thesis.

II.2 – EXPERIMENTAL FLOW STUDIES

Proper design of piping systems in pulp and paper mills must be made with precise knowledge about how the presence of fibers and fiber characteristics, such as fiber aspect-ratio, fibers interactions, and fiber type, influence the flow behaviour. The complex nature of fiber suspensions, which can interfere with internal measurement devices as well as their opacity make their flow visualisation and characterisation difficult. There have been proposed several experimental techniques to investigate the different flow regimes and mechanisms when pulp fiber suspensions are present in the flow, either in straight pipes or channels, with or without turbulence generators. Actually, the complete knowledge of pulp fiber suspensions flows represents an important task. A scarce number of reviews on experimental techniques to

characterise such pulp flows have been published. Table II.5 focuses on the review of the existing literature on experimental visualisation and characterisation of pulp suspensions flow dynamics.

Table II.5 – Papers that present a review on experimental techniques to characterise pulp suspensions flows.

Authors	Title
Duffy (2006)	Measurements, mechanisms and models: Some important insights into the mechanisms of flow of fibre suspensions
Cui and Grace (2007)	Flow of pulp fibre suspension and slurries: A review
Björkman (2008)	The nonlinear history of fibre flow research. Part 1: Background and beginning
Powell (2008)	Experimental techniques for multiphase flows

Duffy (2006) discussed important aspects of flow of pulp fiber suspensions: the mechanisms, measurement techniques and some of the models proposed to correlate the head loss with pulp and flow characteristics. In that review, the author discussed the effects of changing the liquid properties on floc size, pressure drop, and velocity profile. The influence of pipe roughness was discussed. It was also discussed how the channel size could affect the pulp flow. The author presented also how the acceleration and deceleration rates influenced the head loss curve for bleached and unbleached *kraft Pine* pulps. Heat transfer measurements were reviewed and it was discussed the correspondence between the heat transfer coefficient and pressure drop for *Pine, Eucalyptus* and *Spruce* pulps.

The review presented by Cui and Grace (2007) was dedicated to experimental techniques used to study the flow of pulp fiber suspensions and slurries. The authors summarised and discussed works presented in literature related to the flow of pulp suspensions. Those works were divided into two categories: one considering two-phase flows (fibers and water) and another considering three-phase flows (fibers, water and air).

Björkman (2008a) presented a historical review with the developments from the very beginning in pulp fiber suspensions flow. The author showed in that work the historical development to get knowledge about pulp flow until about the 1960s. The continuation of this historical review was presented in Björkman (2008b).

Powell (2008) discussed five experimental methods that could be applied to study the flow of multiphase systems, such as pulp fiber suspensions, tomato paste and starch suspensions. The author discussed in more detail two techniques, magnetic resonance imaging (MRI) and ultrasonic pulsed Doppler velocimetry (UPDV). It was also provided a summary of the techniques discussed by the author in that paper, and the limitations and capabilities of each technique.

The most relevant experimental techniques that have been reported in literature to examine and characterise the flow of pulp suspensions are the electrical impedance tomography (EIT), laser Doppler anemometry (LDA), particle image velocimetry (PIV), nuclear magnetic resonance imaging (NMRI), ultrasonic Doppler profiling (UDP), and ultrasound velocity profiling (UVP). Sections II.2.1 to II.2.3 summarise important works where flow monitoring of fiber suspensions, namely pulp suspensions, are presented and discussed.

II.2.1 –PRESSURE DROP MEASUREMENTS

The numerical research performed in this work, Part B, deals with the simulation of the flow of *Eucalyptus* and *Pine* pulp suspensions in a pipe. The flow behaviour was evaluated in previous experiments, NODESZELOSS project, COOP-CT-2004-512117, by pressure drop and flow rate measurements. However, these measurements in spite of being able to obtain information about the flow dynamics of pulp suspensions is not, on its own, enough to get information about the complexities that take place in the flow of pulp suspensions. Furthermore, the number of studies that have been devoted to study the flow of pulp suspensions in this way is still scarce (see Table II.6). Most of these studies evaluated the flow behaviour of dilute pulp suspensions, consistency in the range 0 to 1 % w/w (Kerekes *et al.*, 1985).

Yokogawa *et al.* (1985) studied the flow of pulp suspensions in a vertical duct for different types of turbulence generators placed at the duct inlet. That study was performed to get knowledge about the correlation between the fiber concentration and the turbulence intensity. The turbulence intensity was obtained based on total and static pressure separate measurements. The two pressure values measured were correlated with mean and variation components of bulk velocity which were then associated with turbulence intensity. The fiber concentration was inferred by measuring the laser light that was transmitted from one side of the duct wall and received by a photo cell embedded in the opposite wall of the duct. Experimental results of distribution of turbulence intensity and distribution of fiber concentration for different flow conditions and pulp consistencies were presented. The type of turbulence generator and bulk velocity revealed to have a significant effect in pulp concentration. The results showed that concentration and turbulence intensity were inversely connected.

Table II.6 – Summary of pressure drop measurement tests to characterise the flow of pulp suspensions.

Reference	Geometry	Fiber type	Experimental data	Conditions analysed
Yokogawa *et al.* (1985)	Vertical channel flow	*Kraft* pulp suspension	Pressure loss	Pulp consistency: 0.44-0.46 % Mean flow velocity: 0.5-3.0 m s^{-1}
Ogawa *et al.* (1990a)	Vertical pipe flow	Beaten hardwood bleached *kraft* pulp suspension	Pressure loss Local velocity	Pulp consistency: 0.15-0.62 % Reynolds number: 5800-19800
Ogawa *et al.* (1990b)	Vertical pipe flow	Beaten hardwood bleached *kraft* pulp suspension	Pressure loss Local velocity	Pulp consistency: 0.13-0.53 % Reynolds number: ~125-1200
Kazi *et al.* (1999)	Horizontal pipe flow	Bleached *kraft* *Pinus Radiata* pulp suspension	Pressure loss Inlet, outlet and wall temperatures Flow rate	Bulk velocity: 0.6-8.0 m s^{-1} Pulp consistency: 0.5-0.8 %
Ventura *et al.* (2008b)	Horizontal pipe flow	Recycled pulp suspension Refined *Eucalyptus* bleached *kraft* pulp suspension *Pine* unbleached *kraft* pulp suspension *Eucalyptus* (90%) and *Pine* (10%) bleached pulp suspension	Pressure loss Flow rate Temperature	**Recycled pulp** Consistency: 0.70-4.30 % Mean flow velocity: 1.5-6.0 m s^{-1} ***Eucalyptus* pulp** Consistency: 0.84-3.50 % Mean flow velocity: 0.1-6.0 m s^{-1} ***Pine* pulp** Consistency: 0.80-3.60 % Mean flow velocity: 0.1-6.0 m s^{-1} ***Eucalyptus* (90%) and *Pine* (10%) pulp** Consistency: 0.90-3.20 % Mean flow velocity: 0.1-6.0 m s^{-1}
Kazi *et al.* (2015)	Horizontal pipe flow	Bleached and unbleached *kraft* softwood *Pine* pulp suspensions	Pressure loss Inlet, outlet and wall temperatures Flow rate	Pulp consistency: 0.05-0.4 % Heat flux: 4.0-85 kW m^{-2} Velocity for pressure drop tests: 0.26-10.5 m s^{-1} Velocity for heat transfer tests: 0.26-4.0 m s^{-1}

Ogawa *et al.* (1990a) carried out experiments to determine pressure drop values and velocity profiles in flow of hardwood bleached *kraft* pulp in a vertical pipe. Pressure transducers were used to measure the pressure drop in transitional and turbulent pulp flow regimes. The velocity profiles were obtained from local velocity measurements made by an electrode probe with an electrochemical technique. The authors presented pressure loss curves for various values of pulp consistency, freeness and flow rate. Additionally, they represented the friction factor versus Reynolds number for different values of pulp consistency. The velocity profile measured allowed them to conclude that in the fully wall layer, the velocity profile was not different between the regions of lower and higher Reynolds number values. For lower Reynolds number the profile started to be more flat in the vicinity of the pipe centre.

Ogawa *et al.* (1990b) studied the flow of hardwood bleached *kraft* pulp in a vertical pipe, similarly to that reported by Ogawa *et al.* (1990a). However, the conditions tested were

different from those presented in Ogawa *et al.* (1990a). The pressure loss and local velocity were obtained using pressure transducers and by an electrochemical technique using an electrode probe, respectively. The flow regime evaluated for the conditions tested was plug flow regime. The representation of friction factor as a function of Reynolds number was presented. Additionally, shear rate data at the wall were represented as a function of flow rate, and an expression was proposed to correlate these data. The correlation between pressure drop data and wall shear stress was discussed. The velocity distributions obtained from the local velocity measurements were used to propose an expression for radial distribution of local viscosity of pulp suspension as an exponential function of radial position.

Kazi *et al.* (1999) investigated the heat transfer and flow dynamics of pulp suspensions in a pipe. The experimental apparatus included a heat transfer section composed of 10 Watlow band heaters around the pipe wall (Kazi *et al.*, 1999). That work discussed both the effects of heat and momentum transfer, evaluated by the heat transfer coefficient, friction factor and drag reduction. The heat and flow information was obtained for different grades of pulp, different pulp consistencies and mean flow velocities. The authors concluded that the presence of fibers in the flow created a *drag reduction* effect and, also, a reduction of heat transfer coefficient.

Ventura *et al.* (2008b) studied the flow of different types of pulp suspensions under different conditions. The authors studied the flow dynamic of four different pulp suspensions: recycled, *Eucalyptus*, *Pine*, and a true mixture of *Eucalyptus* (90 %) with *Pine* (10 %) pulp. Pressure drop was measured using a differential pressure meter, while flow velocity was obtained with a magnetic flow meter. The rig allowed also temperature control and monitoring. The influence of pulp consistency, mean flow velocity, pipe diameter and pipe material was investigated for each type of pulp. A series of tests was performed to investigate the applicability of published design correlations for head loss, before the maximum in the head loss curve, to fit the experimental data. Furthermore, new correlations were proposed to predict the pressure loss after the onset of turbulence in the water annulus. The experimental data and the proposed design correlations showed that pressure drop of pulp suspensions was not changed significantly by the pipe material. However, the pulp consistency, mean flow velocity, and pipe diameter presented a strong influence on the flow dynamics of pulp suspension.

Kazi *et al.* (2015) presented a similar study to the previous one from the same authors, Kazi *et al.* (1999); however, this new study involving heat transfer and flow dynamics of pulp suspension was more complete. The authors investigated if and how pressure drop and

temperatures, for different flow rates, were influenced. They studied the effect of fiber consistency, bleaching, increasing fiber flexibility, different grades of lignin-rich fibers, and fiber variation from different parts of the tree growth ring, on those parameters. The heat and momentum transfer were both influenced in a similar way by those parameters.

II.2.2 – ELECTRICAL PROCESS TOMOGRAPHY

The flow experiments conducted in this work, Part C, were performed using an electrical impedance tomography (EIT) system to get qualitative information about the different types of flow regimes in the flow of pulp suspensions. A scarce number of studies have been dedicated to study the applicability of EIT systems to monitor the flow of pulp fibers. Table II.7 summarises experimental tests from literature where the EIT technique and electrical resistance tomography (ERT) were used for flow measurements in pulp suspensions. From this table, it can be seen that the application of EIT systems to measure the flow of pulp suspensions is rare. The ERT technique despite of being more studied than the EIT system is considered only in few works (see Table II.7).

Zhou and Halttunen (2003) described an EIT system to measure the consistency profile of a concentrated pulp suspension. That system was composed of a 16-electrode sensor; the amplitude and frequency of the injected current were the measurement parameters. A reconstruction algorithm, modified Newton-Raphson algorithm, was used to reconstruct the resistivity profile. The measurements were obtained in a cylindrical tank pipe, diameter of 6 cm, full of pulp, and without pulp flow; plastic tubes with 2 cm of diameter were used to create different areas of resistivity.

Heikkinen *et al.* (2010) discussed the applicability of the ERT technique to measure the flow of pulp suspensions with consistency of 1.69 % in a vertical pipe, and to measure the flow of pulp with consistency of 10 % downstream a mixer to evaluate the homogeneity of the mixture. The flow measurements were performed with an ERT system composed of four different layers of 16 electrodes each, for the flow of a pulp suspension with consistency of 1.69 %, in a vertical pipe, inner diameter of 100 mm, and mean flow velocity 0.36 m s^{-1} (Heikkinen *et al.*, 2010). The tests to evaluate mixture homogeneity downstream a mixer unit were performed with an ERT system with three different layers of 16 electrodes each. The mean volumetric flow rate tested was 150 dm^3 s^{-1} and pulp suspension consistency 10 %

(Heikkinen *et al.*, 2010). The authors showed that ERT was a viable technique to measure on-line the pulp flow and mixing efficiency.

Table II.7 – Summary of electrical process tomography tests to characterise the flow of pulp suspensions.

Reference	Geometry	Fiber type	Experimental data	Conditions analysed
Zhou and Halttunen (2003)	Vertical cylindrical tank	Pulp suspension	Resistivity profiles	Pulp consistency: 3.5 %
Heikkinen *et al.* (2010)	Vertical pipe flow	Pulp suspensions	Conductivity distributions	**Pulp flow measurements** Pulp consistency: 1.69 % Flow velocity: 0.36 m s^{-1} **Pulp measurements after a mixer** Pulp consistency: 10 % Volumetric flow rate: 150 dm^3 s^{-1} Velocity of pulp suspension > 2.0 m s^{-1}
Yenjaichon *et al.* (2011)	Horizontal pipe flow	Mixture of pulp suspension with chlorine dioxide	Conductivity distributions	Flow rate: 390 to 225 dm^3 s^{-1} Consistency: 4.7 to 3.2 %
Yenjaichon *et al.* (2012)	Horizontal pipe flow	Bleached softwood *kraft* pulp suspensions	Conductivity distributions	Pulp consistency: 0.0-3.0 % Mainstream pipe velocity: 0.5-5.0 m s^{-1} Side-stream jet velocity: 1.0-12.7 m s^{-1} Jet-to-pipe diameter ratio: 0.05-0.208
Yenjaichon *et al.* (2013a)	Horizontal pipe flow	Bleached softwood *kraft* pulp suspensions	Conductivity distributions	Pulp consistency: 0.0-3.0 % Superficial pulp velocity: 0.5-5.0 m s^{-1} Superficial gas velocity: 0.11-0.44 m s^{-1}
Yenjaichon *et al.* (2013b)	Horizontal pipe flow	Bleached softwood *kraft* pulp suspensions	Conductivity distributions	Pulp consistency: 0.0-3.0 % Superficial pulp velocity: 0.5-5.0 m s^{-1} Gas volume fraction: 0.02-0.47 Gas mass flow rate: 0.74-4.9 g s^{-1} Superficial gas velocity: 0.11-0.44 m s^{-1}
Faia *et al.* (2015a)	Horizontal pipe flow	Rayon fibers: - length: 2.0 mm - diameter: 60 µm	Conductivity distributions Radial velocity profiles	Suspensions concentration, nL^3 = 5-20 Flow velocity: 0.5-1.5 m s^{-1}
Faia *et al.* (2015b)	Horizontal pipe flow	*Eucalyptus* bleached *kraft* pulp suspension *Pine* unbleached *kraft* pulp suspension	Conductivity distributions Flow velocity	***Eucalyptus* pulp** Consistency: 1.0-2.35 % Mean flow velocity: 0.5-3.0 m s^{-1} ***Pine* pulp** Consistency: 1.0-2.35 % Mean flow velocity: 0.5-3.0 m s^{-1}

Yenjaichon *et al.* (2011) studied the mixing quality between pulp suspension and chlorine dioxide (ClO_2) in an industrial mixer using ERT. This system was placed downstream an industrial static mixer, in the first stage of chlorine dioxide bleaching process, in Howe Sound Pulp and Paper Ltd, Port Mellon, Canada. The authors evaluated the applicability of that technique for different flow conditions, namely, pulp flow rate, pulp consistency and flow rate of chlorine dioxide. The flow rate of chlorine dioxide was tested approximately between 2 and 24 dm^3 s^{-1}, the pulp flow rate between 390 and 225 dm^3 s^{-1}, and pulp consistency in the range 4.7 to 3.2 %. The results presented by the authors allowed them

to conclude that the ERT technique was appropriate to analyse the flow and mixture homogeneity downstream an industrial static mixer for pulp and chlorine dioxide.

Yenjaichon *et al.* (2012) studied the mixing homogeneity of pulp with a brine solution, downstream a 90º tee mixer. The mixing between of Newtonian fluid, water flow, and brine solution was analysed. The mixing quality was evaluated by tomographic images; it was quantified by a modified mixing index calculated based on the coefficient of variation of the local values of conductivity in each image pixel. The ERT system was composed of 8 different layers of 16 circular stainless steel electrodes each (Yenjaichon *et al.*, 2012). Tomographic images were obtained in different sections, equally spaced along the pipe length, which gave information about the mixing quality of brine solution and pulp suspension. The mixing quality was evaluated for different mainstream velocities (0.5 to 5.0 m s^{-1}), jet velocities (1.0 to 12.7 m s^{-1}) and pulp consistencies (0 to 3 %) (Yenjaichon *et al.*, 2012).

Yenjaichon *et al.* (2013a) studied the applicability of ERT to analyse the dispersion of gas into pulp suspensions in a horizontal pipe. The gas holdup and dispersion in the pulp suspensions was investigated downstream a 90º tee, where the gas was mixed with pulp suspension. The fibers had the same characteristics as those studied by Yenjaichon *et al.* (2012) and the ERT system was the same described in Yenjaichon *et al.* (2012). Tomographic images were presented for the mixture air-pulp suspension at different distances from the injection tube. The mixing quality was evaluated with tomographic information given by the ERT system and quantified by gas mixing index. The influence of pulp consistency (0 to 3 %), flow regime of air-pulp suspension and superficial pulp velocity (0.5 to 5.0 m s^{-1}), and superficial gas velocity (0.11 to 0.44 m s^{-1}) was investigated.

In another study, Yenjaichon *et al.* (2013b) presented a similar study to that of Yenjaichon *et al.* (2013a). The mixing of gas with pulp suspensions in the work presented by Yenjaichon *et al.* (2013b) was studied downstream a 90º tee mixer as presented in Yenjaichon *et al.* (2013a) complemented with an in-line mechanical mixer. The ERT system considered was the same in these two works, as well as the fiber characteristics of the pulp suspension (see Table II.7). The ERT measurements were used to infer the mixture evolution along the pipe test section. The mixing quality was improved for plug flow regime of pulp when the in-line mechanical mixer was placed in the test section downstream the 90º tee mixer. The in-line mixer disrupted the plug which improved the mixing between gas and pulp, since the fiber networks were broken.

Recently, Faia *et al.* (2015a, 2015b) described an EIT system applied successfully to obtain flow data for pulp fiber suspensions in pipes. Comparison between three different techniques (MRI, UVP and EIT) applied simultaneously in the same experimental apparatus to study the flow of rayon fibers was performed by Faia *et al.* (2015a). Fibers concentration in terms of nL^3, where n corresponds to fiber number density and L is the fiber half-length, was tested in the range 5 to 20, and, mean flow velocities were tested in the range 0.5 to 1.5 m s^{-1} (Faia *et al.*, 2015a). The radial velocity profiles obtained with the MRI and UVP methods were compared. Good correspondences were obtained between these two techniques. Conductivity distributions obtained with EIT method were presented; distinct radial zones could be observed. Faia *et al.* (2015b) studied the applicability of the EIT system developed in Faia *et al.* (2015a) to characterise the flow of *Eucalyptus* and *Pine* pulp suspensions, both cases tested for consistencies between 1 to 2.35 %. The authors presented conductivity images and related them with the expected behaviour of fibers in the flow. Also, they presented an approach to estimate the flow velocity which was validated with measured data.

II.2.3 – VELOCIMETRY TECHNIQUES

Several techniques based on the same method or principle for flow measurement of suspensions, velocimetry techniques, have been proposed in a vast variety of studies. These studies include monitor the flow of suspensions composed of rigid particles or flexible fibers; characterise the flow dynamics of such systems is quite difficult, mainly when dealing with flexible fibers, as for example, pulp fiber suspensions. In fact, measuring the flow dynamics of pulp suspensions, either by applying or adapting certain methods developed successfully to monitor the flow of other different particles or fluids, is difficult due to the system opacity and possible interaction between fibers and internal measuring systems. Table II.8 presents a review of different techniques that have been used to measure different flow properties of fiber suspensions.

Table II.8 – Review of velocimetry techniques to characterise the flow of pulp suspensions.

Reference	Technique	Advantages	Disadvantages
Li *et al.* (1994)	NMRI	Obtain mean velocity profile Non-invasive method Measure velocity profiles in opaque systems Direct observation from plug flow regime to mixed flow	Thin layer without fibers near the pipe wall cannot be detected if it is thinner than the pixel size
Li *et al.* (1995a)	NMRI	Measure simultaneously mean velocity profile and fluctuating components of the flow Non-invasive technique Requires no tracer particles in fluid Pulp consistency value is not a limitation	-
Arola *et al.* (1998)	NMRI	Non-invasive measurement technique No need to add tracer particles Study of opaque systems	-
Inaba *et al.* (2000)	LDA	Measurement of local velocity	Possibility of refraction of the laser beam at the surface of glass pipe Pulp fibers can disturbe the laser beam
Melander and Rasmuson (2004)	PIV	Measurement of local velocity of fiber phase Use of raw images and a method based on the distinction between empty pixels and pixels containing fibers to infer the volumetric concentration of fibers	Presence of flocs induces error and the volumetric concentration is overestimated Resolution of images is poor to resolve the diameter of fibers Problems of laser sheet for pulp suspension with high consistency and flow too flocculated
Xu and Aidun (2005)	PUDV	Measurement of instantaneous velocity at relatively short sampling time Calculate turbulent intensity based on fluctuations in instantaneous velocity data	Different sampling times dependent on the flow rate
Pettersson *et al.* (2006)	LDA	Obtain velocity and root mean squared profiles near the pipe wall	Lost of penetration depth with increase of consistency
Wiklund *et al.* (2006)	UVP LDA	Obtain noninvasively instantaneous velocity profiles Applicable to strongly opaque systems Obtain velocity profile across almost complete pipe radial section No need of special seeding particles	UVP transducer can be shifted slightly due to mechanical vibrations Possible scattering and multiple reflection effects LDA does not allow to detect velocity gradient close to pipe wall
Fock *et al.* (2009)	UVP	Applicable to opaque and highly concentrated systems Simultaneous measurement of local flow velocity in different radial positions	Presence of air and fines in the flow can negatively affect the measurements
Fock *et al.* (2011)	LDA	High resolution method Applicable to measure velocity and fiber concentration	Pulp opacity limits the penetration depth
Claesson *et al.* (2012)	LDA	Possibility of get turbulence information from concentrated refractive index-matched Continuous measurement technique	Fibers can block the laser beams
Claesson *et al.* (2013)	UVP	Obtain velocity profiles and turbulence characteristics Accurate flow measurement for pulp suspensions	-
Tozzi *et al.* (2013)	MRI	Non-invasive technique Obtain velocity profiles	-
Nikbakht *et al.* (2014)	PUDV	Instantaneous measurement of the average and fluctuating components of velocity for each radial position	Difficulty in measuring the local velocity in the near wall region due to reflection

Inaba *et al*. (2000) presented a study involving LDA to investigate the flow of a suspension composed of short and long pulp fibers in a horizontal pipe. Pettersson *et al.* (2006) studied the flow of bleached *kraft* pulp in a square section channel, with LDA. Fock *et al.* (2011) dedicated their study to investigate the applicability of LDA to get velocity and near-wall information of plug flow of pulp suspension in a channel. Local velocity profiles were obtained with this measurement technique. Some difficulties were associated with pipe material, namely glass pipe, which could create refraction of the laser beam. However, this problem was not observed when pulp was flowing in a channel. Furthermore, the presence of fibers in the flow could cause discontinuities of the laser beam. Claesson *et al.* (2012) applied the LDA technique to extract information about turbulence occurring during the flow of never-dried softwood *kraft* pulp suspensions in the presence of a backward-facing step. The authors calculated the average velocity and root mean square velocity from the data measured experimentally using LDA. They observed that root mean square velocity decreased with the increase of fiber consistency which could be due to strongest fiber network resulting in a higher damping effect.

Fock *et al.* (2009) investigated the applicability of the UVP technique to obtain velocity profiles in the cross section of a square horizontal channel for plug flow regime of bleached *kraft* pulp suspension flow; different flow rates and pulp consistencies were investigated. Claesson *et al.* (2013) applied this method to obtain velocity profiles as well as root mean square (RMS) velocities profiles in cross sections, for different positions in the flow direction, of a square horizontal channel, for flow of bleached never-dried *kraft* pulp suspension downstream a sudden expansion. The main advantage of this technique was its applicability to measure the instantaneous velocity profile for systems composed of highly concentrated and opaque suspensions. Also, the UVP method could be used to characterise turbulence in pulp suspensions flow, namely, by obtaining RMS velocities profiles. However, the presence of air in the suspension, moving with a different velocity from that of fibers and water, affected the velocity gradient measured representing a weakness of this technique.

Wiklund *et al.* (2006) carried out flow measurements of *Pine* and *Spruce* bleached *kraft* pulp suspension in pipe, with both UVP and LDA methods. The main purpose was to test those techniques to obtain rheological data and flow knowledge for pulp suspensions. In spite of measurements differing in the region closer to the pipe wall, both techniques were applied successfully to study the flow of high concentrated pulp suspensions.

Melander and Rasmuson (2004) tested the PIV method to study the flow of *Pine* pulp suspended in air, during vertical channel flow. This technique was applied to obtain local

velocity data and from the raw images infer the volumetric concentration of fibers. The main limitation of PIV was to its applicability to concentrated systems. The laser sheet was not able to penetrate through high concentrated pulp systems. Additionally, the presence of flocs in the flow was increased when pulp consistency increased and, also, the error of the measurements obtained with this technique, resulting from the presence of flocs, was increased.

Xu and Aidun (2005) applied the ultrasonic pulsed Doppler velocimetry (UPDV) method to obtain velocity profiles and turbulent intensity data for the flow of natural flexible cellulose wood fibers suspension in a horizontal channel. Nikbakht *et al.* (2014) performed experimental trials concerning the flow of Northern bleached softwood *kraft* (NBSK) and *Aspen* pulp suspensions in a horizontal pipe, using the same technique. The main purpose of that work was to investigate the plug radius during the transition from plug flow regime to turbulence. This technique was able to capture variations in the instantaneous velocity data acquired to calculate turbulent intensity. The time specified to sampling tested by Xu and Aidun (2005) was different depending on the flow rate tested. This technique, when applied to pipe flow, revealed to have uncertainties associated in measuring local velocity near the pipe wall due to reflection effects.

NMRI and MRI are non-invasive techniques to measure velocity profiles. Li *et al.* (1994) applied nuclear magnetic resonance imaging (NMRI) to observe the flow of bleached hardwood *Birch kraft* and bleached softwood *Douglas fir kraft* pulp suspensions in a pipe. Li *et al.* (1995a) used the NMRI method to analyse its applicability to visualise and obtain velocity data for the flow of bleached hardwood *Birch kraft* pulp suspension in a pipe with an abrupt contraction. Different contraction geometries, conical contraction, were evaluated by Li *et al.* (1995b) for the same type of pulp; NMRI method was applied to visualise the pulp flow in four different positions in the conical contraction. Bleached hardwood *Birch kraft* pulp was also used by Arola *et al.* (1998) to test the NMRI technique to obtain velocity profiles during the flow of that suspension in a pipe with an abrupt axisymmetric pipe expansion. Tozzi *et al.* (2013) investigated with a magnetic resonance image (MRI) system, the flow of cellulosic suspensions composed of short and medium length of delignified cellulosic fibers through a horizontal pipe. The authors observed asymmetry in the velocity profiles for certain flow velocities caused by gravity. These techniques could give erroneous results if the range of concentration and flow velocity was low enough to cause settling, which was observed by spatially changing properties of effective medium (Tozzi *et al.*, 2013). When important effects were present in the thin layer near the pipe wall, with thickness lower than the pixel size, this method was not able to capture them (Li *et al.*, 1994).

The flow of pulp fiber suspensions is difficult to investigate even with new techniques supplying information on velocity measurements and flow visualisation such as techniques based on ultrasounds, NMRI or optical techniques. The precise knowledge of those flows is not complete despite of their importance for the pulp and paper sector. Different methods have been investigated to capture the most important phenomena occurring during different flow conditions of different types of fibers. Most of them had limitations in obtaining data until very near the pipe or channel wall, suggesting that accurate information to describe a complete profile in cross section to flow is still not available. Both opacity of pulp suspensions and poor resolution of different techniques may cause highly uncertainty in the measurements. In addition, combining different methods to study the same pulp flow under the same conditions can give complementary results and better knowledge can be achieved. Therefore, it seems that a deep understanding of the flow of pulp suspensions is not yet complete, and the development of other strategies such as, computational tools to simulate the flow of pulp suspensions, can help on providing an accurate insight to the pulp suspension flows behaviour.

II.3 – SIMULATION APPROACHES FOR FIBER SUSPENSIONS FLOW

A deep knowledge and the development of computational tools to simulate fiber flow processes are of relevant importance for the better and proper design of flow systems. The appropriate knowledge of fiber suspension flow dynamics and behaviour is necessary for the development of suitable mathematical models which are still not completed due to the complexity of these systems. Different numerical strategies to predict the flow of fiber suspensions have been proposed, either to predict the flow of rigid fibers as well as to predict the flow of flexible particles. Table II.9 summarises existing literature on models for prediction of fiber suspension flows with special consideration to pulp fiber suspensions.

Table II.9 – Papers that present a review on models for the prediction of fiber suspensions flows.

Authors	Title	Main Topics
Duffy (1976)	A review and evaluation of design methods for calculating friction loss in stock piping systems	Detailed discussion concerning published design correlations for pressure loss estimation
Duffy (2003)	The significance of mechanistic-based models in fiber suspension flow	Pulp fiber suspensions flow behaviour and dynamic. Rheological characterisation; flow mechanisms and flow models
Cui and Grace (2006)	Pneumatic conveying of biomass particles: a review	Brief discussion of modelling strategies for pneumatic conveying of biomass particles, namely, pulp fiber suspensions
Cui and Grace (2007)	Flow of pulp fiber suspension and slurries: a review	Brief discussion of modelling flow behaviour and dynamic of fiber suspensions: fiber motion, hydrodynamic properties, rheological characteristics, fiber orientation, flocculation
Blanco *et al.* (2009)	Use of modelling and simulation in the pulp and paper industry	Detailed discussion concerning modelling and simulation in pulp and paper industry
Hämäläinen *et al.* (2011a)	Rheology in papermaking – from fiber suspension flows to mechanics of solid paper	Brief review of modelling strategies and numerical studies of flow of pulp fiber suspensions
Hämäläinen *et al.* (2011b)	Papermaking fiber-suspension flow simulations at multiple scales	Application of modelling and simulation techniques for flow of pulp fiber suspensions in pulp and paper lines discussed in detail
Lundell *et al.* (2011)	Fluid mechanics of papermaking	Brief review of main important steps in pulp and paper process. Detailed review of experiments and numerical studies related to pulp fiber suspensions
Lu *et al.* (2015)	Discrete element models for non-spherical particle systems: from theoretical developments to applications	Detailed discussion of discrete element method applied to modelling non-spherical particles

Duffy (1976) carried out a review of different methods proposed to estimate the friction loss in piping systems based on empirical correlations of the form:

$$\frac{\Delta H}{L} = KV^{\alpha}C^{\beta}D^{\gamma} \tag{II.1}$$

where V represents the mean bulk velocity, C corresponds to the moisture-free consistency, D is the internal pipe diameter, K represents a numerical coefficient which is constant for a certain pulp, and α, β, γ are indices of the model and also constants for a given pulp. A summary of different design correlations for the determination of pipe friction loss was presented. A comparison between the friction loss predicted for a flow of *kraft* pulp in a smooth pipe for different sets of pipe diameter, pulp consistency, and flow velocity, using different correlations was reported. Duffy (2003) reviewed different models and correlations proposed for pulp fiber suspension flow. Various models suggested to describe the flow dynamics of pulp suspensions were presented and analysed. The flow mechanisms and flow models of pulp suspensions were reviewed. The flow mechanisms consist mainly in three distinct flow regimes: (*i*) plug flow, (*ii*) transition flow, and (*iii*) turbulent flow (see Figure I.4). Four different models to establish correlations in order to describe the flow mechanisms

of pulp fiber suspensions were reviewed. For plug flow regime, the head loss correlation had the same form as Equation (II.1). After the maximum in the head loss curve on plug flow regime (Figure I.4 – V_m) and before the onset of the drag reduction effect (Figure I.4 – V_W), a wall slip model was proposed. For the transition regime a summary of literature works involving models for wall shear stress was presented. Models for predicting friction loss were reviewed for the transition and turbulent pulp flow regimes. An attempt to correlate the velocity of the maximum in the head loss curve (Figure I.4 – V_m) with pulp suspensions consistency was presented in Li *et al.* (2001a, 2001b) and Ventura *et al.* (2008b). The authors proposed the following expression:

$$V_m = KC^{\alpha} \tag{II.2}$$

where K is a numerical coefficient, and α corresponds to an exponent, both parameters are constant for a certain pulp. Cui and Grace (2006) dedicated a short section of their work to the review of existing literature works related to modelling the flow of biomass particles including pulp fiber suspensions. Cui and Grace (2007) discussed briefly literature studies concerning modelling flow of fiber suspensions like rheological modelling, fiber orientation, flocculation, pulp flow, and fiber motion. Blanco *et al.* (2009) presented and discussed in their work modelling and simulation methods used in the pulp and paper industries. Different topics were addressed in that review work such as methods for the data analysis, software used and level of detail in modelling and simulation, off-line and on-line use of simulation in the pulp and paper process. Additionally, the authors presented an overview of research that was still needed to improve the pulp and paper process. Hämäläinen *et al.* (2011a, 2011b) focused on reviewing the existing literature studies dedicated to model and simulate the flow of pulp fiber suspensions at different stages in the pulp and paper process which required different approaches. Different simulations strategies and models at fiber level, meso-scale and macro-scale were discussed. Lundell *et al.* (2011) presented a brief introduction to paper making process and the steps where fluid dynamics presents an important role. The authors discussed modelling and calculation strategies used in different parts of sheet forming in the papermaking process (flow distributor, headbox diffuser, contraction, headbox jet, dewatering on the roll and blade dewatering). Lu *et al.* (2015) discussed the modelling of the flow of non-spherical particles using discrete element models (DEM). The authors covered in that work topics related to the numerical complexity of DEM for non-spherical particles and the representation of that type of particles for DEM simulation. Also, the authors reviewed the

applicability of DEM for particle packing, shear flow, discharge of hoppers, vibrated beds, particle-fluid flows and flow in rotating cylinders and drums.

Different attempts have been made to model the flow of fiber suspensions, namely, the flow of pulp fiber suspensions. However, this represents a real challenge due to the complexity of systems and phenomena involved. Multiphase models and pseudo-homogeneous models have been addressed in literature to predict the flow of such systems. Sections II.3.1 and II.3.2 present and summarise important simulation approaches to deal with the flow of fiber suspensions.

II.3.1 – PSEUDO-HOMOGENEOUS MODELS

The pseudo-homogeneous models can be regarded as very powerful tools to deal with concentrated fiber suspensions since they consider only single-phase models adapted to take into account the presence of fibers in the flow. This kind of models requires the proper rheological information and constitutive model. A scarce number of studies have been dedicated to predict the flow of fiber suspensions with this type of models. Table II.10 summarises existing literature studies for prediction of fiber suspensions flows using single-phase models. Furthermore, the applicability of pseudo-homogeneous models to predict and capture the most important phenomena occurring during the flow of fiber suspensions in different geometries from that of pipe or channel, have been studied only by few authors. For example, in the pulp suspensions flow, Wikström and Rasmuson (2002) and Niklas and Asendrych (2006) applied a pseudo-homogeneous model to simulate the flow of pulp suspensions in a pressurized pulp screen and in a hydropulper, respectively.

Steen (1991) carried out a numerical study of the flow of fiber suspensions in a straight pipe and in a pipe equipped with a circular step diffuser. The flow of softwood fiber suspension in a vertical pipe was also simulated. The main objective of that study was to develop a mathematical model able to deal with fiber flocculation in turbulent flow. The standard k-ε turbulence model was applied considering additional terms to take into account both the effects of aggregation and rupture of fiber flocs. Different flow conditions were analysed – see Table II.10. The results of mean velocity profile and turbulent kinetic energy profiles agreed reasonably with experimental data and data from literature.

Table II.10 – Summary of single-phase models to calculate the flow of fiber suspensions.

Reference	Rheological model	Turbulence model	Conditions analysed
Steen (1991)	-	Standard *k*-*ε* turbulence model	Flexible fiber suspension Softwood fiber suspension **Abrupt pipe expansion** Velocity centreline: 4 m s^{-1} **Pipe flow** Velocity centreline: 1 and 4 m s^{-1} Fiber consistency: 0.5 % **Vertical pipe flow after an orifice** Fiber consistency: 0.17 % Velocity centreline: 1 and 3 m s^{-1}
Huhtanen and Karvinen (2005)	**Mixing tank** Constant viscosity Power-law Bingham plastic Herschel-Bulkley Bird-Carreau **Pipe flow** Power-law model **Converging channel** Power-law **Backward-facing step** Power-law	**Mixing tank** Standard *k*-*ε* turbulence model Reynolds stress model **Pipe flow** No turbulent simulations **Converging channel** Reynolds stress model **Backward-facing step** Standard *k*-*ε* turbulence model Reynolds stress model	**Flow in a mixing tank** Bleached softwood *kraft* pulp suspension Pulp consistency: 2-10 % **Pipe flow** Pulp consistency: 0.67-3.41 % **Flow in a converging channel and over a backward-facing step** Water-fiber suspensions
Ventura *et al.* (2011)	Apparent viscosity as a function of local velocity	Standard *k*-*ε* turbulence model	**Horizontal pipe flow** **Recycled pulp** Consistency: 0.61-2.70 % Mean flow velocity: 2.0-6.5 m s^{-1} ***Eucalyptus* pulp** Consistency: 0.77-1.50 % Mean flow velocity: 2.0-6.5 m s^{-1} ***Pine* pulp** Consistency: 0.71-1.30 % Mean flow velocity: 3.0-6.5 m s^{-1} ***Eucalyptus* (90 %) and *Pine* (10 %) pulp** Consistency: 0.66-1.00 % Mean flow velocity: 2.7-6.5 m s^{-1}

Huhtanen and Karvinen (2005) simulated the flow of fiber suspensions in four different geometries. The authors studied numerically the flow of water-fiber suspensions in a converging channel and in a backward-facing step, and the flow bleached softwood *kraft* pulp in a mixing tank and in a pipe. Two different turbulence models were tested: Standard *k*-*ε* turbulence model and Reynolds stress model. The models tested took into account the presence of fibers in the flow just by considering the fluid as non-Newtonian. The authors mentioned that they did not perform simulations of turbulent flow in the pipe, instead, they compared calculated pressure drop values obtained from correlations with experimental data. However, they simulated the laminar flow of pulp suspensions in a pipe.

Ventura *et al.* (2011) performed simulations of fully developed turbulent flow of four different types of pulp fiber suspensions in a straight smooth pipe. The authors tried to

reproduce the experimental data reported in Ventura *et al.* (2008b) when the flow was fully developed and for the turbulent regime. The model developed consisted of standard *k-ε* turbulence model for Newtonian fluids modified considering the fluid viscosity as a function of local velocity, supposing a non-Newtonian behaviour of the pulp suspensions. Additionally, the authors tested modifications of the turbulence length scale and turbulence intensity, at the inlet, to see how and if these parameters influence the numerical predictions. The model proposed was able to predict the pressure drop values of pulp suspension flows for the conditions tested.

II.3.2 – MULTIPHASE MODELS

Simulation techniques based on multiphase models to model the flow of fiber suspensions have been widely studied by several authors and different strategies have been proposed. Many different studies have been published concerning the fiber geometry modelled, the most important factors occurring in the fiber flow to take into account in the model and assumptions to be made, as well as the complexity level of the model to be developed. This type of models deals with high level of flow and fiber detail, and can have a more realistic character than the pseudo-homogeneous models. However, they need more computational resources and, nowadays, they are still only applied for very dilute systems or for a small volume where a higher number of fibers can be present. In recent years, the improvement of computational technologies leads to a growing interest on these models and, also, to new developments on the different multiphase modelling strategies.

II.3.2.1 – EULERIAN-EULERIAN APPROACH

The Eulerian-Eulerian approach also designated as two-fluid modelling has been applied to simulate the flow of fiber suspensions. In this approach, the discrete phase is treated as a continuum. The modelling strategy is based on the conservation equations for mass and momentum of each mixture phase. Also, this model takes into account the effects of turbulence on the distribution and motion of each phase, by considering closure equations for turbulence. The complete system of equations is composed of sets of conservation equations, one for each phase; however, the general form is similar for each phase. An important concept is the volume fraction since it gives information concerning the volume which is occupied by

a phase in the total volume. It is assumed that the volume fractions do not have discontinuities in space and time, and the sum of all individual volume fractions is equal to 1.0. This model does not take into account the number of particles neither their shape which can result in less computational efforts; however, since this model requires conservation equations for each phase this can increase the computational resources needed. Table II.11 presents an overview of relevant works from literature dealing with Eulerian-Eulerian modelling of flow of non-spherical particles, mainly, in dilute and semi-dilute regimes.

Table II.11 – Review of Eulerian-Eulerian model approaches for the prediction of flow of fiber suspensions.

Reference	Suspension type	Main characteristics of the model
Paschkewitz *et al.* (2004)	Rigid fibers	Model is based on Cauchy's motion equations for fluid flow and equation of conservation of probability of orientation Stress tensor in motion equations includes additional fiber stress
Jian-Zhong *et al.* (2005)	Rigid cylindrical fibers	Model developed based on mean motion equation of turbulent fiber suspensions, equation of probability distribution function for mean fiber orientation Mean motion equation includes the Reynolds stress and the effect of fibers Equation of probability function for mean fiber orientation includes the fluctuating quantities Zero-order approximation solution for mean flow velocity: mean velocity of turbulent Newtonian fluid
Lin *et al.* (2006b) Shen and Lin (2010) Lin and Shen (2010a)	Rigid cylindrical fibers	Model developed based on mean motion equation of turbulent fiber suspensions, equation of probability distribution function for mean fiber orientation, k-ε closure turbulence model Mean motion equation includes the Reynolds stress and the effect of fibers Equation of probability function for mean fiber orientation includes the fluctuating quantities
Gillissen *et al.* (2007a, 2007b)	Rigid cylindrical fibers	The model developed is based on the Navier-Stokes equations with extra fiber stress tensor and fiber distribution function Additional fiber stress calculated from the fourth order moment of the fiber distribution function
Lin *et al.* (2008)	Rigid cylindrical fibers	Model developed based on mean motion equation of turbulent fluid flow, equation of probability distribution function for mean fiber orientation, k-ε closure turbulence model Equation of probability function for mean fiber orientation includes the fluctuating quantities
Krochak *et al.* (2009)	Rigid cylindrical fibers	Model is based on Cauchy's motion equations for fluid flow and probability density function to describe the evolution of fiber orientation Stress tensor in motion equation includes fiber stress term
Latz *et al.* (2010)	Rigid cylindrical fibers	Model is based on the Navier-Stokes equations and probability distribution function Equations of motion coupled with probability distribution function through stress tensor
Lin and Shen (2010b) Yang *et al.* (2013)	Rigid cylindrical fibers	Model developed based on mean motion equation for turbulent fluid flow, equation of probability distribution function for mean fiber orientation, k-ε closure turbulence model with additional source-terms for fibers Equation of probability function for mean fiber orientation includes the fluctuating quantities
Sattari *et al.* (2014)	Rigid fibers	Model is based on Navier-Stokes equations and in fiber orientation probability distribution

Paschkewitz *et al.* (2004) presented a numerical strategy to simulate the turbulent flow of rigid particles in a channel. Cauchy's equations of motion were selected to describe the fluid flow. The presence of fibers in the flow was taken into account in the model by an extra stress tensor representing the fiber contribution. That extra stress of fibers was calculated from the equation of conservation of probability of orientation. The model was developed to simulate experimental data for channel flow available from literature. Krochak *et al.* (2009) simulated the laminar flow of rigid fibers in a tapered channel. The model tested was based on the Cauchy's equations of motion to describe the fluid flow, including as well an additional term in the fluid stress tensor, fiber stress term. That term related to fibers, depended on the probability density function of the evolution of fiber orientation. The authors investigated the effect of considering different fiber orientation at the inlet of the channel and on the flow field and of the orientation distribution.

Jian-Zhong *et al.* (2005), Shen and Lin (2010) and Yang *et al.* (2013) studied the turbulent flow of rigid cylindrical particles in a horizontal pipe; Lin *et al.* (2006b, 2008) and Lin and Shen (2010a, 2010b) simulated the flow of rigid cylindrical particles in a horizontal channel. The proposed model assumed that the fluid and fibers were flowing with the same velocity. It was based on the mean motion equation of turbulent fiber suspensions, considering the kinematic viscosity of the suspending fluid and an additional term involving the apparent viscosity of the fiber suspension. Also, the model included the second and fourth orientation tensors of fibers obtained from the differential equation representing the probability distribution function for mean fiber orientation. Additionally, Lin *et al.* (2006b, 2008), Shen and Lin (2010) and Lin and Shen (2010a) considered the k-ε turbulence model. Lin and Shen (2010b) and Yang *et al.* (2013) proposed additional source terms for the equations of turbulent kinetic energy and its dissipation rate, related to fibers properties, second and fourth orientation tensor of fiber. It should be noticed that the model proposed by Lin *et al.* (2008) was based on the mean motion equations for fluid flow without considering terms related to the fibers, since the fiber volume fraction evaluated in that study was very low.

The model proposed by Jian-Zhong *et al.* (2005) was validated through comparison of the numerical results with results obtained experimentally for the flow of a glass fiber suspension. Lin *et al.* (2006b) validated their model with experiments of turbulent flow in a horizontal channel of nylon fibers. Additionally, the model was also validated by comparing the numerical results with results from literature. The probability distribution for fiber orientation, distribution of mean velocities and distribution of streamwise relative turbulent

intensities were presented in Jian-Zhong *et al.* (2005), Lin *et al.* (2006b). The model proposed by Lin *et al.* (2008) was only validated by comparing numerical results of distribution of dimensionless velocity, turbulent kinetic energy and its dissipation rate, distribution of fibers orientation, three components of the fourth-order orientation tensor, and shear stress, with data from other authors. Lin and Shen (2010a, 2010b) and Yang *et al.* (2013) validated the model by comparing the numerical profiles of velocity, dimensionless velocity, turbulent kinetic energy and its dissipation rate for different Reynolds number, fiber concentration and fiber aspect-ratio, with data from literature. In Shen and Lin (2010) the model was validated only by comparison between numerical data and data from literature, for mean velocity profile and dimensionless velocity profile for different Reynolds number, fiber concentration and fiber aspect-ratio.

Gillissen *et al.* (2007a, 2007b) simulated the turbulent flow of rigid fibers in a channel. Navier-Stokes equations were used considering an extra term, fiber stress tensor, derived from the fiber distribution function. Latz *et al.* (2010) carried out simulations concerning the flow of rigid fibers in a channel, 8:1 contraction flow and flow around a cylinder. The models tested were based on the Navier-Stokes equations coupled with the probability distribution function through the stress tensor. Sattari *et al.* (2014) studied the turbulent flow of rigid fibers through a contracting channel with straight walls and with curved walls. The applied model was based on the Navier-Stokes equations considering the fiber orientation distribution. The model was validated with data from literature for channel with straight and curved walls.

II.3.2.2 – EULERIAN-LAGRANGIAN APPROACH

The Eulerian-Lagrangian approach has been widely studied to predict the flow of non-spherical particle suspensions for very specific systems. This method considers the dispersed phase not as a continuum but instead individual particles are considered. Usually, the dispersed phase is represented by a group of particles with the same shape and size. Positions of particles and velocity are determined with proper equations. Newtonian equation of motion is used to calculate the flow field of particles, while Navier-Stokes equations are applied to obtain the flow field of the fluid phase. The dispersed phase is modelled in a Lagrangian frame of reference by tracking particles with inter-particle collisions, sampling particle phase properties and source terms. The fluid flow is calculated similarly to the Eulerian-Eulerian models, the average fluid phase equations including particle phase source terms. Since this

method tracks the trajectory of particles and calculates its location, it is important that all the relevant forces acting on the particles are considered. This method requires high computational sources and usually it is applied to study systems composed of a restricted number of particles or fibers. Table II.12 presents a brief summary of relevant works from literature based on Eulerian-Lagrangian approach to simulate the flow of non-spherical particles.

Table II.12 – Brief summary of Eulerian-Lagrangian models for the prediction of the flow of fiber suspensions.

Reference	Fiber model	Main features
Yamamoto and Matsuoka (1993)	Chain of spheres lined up and bonded to each neighbour	Particle simulation method to simulate the flow of rigid and flexible fibers in a shear flow Model applied to simulate the flow of a rigid fiber, a slightly flexible fiber and a fairly flexible fiber The flow field is assumed to be known
Fan *et al.* (1998)	Cylinders with large aspect-ratio	Direct simulation method to simulate the flow of fibers in shear flow The flow velocity is assumed to be a function of the shear rate applied
Dong *et al.* (2003)	Chain of spheroids linked by joints	Flow field obtained by two methods: Random-walk method and large eddy simulation Motion of fibers calculated from the translation and rotation equations for each spheroid Calculation of suspension flow without taking into account the influence of particle-phase on the fluid flow, one-way coupling
Jafari *et al.* (2007)	Fiber network of five straight cylindrical fibers Circular cylinders with irregular surface shape	Hybrid method between Direct Numerical Simulation and Large Eddy Simulation Calculation of suspension flow taking into account the influence of particle-phase on the fluid flow, two-way coupling between phases
Lindström and Uesaka (2007, 2008)	Chain of fiber segments of circular cross section	Fluid motion obtained from the Navier-Stokes equations Calculation of suspension flow taking into account the influence of particle-phase on the fluid flow, two-way coupling between phases Momentum conservation equation considers the forces exerted by the fibers in the fluid phase
Mäkipere and Zamankhan (2007)	Fiber network of five straight cylindrical fibers Prolate spheroid Circular cylinders with irregular surface shape	Flow field obtained from the Navier-Stokes equations, Large Eddy Simulation Calculation of suspension flow taking into account the influence of particle-phase on the fluid flow, two-way coupling between phases Equations of particles motion includes the interaction between fluid-solid particles and solid-solid particles
Mortensen *et al.* (2008)	Prolate ellipsoids	Fluid motion calculated from Navier-Stokes equations, direct numerical simulation method Calculation of suspension flow without accounting for the influence of particle-phase on the fluid flow, one-way coupling

Table II.12 – Brief summary of Eulerian-Lagrangian models for the prediction of the flow of fiber suspensions (continued).

Reference	Fiber model	Main features
Marchioli *et al.* (2010)	Prolate ellipsoidal particles	Fluid flow obtained from continuity and Navier-Stokes equations, direct numerical simulation method Solid phase treated in similar way to Mortensen *et al.* (2008) Calculation of suspension flow considering the influence of particle-phase on the fluid flow, two-way coupling
Sasic and Almstedt (2010)	Chain of fiber segments of circular cross section	Fluid motion calculated from Navier-Stokes equations and k-ε turbulence model Calculation of suspension flow without accounting for the influence of particle-phase on the fluid flow, one-way coupling
Lin *et al.* (2011)	Cylindrical fiber	Fluid motion calculated from Navier-Stokes equations and k-ε turbulence model Calculation of suspension flow without accounting for the influence of particle-phase on the fluid flow, one-way coupling Calculation of fiber motion without considering the interactions between fibers
Kondora and Asendrych (2013)	Chain of rigid segments (spheres) connected by ball and socket joints	Particle-level method to simulate the flow of flexible fibers in a converging channel of a papermachine headbox, and rigid fibers in simple shear flow Calculation of suspension flow without accounting for the influence of particle-phase on the fluid flow, one-way coupling Reynolds Stress Model to model turbulence
Marchioli and Soldati (2013)	Ellipsoidal particles	Fluid phase simulations with direct numerical simulation method Solid phase treated in similar way to Mortensen *et al.* (2008)
Zhao *et al.* (2013)	Ellipsoidal particles	Mass continuity and momentum equations Calculation of suspension flow without accounting for the influence of particle-phase on the fluid flow, one-way coupling Translational motion of fibers governed by Newton's second law Rotational motion of fibers governed by Euler's equation for rigid body
Zhao *et al.* (2014)	Point-wise rigid prolate, elastically rebounding spheroids	Fluid flow obtained from continuity and Navier-Stokes equations, direct numerical simulation method Solid phase treated in similar way to Mortensen *et al.* (2008) Calculation of suspension flow considering the influence of particle-phase on the fluid flow, two-way coupling Study of slip velocity between fibers and fluid phase

Yamamoto and Matsuoka (1993) studied the dynamic behaviour of a fiber composed of spherical particles. Those spherical particles gave rigidity or flexibility to the fiber simulated, since they can stretch, bend and twist, which was implemented in the model by modifying parameters related to those phenomena. That work was mainly related to the fiber modelling assuming that the velocity field is known, and with special emphasis on the translational and rotational equations of fiber motion. Fan *et al.* (1998) simulated the motion of fibers in shear flow. Cylindrical fibers with high aspect-ratio were considered, and the flow velocity was considered known from the applied shear rate. The authors presented results of the evolution of fibers distribution. Also, results of some components of moment tensors were discussed and compared with available data. That model took into account the possibility of interaction between the fibers. Dong *et al.* (2003) evaluated fiber concentration in turbulent channel flow of fibers represented by spheroids linked by joints. The turbulent flow was obtained by two

different methods: random-walk method and large eddy simulation (LES). The motion of fibers was calculated by translation and rotation equations for each spheroid. An important feature of that model was that it took into account if the fiber or the spheroid touches the wall. A proper wall model was proposed in that work considering that the normal force for the spheroid when it touched the wall was perpendicular to the wall. The authors divided the channel into 8 equal parts; they evaluated the ratio between the number of fibers in the each channel section to the total number of fibers flowing in the complete channel (concentration ratio). The concentration profile was validated by comparing the results with experimental data from Olson (1996). The profile of fiber concentration obtained showed a constant value in the core region, but in a region near the wall until about a one-half fiber length distance to the pipe wall it tended to increase from a very low value until it reached its maximum value of concentration, and, it decreases until a distance of about a fiber length distance to the pipe wall where it reached the constant value in the core region. Lindström and Uesaka (2007, 2008) proposed a model to describe the flow of flexible fibers composed of chains of fiber segments. That model included the effect of fibers in the fluid phase through momentum equations for fluid phase. In Lindström and Uesaka (2007) the authors validated the model for the flow of an isolated fiber. The model was applied to simulate the flow of semidilute suspensions (Lindström and Uesaka, 2008). Jafari *et al.* (2007) studied numerically the flow of single fiber network composed of five straight cylindrical fibers flowing in a channel, and the flow of two circular cylinders with irregular shape in a pipe. The model proposed was based on a hybrid method between direct numerical simulations (DNS) and LES. The model involved the influence that fibers have on the fluid phase field. Also, it included the fiber-fiber interaction. However, the authors mentioned that the numerical results when compared with other experimental and numerical results revealed only a more qualitative meaning, and further improvements on the model needed to be done to develop a more efficient model. Similar fiber geometry was considered in the work of Mäkipere and Zamankhan (2007). However, the flow field was obtained by LES. The authors simulated different fiber suspensions configurations such as: single fiber network composed of five straight cylindrical fibers flowing in a channel, prolate spheroids flowing in a duct, and the flow of two circular cylinders with irregular shape. That model was developed to take into account the fluid-fiber interaction and the interaction between fibers. Mortensen *et al.* (2008) carried out simulations considering ellipsoidal particles in a turbulent channel flow. Marchioli *et al.* (2010), and Marchioli and Soldati (2013) simulated the flow of ellipsoidal fibers in a turbulent channel flow. The fibers were modelled in a similar way to that presented in Mortensen *et al.* (2008).

The fluid phase field was obtained by a DNS method. A two-way coupling between the solid phase and the fluid phase was tested by Marchioli *et al.* (2010). Marchioli and Soldati (2013) applied a one-way coupling strategy. Marchioli *et al.* (2010) analysed the fiber orientation and alignment frequency, and they investigated the fiber deposition and wall accumulation. The work presented by Marchioli and Soldati (2013) was more focused on the study of the fiber rotation and how it was affected by the local shear and flow anisotropy. Sasic and Almstedt (2010) simulated the turbulent flow of flexible fibers in air for a computational domain composed of a periodic box. It was considered a dilute suspension, and the effect of fibers in the fluid flow field was neglected. Lin *et al.* (2011) simulated the turbulent flow of rigid fibers in an axisymmetric contraction. The authors considered dilute suspensions composed of rigid fibers modelled as cylinders. The presence of fibers and their effect on the fluid phase was neglected as well as the interactions between fibers. Kondora and Asendrych (2013) simulated the flow of very dilute flexible fiber suspensions in a converging channel of a papermachine headbox. The model was validated by comparing the fiber orientation probability distribution with available experimental data. Zhao *et al.* (2013) proposed an Eulerian-Lagrangian strategy to deal with rigid particles in a turbulent channel flow. The authors studied the flow of those particles in dilute regime where the model did not need to take into account the influence of fibers in the fluid field. The Lagrangian modelling of fibers was based on the translational motion and rotational motion equations for single particles. Zhao *et al.* (2014) presented a study considering the turbulent flow of rigid particles in a channel. That study was developed with the main objective of studying the slip velocity between fibers and the fluid phase.

Numerous theoretical approaches have been made to simulate the flow of fiber suspensions. However, most of the modelling strategies are based on multiphase models which are not suitable for concentrated systems. Also, the models developed and assumptions made so far, do not guarantee that all important phenomena are taken into account in the model. The simulations are usually computational time and resources consuming, even if the model does not include all relevant information. Although some modelling strategies have been implemented to deal with the presence of fibers in the flow, some limitations of applicability to pulp suspension flows can arise due to the fact that the models were developed to predict the flow of rigid fibers and usually only for dilute systems. Moreover, the lack of experimental information for different flow conditions in order to validate numerical calculations as well as the numerical limitations mentioned previously turns on the needed of research for new experimental and numerical approaches. Thus, in the present work, pseudo-

homogeneous models will be investigated for the simulation of the flow of concentrated pulp fiber suspensions. This will be discussed in more detail in the next chapters of this thesis.

II.4 – CONCLUSIONS

As the aforementioned general literature description indicates, improvements in the knowledge of the flow behaviour of pulp fiber suspensions are still needed. Relevant works are carried out in three different areas: rheology, experimental techniques and numerical approaches. These different areas are interconnected with the output data from each area giving the input information for the other ones. The modelling treatment represents a powerful tool which, together with experiments, aims to be a comprehensive and complementary reliable simulation tool for industry in the near future.

To attain a suitable model to address the flow of pulp suspensions in pipes, both the rheological and experimental information needs to be available. Reviews on pulp's rheology have shown that there are still not yet standard strategies for the pulp's rheological behaviour evaluation to obtain the complete rheological information. Most of the rheological devices used for pulp suspensions are not able to measure accurately rheological information for the lower shear rate zones. Moreover, erroneous measurements can arise due non-homogeneity of pulp distribution and to wall effects. Additionally, experiments to obtain the most relevant information regarding the flow of pulp suspensions in pipes are still receiving a lot of attention. Those facts justify, in this work, the development of a numerical model, for the flow of pulp suspensions, based on a rheological model obtained from fitting the data obtained in a rotational rheometer. Experimental information is still not complete; most of the experimental devices are not accurate to give information until very near the pipe wall, and difficulties due to the opacity of fibers, mainly for high concentrated systems, can be present. Regarding the flow experiments, the complete set of flow conditions selected are based on pipe flow tests, which in some cases include information about the flow and pulp distribution in the pipe cross section. Two different types of fibers will be studied (*Eucalyptus* and *Pine* fibers), typical of the Portuguese pulp and paper industry.

Several modelling strategies have been proposed to simulate turbulent flow of fiber suspensions. A major importance was given to multiphase models either Eulerian-Eulerian approaches as well as Eulerian-Lagrangian approaches. Those models are still disadvantageous to deal with turbulent flow of pulp fiber suspensions. They present a high

level of complexity with fiber-fiber and fiber-fluid interactions being represented leading to high computational efforts and to the applicability of these models for very dilute systems. Even if those models are applied to very dilute systems some difficulties can be present in taking into account all the fiber-fiber and fiber-fluid interactions. Single-phase models have also been used to simulate the flow of pulp fiber suspensions. However, those models are still not completely developed to simulate the flow of pulp fiber suspensions. Proper model parameters for turbulence and rheological information need to be tuned based on experimental information and pulp characteristics, i.e. each pulp fiber needs to be correctly taken into account in the model as well as its effect on turbulence damping.

Despite of all the efforts mentioned for predicting the flow of fiber suspensions, further studies to develop a model for fiber suspensions flow, such as pulp fibers, of more concentrated systems are still needed. In this scenario, the present work is focused on the development of a CFD model, based on a pseudo-homogeneous approach, to simulate the flow of pulp suspensions in pipes, since multiphase models are still restricted to those cases where a limited and low number of fibers can be considered, i.e. very dilute systems. Also, the description of the fibers is still far from the real system. The influence of different flow rate, pulp consistency, pulp type, pipe diameter, and flow regime are investigated by considering the head loss as the control variable.

PART B. PSEUDO-HOMOGENEOUS APPROACH: CFD STUDIES

The second part of this thesis focuses on modelling of turbulent pulp flow in a pipe. CFD strategies based on pseudo-homogeneous approach are investigated to predict the flow of pulp suspensions in turbulent regime. Pulp's viscosity expression is derived based on data obtained from rheograms. Two different strategies to model turbulence are investigated, standard high Reynolds and low-Reynolds-number k-ε turbulence models.

Chapter III presents the model developed based on a modified wall treatment. The applicability of different low-Reynolds-number k-ε turbulence models to calculate the flow of pulp suspensions is described in chapter IV.

Different simulation runs are performed to investigate the effect of flow rate, pulp consistency, and pulp type on pressure drop. Additionally, it is investigated the possibility of tuning different parameters related to the turbulence modelling, based on information from rheological and experimental flow data, in order to better describe the flow of pulp suspensions.

III – CFD SIMULATION WITH MODIFIED WALL TREATMENT

This chapter aims to describe a CFD method based on a modified wall treatment to simulate the pulp flow problem under study. Taking into account the non-Newtonian behaviour of pulp suspensions expressed in terms of the dependence of viscosity on local shear rate, the presence of fibers in the flow is considered in the model. Additionally, the wall treatment in the standard *k-ε* turbulence model was modified accordingly to an expression from literature. The model developed was applied to simulate the turbulent flow of refined *Eucalyptus* bleached pulp with characteristics presented in Table III.1, for different pulp consistencies and representative flow rates for each consistency. The calculations were validated by confronting calculated pressure drop values with literature data (Ventura *et al.*, 2008a, 2008b, 2011) and unpublished data from the NODESZELOSS project. Those published and unpublished data are referred here as experimental data. Detailed information concerning the rheometer and pilot rig developed to investigate the rheology and flow properties of pulp fiber suspensions can be found in (Blanco *et al.*, 2007; Ventura *et al.*, 2007, 2008a, 2008b, 2011). The CFD calculations were able to reproduce the *drag reduction* effect.

Table III.1 – *Eucalyptus* fibers characteristic properties (Ventura *et al.*, 2007, 2008b).

	Eucalyptus
Average fiber length, L_{fiber} [mm]	0.706
Average fiber diameter, d_{fiber} [mm]	0.016
Freeness, ºSR	33

III.1 – INTRODUCTION

In this chapter, the methodology used to simulate the fully developed turbulent flow of refined *Eucalyptus* bleached pulp in a pipe is described. It is tested a new strategy to deal with the effect that the presence of fibers in the flow has on turbulence since a *drag reduction* effect is observed in experiments (Ventura *et al.*, 2008a, 2008b, 2011). The modelling strategy is based on a commercial CFD solver, ANSYS Fluent 13.0 (Ansys Inc., 2010). The mathematical model is described by the equations governing the transport phenomena in the single fluid motion: mass and momentum conservation equations, i.e. continuity and Navier-

Stokes equations. Transport equations for turbulent kinetic energy, k, and its dissipation rate, ε, complete the system of equations to be solved. These two additional turbulent quantities are included in momentum conservation equations in the terms of turbulent viscosity used to close those equations. The mathematical model does not take into account the viscous effects near the pipe wall instead a near wall treatment is applied, which requires less grid points near the pipe wall. Thus, the standard high Reynolds k-ε turbulence model is tested with a modified wall function accordingly to the proposal of Jäsberg (2007).

User-Defined Functions (UDFs) were constructed in order to implement the modifications proposed in this chapter, concerning (*i*) the non-Newtonian behaviour of pulp suspension, represented by an expression for viscosity as a function of shear rate, considering a very thin water layer surrounding the core region, and (*ii*) the modified near-wall treatment.

Thus, in this chapter it will be presented the domain considered, the main characteristics of the pulp flow model, namely, the system of equations and turbulence modelling. Also, the boundary conditions and wall functions needed to close properly the system of equations will be presented and discussed. The numerical method to solve the model will also be presented. The final part of this chapter will be dedicated to present and discuss the numerical results.

It should be noted that the study presented in this chapter is based on the published paper Cotas *et al.* (2015b).

III.2 – COMPUTATIONAL FLOW DOMAIN

The choice of the computational domain is based on the experimental test section of the pilot rig schematically represented in Figure III.1. The test section composed of a smooth pipe is included in a horizontal pipe 11.5 m long and of 0.0762 m diameter (Ventura *et al.*, 2008b). An entrance section of 4 m was included to guarantee fully developed turbulent flow (Ventura *et al.*, 2008b). The distance between the pressure taps was equal to 4 m (Ventura *et al.*, 2008b). After the test section, an appropriate pipe length was installed to guarantee that the exit effects can be neglected.

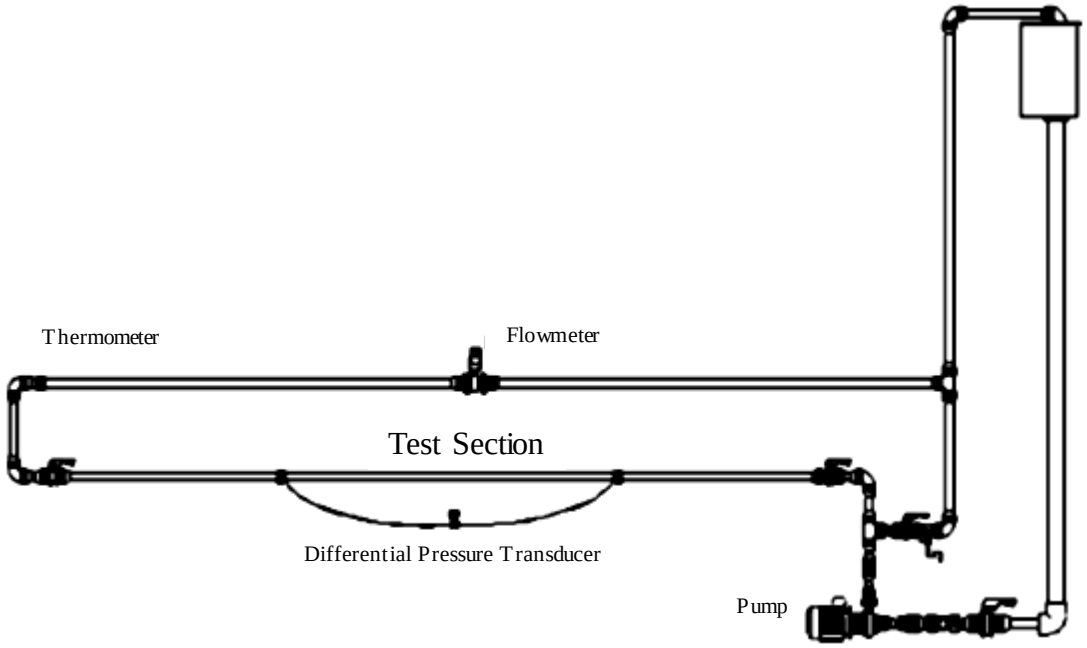

Figure III.1 – Schematic diagram of the pilot rig (adapted from Ventura *et al.* (2008b)).

At the numerical level, Figure III.2 shows the computational domain considered, $L \times R$: 1 m × 0.0381 m (*length* × pipe *radius*). It was considered a 2D axisymmetric geometry, and only a total length of 1 m since fully developed turbulent flow in the test section was assumed. The *Eucalyptus* pulp is introduced into the pipe domain through the cross-section at the left and leaves it through the cross-section at the right.

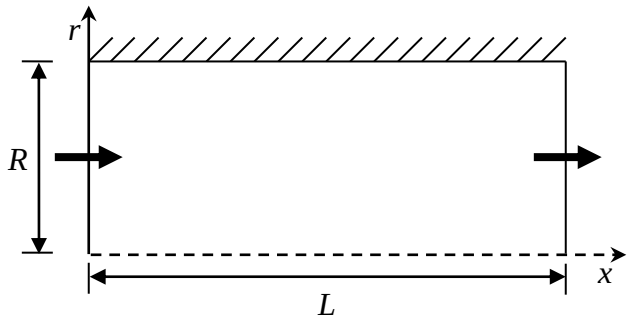

Figure III.2 – Axisymmetric geometry considered in the numerical studies.

III.3 – CFD MODELLING AND MATHEMATICAL MODEL

In the following section the modelling strategy considered in this chapter is presented. The implementation of the model is discussed in terms of the conservation equations, turbulence modelling, numerical method, and boundary conditions.

III.3.1 – GOVERNING FLOW EQUATIONS

In the present work, the pipe flow of pulp suspensions was modelled using a single-phase flow approach assuming the incompressible, isothermal, steady state flow of the non-Newtonian fluid.

III.3.1.1 – RHEOLOGICAL MODEL

The non-Newtonian behaviour of the pulp suspension was introduced into the model by means of the local dynamic viscosity, assuming that the apparent pulp viscosity, μ_{app}, corresponds to the viscosity of a Newtonian fluid that presents the same resistance to the flow as the pulp flow (Ventura *et al.*, 2011). Additionally, the model proposed in this chapter takes into account a very thin layer near the pipe wall where the presence of fibers was not considered, i.e. a pure water annulus was assumed. The thickness of that layer was assumed to be equal to the average fiber length of the *Eucalyptus* pulp, 0.706 mm (Ventura *et al.*, 2007, 2008b), based on the study presented by Dong *et al.* (2003).

The non-Newtonian power-law model was applied to fit the apparent viscosity data presented in Figure III.3 (pulp consistency, c = 1.50, 1.80 and 2.50 %), and expressions for apparent viscosity as a function of shear rate, $\dot{\gamma}$, were derived. The apparent viscosity of the pulp suspension was expressed by:

$$\mu_{app} = K\left(\dot{\gamma}\right)^{n-1} \tag{III.1}$$

with the values of consistency coefficient, K, and the flow behaviour index, n, obtained from data adjustment for each pulp consistency analysed, as presented in Table III.2.

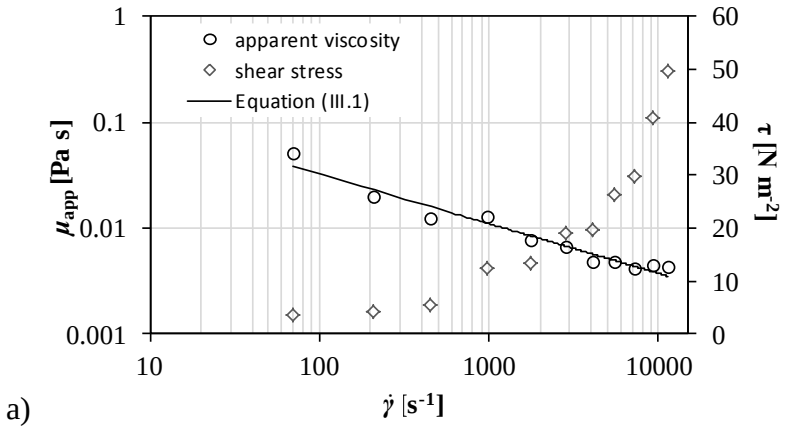

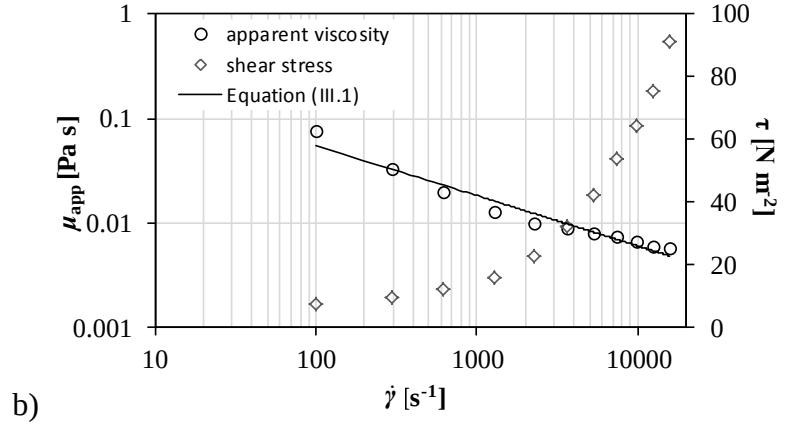

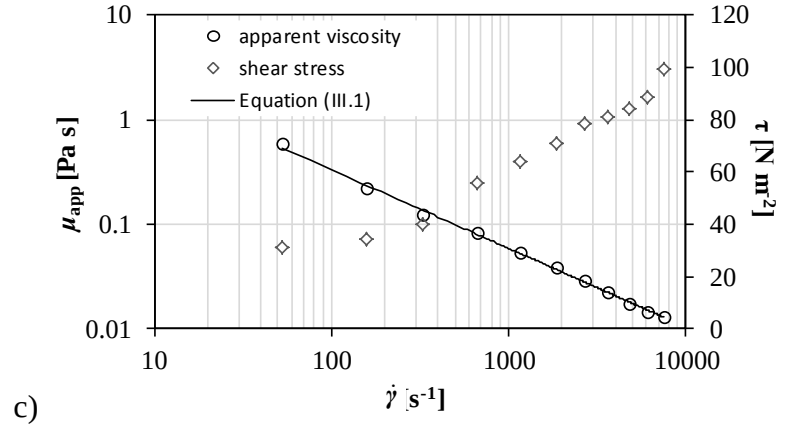

Figure III.3 – Rheograms and apparent viscosities for *Eucalyptus* pulp suspension for consistency, *c*, equal to (a) 1.50 %, (b) 1.80 %, and, (c) 2.50 %.

Table III.2 – Consistency coefficient and flow behaviour index for Equation (III.1) and the correlation coefficient, *Eucalyptus* pulp suspension.

c **[%]**	***K*** **[Pa s^n]**	***n***	**R^2**
1.50	0.28	0.53	0.96
1.80	0.51	0.52	0.96
2.50	10.72	0.25	1.00

III.3.1.2 – FLOW MODELLING

As mentioned, the flow of pulp suspension in the pipe was modelled using a single phase approach. The CFD problem was solved through a commercial CFD software, ANSYS Fluent. In the pseudo-homogeneous approach applied in this work, the different phases are treated as only one fluid phase and their mixture in not distinguished with the main features of the multiphase pulp flow represented by its rheology and turbulence. The governing flow equations for the problem under study are derived from the instantaneous continuity and Navier-Stokes equations replacing the flow variables in the instantaneous equations by the mean and fluctuating components. The instantaneous equations are obtained through mass and momentum balances, applying differential equations to translate the conservation of the quantity evaluated in a certain control volume of the flow domain. It was chosen here to present the continuity and the Navier-Stokes equations in its ensemble-average form. A detailed description concerning how to obtain the governing flow equations presented in this section can be found for example in Patankar (1980), Bird *et al.* (2002), Ansys Inc. (2010) and Oliveira and Lopes (2010).

The governing equations of flow transport phenomena in a single fluid motion, which are applied in the present study, i.e. the continuity and the Navier-Stokes equations for the turbulent flow, with the simplifications assumed for the pulp suspensions flow under analysis, can be written as:

Continuity equation

$$\frac{\partial u}{\partial x}+\frac{\partial v}{\partial r}+\frac{v}{r}=0 \tag{III.2}$$

Navier-Stokes equation – x-component

$$\frac{\rho}{r}\left[\frac{\partial}{\partial x}(ruu)+\frac{\partial}{\partial r}(rvu)\right]=-\frac{\partial p}{\partial x}+\frac{1}{r}\left[\frac{\partial}{\partial x}\left(r\mu_{\text{eff}}\,\frac{\partial u}{\partial x}\right)+\frac{\partial}{\partial r}\left(r\mu_{\text{eff}}\,\frac{\partial u}{\partial r}\right)\right] + \frac{\partial}{\partial x}\left(\mu_{\text{eff}}\,\frac{\partial u}{\partial x}\right)+\frac{1}{r}\frac{\partial}{\partial r}\left(r\mu_{\text{eff}}\,\frac{\partial v}{\partial x}\right) \tag{III.3}$$

Navier-Stokes equation – r-component

$$\frac{\rho}{r}\left[\frac{\partial}{\partial x}(ruv)+\frac{\partial}{\partial r}(rvv)\right]=-\frac{\partial p}{\partial r}+\frac{1}{r}\left[\frac{\partial}{\partial x}\left(r\mu_{\text{eff}}\,\frac{\partial v}{\partial x}\right)+\frac{\partial}{\partial r}\left(r\mu_{\text{eff}}\,\frac{\partial v}{\partial r}\right)\right] + \frac{\partial}{\partial x}\left(\mu_{\text{eff}}\,\frac{\partial u}{\partial r}\right)+\frac{1}{r}\frac{\partial}{\partial r}\left(r\mu_{\text{eff}}\,\frac{\partial v}{\partial r}\right) - 2\mu_{\text{eff}}\,\frac{v}{r^2} \tag{III.4}$$

here, the effective viscosity, μ_{eff}, is defined by:

$$\mu_{\text{eff}} = \mu + \mu_{\text{t}} \tag{III.5}$$

where the fluid viscosity, μ, is given by the apparent pulp viscosity – Equation (III.1). The turbulent viscosity, μ_{t}, appears due to assuming the Boussinesq hypothesis to model Reynolds stresses terms representing the effects of turbulence and not as a property of the pulp suspension. Since the standard high Reynolds *k*-ε turbulence model was chosen, μ_{t} is given by (Ansys Inc., 2010):

$$\mu_{\text{t}} = \rho C_{\mu}\,\frac{k^2}{\varepsilon} \tag{III.6}$$

where C_{μ} is an empirical constant equal to 0.09. Equation (III.6) was derived from the Prandtl-Kolmogorov relation for turbulent viscosity. It is obtained from the prediction of two additional transport equations for turbulent quantities, turbulent kinetic energy (*k*) and its dissipation rate (*ε*). Section III.3.2 presents how these two additional quantities are modelled.

III.3.2 – TURBULENCE MODELLING

Several different models can be applied to study turbulence and complete the system of flow conservation equations. Usually, they are divided into: (*i*) Reynolds-averaged Navier-Stokes (RANS) based models, (*ii*) large eddy simulations (LES), (*iii*) direct numerical simulations (DNS), and (*iv*) detached eddy simulations (DES) and other hybrid models. RANS based models introduce the equations for quantities representing turbulence and relate them with Reynolds stresses through turbulent viscosity. LES admit that eddies of smaller

scale present universal structures according to Kolmogorov scale and large eddies are related to the domain geometry. DNS models are based on the complete solution of the Navier-Stokes equations without any turbulence model, which can lead to extra computational effort and simulation time because of the extremely fine mesh. DES and other hybrid models emerged to deal with the difficulty in the near wall region of LES models, applying there a strategy similar to RANS and the LES model in the flow interior.

In this work, it was decided to apply a linear eddy viscosity model, RANS based turbulence model, since they are widely used in CFD simulations at the academic and industrial level. Also, they are simple and robust models, the solution has reasonable accuracy, and the costs in terms of computational time are relatively low. These models are classified based on the additional variables representing the turbulent quantities and respective equations chosen: (*i*) zero-equation models, (*ii*) one-equation models, and (*iii*) two-equation models. In the first class of RANS referred, zero-equation models, the turbulent viscosity is not obtained by solving additional turbulence conservation equations, but instead it is calculated based on some algebraic equations. On the other hand, turbulent viscosity, in one-equation and two-equation models, is calculated from turbulent quantities obtained from one or two differential equations, respectively.

The governing flow equations, Equations (III.2) to (III.4), can be solved when the turbulent quantities k and ε are known. As mentioned in Section III.1, turbulence was modelled with a RANS two-equation based model, k-ε turbulence model, in its standard version for high Reynolds numbers, in order to close mathematically the system of governing flow equations. The two additional transport equations for k and ε can be written in its ensemble-average form as:

Transport equation of turbulent kinetic energy

$$\frac{\rho}{r}\left[\frac{\partial}{\partial x}(ruk)+\frac{\partial}{\partial r}(rvk)\right]=\frac{1}{r}\left\{\frac{\partial}{\partial x}\left[r\left(\mu+\frac{\mu_t}{\sigma_k}\right)\frac{\partial k}{\partial x}\right]+\frac{\partial}{\partial r}\left[r\left(\mu+\frac{\mu_t}{\sigma_k}\right)\frac{\partial k}{\partial r}\right]\right\} + P_k-\rho\varepsilon \tag{III.7}$$

Transport equation for dissipation rate of turbulent kinetic energy

$$\frac{\rho}{r}\left[\frac{\partial}{\partial x}(ru\varepsilon)+\frac{\partial}{\partial r}(rv\varepsilon)\right]=\frac{1}{r}\left\{\frac{\partial}{\partial x}\left[r\left(\mu+\frac{\mu_t}{\sigma_\varepsilon}\right)\frac{\partial \varepsilon}{\partial x}\right]+\frac{\partial}{\partial r}\left[r\left(\mu+\frac{\mu_t}{\sigma_\varepsilon}\right)\frac{\partial \varepsilon}{\partial r}\right]\right\} + (C_{\varepsilon 1}P_k-C_{\varepsilon 2}\rho\varepsilon)\frac{\varepsilon}{k} \tag{III.8}$$

with the term representing the generation of turbulent kinetic energy due to mean velocity gradients, P_k, expressed by:

$$P_k = \mu_t \left\{ 2\left[\left(\frac{\partial u}{\partial x} \right)^2 + \left(\frac{\partial v}{\partial r} \right)^2 + \left(\frac{v}{r} \right)^2 \right] + \left(\frac{\partial v}{\partial x} + \frac{\partial u}{\partial r} \right)^2 \right\} \tag{III.9}$$

The model constants $C_{\varepsilon 1}$ and $C_{\varepsilon 2}$ are equal to 1.44 and 1.92, respectively (Ansys Inc., 2010). The turbulent Prandtl numbers, σ_k and σ_ε have the values of 1.0 and 1.3, respectively (Ansys Inc., 2010).

A detailed description of how to obtain Equations (III.7) and (III.8) is presented for example in Costa (1996).

III.3.3 – NUMERICAL STRATEGY, BOUNDARY CONDITIONS AND WALL FUNCTIONS

The pulp flow under study is described by the complete system of differential equations composed of Equations (III.2) to (III.4), Equations (III.7) and (III.8). This complete system is composed of equations that are rather complex, with derivative terms of first and second order in space, and highly non-linear. Numerical methodologies are widely used to solve numerically complete systems of transport equations. In the present study, the system of transport equations was solved using the CFD solver ANSYS Fluent with the numerical solution method provided by the commercial CFD software. The objective is to obtain algebraic equations from the differential equations, without modifying the conservative behaviour of each quantity, which can then be solved through an iterative algorithm leading to a converged solution.

To better describe the solution process to solve numerically the complete system of transport equations in this chapter, the differential equations of the dependent variables (Equations (III.2) to (III.4), Equations (III.7) and (III.8)) can be expressed by the general differential equation:

$$\frac{\rho}{r}\left[\frac{\partial}{\partial x}(ru\phi) + \frac{\partial}{\partial r}(rv\phi) \right] = \frac{1}{r}\left[\frac{\partial}{\partial x}\left(r\Gamma_\phi \frac{\partial \phi}{\partial x} \right) + \frac{\partial}{\partial r}\left(r\Gamma_\phi \frac{\partial \phi}{\partial r} \right) \right] + S_\phi \tag{III.10}$$

respecting the generalized conservation principle. In the general differential equation, ϕ represents the dependent variable, Γ_ϕ corresponds to the diffusion coefficient and the source-term is symbolized by S_ϕ. The pulp flow phenomena are described by terms of convection, diffusion and source terms in Equation (III.10). The model terms ϕ, Γ_ϕ and S_ϕ are presented in Table III.3 for the different transport equations.

Table III.3 – Model parameters ϕ, Γ_ϕ and S_ϕ – Equation (III.10).

Equation	***Transported property***	ϕ	Γ_ϕ	S_ϕ
Continuity (Equation (III.2))	Mass	1	0	0
Navier-Stokes – *x*-component (Equation (III.3))	Momentum in *x*-direction	u	μ_{eff}	$-\frac{\partial p}{\partial x}+\frac{\partial}{\partial x}\left(\mu_{\text{eff}}\frac{\partial u}{\partial x}\right)+\frac{1}{r}\frac{\partial}{\partial r}\left(r\mu_{\text{eff}}\frac{\partial v}{\partial x}\right)$
Navier-Stokes – *r*-component (Equation (III.4))	Momentum in *r*-direction	v	μ_{eff}	$-\frac{\partial p}{\partial r}+\frac{\partial}{\partial x}\left(\mu_{\text{eff}}\frac{\partial u}{\partial r}\right)+\frac{1}{r}\frac{\partial}{\partial r}\left(r\mu_{\text{eff}}\frac{\partial v}{\partial r}\right)$ $-2\mu_{\text{eff}}\frac{v}{r^2}$
Turbulent kinetic energy (t.k.e.) (Equation (III.7))	Turbulent kinetic energy	k	$\mu+\frac{\mu_t}{\sigma_k}$	P_k - $\rho\varepsilon$
Dissipation rate of turbulent kinetic energy (t.d.r.) (Equation (III.8))	Dissipation rate of k	ε	$\mu+\frac{\mu_t}{\sigma_\varepsilon}$	$\left(C_{\varepsilon 1}P_k-C_{\varepsilon 2}\rho\varepsilon\right)\frac{\varepsilon}{k}$

III.3.3.1 – NUMERICAL METHODOLOGY

The general scalar transport equation is solved numerically with a control-volume-based technique. Detailed information about this technique and its implementation in the CFD solver can be found in Ansys Inc. (2010). Here, it was chosen to describe the basic principles of ANSYS Fluent solver methodology used to obtain the numerical solution of Equation (III.10).

To obtain the distribution of the dependent quantity, the flow domain (continuum domain) is divided into a set of finite small elements (cells) creating the numerical mesh (see Figure III.4), i.e. a discretized domain, where the distribution of the scalar variables can be obtained through the discretized version of Equation (III.10). Each of these finite parts represents a control volume for which the transport equations for scalar properties are integrated leading to discrete equations respecting the conservation laws on the control

volume. Integration of Equation (III.10) is done for each control volume in the numerical domain.

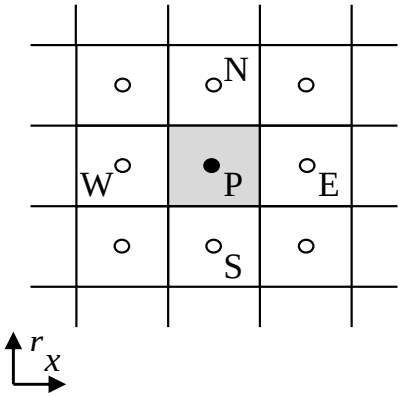

Figure III.4 – Control volume used to exemplify the discretization scheme, two-dimensional situation, where N, W, S and E are the neighbour cells.

It should be mentioned that the source-term presented in Equation (III.10) is replaced by:

$$S_{\phi} = S_{\mathrm{C}} + S_{\mathrm{P}}\phi \tag{III.11}$$

before the integration and linearization process. S_C represents the constant part and S_P is the coefficient of ϕ.

The integration of Equation (III.10) for an arbitrary control volume leads to a discretized scalar transport equation which includes information about the scalar property in the cell centre of that control volume as well as information of the surrounding cells. That discretized scalar transport equation is, in general, non-linear in relation to the scalar transport variable and needs to be linearized. The linearized form of the discretized equation for the control volume, Figure III.4, is expressed by:

$$a_{\mathrm{P}}\phi_{\mathrm{P}} = a_{\mathrm{N}}\phi_{\mathrm{N}} + a_{\mathrm{S}}\phi_{\mathrm{S}} + a_{\mathrm{E}}\phi_{\mathrm{E}} + a_{\mathrm{W}}\phi_{\mathrm{W}} + b \tag{III.12}$$

or in a more general form

$$a_{\mathrm{P}}\phi_{\mathrm{P}} = \sum_{\mathrm{nb}} a_{\mathrm{nb}}\phi_{\mathrm{nb}} + b \tag{III.13}$$

where the subscript nb means neighbour cells, a represents the linearized coefficients for the scalar variable ϕ in the cell (subscript P) and neighbour cells (subscript nb). The linearized coefficient a_P is given by:

$$a_P = \sum_{nb} a_{nb} + S_P \Delta V \tag{III.14}$$

and b is expressed by:

$$b = S_C \Delta V \tag{III.15}$$

where ΔV corresponds to the volume of the control volume.

Applying Equation (III.13) for each mesh cell results in a set of algebraic linear equations for the corresponding scalar quantity. However, some non-linearity can be present since some of the coefficients in that equation can be expressed as a function of the dependent variables. This situation is solved by an iterative process where new values of coefficients and dependent variables are obtained until a convergence state is obtained.

The coefficients a_{nb} are calculated based on the convective and diffusive fluxes in the interfaces between cells. For example, the velocity components (Figure III.5) are calculated not in the cell centre but instead they are obtained in a mesh point located in the cell interface. However, the discrete values of the dependent variables are stored in the cell centre. A strategy should be applied to get the values at the cell interfaces from those in the cell centre. This is completed through an upwind scheme in which the interface value is derived by the quantities in the cell upstream. A first-order upwind scheme was chosen in which it is assumed that the value at the cell interface is equal to the value at the cell centre in the upstream cell.

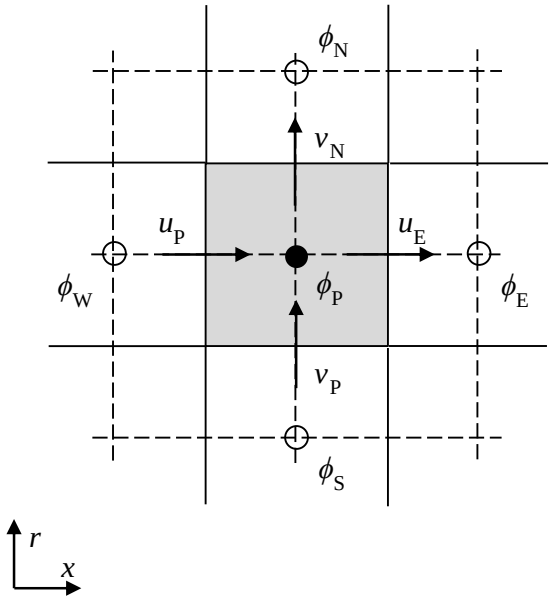

Figure III.5 – Control volume with dependent variables and components of velocity, two-dimensional situation.

A pressure-based solver approach was followed. The solution process includes the following steps: (*i*) discretization of Navier-Stokes equations, (*ii*) discretization of continuity equation, (*iii*) pressure-velocity coupling algorithm, and (*iv*) steady-state iterative algorithm. In this approach, the pressure field is determined through a pressure equation obtained by combining continuity and momentum equations. The discretization process applied is the same as described before. The discretized equations resulting from the momentum equations take into account that the components of velocity are calculated not in the cell centres but for the cell interfaces, and the mass fluxes are known at cell interfaces. The discretized equation applied for the momentum equation in *x*-direction results in:

$$a_P u_P = \sum_{nb} a_{nb} u_{nb} + b + A_w \left(p_W - p_P \right) \tag{III.16}$$

where $A_w(p_W - p_P)$ represents the pressure that is applied in the interface on the control volume with an area A_w, while for the *r*-direction it becomes:

$$a_P v_P = \sum_{nb} a_{nb} v_{nb} + b + A_s \left(p_S - p_P \right) \tag{III.17}$$

Equations (III.16) and (III.17) can only be solved when the pressure field is known. The pressure field is not expressed by a conservation equation, but instead it is obtained by combining other dependent variables. Pressure-velocity SIMPLE (Semi-Implicit Method for Pressure-Linked Equations) coupling algorithm is applied to obtain the unknown pressure

field by coupling the Navier-Stokes equations with the continuity equation. This method is described in detail in Patankar (1980).

Assuming that an initial guess for the pressure field, p^*, is used as start point in the calculations, or that during the calculations that pressure field is considered equal to that obtained in the previous iteration, Equations (III.16) and (III.17) can be expressed as:

$$a_P u_P^* = \sum_{nb} a_{nb} u_{nb}^* + b + A_w \left(p_W^* - p_P^* \right) \tag{III.18}$$

and,

$$a_P v_P^* = \sum_{nb} a_{nb} v_{nb}^* + b + A_s \left(p_S^* - p_P^* \right) \tag{III.19}$$

However, if the initial guess for pressure is not the most appropriate it can lead to a velocity field where the continuity condition is not satisfied, i.e.

$$\sum_{f}^{nf} J_f A_f \neq 0 \tag{III.20}$$

where J_f is the mass flux through the interface f of the control volume, ρu or ρv.

Nevertheless, a correction for pressure can be applied, p', in order to get a correct pressure through:

$$p = p^* + p' \tag{III.21}$$

and, correct velocity components

$$u = u^* + u' \tag{III.22}$$

$$v = v^* + v' \tag{III.23}$$

Subtracting Equations (III.18) and (III.19) from Equations (III.16) and (III.17), respectively, it is obtained

$$a_P u_P' = \sum_{nb} a_{nb} u_{nb}' + A_w \left(p_W' - p_P' \right) \tag{III.24}$$

and,

$$a_P v_P' = \sum_{nb} a_{nb} v_{nb}' + A_s \left(p_S' - p_P' \right) \tag{III.25}$$

which now satisfies the continuity equation.

In order to avoid the complexity linked to the terms $\sum_{nb} a_{nb} u_{nb}'$ and $\sum_{nb} a_{nb} v_{nb}'$, it is assumed that these terms can be eliminated from the formulation in the SIMPLE method, leading to:

$$a_P u_P' = A_w \left(p_W' - p_P' \right) \tag{III.26}$$

or

$$u_P' = d_w \left(p_W' - p_P' \right) \tag{III.27}$$

and,

$$a_P v_P' = A_s \left(p_S' - p_P' \right) \tag{III.28}$$

or

$$v_P' = d_s \left(p_S' - p_P' \right) \tag{III.29}$$

The discrete equations for the velocity correction are obtained by modifying Equations (III.22) and (III.23) considering Equations (III.27) and (III.29):

$$u_P = u_P^* + d_w \left(p_W' - p_P' \right) \tag{III.30}$$

$$v_P = v_P^* + d_s \left(p_S' - p_P' \right) \tag{III.31}$$

The flux correction equations, Equations (III.30) and (III.31), in the SIMPLE algorithm, are placed in the discrete continuity equation ($\sum_{f}^{nf} J_f A_f = 0$) to obtain the discrete equation for the pressure correction:

$$a_P p_P' = \sum_{nb} a_{nb} p_{nb}' + b \tag{III.32}$$

with *b* representing the net flow rate

$$b = \sum_{\mathrm{f}}^{\mathrm{nf}} J_{\mathrm{f}}^{*} A_{\mathrm{f}} \tag{III.33}$$

The complete system of discretized equations is now complete and can be solved in order to get a converged solution for the problem under study. Nevertheless, it is necessary to control the change of dependent variables, since an iterative process is applied with discrete equations for velocity and pressure correction. Not to control the high or low amplitude of change of the dependent variables can lead to convergence problems or even to divergence during the calculation process, and incorrect values. This problem can be controlled using a sub-relaxation strategy. It consists in limiting the magnitude that dependent variables can change between iterations, by imposing the value of the new dependent variable, ϕ_{new}, as a function of the old value, ϕ_{old}, and the calculated value, ϕ_{cal}, through:

$$\phi_{\mathrm{new}} = \alpha \phi_{\mathrm{cal}} + (1-\alpha)\phi_{\mathrm{old}} \tag{III.34}$$

If the above expression is applied in the system of discretized variables (Equation (III.13)), it results in the following discretized expression

$$\frac{a_{\mathrm{P}}\phi_{\mathrm{P}}}{\alpha} = \sum_{\mathrm{nb}} a_{\mathrm{nb}}\phi_{\mathrm{nb}} + b + \frac{1-\alpha}{\alpha} a_{\mathrm{P}}\phi_{\mathrm{old}} \tag{III.35}$$

After a solution of the discretized system of equations is obtained, the pressure is corrected using the under-relaxation factor:

$$p = p^{*} + \alpha\, p' \tag{III.36}$$

The linear system composed of Equations (III.13) and (III.32) are solved in ANSYS Fluent through a point implicit linear equation solver, Gauss-Seidel method, together with an algebraic multigrid method (AMG). In this way, the linear system of equations is solved sequentially, using at the same time, the results obtained in the previous iteration. The resolution is performed in two sweeps, forward and backward directions in the domain. A better description of the process can be found in Ansys Inc. (2010) and Patankar (1980).

The convergence of the iterative process is controlled by evaluating the imbalance in Equation (III.13) summed over all the domain cells *P* and scaled globally:

$$R_{\phi} = \frac{\sum_{\text{cellsP}} \left| \sum_{\text{nb}} a_{\text{nb}} \phi_{\text{nb}} + b - a_{\text{P}} \phi_{\text{P}} \right|}{\sum_{\text{cellsP}} \left| a_{\text{P}} \phi_{\text{P}} \right|} \tag{III.37}$$

For the continuity equation the residual convergence criteria is evaluated by the scaled residual

$$R_{c} = \frac{\sum_{\text{cellsP}} \left| \text{rate of mass creation in cell P} \right|_{\text{iteration N}}}{\sum_{\text{cellsP}} \left| \text{rate of mass creation in cell P} \right|_{\text{iteration 5}}} \tag{III.38}$$

where $\sum_{\text{cellsP}} \left| \text{rate of mass creation in cell P} \right|_{\text{iteration 5}}$ is evaluated in the first five iterations and corresponds to the largest absolute value of residual of continuity. For the present work, the convergence criterion considered is that the scaled residuals of all equations must be less than 1×10^{-5}.

To summarise, the solution method based on the control-volume technique includes three main steps: (*i*) numerical domain partition into control volumes, (*ii*) integration, discretization and linearization of equations for the dependent variables, and (*iii*) solution of the linear system of equations through an appropriate algorithm. The pressure-based solver implemented in ANSYS Fluent and, pressure-velocity coupling SIMPLE algorithm, consists of the following steps (Ansys Inc., 2010): (*i*) initializing the dependent variables field values, (*ii*) updating fluid properties and turbulent properties based on the actual known values, (*iii*) solving the momentum equations sequentially considering the updated values of pressure and interface mass fluxes, (*iv*) solving the pressure correction equation with the updated velocity field and mass fluxes, Equation (III.32), (*v*) correcting the velocity field through Equations (III.30) and (III.31), (*vi*) correcting the pressure field by Equation (III.36), (*vii*) solving additional scalar equations for turbulent quantities represented by Equation (III.13), applying the updated values obtained in the previous steps, (*viii*) evaluating solution convergence, if it not converged return to step (*ii*).

The numerical calculation was initialized considering that the initial variables field specified was equal to zero, except for the turbulent kinetic energy and its dissipation rate which were initialized with 1 $m^2\ s^{-2}$ and 1 $m^2\ s^{-3}$, respectively.

III.3.3.2 – BOUNDARY CONDITIONS AND WALL FUNCTIONS

The complete system of equation describing the problem under study, Equation (III.10), can only be integrated and solved numerically when boundary conditions are correctly specified. That system requires two boundary conditions for each spatial coordinate since it is represented by second-order differential equations. In this way, giving the correct variables specifications in the boundaries guarantees that the solution obtained is the most appropriate for the current study. Also, the discretized equation, Equation (III.13), is applied for all control volumes in the domain, including the control volumes in which interfaces are the same as boundaries. Boundary conditions are needed to perform the numerical calculation (to link boundary nodes with interior nodes) and to specify the numerical treatment to be applied between the boundary condition at the interface and the mesh node in contact with the corresponding boundary. Typically, boundary conditions can be: (*i*) fix dependent variable value (Dirichlet boundary conditions) or (*ii*) fix gradient (von Neumann boundary conditions).

Usually, boundary conditions are implemented based on the following steps: (*i*) turns off the a_{nb} coefficient in the linearized form of the discretized equation corresponding to the boundary, and (*ii*) boundary condition is implemented through additional source-terms which include the fluxes through the boundaries.

In the present study, boundary conditions are needed at the (*1*) inlet and (*2*) outlet of the flow domain, at the (*3*) pipe axis and at the (*4*) pipe wall (see Figure III.6). Periodic boundary conditions are selected to link inlet and outlet flow. The pipe symmetry axis is considered by selecting axis boundary condition. At the pipe wall, a wall boundary condition is applied. The boundary conditions are internally implemented by default in the CFD solver. However, it is possible to modify and create own-developed boundary conditions specifications using User-Defined Functions (UDFs).

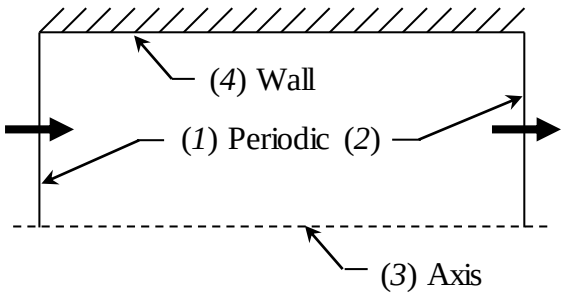

Figure III.6 – Numerical axisymmetric geometry studied (see Figure III.2) and boundary conditions applied.

(*1*) (*2*) *Inlet and outlet of the flow domain:* As mentioned previously, inlet and outlet boundaries are linked as periodic boundary conditions. This option is suitable for the flow under study since fully developed turbulent flow is observed and, also, because geometry presents periodicity repeating configuration. The present pulp flow is characterised by flow and geometry translational periodic condition. This condition is adequate to simulate a shorter pipe length (1 m instead of 4 m, see Section III.2), and, also, to avoid including an entrance region to guarantee fully developed flow. Two options are available in the CFD software concerning pressure and mass flow rate specifications for this type of boundary conditions. In ANSYS Fluent it is possible to specify the value of mass flow rate, and the respective pressure gradient is calculated during the simulation process, or, alternatively, it is specified the pressure gradient. In the present work, the main variable to evaluate the quality of numerical calculations is the pressure drop. Different flow conditions, namely, different mass flow rates were tested. A pressure-drop periodic flow condition was, then, selected, specifying the mass flow rate for each case tested, required to obtain the pressure gradient to validate the numerical results.

In this type of boundary condition, inlet conditions for turbulent quantities are not needed to be specified instead they are calculated after momentum equations are solved respecting the flow governing equations. The mass flow rate specified is considered to be equal both at the inlet and outlet of the domain, or that the velocity entering a cell volume of periodic boundary (*2*) equals the velocity going out of the previous cell volume (*1*). As described in Ansys Inc. (2010), the outlet section (*2*) is treated as a direct neighbour to the cells adjacent to the inlet section (*1*). The flow calculated through the periodic boundary adjacent to a fluid cell, uses the flow conditions at the fluid cell adjacent to the periodic plane (Ansys Inc., 2010). Periodicity is considered for flow quantities in the flow direction, expressed by (Ferziger and Perić, 2002):

$$\frac{\partial(\bullet)}{\partial x} = 0 \tag{III.39}$$

However, periodicity is not observed for pressure which has a linear gradient in the flow direction

$$\frac{\partial p}{\partial x} = \text{constant} \tag{III.40}$$

Pressure is treated in the periodic boundary conditions methodology, by considering that the pressure gradient is composed of two terms (see Equation (III.41)): the first term on the right side is applied to guarantee the mass flow rate specified and the second term is the gradient of the periodic pressure. The first term corresponds to the constant value in Equation (III.40) (pressure used to validate the numerical model).

$$\nabla p = \nabla p_{\text{constant}} + \nabla p_{\text{varying}} \tag{III.41}$$

The numerical calculation of pressure gradient which satisfies the mass flow rate specified is controlled by two factors, the relaxation factor and the number of iterations defined for the periodic conditions. The number of iterations corresponds to the limit number of sub-iterations for which the pressure correction equation, Equation (III.32), is iterated in the SIMPLE algorithm in each step. The relaxation factor, under-relaxation factor, is used in order to control the convergence of this sub-step. The suitability of these values was evaluated by checking the overall flux conservation through net flux imbalance value.

(*3*) *Pipe axis:* This option was used for the boundary at the pipe axis and corresponds to the centreline of the axisymmetric geometry. As mentioned in the preceding section, a 2D axisymmetric geometry was considered assuming that radial homogeneity in flow and fibers distribution is present, i.e. for example there is no deposition of fibers in the bottom of the pipe during the pulp flow, which could lead to radial flow inhomogeneity.

In ANSYS Fluent, this type of boundaries does not need any additional specification. The numerical treatment is implemented and there is no need to give additional information.

(*4*) *Pipe wall:* The effect of the solid boundary in the numerical calculation is introduced as wall boundary. This type of boundary condition is internally implemented in ANSYS Fluent. However, different parameters and formulations can be applied using UDFs. Since the pulp flow is represented by four main variables, velocity components and turbulent quantities, it is required to specify a wall boundary condition for each dependent variable. The no-slip velocity condition was considered for velocity at the pipe wall:

$$u_{\text{wall}} = v_{\text{wall}} = 0 \tag{III.42}$$

Boundary conditions for momentum equations considering semi-empirical formulas to connect wall and fully turbulent wall layer are assigned at the pipe wall. This approach uses wall functions allowing to avoid that the strongly viscosity affected region is solved. The approach considering modelling the near wall region all the way to the wall will be presented

and discussed in Chapter IV. In order to use wall functions to link momentum quantities between wall and fluid flow region, the corresponding expressions to bridge those two regions should be known.

In this work, wall functions are computed based on the approach implemented in ANSYS Fluent for the two-layer standard high Reynolds *k-ε* turbulence model. Also, new wall functions are proposed in this chapter. UDFs were used to modify wall functions implemented imposing new expression for the dimensionless velocity expression – this point is discussed later in this section. The two-layer standard high Reynolds *k-ε* turbulence model is based on the wall treatment proposed by Launder and Spalding (1974). This strategy assumes that the near wall region can be decomposed in three different regions: (*i*) viscous sublayer, (*ii*) buffer layer, and (*iii*) fully turbulent wall layer. The viscous sublayer is dominated by molecular diffusion, a property of the fluid, and characterized by an almost laminar flow. The fully turbulent wall layer is dominated by turbulence, a property of the flow; here the effects due to resistance to the flow by the fluid are not as important as in the viscous sublayer. A region located between the viscous sublayer and the fully turbulent wall layer, where both turbulence and molecular diffusion are equally important, is designated as buffer layer. Standard wall functions are applied depending on the sublayer where the cell centre P is located (see Figure III.7). In Figure III.7 it is represented schematically the near wall treatment for a control volume adjacent to the wall (cell centre P) and a neighbour cell to that control volume (cell centre S). The border of viscous sublayer is represented by y_v, y_P indicates the distance to the wall from point P, and y_n corresponds to the distance to the wall from the interface between cell P and neighbour cell S.

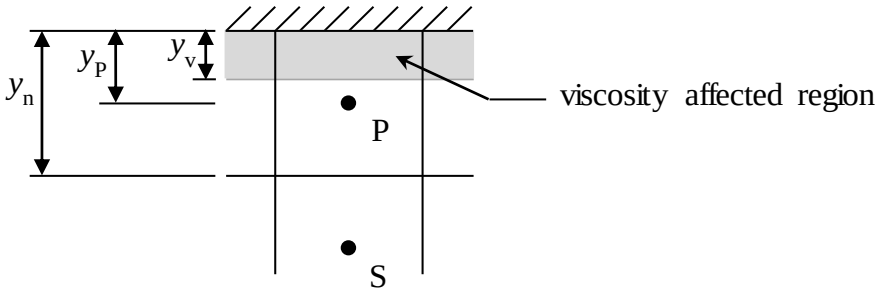

Figure III.7 – Near wall region and control volume adjacent to the wall (adapted from Costa (1996)).

The standard formulation considers a linear relation between velocity and the distance to the pipe wall in the viscous sublayer; whereas, for the fully turbulent wall layer, it considers a logarithmic expression. Those functions are expressed in terms of dimensionless variables, *u** and *y** (Ansys Inc., 2010):

$$y^* = \frac{\rho C_\mu^{1/4} k_P^{1/2} y_P}{\mu} \tag{III.43}$$

$$u^* = \frac{u_P C_\mu^{1/4} k_P^{1/2}}{\tau_w / \rho} \tag{III.44}$$

In the majority of text books related to turbulence and wall functions those functions are represented in terms of y^+:

$$y^+ = \frac{\rho u_\tau y}{\mu_w} \tag{III.45}$$

$$u^+ = \frac{u}{u_\tau} \tag{III.46}$$

with the friction velocity computed from wall shear stress as:

$$u_\tau = \sqrt{\frac{\tau_w}{\rho}} \tag{III.47}$$

where the wall shear stress (τ_w) is predicted using the properties of the fluid in the adjacent control volume to the wall considering the momentum wall functions. However, the corresponding dimensionless quantities presented above (u^* and u^+) should have no significant differences in the fully turbulent wall layer. The difference in the formulation corresponds to the turbulent velocity scale considered to compute the dimensionless distance to the pipe wall.

It was chosen here to present only the final expression of momentum wall functions. A detailed discussion concerning its development can be found for example, in Costa (1996). The standard momentum wall functions, implemented by default in ANSYS Fluent, are expressed by:

$$u^* = y^* \qquad (y^* \le y_v^*) \tag{III.48}$$

$$u^* = \frac{1}{\kappa} \ln(E y^*) \qquad (y^* > y_v^*) \tag{III.49}$$

where y_v^* corresponds to the physical viscous sublayer thickness, equal to 11.225 (Ansys Inc., 2010); κ is the von Kármán constant (=0.4187) and E is an empirical constant (=9.793) (Ansys Inc., 2010).

The wall shear stress, τ_w, is computed from the standard momentum equations (Equations (III.48) and (III.49)), considering the dimensionless variables, u^* and y^*, defined by Equations (III.43) and (III.44), which leads to:

$$\tau_w = \frac{\mu u_P}{y_P} \qquad (y^* \le y_v^*) \tag{III.50}$$

$$\tau_w = \frac{u_P C_\mu^{1/4} k_P^{1/2} \rho \kappa}{\ln\left(E y_P^*\right)} \qquad (y^* > y_v^*) \tag{III.51}$$

In terms of turbulent quantities, the boundary condition for turbulent kinetic energy at the wall is implemented by imposing a constant flux value equal to zero, i.e.

$$\left.\frac{\partial k}{\partial n}\right|_{wall} = 0 \tag{III.52}$$

where n represents the local radial coordinate of the adjacent cells to the wall (Ansys Inc., 2010). Whereas dissipation rate of k is calculated for the adjacent cells to the wall from the knowledge of k at that cells by (Ansys Inc., 2010):

$$\varepsilon_P = \frac{C_\mu^{3/4} k_P^{3/2}}{\kappa y_P} \tag{III.53}$$

and, not by solving the differential equation for ε at these cells. Additionally, the production of kinetic energy, P_k, that appears in the source term of k and ε, as defined in Equation (III.9), depends on velocity gradients. It is assumed that production of k and its dissipation rate are equal in the control volume adjacent to the wall, i.e. local equilibrium hypothesis for turbulence. The production of kinetic energy is calculated, assuming the logarithmic law given by (Ansys Inc., 2010):

$$P_k \approx \tau_w \frac{\partial u}{\partial y} = \tau_w \frac{\tau_w}{\kappa \rho C_\mu^{1/4} k_P^{1/2} y_P} \tag{III.54}$$

Modified momentum wall functions

Experimentally, it was observed that pulp flow suspensions present a peculiar S-shaped profile for the measured velocity near the wall, either for turbulent flow of *Birch* and *Pine* pulp in a pipe (Jäsberg, 2007) as well as for the turbulent flow of natural flexible cellulose wood fibers in a channel (Xu and Aidun, 2005). Different expressions were proposed in those two research works for dimensionless velocity as a function of dimensionless distance to the wall in the fully turbulent region, based on a turbulent velocity scale represented by friction velocity, u_τ – Equations (III.45) and (III.46). Due to limitations of experimental techniques used to obtain velocity data, the velocity profiles, and, velocity profiles presented in non-dimensional wall layer coordinates as presented by Xu and Aidun (2005) and Jäsberg (2007) are only for the fully turbulent wall layer ignoring the viscous sublayer. Therefore, the strategy applied in this chapter was to modify the common momentum wall law function, according to the experimental observations and mathematical adjustment proposed by Jäsberg (2007).

The velocity profile adapted from Jäsberg (2007), presented in non-dimensional wall layer coordinates, based on the standard logarithmic law, Figure III.8, can be expressed by:

$$u^+ = \frac{1}{\kappa}\ln\left(y^+\right) + B + \Delta u^+ \tag{III.55}$$

with B representing an empirical constant (=5.5) (Ansys Inc., 2010), and

$$\Delta u^+ = \begin{cases} 0 & (y_{\mathrm{v}}^+ < y^+ \le y_{\mathrm{L}}^+) \\ \dfrac{\alpha}{\kappa}\ln\left(\dfrac{y^+}{y_{\mathrm{L}}^+}\right) & (y_{\mathrm{L}}^+ < y^+ \le y_{\mathrm{C}}^+) \\ \dfrac{\alpha}{\kappa}\ln\left(\dfrac{y_{\mathrm{C}}^+}{y_{\mathrm{L}}^+}\right) - \dfrac{\beta}{\kappa}\ln\left(\dfrac{y^+}{y_{\mathrm{C}}^+}\right) & (y_{\mathrm{C}}^+ < y^+ \le R^+) \end{cases} \tag{III.56}$$

$$R^+ = \frac{\rho u_\tau R}{\mu_{\mathrm{w}}} \tag{III.57}$$

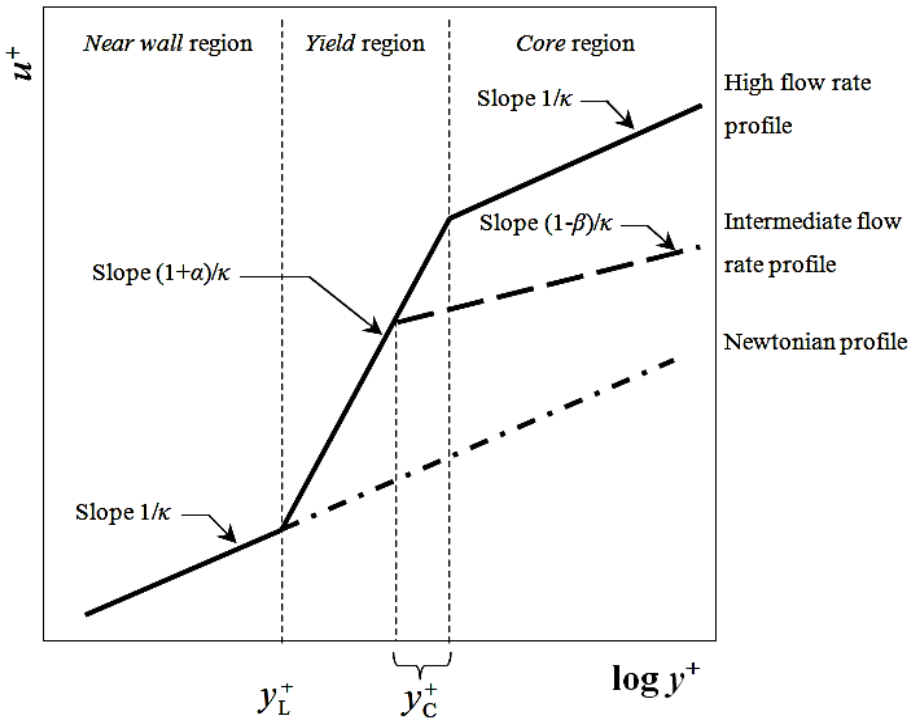

Figure III.8 – Dimensionless velocity profiles (adapted from Jäsberg (2007)).

According to Figure III.8, the derivation of the wall function made by Jäsberg (2007) considers three different zones in the turbulent region: *near wall*, *yield* and *core* regions. The *near wall* region is characterised by a profile similar to that expected by applying the standard logarithmic law, and it extends from $y_v^+ (= y_v^*)$ to y_L^+. The *yield* region is represented by a higher slope (= $(1+\alpha)/\kappa$) than that predicted by the standard logarithmic law resulting from the reduction of wall induced turbulence. Since fibers are present in the flow, the turbulent transfer of momentum from pipe wall is increased, fiber concentration is also increased from pipe wall to core region which leads to attenuation of turbulence. This region extends from the end of the *near wall* region up to the beginning of the *core* region (y_L^+ to y_C^+). At not very high flow rates, the end of *yield* region indicates the border of the plug of fibers (y_C^+). For intermediate flow rates, the attenuation of turbulence in core region starts to fail, the plug core starts to disrupt as flow rate increases leading to a decrease on dimensionless velocity slope (= $(1-\beta)/\kappa$). In the *core* region, for high flow rates the slope tends to follow the tendency of the standard logarithmic law ($1/\kappa$), but now with a vertical translation, due to the fact that when velocity is increased, turbulence is also increased towards the core region, the attenuation of larger turbulent eddies starts to fail and a profile similar to the turbulent Newtonian fluids, standard logarithmic law, appears. Flow fluidization starts in the *near wall* and progresses to

the *yield* region. Whereas the core region is related to fiber plug, i.e. flow region where higher resistance to the flow is present.

The adjustable parameters α and β are directly related to the slope of the dimensionless velocity profile in the *yield* and *core* regions, respectively. The parameters y_L^+ and y_C^+ correspond to the borders of the *yield* region with the *near wall* and *core* regions, respectively. The simulations performed with the *standard* Jäsberg adjustable parameters (α, β, y_L^+ and y_C^+) have considered those values presented in Jäsberg (2007) for the *Birch* flow case – Table III.4 since the size of these fibers is more similar to the refined *Eucalyptus* fibers. It should be pointed out that Jäsberg (2007) presented flow results for *Pine* pulp, consistency of 1 %, and *Birch* pulp, consistency of 2 %.

Table III.4 – *Standard* Jäsberg adjustable parameters for turbulent flow of *Birch* pulp, c = 2 % – Equation (III.59) (Jäsberg, 2007).

Parameter	α	β	y_L^+	y_C^+
Value	2.4	0.0	50	320

III.4 – RESULTS AND DISCUSSION

Pulp flow calculations were validated using experimental data for pressure drop. The simulations were performed for pulp composed of refined *Eucalyptus* fibers with characteristic properties presented in Table III.1. Different flow conditions and pulp consistencies were simulated for fully developed turbulent flow as shown in Table III.5. Crowding factor (see the definition Equation (III.58)) values are also presented in Table III.5. This parameter represents the average number of fibers present in a spherical volume with diameter equal to fiber length (Kerekes and Schell, 1992):

$$N = \frac{2}{3} c \left(\frac{L_{\text{fiber}}}{d_{\text{fiber}}} \right)^2 \qquad \text{(III.58)}$$

Table III.5 – Experimental conditions and flow data – *Eucalyptus* pulp (Ventura *et al.*, 2008b, 2011).

Flow case	***c*** **[%]**	***N crowding factor***	U_b **[m s^{-1}]**	$\dot{m}_b$ **[kg s^{-1}]**	$\Delta p/L_{water}$ **[Pa m^{-1}]**	$\Delta p/L_{pulp}$ **[Pa m^{-1}]**
A	1.50	1947	4.5	20	1744	829
B	1.50	1947	6.2	28	3184	1289
C	1.80	2336	4.5	20	1744	843
D	1.80	2336	6.2	28	3184	1203
E	2.50	3245	4.9	22	2046	1579
F	2.50	3245	5.6	25	2582	1754

The CFD parameters used in the simulation are summarised in Table III.6. The successful numerical calculations depend on the mesh quality (Ansys Inc., 2010). A poor mesh quality is not desirable, but also an extremely refined mesh near solid walls is not appropriate to deal with problems where standard high Reynolds *k-ε* turbulence models are applied, besides leading to larger computational times. In the study presented in this chapter, it was considered appropriate to use a uniform mesh to deal with the pulp flow and geometry domain (Figure III.9). All meshes tested for the numerical domain were created using the meshing commercial program GAMBIT 2.4.6 (Fluent Inc., 2007). In all cases, the first mesh node was placed in the fully turbulent wall layer at $y^+ > 11.225$ (Ansys Inc., 2010). Additionally, an attempt was made to place it at $y^+ > 30$ as indicated in Fluent Inc. (2007). First an extensive mesh independence study was made considering meshes with total number of nodes of 340 (10(axial)×34(radial) nodes), 680 (10(axial)×68(radial) nodes), 880 (20(axial)×44(radial) nodes), 1080 (20(axial)×54(radial) nodes), 1620 (30(axial)×54(radial) nodes), 1920 (30(axial)×64(radial) nodes) and 2040 (20(axial)×102(radial) nodes), using the default standard high Reynolds *k-ε* turbulence model and considering only the flow of water in the test rig. Base on the results of that study, mesh optimization was also conducted for *Eucalyptus* fibers suspension flow, using the modified momentum wall function with the *standard* values according to Jäsberg (2007). The final mesh was selected considering the accuracy of the solution evaluated by comparing pressure drop values obtained with the different meshes tested. The mesh composed of 1080 total number of nodes was selected.

Figure III.9 – Mesh section represented for the section at the inlet of the domain.

Table III.6 – CFD parameters.

Parameter	Value
Mesh (1 m of pipe)	20 (axial) × 54 (radial) nodes
Total number of quadrilateral cells	1007
Total number of nodes	1080
Total number of interfaces	2033
Iterations – Periodic boundary	2
Relaxation factor – Periodic boundary	0.5
Turbulence model	Standard *k-ε* model (User-Defined Wall Functions)
Under-relaxation parameters	0.3 (pressure), 0.7 (momentum), 0.8 (t.k.e.), 0.8 (t.d.r.)
Pulp viscosity	Core region: Equation (III.1)
	Water annulus: water viscosity (293 K)
Pulp density	Water density (293K)

III.4.1 – STANDARD WALL FUNCTIONS

Two different terms in the CFD model are possible of being modified to take into account the presence of fibers in the flow. One of them is related to the fluid and another one is related to the flow character. In this subchapter only the diffusion term, through the property of the fluid, the molecular viscosity, considering the pulp as non-Newtonian fluid, was modified.

The numerical results obtained modifying the fluid property (viscosity) in the CFD model without further modifications are presented in Table III.7 – Cases III.ST.FN, where ST indicates the standard high Reynolds *k-ε* turbulence model, F corresponds to the flow case of Table III.5, and N is related to the identification of test cases. In accordance with the results in Table III.7, it is not possible to reproduce the experimental measurements only by modifying the fluid viscosity. The comparison between numerical predictions and experimental data shows high relative error values ($\delta = 100\times|\Delta p/L_{exp} - \Delta p/L_{standard\ k\text{-}\varepsilon}|/\Delta p/L_{exp}$). Therefore, as the pulp consistency increases, the pressure drop predicted also increases due to the fact that higher values of viscosity are obtained for the higher pulp consistency. Additionally, the effect that the presence of fibers has on the flow properties was not taken into account in the CFD model. With this simplistic approach it was not possible to reproduce the drag reduction effect observed experimentally for this type of systems (turbulent flow of pulp fiber suspensions). In fact, it is expected that near the wall larger gradients for flow variables are present. Therefore, pulp flow evaluated through pressure drop values is not only characterized by the non-Newtonian behaviour of pulp suspension, but other flow characteristics must be considered in the development of the CFD model. Modifying the near wall treatment by

considering the new momentum wall function described in Section III.3.3.2 can be a complementary strategy to modify the CFD model. That modification is evaluated in Section III.4.2.

Table III.7 – Pressure drop values – standard high Reynolds k-ε turbulence model.

c [%]	U_b [m s^{-1}]	$\dot{m}_b$ [kg s^{-1}]	$\Delta p/L_{water}$ [Pa m^{-1}]	$\Delta p/L_{exp}$ [Pa m^{-1}]	CASE	$\Delta p/L_{standard\ k\text{-}\varepsilon}$ [Pa m^{-1}]	δ [%]
1.50	4.5	20	1744	829	III.ST.A0	1741	110
1.50	6.2	28	3184	1289	III.ST.B0	3425	166
1.80	4.5	20	1744	843	III.ST.C0	1997	137
1.80	6.2	28	3184	1203	III.ST.D0	3545	195
2.50	4.9	22	2046	1579	III.ST.E0	3313	110
2.50	5.6	25	2582	1754	III.ST.F0	3742	113

III.4.2 – JÄSBERG MOMENTUM WALL FUNCTION

III.4.2.1 – STANDARD JÄSBERG ADJUSTABLE PARAMETERS

After testing the standard high Reynolds k-ε turbulence model considering the non-Newtonian behaviour of pulp suspension, a new momentum wall function was utilized to predict the head loss and to evaluate the effect of modifying the standard logarithmic law-of-the-wall for the fully turbulent wall layer.

In order to define the wall function given by Equation (III.55) for the fully turbulent wall layer, it was introduced an additional source code to that defined to modify molecular viscosity in the UDF. It should be noted that complete Equation (III.55) was considered due to difficulties in controlling the location of point P in the fully turbulent wall layer (see Figure III.7) i.e. if it is placed in the *near wall*, *yield* or *core* region. The wall function treatment in the viscous sublayer was the default from ANSYS Fluent, even if mesh studies were performed to guarantee that the first node in the domain is placed in the fully turbulent wall layer.

Pressure drop values are presented in Table III.8, Cases III.J.FN (J indicates standard Jäsberg adjustable parameters, F corresponds to the flow case of Table III.5, and N is related to the identification of test cases), for the different conditions tested using the modified momentum wall function with *standard* Jäsberg adjustable parameters (see Table III.4). In fact, modifying the wall function improves the numerical predictions mainly for the higher

consistency. The *drag reduction* effect was predicted with the strategy presented here: pressure drop was reduced when compared to the initial prediction when only the non-Newtonian behaviour of pulp was implemented (see Section III.4.1, Table III.7). Also, the relative error (see $\delta = 100\times|\Delta p/L_{exp} - \Delta p/L_{num}|/\Delta p/L_{exp}$ in Table III.8) was reduced when comparing with the results of Table III.7. However, the pressure drop predicted has still higher values than those measured experimentally. In this preliminary study, the Jäsberg adjustable parameters (α, β, y_L^+ and y_C^+) considered were those resulting from adjustment of experimental data for *Birch* pulp flow, c = 2 %, presented in Jäsberg (2007). Even if the *Eucalyptus* and *Birch* fibers have similar length, their properties are different. In this way, the discrepancies between the numerical and experimental pressure drop values can be due to the fact that for the *Eucalyptus* pulp flow, the parameters in the Jäsberg wall function should have different values from those considered here.

Table III.8 – Pressure drop values – modified momentum wall function, according to *standard* Jäsberg function (Jäsberg, 2007).

c [%]	U_b [m s^{-1}]	$\dot{m}_b$ [kg s^{-1}]	$\Delta p/L_{water}$ [Pa m^{-1}]	$\Delta p/L_{exp}$ [Pa m^{-1}]	CASE	$\Delta p/L_{num}$ [Pa m^{-1}]	δ [%]
1.50	4.5	20	1744	829	III.J.A0	1324	60
1.50	6.2	28	3184	1289	III.J.B0	2147	67
1.80	4.5	20	1744	843	III.J.C0	1359	61
1.80	6.2	28	3184	1203	III.J.D0	2220	85
2.50	4.9	22	2046	1579	III.J.E0	2299	46
2.50	5.6	25	2582	1754	III.J.F0	2814	61

In order to describe the effects of modifying simultaneously, molecular viscosity and momentum wall functions, radial distributions of viscosity, dimensionless velocity and turbulent kinetic energy were investigated.

In Figure III.10 there are plotted the radial viscosity profiles for the three sets of pulp consistency tested and for the two mean flow rates in each set. As can be seen from these data, the higher viscosities are observed near the pipe centre, due to lower shear rates, and viscosity decreases towards the pipe wall. This trend is more notorious for the higher consistency cases (i.e. 2.50 %, Figure III.10c)) where the larger amount of fibers in the flow was taken into account in the viscosity expression. It should be pointed out that the larger differences in the order of magnitude of viscosity between the higher consistency cases, c = 2.50 %, and the lower consistency cases, c = 1.50 and 1.80 %, result from the rheological pulp properties presented in the rheograms (Figure III.3). Due to the lack of experimental rheological information for lower shear rates (< 50 s^{-1}), which was a limitation of the

experimental rheometer, that difference in the order of magnitude of viscosity near the pipe centre is more observable in the numerical flow predictions. It is evident that smaller velocity gradients are estimated near the pipe centre; thus, values of shear rate lower than those achieved experimentally in the rheological tests are predicted and, in this way, viscosity values out of the experimental range are achieved numerically for the different pulp consistencies tested.

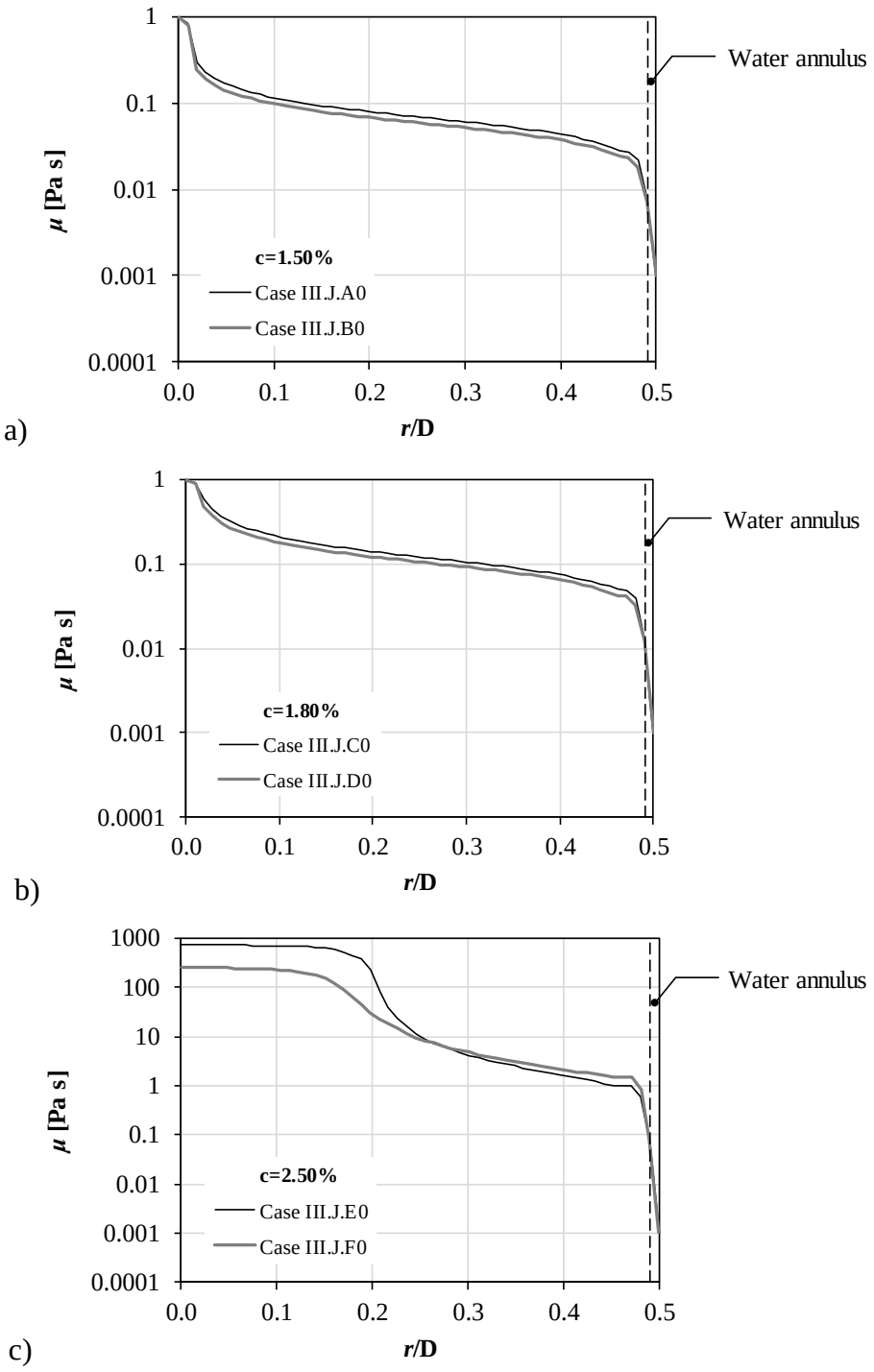

Figure III.10 – Radial viscosity profiles predicted for (a) 1.50 %, (b) 1.80 %, and, (c) 2.50 % with the *standard* Jäsberg parameters.

The non-dimensional velocity profiles are plotted in Figure III.11. According to what is presented in this plot, the first control volume, near the wall, is placed in the *yield* region, which is in accordance with the two distinct regions identified: the *yield* and *core* region. For the higher consistency (i.e. 2.50 %), the flow resistance is greater in the core region which is reproduced by a more uniform velocity distribution in the core region (see Figure III.11c)). A smooth velocity distribution for the higher consistency case was expected, near the pipe centre, leading to zones where lower values of shear rate are present.

Significant deviations from the standard *k-ε* momentum wall functions are observed in Figure III.11. The wall shear stress obtained from the modified momentum wall functions adapted from Jäsberg (2007) is defined, for the fully turbulent wall layer, by Equation (III.59):

$$\tau_{\mathrm{w}} = \frac{u_{\mathrm{P}} C_{\mu}^{1/4} k_{\mathrm{P}}^{1/2} \rho}{\frac{1}{\kappa}\ln\left(y_{\mathrm{P}}^{*}\right) + B + \Delta u^{+}} \quad (y^{*} > y_{\mathrm{v}}^{*}) \tag{III.59}$$

instead of Equation (III.54).

The wall shear stress calculated by Equation (III.59) is also used to calculate the production of kinetic energy (see Equation (III.54)). The Jäsberg momentum wall functions are introduced into the commercial CFD software through the wall shear stress. The additional term Δu^{+} is included in this input information. This term is related to the slope of the dimensionless velocity profile in the *yield* and *core* regions. In this case the first node of the mesh is placed in the *yield* region and the non-dimensional velocity profiles predicted from CFD calculations exceed the ones calculated with standard *k-ε* momentum wall functions given by Equation (III.49).

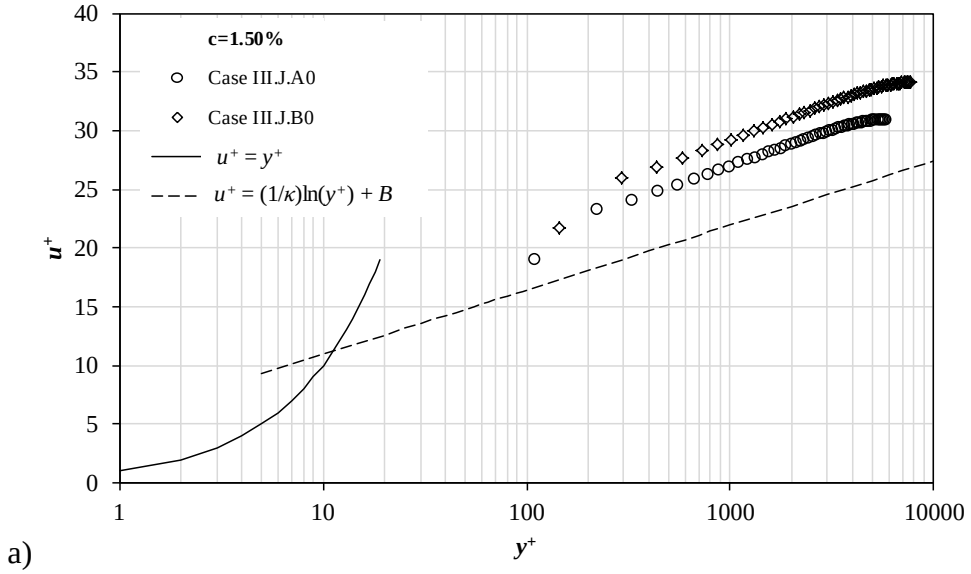

a)

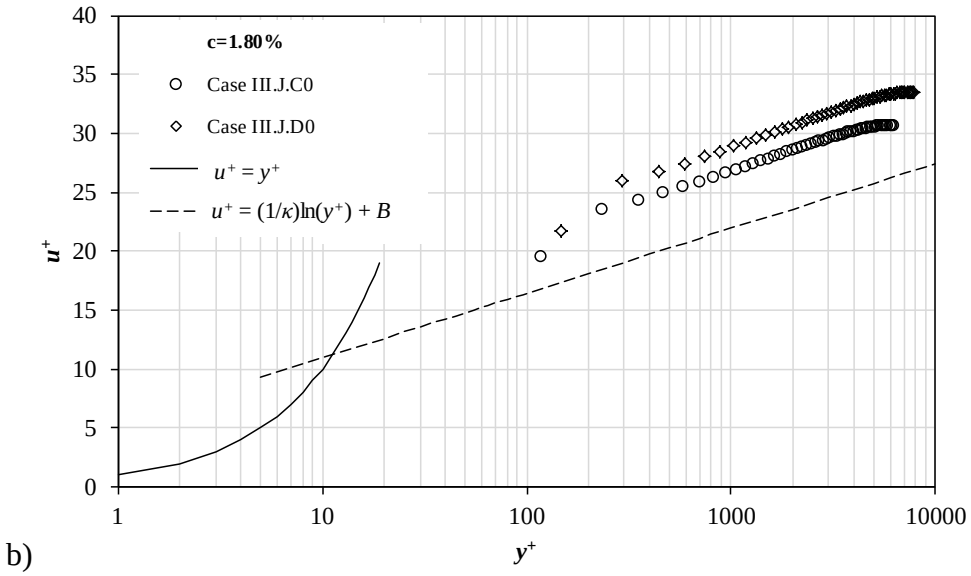

b)

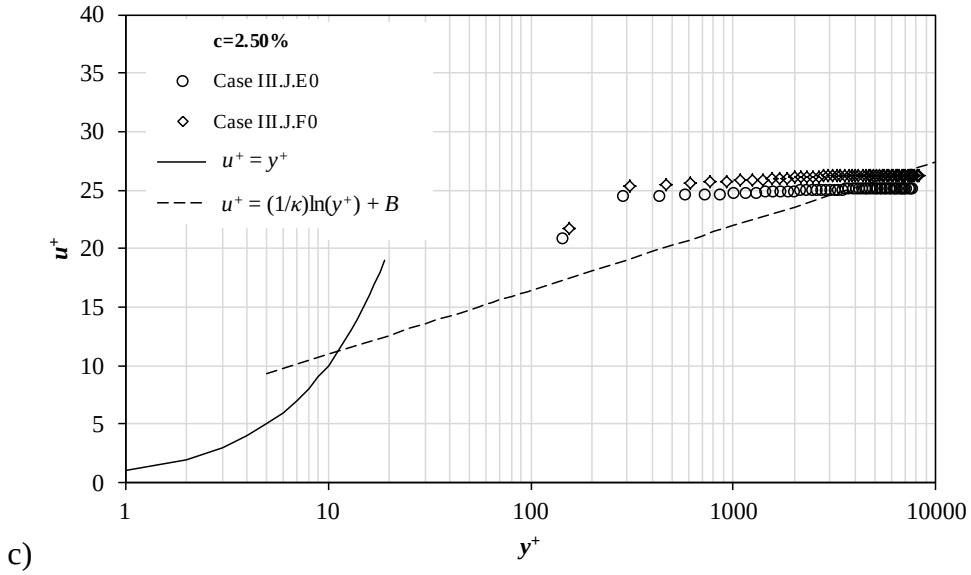

c)

Figure III.11 – Dimensionless velocity radial profiles predicted for (a) 1.50 %, (b) 1.80 %, and, (c) 2.50 % with the *standard* Jäsberg parameters.

In Figure III.12 the radial profiles of turbulent kinetic energy are shown. Generally, as can be seen from Figure III.12, higher turbulent variation occurs near the pipe wall. The turbulent kinetic energy profiles for consistency case of 2.50 % correspond to larger values than those obtained for the two lower consistencies tested (i.e. 1.50 and 1.80 %), which is in line with the pressure drop predicted. The turbulent kinetic energy decreases from the pipe wall to the pipe axis contrarily to the viscosity profile. As the fluid presents a non-Newtonian behaviour, even more pronounced for the higher consistency case (i.e. 2.50 %), the principal phenomena described in the regions defined in Section III.3.3.2 (viscous sublayer and fully turbulent wall layer) are now different. For example, for the lower consistencies and in the fully turbulent wall layer, both flow and fluid properties are important. Analysing the results obtained (Figures III.10 to III.12), it is obvious that for the pulp consistency of 2.50 %, turbulent quantities are overpredicted. To improve the results it may be necessary to tune the parameters in the wall functions, which may require values different from those proposed by Jäsberg (2007) and even different for the different cases tested.

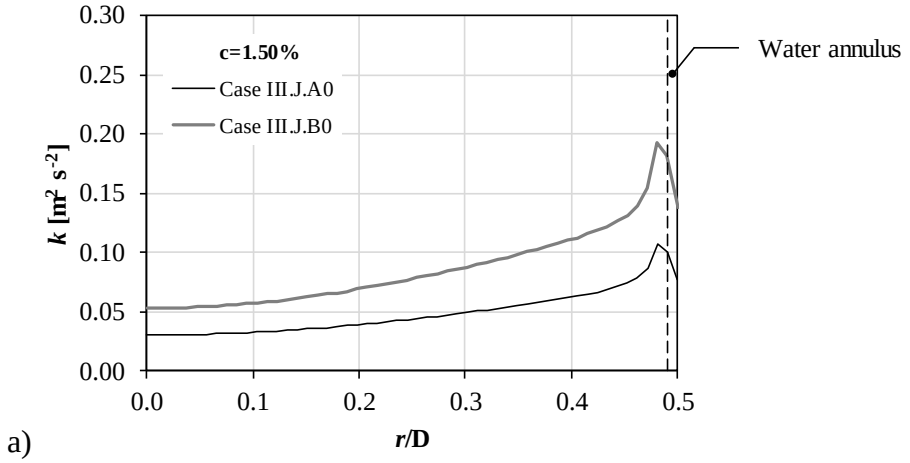

a)

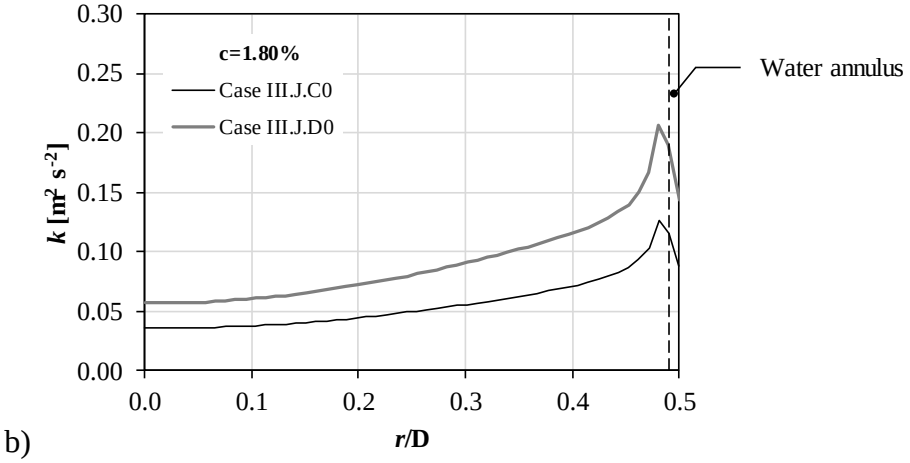

b)

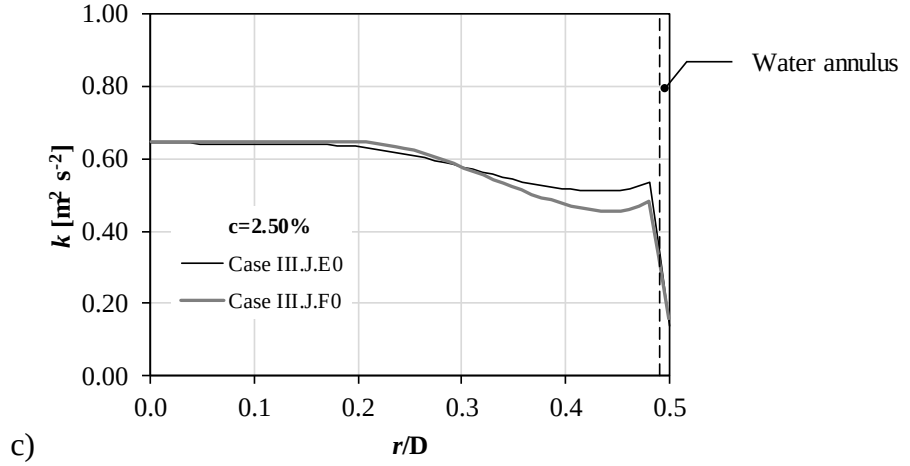

c)

Figure III.12 – Radial profiles of turbulent kinetic energy predicted for (a) 1.50 %, (b) 1.80 %, and, (c) 2.50 % with the *standard* Jäsberg parameters.

III.4.2.2 – MODIFIED JÄSBERG ADJUSTABLE PARAMETERS

As aforementioned, series of simulations was carried out to investigate the influence of different Jäsberg adjustable parameters (α, β, y_L^+ and y_C^+) on the results. The results were evaluated quantitatively in terms of pressure drop, and qualitatively through the dimensionless velocity profile. It was chosen here to present results for three reference cases: (*i*) c = 1.50 %, U_b = 6.2 m s^{-1}; (*ii*) c = 2.50 %, U_b = 4.9 m s^{-1}; (*iii*) c = 2.50%, U_b = 5.6 m s^{-1}. This selection can be explained due to the worst predictions obtained with the *standard* Jäsberg parameters for the higher consistency case (i.e. 2.50 %), and due to the fact that the profiles of viscosity, dimensionless velocity and turbulent kinetic energy are very similar for the two lower consistencies studied (i.e. 1.50 and 1.80 %) with the Jäsberg momentum wall function, considering the *standard* adjustable parameters of Jäsberg (2007).

The modification strategy was based on modifying the parameter α assuming that in the *yield* region the velocity gradient should be higher for the larger pulp consistency and flow rates tested and also for the fibers used in the present study. Moreover, the velocity gradient in the *core* region was also altered, an attempt to obtain a lower gradient by increasing the parameter β having pursued. It is expected that if the gradient in the yield region increases then an opposite trend should be observed in the core region. Moreover, if the velocity in the *yield* region increases, the thickness of the *yield* region has to decrease, i.e. y_C^+ has to be reduced. The thickness of the *near wall* region was considered equal to the *standard* value proposed in Jäsberg (2007), y_L^+ = 50. This assumption was made since from the results presented by Jäsberg (2007), it seems that y_L^+ is constant for the different flow rates tested for the flow of *Birch* pulp suspension (c = 2 %), i.e. y_L^+ depends only on the type of pulp fiber. Also, the non-dimensional velocity profiles described for the *Birch* pulp suspension indicated that the *near wall* region is placed closer to the pipe wall than for the *Pine* pulp suspension. It was concluded from preliminary results that to consider y_L^+ = 50 is appropriate to simulate the flow of *Eucalyptus* pulp selected in the present study.

The variation of the pressure drop values for the conditions selected for the adjustable Jäsberg adjustable parameters is presented in Table III.9 – Cases III.JM.FN (JM indicates modified Jäsberg adjustable parameters, F corresponds to the flow case of Table III.5, and N is related to the identification of test cases where 0 corresponds to tests with standard Jäsberg adjustable parameters). Looking at the pressure drop results, significant improvements can be

observed, in all cases, with the modification of the Jäsberg adjustable parameters (compare Cases III.J. with Cases III.JM. – Table III.9). Now, the *drag reduction* effect could be reproduced for the higher consistency case (i.e. 2.50 %) and, the highest improvement in pressure drop calculation was observed for that consistency.

Table III.9 – Pressure drop values – modified momentum wall function (Jäsberg, 2007), modified Jäsberg parameters.

c [%]	U_b [m s^{-1}]	$\dot{m}_b$ [kg s^{-1}]	$\Delta p/L_{water}$ [Pa m^{-1}]	$\Delta p/L_{exp}$ [Pa m^{-1}]	CASE	Parameter $y_L^+ = 50$			$\Delta p/L_{num}$ [Pa m^{-1}]	δ [%]
						α	β	y_C^+		
1.50	6.2	28	3184	1289	III.J.B0	2.4	0	320	2147	67
1.50	6.2	28	3184	1289	III.JM.B1	3.6	0	160	1867	45
1.50	6.2	28	3184	1289	III.JM.B2	3.6	0.5	160	1867	45
1.50	6.2	28	3184	1289	III.JM.B3	4.4	0	100	1731	34
1.50	6.2	28	3184	1289	III.JM.B4	4.4	0.9	100	1731	34
2.50	4.9	22	2046	1579	III.J.E0	2.4	0	320	2299	46
2.50	4.9	22	2046	1579	III.JM.E1	3.6	0	160	1888	20
2.50	4.9	22	2046	1579	III.JM.E2	3.6	0.5	160	1841	17
2.50	4.9	22	2046	1579	III.JM.E3	4.4	0	100	1703	8
2.50	4.9	22	2046	1579	III.JM.E4	4.4	0.9	100	1603	2
2.50	5.6	25	2582	1754	III.J.F0	2.4	0	320	2814	61
2.50	5.6	25	2582	1754	III.JM.F1	3.6	0	160	2234	27
2.50	5.6	25	2582	1754	III.JM.F2	3.6	0.5	160	2234	27
2.50	5.6	25	2582	1754	III.JM.F3	4.4	0	100	2047	17
2.50	5.6	25	2582	1754	III.JM.F4	4.4	0.9	100	1899	8

In what concerns to the new parameters values and the better predictions observed for the higher consistency case (see Table III.9), it can be proposed that when the pulp consistency is higher, the thickness of the *yield* region should be lower and the velocity slope in this region higher. This must also induce a flatter profile in the *core* region. As expected, for the pulp case where the non-Newtonian behaviour of the pulp suspension is more notorious, the logarithmic law-of-the wall should be different from that developed for Newtonian flow cases.

Figure III.13 presents the radial profiles of viscosity for the cases presented in Table III.9. Again, as observed with the *standard* Jäsberg parameters values, also with the new values tested, larger viscosity gradients are observed for the higher consistency cases which reflect the stronger non-Newtonian behaviour of pulp suspension. As expected, for the lower consistency case the viscosity profiles are very similar for the different sets tested. This is representative of flow behaviour more similar to a Newtonian fluid. For the higher consistency (i.e. 2.50 %), significant differences between the different cases observed in Figures III.13b) and III.13c) are related to the dependency of pulp viscosity on shear

rate (see Equation (III.1)).

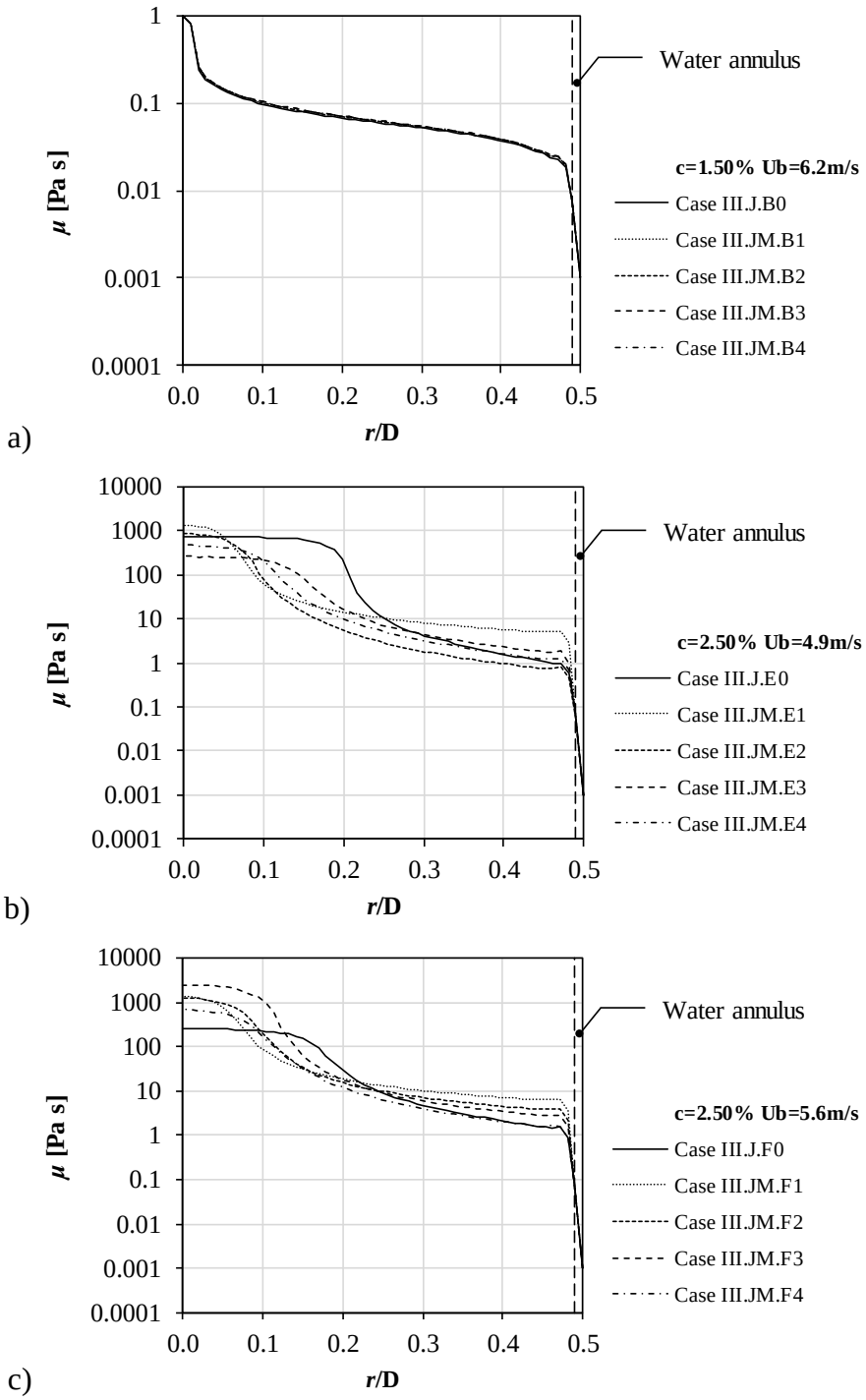

Figure III.13 – Radial viscosity profiles predicted with varying Jäsberg adjustable parameters, for (a) c = 1.50 % U_b = 6.2 m s^{-1}, (b) c = 2.50 % U_b = 4.9 m s^{-1}, and, (c) c = 2.50 % U_b = 5.6 m s^{-1}.

Shear rate is given by (Ansys Inc., 2010):

$$\dot{\gamma} = \sqrt{2\left[\left(\frac{\partial u}{\partial x}\right)^2 + \left(\frac{\partial v}{\partial r}\right)^2 + \left(\frac{v}{r}\right)^2\right] + \left(\frac{\partial v}{\partial x} + \frac{\partial u}{\partial r}\right)^2} \tag{III.63}$$

This pulp (c = 2.50 %) exhibits a strong non-Newtonian behaviour, as expressed by a high value of consistency index, K, and low value for flow index, n, in Equation (III.1). Numerical predictions of smaller values for the derivatives of velocity components are expected with the modifications of the Jäsberg adjustable parameters. In this way, lower values of shear rate and, consequently, higher pulp viscosity is predicted (Figures III.13b) and III.13c)). Regarding the consistency of 1.50 % it is expected that the velocity gradient must be very similar for the different cases considered in Table III.9.

Figure III.14 shows the non-dimensional velocity profiles for the cases presented in Table III.9. As can be observed in Figure III.14a), the y^+ of the first interior domain point is placed always in the *yield* region for the lower consistency (c = 1.50 %), i.e. $y_L^+ < y^+ < y_C^+$ (see values of y_L^+ and y_C^+ in Table III.9, Cases III.J.B0 and III.JM.B1 to III.JM.B4). However, for the highest consistency, when y_C^+ = 100 (see Figures III.14b) and III.14c), Cases III.JM.E3 to III.JM.E4 and III.JM.F3 to III.JM.F4), the first point of the interior domain is placed in the *core* region. In this way, considering a flatter core region, i.e. increase of β leads to significant improvements in the velocity profiles for the higher consistency tests. Also, the pressure drop predicted is closer to the experimental data due to the larger thickness of the plug assumed by a smaller value of y_C^+ (see Table III.9, Cases III.JM.E3, III.JM.E4, III.JM.F3 and III.JM.F4).

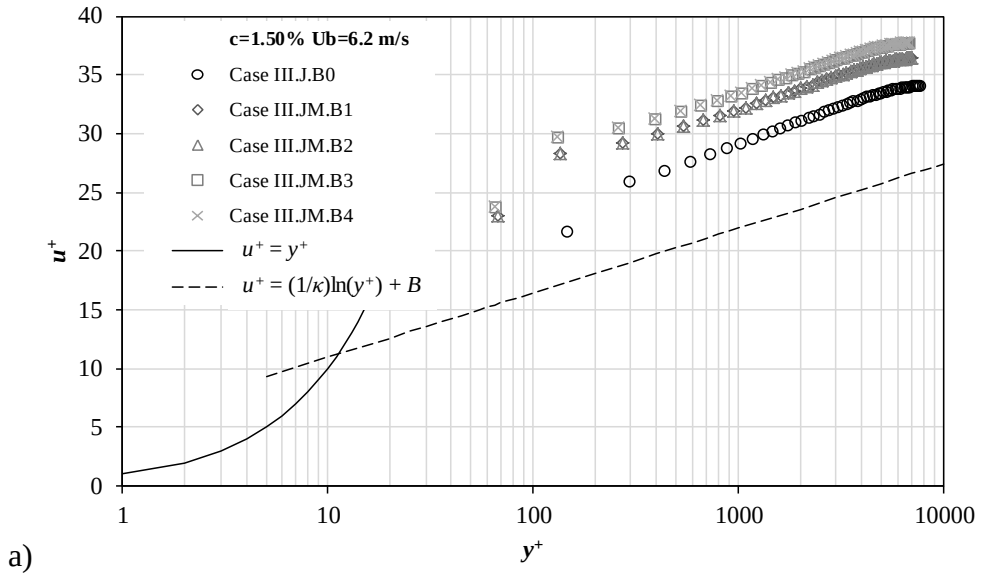

a)

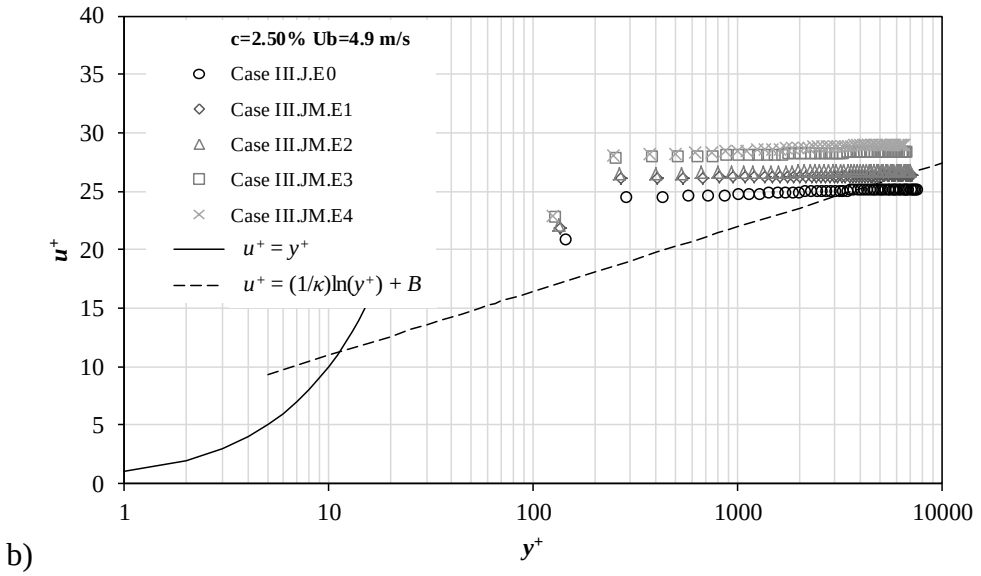

b)

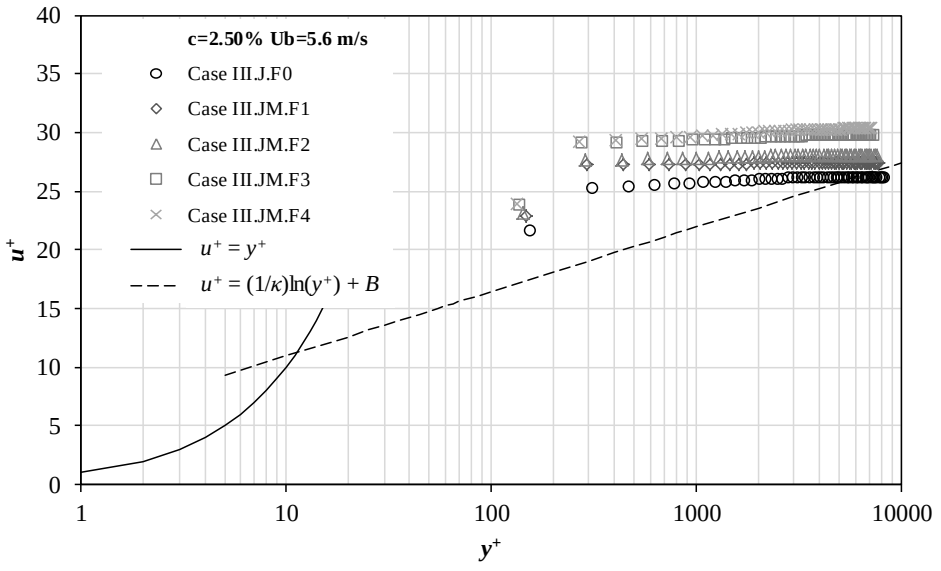

c)

Figure III.14 – Dimensionless velocity profiles with varying Jäsberg adjustable parameters, for (a) c = 1.50 % U_b = 6.2 m s^{-1}, (b) c = 2.50 % U_b = 4.9 m s^{-1}, and, (c) c = 2.50 % U_b = 5.6 m s^{-1}.

Turbulent kinetic energy profiles as a function of normalized distance to the pipe wall are plotted in Figure III.15. As can be seen from these data, the larger values of the *k* profiles are observed for the higher consistency cases (i.e. 2.50%, Figures III.15.b) and III.15.c)). Also, for this consistency, the profiles are more dependent on the values of the adjustable parameters. As expected, better pressure drop predictions are obtained when turbulent quantities are lower, especially at the pipe wall. The higher decrease in the turbulent kinetic energy is observed for the cases where the thickness of *yield* region is lower and slope is higher, and the slope of *core* region is lower. The optimal values of Jäsberg parameters for the higher pulp consistency (i.e. 2.50 %) are: α = 4.4, β = 0, y_L^+ = 50 and y_C^+ = 100. For the lower pulp consistency, the first mesh node is place in the *yield* region in all cases tested and, the optimal value of Jäsberg parameters are: α = 4.4, β = 0, y_L^+ = 50 and y_C^+ = 100. It can be concluded that the Jäsberg parameters α, β, y_L^+ and y_C^+ have a strong impact on the numerical calculations as well as on the location of the first control volume. Thus, they must be tuned as consistency varies, or, at least, for different consistency ranges.

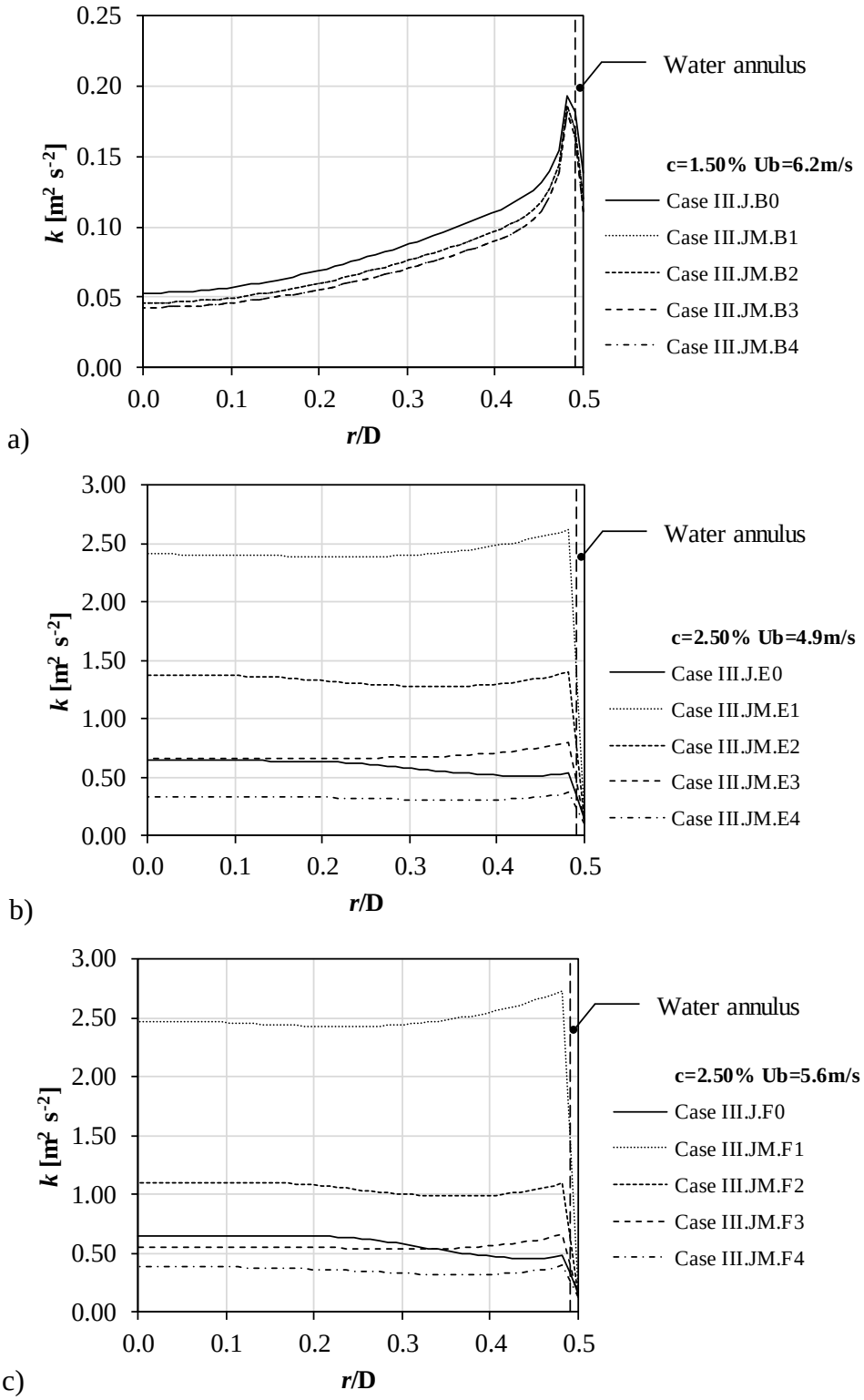

Figure III.15 – Radial profiles of turbulent kinetic energy predicted with varying Jäsberg adjustable parameters, for (a) c = 1.50 % U_b = 6.2 m s^{-1}, (b) c = 2.50 % U_b = 4.9 m s^{-1}, and, (c) c = 2.50 % U_b = 5.6 m s^{-1}.

III.5 – CONCLUSIONS

A 2D axisymmetric CFD model has been proposed to simulate the turbulent flow of refined *Eucalyptus* bleached pulp suspension in a pipe, for predicting the pressure drop. The CFD approach was based on the complete fluid transport equations. The starting point was the Newtonian single-phase fluid model. The model was modified to take into account the presence of fibers in the flow by inclusion of the non-Newtonian properties of pulp suspensions, namely by expressing pulp viscosity as a function of local shear rate. The complete system of transport equations was obtained with two additional transport equations of turbulent quantities, i.e. k and ε. Additionally, the CFD model was modified by considering a new momentum wall function for the logarithmic law-of-wall, according to the observations proposed in Jäsberg (2007). The independency of numerical solution of the mesh density used numerically was performed.

The effect of variation of for the four different Jäsberg parameters was evaluated. It has been found that for the refined *Eucalyptus* bleached pulp flow analysed, those parameters should have different values from those proposed in Jäsberg (2007) to reflect different fibers properties. In all cases tested with the new Jäsberg parameters, a *drag reduction* effect could be reproduced. The Jäsberg parameters need to be tuned considering that for the higher consistency cases the slope in the *yield* region is higher than those considered with the *standard* parameters, and, also the thickness of that region must be reduced. For this situation, the slope in the *core* region must also be reduced, accordingly, since the fibers plug will be more notorious. The pressure drop predicted by the modified model agrees well with the experimental data. In those cases, the existence of *yield* and *core* regions in the dimensionless velocity profiles is more notorious. In fact, besides the correct predictions of pressure drop, the velocity profiles should also agree qualitatively with the model reported in Jäsberg (2007).

Finally, modifying the near wall treatment has shown that an adequate wall function approach plus the inclusion of the non-Newtonian behaviour of the pulp, is able to reproduce the experimental data. The transfer of momentum and turbulent quantities plays an important role near the pipe wall. This indicates that a near-wall model approach with near-wall region resolved to the wall, including the viscous sublayer, is worth testing for the flow of pulp suspensions.

IV – CFD STUDIES WITH LOW-REYNOLDS-NUMBER *k-ε* TURBULENCE MODELS

This study aims to investigate the applicability of CFD models based on the complete set of transport equations, resolved all the way down to the wall, to predict the pulp flow characteristics evaluated in terms of pressure drop values. A new expression for the non-Newtonian behaviour of pulp suspensions was taken into account, i.e. local viscosity was related to local shear rate and pulp consistency, instead of being expressed only as a function of local shear rate, as considered in Chapter III. According to literature cases for systems where a *drag reduction* effect is observed, different low-Reynolds-number (LRN) *k-ε* turbulence models in the CFD model were applied and modified, considering different damping functions used successfully to predict the flow of *drag reducing* fluids.

The CFD simulations as described in the previous chapter were validated with experimental data of pressure drop from literature (Ventura *et al.*, 2008a, 2008b, 2011) and unpublished data from the NODESZELOSS project. Also, those data are mentioned here as experimental data. The model was validated with turbulent flow data of refined *Eucalyptus* bleached pulp and *Pine* unbleached pulp in the same test rig described in Chapter III. The predicted CFD pressure drop values were in good agreement with the experimental ones as well as the dimensionless velocity profiles were in qualitative accordance with those described in the literature (Jäsberg, 2007).

IV.1 – INTRODUCTION

Major improvements of the CFD predictions of turbulent pulp flow were planned be obtained from the proper knowledge of transport quantities in the near wall region and their appropriate implementation into the CFD model. The existing studies devoted to the simulations of the flow indicating a *drag reduction* effect suggest the application of low-Reynolds-number (LRN) *k-ε* turbulence models. From the author's knowledge, the applicability of LRN *k-ε* turbulence models to study the flow of pulp suspensions is not widely described in the literature. In fact, as reported in Chapter II, a scarce number of studies

have been proposed in literature to deal with the flow of pulp suspensions considering a pseudo-homogeneous approach, and, even the multiphase models do not take into account the applicability of LRN *k*-*ε* turbulence models to describe turbulence in the fluid phase.

Again, the commercial CFD solver, ANSYS Fluent 13.0 (Ansys Inc., 2010) was used to perform the numerical simulations. The transport phenomena are described mathematically by the continuity and Navier-Stokes equations. The complete system of mathematical equations is obtained with the two additional differential equations for turbulent kinetic energy, *k*, and its dissipation rate, *ε*. The mathematical model does not take into account the near wall treatment applied in Chapter III (wall function approach) and, instead, new turbulence models that are solved all the way down to the wall were applied. They require mesh nodes near the pipe wall, with a good mesh refinement. The LRN *k*-*ε* turbulence models studied were implemented in the commercial CFD code ANSYS Fluent by User-Defined Functions (UDFs), own developed code, in order to implement the non-Newtonian character of pulp suspension expressed by viscosity as a function of shear rate and consistency, considering a very thin lubrication layer surrounding the core region where the presence of fibers was also investigated. The different LRN *k*-*ε* turbulence models were implemented. Moreover, the CFD code was validated by comparing numerical results of own developed code with the corresponding results obtained with the default models from ANSYS Fluent, to confirm the adequacy of the own developed routines.

In order to present the CFD study conducted in this chapter, first the modelling strategy and the main differential equations governing the pulp flow will be described. Also, the standard damping functions of the LRN *k*-*ε* turbulence models and new expressions for them will be presented. The numerical procedure and strategy applied to implement the different LRN *k*-*ε* turbulence models tested will be also reported. This chapter will be completed with the presentation and discussion of the numerical results obtained.

The study presented in this chapter is based on the published conference papers Cotas *et al.* (2015c, 2015d). It should be pointed out that in Cotas *et al.* (2014, 2015a) a similar study was published considering the pulp non-Newtonian behaviour previously described in Chapter III, Section III.3.1.1. Whereas, the results presented in Cotas *et al.* (2015c, 2015d) consider the new fitting to viscosity data proposed in this chapter.

IV.2 – MODELLING APPROACH AND GOVERNING EQUATIONS

In the present chapter, the flow of pulp suspensions was modelled using a CFD pseudo-homogeneous model incorporated into the ANSYS Fluent software, by modifying the expressions of molecular viscosity and turbulent viscosity. Following the strategy presented in Chapter III, the current model formulation has used as starting point the single-phase fluid model implemented by default into the commercial CFD code. Also, the same flow assumptions made in the previous chapter were considered (incompressible flow, isothermal, steady state and non-Newtonian fluid).

The computational flow domain had the same specifications as described in Chapter III, Section III.2. The pulp flow in 1 meter of pipe with pipe radius of 0.0381 meters, considering a 2D axisymmetric geometry was simulated.

IV.2.1 – GOVERNING PULP FLOW EQUATIONS

The governing pulp flow equations, continuity and Navier-Stokes equations, were presented in Chapter III (Equations (III.2) to (III.4)). A new formulation to model viscosity data of *Eucalyptus* bleached pulp and *Pine* unbleached pulp was derived.

IV.2.1.1 – MODELLING PULPS RHEOLOGY

According to Fock *et al.* (2011), a CFD model to be able to reproduce the flow of pulp suspensions should deal adequately with the wall effect and turbulence in the flow field. Also, the model needs to take into account the decrease of pulp consistency towards the pipe wall. Olson (1996) and Dong *et al.* (2003) studied experimentally and numerically the turbulent flow of fiber suspensions. They found that near the channel wall a decrease of suspension concentration is observed. Thus, aiming to describe the influence of fibers in the lubrication layer (very thin layer near the pipe wall surrounding the flow core region), a new fitting to the rheological data was made since viscosity has to be considered dependent on fiber consistency in the lubrication layer.

The present viscosity model proposal is based on the viscosity data presented in Figure IV.1. These data for both refined *Eucalyptus* bleached and *Pine* unbleached pulp suspensions were obtained with the use of a Searle-type plate rotational rheometer, as presented in Chapter III. In the present study, the viscosity data for refined *Eucalyptus* bleached pulp suspensions used in the fitting (Figure IV.1a)) encompassed consistencies of 1.50, 1.80, 2.50, 2.90, 3.20 and 3.50 % and, for *Pine* unbleached pulp suspensions (Figure IV.1b)), the consistencies were 1.40, 1.90, 2.30, 2.60, 3.10 and 3.40 %.

The description of the non-Newtonian behaviour of the pulp suspensions was proposed to be expressed by relating their viscosity to shear rate and fiber consistency according the following expression:

$$\mu_{app} = K' c^{\alpha} (\dot{\gamma})^{\beta c} \tag{IV.1}$$

with the parameters K', α and β dependent on fiber type as presented in Table IV.1. This expression is identical as that one defined by Equation (III.1), power-law fluid, if it is assumed that the consistency coefficient and the flow behaviour index of Equation (III.1) are expressed as functions of pulp consistency. In this way, the decrease of pulp consistency towards the pipe wall could be taken into account in the CFD model.

Table IV.1 – Parameters K', α and β for Equation (IV.1) and the correlation coefficient, *Eucalyptus* and *Pine* pulp suspensions.

Pulp suspension type	***K'*** **[Pa s$^{1+\beta}$]**	***α***	***β***	**R^2**
Eucalyptus	0.0085	6.97	-0.26	0.98
Pine	0.0754	5.90	-0.28	0.94

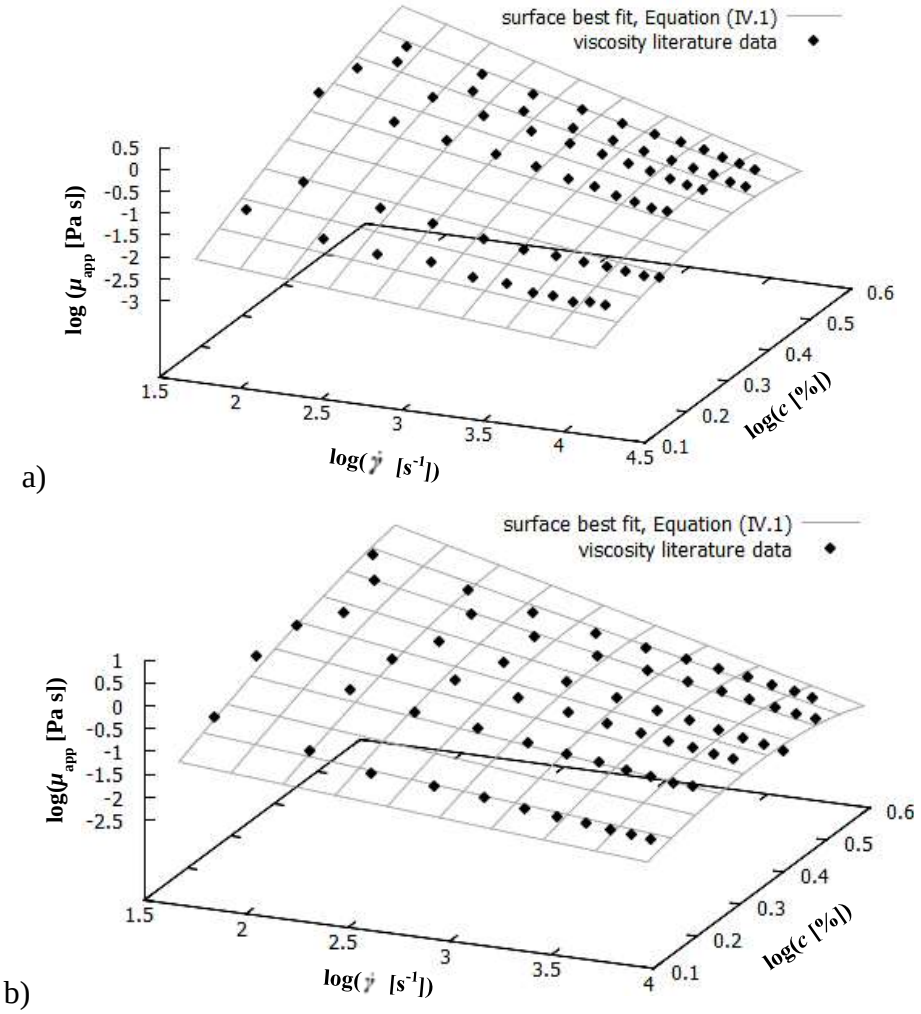

Figure IV.1 – Measured apparent viscosity and surface best fit Equation (IV.1) for (a) *Eucalyptus*, and, (b) *Pine* pulps.

As mentioned before, Olson (1996) reported that the fiber consistency of nylon fibers in the boundary layer diminished in a linear way with the distance to the pipe wall. The results showed that fiber concentration variation is observed in the wall vicinity of the thickness equal to about 1/3 of fiber length, from the mean fiber concentration to the minimum value at the pipe wall. Also, Dong *et al.* (2003) reported a similar profile obtained through numerical simulations. However, their numerical results showed that the fiber consistency increases from the pipe wall up to a distance of about half a fiber length where it reaches its maximum, and, then it decreases up to a distance of about the fiber length from the pipe wall, where the mean pulp consistency is reached.

In order to include in the CFD code the observations of radial variation of concentration as described in Olson (1996) and Dong *et al.* (2003) it was assumed that consistency is expressed as a function of distance to the pipe wall by:

$$c(r) = -\frac{\bar{c}}{L_{\text{fiber}}}\left[r-(R-L_{\text{fiber}})\right]+\bar{c} \quad (r \geq R - L_{\text{fiber}}) \tag{IV.2}$$

with lubrication layer thickness equal to fiber length, in spite of Olson (1996) having considered it equal to 1/3 of fiber for rigid nylon fibers. Since pulp fibers can be interlinked creating groups of fibers which can lead to the presence of larger amount of fibers in the core region than in the case of rigid fibers, and a lubricating layer with wider thickness as it was considered by the author for pulp flow simulations.

Accordingly, two situations were evaluated (see Figure IV.2 and Table IV.2): (*i*) lubrication layer without fibers, pure water annulus, and (*ii*) fibers in the lubrication layer and consistency represented as a linear function of distance to the pipe wall. The situation reported in situation (*i*) is designated as case NF whereas situation (*ii*) is chosen as case F.

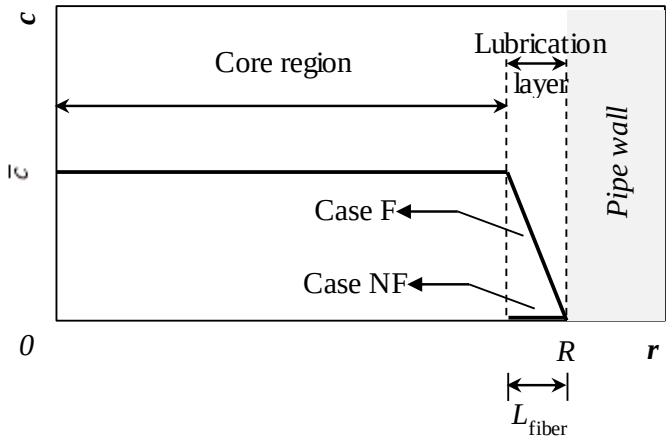

Figure IV.2 – Assumed radial consistency profiles in the near-wall region.

Table IV.2 – Consistency and viscosity expressions according to consistency profiles shown in Figure IV.2.

Consistency case	***Consistency, c(r)***		***Viscosity, μ(r)***	
NF	0	$(R - L_{\text{fiber}} \leq r \leq R)$	μ_{water}	$(R - L_{\text{fiber}} \leq r \leq R)$
	$\bar{c}$	$(r < R - L_{\text{fiber}})$	Equation (IV.1)	$(r < R - L_{\text{fiber}})$
F	Equation (IV.2)	$(R - L_{\text{fiber}} \leq r \leq R)$	Equation (IV.1)	$(r \leq R)$
	$\bar{c}$	$(r < R - L_{\text{fiber}})$		

IV.2.1.2 – FLOW EQUATIONS

In accordance with the modelling approach already presented and discussed in Chapter III, Section III.3.1.2, the pulp suspension flow was modelled considering the conservation of mass and momentum through a certain control volume represented by the ensemble-average form of the continuity and Navier-Stokes equations. These equations (Equations (III.2) to (III.4)) for single fluid motion assuming, as previously, the flow as incompressible, isothermal, steady state steady, the fluid as non-Newtonian and 2D axisymmetric geometry, are expressed as:

Continuity equation

$$\frac{\partial u}{\partial x}+\frac{\partial v}{\partial r}+\frac{v}{r}=0 \tag{III.2}$$

Navier-Stokes equation – x-component

$$\frac{\rho}{r}\left[\frac{\partial}{\partial x}(ruu)+\frac{\partial}{\partial r}(rvu)\right]=-\frac{\partial p}{\partial x}+\frac{1}{r}\left[\frac{\partial}{\partial x}\left(r\mu_{\text{eff}}\,\frac{\partial u}{\partial x}\right)+\frac{\partial}{\partial r}\left(r\mu_{\text{eff}}\,\frac{\partial u}{\partial r}\right)\right] + \frac{\partial}{\partial x}\left(\mu_{\text{eff}}\,\frac{\partial u}{\partial x}\right)+\frac{1}{r}\frac{\partial}{\partial r}\left(r\mu_{\text{eff}}\,\frac{\partial v}{\partial x}\right) \tag{III.3}$$

Navier-Stokes equation – r-component

$$\frac{\rho}{r}\left[\frac{\partial}{\partial x}(ruv)+\frac{\partial}{\partial r}(rvv)\right]=-\frac{\partial p}{\partial r}+\frac{1}{r}\left[\frac{\partial}{\partial x}\left(r\mu_{\text{eff}}\,\frac{\partial v}{\partial x}\right)+\frac{\partial}{\partial r}\left(r\mu_{\text{eff}}\,\frac{\partial v}{\partial r}\right)\right] + \frac{\partial}{\partial x}\left(\mu_{\text{eff}}\,\frac{\partial u}{\partial r}\right)+\frac{1}{r}\frac{\partial}{\partial r}\left(r\mu_{\text{eff}}\,\frac{\partial v}{\partial r}\right) - 2\mu_{\text{eff}}\,\frac{v}{r^2} \tag{III.4}$$

The effective viscosity, μ_{eff}, is defined as previously by:

$$\mu_{\text{eff}}=\mu+\mu_{\text{t}} \tag{III.5}$$

For the present study, the fluid viscosity, μ, is represented by the apparent pulp viscosity as a function of shear rate and pulp consistency, Equation (IV.1). The flow of fluids for which a *drag reduction* effect is present can be reproduced by CFD codes providing that turbulent viscosity, μ_{t}, representing a property of the flow, includes an extra function (damping function

f_μ) when compared to the expression of Equation (III.6) (standard high Reynolds *k*-*ε* turbulence model):

$$\mu_t = \rho C_\mu f_\mu \frac{k^2}{\varepsilon} \tag{IV.3}$$

Also, two additional transport equations for turbulent quantities, i.e. turbulent kinetic energy (*k*) and its dissipation rate (*ε*), must be derived. Section IV.2.2 describes the formulation of these two additional quantities of the default LRN *k*-*ε* turbulence models of ANSYS Fluent.

IV.2.2 – TURBULENCE LOW-REYNOLDS-NUMBER *k*-*ε* MODELS

Turbulence effects were modelled using LRN *k*-*ε* turbulence models available in the commercial CFD software ANSYS Fluent. Six different LRN *k*-*ε* turbulence models are implemented by default in the CFD commercial code: Abid, AB (Abid, 1993); Lam-Bremhorst, LB (Lam and Bremhorst, 1981); Launder-Sharma, LS (Launder and Sharma, 1974); Yang-Shih, YS (Yang and Shih, 1993); Abe-Kondoh-Nagano, AKN (Abe *et al.*, 1994); Chang-Hsieh-Chen, CHC (Chang *et al.*, 1995; Hsieh and Chang, 1996). However, only two of them (AKN and CHC) were selected to be tested in the present numerical study. Preliminary results with the pulp viscosity represented by the power-law model as described in Chapter III have shown that these two models were the most appropriate to fit the experimental results. Additionally, preliminary results with default LRN *k*-*ε* turbulence models from the commercial code considering the non-Newtonian behaviour of pulp have shown that numerical problems arise when the YS turbulence model was applied mainly for highly non-Newtonian pulp suspensions. Moreover, the predictions with the LS model presented the largest deviations from the experimental data including the pressure drop values obtained which were out of the range predicted with the remaining four LRN *k*-*ε* turbulence models.

The different LRN *k*-*ε* turbulence models implemented by default in ANSYS Fluent were developed and tested in their standard versions to simulate the flow of different fluids under different conditions that could be reproduced using the features of these turbulence models. The AB model was developed to investigate the influence of free-stream turbulence on a flat plate in predicting natural transition for zero pressure gradient boundary-layer flows (Abid, 1993). The model was developed to deal with the transition from laminar to turbulent flow. The laminar boundary layer starts to be unstable when a critical value of Reynolds

number is exceeded; that instability begins to be three-dimensional and vortex loops start to appear; at the end, turbulent spots are formed in extremely fluctuating parts on the flow. The LB model was implemented originally by Lam and Bremhorst (1981) to predict fully developed pipe flow in isothermal conditions till the pipe wall, without using wall functions. Launder and Sharma (1974) proposed a LRN *k*-*ε* turbulence model to simulate swirling flows generated by a rotating disc where both heat and species transfers were considered. The model proposed by Yang and Shih (1993) predicted quite well the turbulent channel flow for different flow velocities with and without pressure gradients on the turbulent boundary layers. The AKN model was developed to predict flows with separation and heat transfer such as separating and reattaching flows downstream a backward-facing step. The CHC model was proposed to predict recirculating isothermal flow in sudden-expansion pipe without swirl effect and fully developed pipe flow (Chang *et al.*, 1995). Also, the model was tested to calculate non-isothermal flow in sudden-expansion pipe without swirl effect.

In the situations reported above, the logarithmic law-of-wall is not appropriate to deal with complex flow cases. So, the application of standard high Reynolds *k*-*ε* turbulence model with empirical wall functions fails to describe the different complex flows addressed, leading to the development of new turbulence models that can be integrated all way down to the wall. In these models, the effect of molecular viscosity is taken into account in turbulence (turbulent Reynolds numbers). In the viscous sublayer the gradients of flow properties requires the applicability of LRN *k*-*ε* turbulence models to deal with the problems under study.

The turbulence formulation used in this work uses a Reynolds-averaged Navier-Stokes (RANS) two-equation based model, with two extra transport equations for turbulent quantities *k* and *ε*, given by Equations (III.7) and (IV.4):

Transport equation of turbulent kinetic energy

$$\frac{\rho}{r}\left[\frac{\partial}{\partial x}(ruk)+\frac{\partial}{\partial r}(rvk)\right]=\frac{1}{r}\left\{\frac{\partial}{\partial x}\left[r\left(\mu+\frac{\mu_t}{\sigma_k}\right)\frac{\partial k}{\partial x}\right]+\frac{\partial}{\partial r}\left[r\left(\mu+\frac{\mu_t}{\sigma_k}\right)\frac{\partial k}{\partial r}\right]\right\} + P_k-\rho\varepsilon \tag{III.7}$$

Transport equation for dissipation rate of turbulent kinetic energy

$$\frac{\rho}{r}\left[\frac{\partial}{\partial x}(ru\varepsilon)+\frac{\partial}{\partial r}(rv\varepsilon)\right]=\frac{1}{r}\left\{\frac{\partial}{\partial x}\left[r\left(\mu+\frac{\mu_t}{\sigma_\varepsilon}\right)\frac{\partial \varepsilon}{\partial x}\right]+\frac{\partial}{\partial r}\left[r\left(\mu+\frac{\mu_t}{\sigma_\varepsilon}\right)\frac{\partial \varepsilon}{\partial r}\right]\right\} + \left(C_{\varepsilon 1}f_1P_k-C_{\varepsilon 2}f_2\rho\varepsilon\right)\frac{\varepsilon}{k} \tag{IV.4}$$

with generation of turbulent kinetic energy due to mean velocity gradients calculated from:

$$P_k = \mu_t \left\{ 2\left[\left(\frac{\partial u}{\partial x}\right)^2 + \left(\frac{\partial v}{\partial r}\right)^2 + \left(\frac{v}{r}\right)^2 \right] + \left(\frac{\partial v}{\partial x} + \frac{\partial u}{\partial r}\right)^2 \right\} \quad \text{(III.9)}$$

The LRN *k-ε* turbulence models selected to close the system of transport equations to simulate the experimental flow conditions of pulp suspensions imply that the differential equation of *k* is represented by the same transport equation as presented in the standard high Reynolds *k-ε* turbulence model; however, in LRN *k-ε* turbulence models formulations the turbulent viscosity is expressed with an additional damping function in μ_t. The transport equation for the dissipation rate of *k* in the LRN *k-ε* turbulence models formulation includes the damping functions f_1 and f_2 in which the model incorporates the effect of turbulent Reynolds number on the destruction and production of ε in Equation (IV.4).

The model constants C_μ, $C_{\varepsilon 1}$, $C_{\varepsilon 2}$, σ_k and σ_ε have the values presented in Table IV.3 depending on the LRN *k-ε* turbulence model. The damping functions f_μ, f_1 and f_2 are presented in Table IV.4.

Table IV.3 – Model constants for the different standard LRN *k-ε* turbulence models tested.

Code	C_μ	$C_{\varepsilon 1}$	$C_{\varepsilon 2}$	σ_k	σ_ε
AKN	0.09	1.50	1.90	1.4	1.4
CHC	0.09	1.44	1.92	1.0	1.3

Table IV.4 – Damping functions for the tested standard LRN *k-ε* turbulence models.

Code	f_μ	f_1	f_2
AKN	$\left[1-\exp\left(-\frac{Re_\varepsilon}{14}\right)\right]^2 \times \left\{1+\frac{5}{Re_t^{3/4}}\exp\left[-\left(\frac{Re_t}{200}\right)^2\right]\right\}$	1.0	$\left[1-\exp\left(-\frac{Re_\varepsilon}{3.1}\right)\right]^2 \times \left\{1-0.3\exp\left[-\left(\frac{Re_t}{6.5}\right)^2\right]\right\}$
CHC	$\left[1-\exp(-0.0215Re_k)\right]^2 \times \left[1+\frac{31.66}{Re_t^{5/4}}\right]$	1.0	$\left[1-0.01\exp\left(-Re_t^2\right)\right] \times \left[1-\exp\left(-0.0631Re_k\right)\right]$

$$Re_t = \frac{k^2}{\varepsilon v}\,;\quad Re_k = \frac{yk^{1/2}}{v}\,;\quad Re_\varepsilon = \frac{y\left(\frac{\mu\varepsilon}{\rho}\right)^{1/4}}{v}$$

IV.2.3 – TURBULENCE MODEL MODIFICATIONS

None of the default LRN *k-ε* turbulence models from ANSYS Fluent (AB, LB, LS, YS, AKN and CHC) described in the previous section was originally developed to calculate fully developed turbulent flow of non-Newtonian fluids or even fully turbulent flow in the presence of *drag reduction* effects. However, the applicability of low-Reynolds-number (LRN) *k-ε* turbulence models to study flows where a *drag reduction* effect is present, namely, turbulent flow of polymers and solid particles has been studied in the literature. In order to apply successfully LRN *k-ε* turbulence models to predict the flow of pulp suspensions, it was opted here to implement a modelling strategy similar to those from literature to deal with the flow of polymers or particles, but properly modified to take into account the presence of fibers in the flow which are quite different from spherical particles or polymer molecules.

Due to inherent difficulties in modelling pulp suspensions flow, namely, at the turbulence modelling level, it was investigated in the published literature studies related to numerical simulations of the turbulent flow of polymers and particles. Different strategies were found to reproduce the *drag reduction* effect, namely, the flow of particles is mostly investigated with multiphase models by modifying source terms in transport equations taking into account the difference between the fluid and particles velocity (Hsu *et al.*, 2003; Jha and Bombardelli, 2009; Mandø *et al.*, 2009; Kartushinsky *et al.*, 2010); whereas, for the flow of polymers and non-Newtonian fluids single-phase models are applied with turbulence modelled using LRN *k-ε* turbulence models with adapted damping function f_μ (Malin, 1997a, 1998; Cruz and Pinho, 2003; Cruz *et al.*, 2004; Resende *et al.*, 2006; Dhotre *et al.*, 2007; Mehrabadi and Sadeghy, 2008; Pinho *et al.*, 2008). Also, pulp suspension flow of dilute suspensions has been investigated with multiphase models with adapted source terms to take into account the presence of fibers in the flow, with additional or modified terms related to the probability distribution function of mean fiber orientation (Jian-Zhong *et al.*, 2005; Lin *et al.*, 2006b, 2008, 2013; Lin and Shen, 2010a, 2010b; Shen and Lin, 2010). In this study, it was decided to test three different damping functions applied successfully to simulate the flow of spherical particles (Bartosik, 2010, 2011a; Bartosik, 2011b) and power-law fluids (Malin, 1997b).

IV.2.3.1 – MALIN DAMPING FUNCTION f_μ

Malin (1997b) derived an expression for the damping function f_μ based on the standard LB model with an additional parameter $n^{1/4}$. The Malin damping function f_μ was expressed as follows (Malin, 1997b):

$$f_\mu = \left[1 - \exp\left(-\frac{0.0165 Re_k}{n^{1/4}}\right)\right]^2 \left(1 + \frac{20.5}{Re_t}\right) \tag{IV.5}$$

where n corresponds to the flow behaviour index in the non-Newtonian power-law model. All the numerical tests reported in Malin (1997b) were performed to simulate the flow of non-Newtonian fluids (power-law fluids) in which the stronger non-Newtonian behaviour was controlled by the parameter n. The author has shown that predictions for strongly non-Newtonian fluids were improved by including the additional parameter $n^{1/4}$ in the standard damping function f_μ in the LB model. The model was applied successfully to calculate the flow of pseudoplastics fluids (low values of n) and dilatant fluids (high values of n).

In the present study, the Malin damping function tested includes pulp's rheological information. The flow behaviour index n was obtained by fitting the viscosity data, as described in Chapter III, Section III.3.1.1, with the non-Newtonian power-law model:

$$\mu_{app} = K(\dot{\gamma})^{n-1} \tag{III.1}$$

where the values of flow behaviour index, n, for the *Eucalyptus* pulp are presented in Table III.2 (see Chapter III, Section III.3.1.1). The flow simulations presented in the current chapter involve additionally the flow of *Pine* pulp suspensions. In Chapter III, Section III.3.1.1, it was already described the procedure used to obtain the flow behaviour index for *Eucalyptus* pulp suspensions. For the case of the *Pine* suspensions, the apparent viscosity data Figure IV.3 (pulp consistency, c = 0.80 and 2.30 %), were fitted with the non-Newtonian power-law model, Equation (III.1), allowing to obtain the values of the coefficients K and n (Table IV.5).

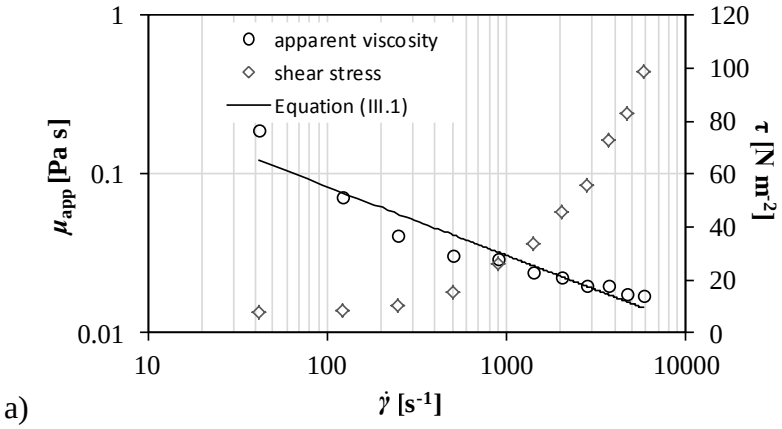

a)

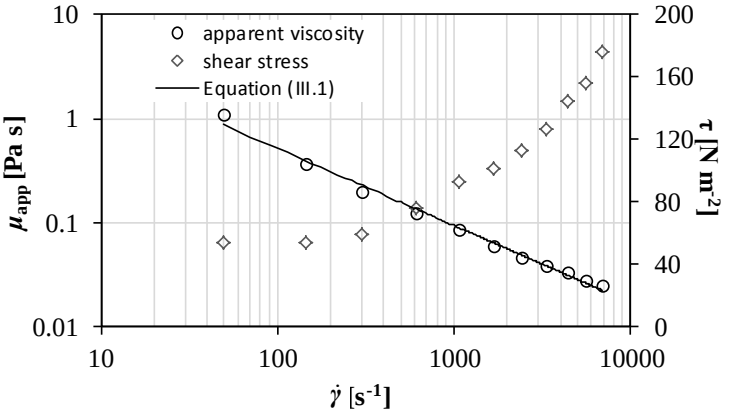

b)

Figure IV.3 – Rheograms and apparent viscosities for *Pine* pulp suspension for consistency, *c*, equal to (a) 0.80 %, and, (b) 2.30 %.

Table IV.5 – Consistency coefficient and flow behaviour index for Equation (III.1) and the correlation coefficient, *Pine* pulp suspension.

c **[%]**	***K*** **[Pa s^n]**	***n***	**R^2**
0.80	0.62	0.57	0.91
2.30	15.85	0.26	0.99

In addition to replacing the damping function on LRN *k*-*ε* turbulence models by the standard Malin damping function, the influence of terms containing turbulence Reynolds number on a modified Malin damping function was studied. New values of the Malin constants C_{M1}, C_{M2} and C_{M3} as shown in Equation (IV.6), were also evaluated:

$$f_\mu = \left[1 - \exp\left(-\frac{C_{M1} Re_k}{n^{C_{M2}}}\right)\right]^2 \left(1 + \frac{C_{M3}}{Re_t}\right) \qquad \text{(IV.6)}$$

Due to inherent differences in the flow of pulp suspensions for different pulp characteristics and flow conditions, the parameters C_{M1}, C_{M2} and C_{M3} will have to be tuned for each case tested, mainly for highly non-Newtonian pulps. This issue will be discussed further later in this chapter.

IV.2.3.2 – BARTOSIK DAMPING FUNCTION f_μ

Another approach applied in this work was to replace the damping function f_μ of the LRN *k-ε* turbulence models by a damping function from the literature used in modelling the flow of spherical particles. Two different damping functions from the same author were tested: (*i*) Bartosik (2010, 2011a), and (*ii*) Bartosik (2011b). Bartosik (2010) studied the fully developed flow of kaolin slurry in a pipe. Bartosik (2011a) investigated the flow of solid particles with median particle diameters 5 and 30 μm. In Bartosik's studies two different rheological models were considered, namely Bingham (Bartosik, 2010, 2011a) and Herschel-Bulkley (Bartosik, 2010) models. The model developed was based on the LS *k-ε* turbulence model, and a new damping function f_μ was proposed. In spite of the mixture being modelled as a multiphase system, the fluid and solid phases were treated as a homogeneous mixture. It was assumed that higher flow velocities lead to greatest homogeneity of the mixture. Bartosik (2011b) studied also the flow of medium solid particles (particles diameter between 0.1 and 0.8 mm) with moderate and high concentrations. In this case, the slurry viscosity was assumed to be equal to the fluid phase (water) that is a Newtonian fluid. In this study, the LS *k-ε* turbulence model was applied to simulate the slurry flow under analysis and a new damping function was proposed and adjusted based on comparison between numerical and experimental data of pressure drop, for different flow conditions.

Bartosik (2010, 2011a) reported a damping function, designated in this work as Bartosik I damping function, expressed by:

$$f_\mu = \exp\left[-\frac{3.4\left(1+\frac{\tau_y}{\tau_w}\right)}{\left(1+\frac{Re_t}{50}\right)^2}\right] \tag{IV.7}$$

where the wall shear stress is obtained from (Ogawa *et al.*, 1990b; Bartosik 2010, 2011a):

$$\tau_{\mathrm{w}} = \frac{\Delta p}{L}\frac{R}{2} \tag{IV.8}$$

the yield stress have been obtained by fitting the rheological data with the Herschel-Bulkley model, $\tau=\tau_y+K\left(\dot{\gamma}\right)^n$, and considering it as a power function of pulp consistency:

$$\tau_y = kc^{\alpha} \tag{IV.9}$$

The parameters *k* and *α* for *Eucalyptus* and *Pine* pulp suspensions are presented in Table IV.6.

Table IV.6 – Parameters values for Equation (IV.9) and the correlation coefficient.

Pulp suspension	***k*** **[N m^{-2}]**	***α***	**R^2**
Eucalyptus	1.59	2.32	0.97
Pine	7.94	2.08	0.98

Bartosik (2011b) proposed a new damping function for slurry flow, named in this work as Bartosik II damping function, given by:

$$f_{\mu} = \exp\left\{-\frac{3.4\left[1+\mathrm{A_S^3}d^2\left(8-88\mathrm{A_S}d\right)c_v^{0.5}\right]}{\left(1+\frac{Re_{\mathrm{t}}}{50}\right)^2}\right\} \tag{IV.10}$$

where $\mathrm{A_S}$ is an empirical constant, *d* represents the particles diameter and c_v is the volumetric concentration of solids. This damping function was tested for the pulp cases assuming that the value of $\mathrm{A_S}$ was the same as used by Bartosik (2011b) (=100), c_v was equal to pulp fiber consistency, and *d* was equal to the fiber diameter.

The standard Bartosik II damping function was tested taking into account that the parameters related to the slurry properties in Bartosik (2011b) were represented for pulp cases by pulp consistency and fiber diameter, and that the empirical constant $\mathrm{A_S}$ had the same value as for the slurry flow cases. However, when dealing with fiber suspensions the influence of the parameter $\mathrm{A_S}$ has to be evaluated, as well as the influence of considering fiber length instead of the fiber diameter to characterise the fibers should be investigated. This study was

made assuming that Bartosik II damping function is represented by a modified version, designated as Bartosik II damping function modified, expressed by Equation (IV.11):

$$f_\mu = \exp\left\{-\frac{3.4\left[1+C_{B1}^3 C_{B2}^2\left(8-88C_{B1}C_{B2}\right)c_v^{0.5}\right]}{\left(1+\frac{Re_t}{50}\right)^2}\right\} \tag{IV.11}$$

where the Bartosik II parameters C_{B1} and C_{B2} have to be tuned for the different pulp cases, taking into account that C_{B2} should be related to a fiber characteristics.

The main contribution of this work to modelling and simulation of turbulent flow of pulp suspensions in pipes was the proposal of a new damping function based on the Bartosik I damping function, properly modified and validated, to calculate the turbulent flow of refined *Eucalyptus* bleached and *Pine* unbleached pulp suspensions for different flow conditions. This new damping function includes a fiber characteristics represented by fiber aspect-ratio (*r*), i.e. ratio between fiber length and fiber diameter, and it was expressed by Equation (IV.12). A similar modification was tested on the Bartosik II damping function – Equation (IV.13).

New Bartosik I damping function

$$f_\mu = \exp\left[-\frac{3.4\left(1+\frac{\tau_y}{\tau_w}\right)+r^{1/4}\left(1+\frac{Re_t}{50}\right)^2}{\left(1+\frac{Re_t}{50}\right)^2}\right] \tag{IV.12}$$

New Bartosik II damping function

$$f_\mu = \exp\left\{-\frac{3.4\left[1+A_S^3 d^2\left(8-88A_S d\right)c_v^{0.5}\right]+r^{1/4}\left(1+\frac{Re_t}{50}\right)^2}{\left(1+\frac{Re_t}{50}\right)^2}\right\} \tag{IV.13}$$

where the definition of the turbulent Reynolds number, Re_t, was given in Table IV.4.

At the end, it is proposed in this work to apply the new damping function represented by Equation (IV.12) for pulp cases, rather than Equation (IV.13). The model tested by Bartosik (2010, 2011a) was developed considering the non-Newtonian behaviour of the particulate

system. The Herschel-Bulkley and Bingham rheological models were applied to predict the slurry viscosity. Also, the standard turbulence damping function of the LS k-ε turbulence model was modified to take into account the presence of fine spherical particles in the flow (Bartosik 2010, 2011a). In this way, turbulence modelling with the new damping function, based on the Bartosik I damping function presents physical meaning, by taking into account the yield stress corresponding to the stress that, when surpassed, leads to the flow of pulp. Moreover, Bartosik (2011b) studied the applicability of the Bartosik II damping function and corresponding CFD model to simulate the turbulent flow for which the viscosity representing the slurry was considered constant.

The inclusion of a new variable related to fiber aspect-ratio represented by $r^{1/4}$ is in line with research findings for the flow of non-spherical particles, even if only a scarce number of studies have reported the influence of particles with different aspect-ratios on the flow properties. In agreement with different literature studies about the flow of non-spherical particles, the particle aspect-ratio is an important parameter to predict the orientation distribution of non-spherical particles, which in turn is important for example in multiphase models, namely in Eulerian-Eulerian approaches. According to Zhang *et al.* (2001), ellipsoidal particles with higher aspect-ratio tend to influence the near wall turbulent eddies and to interfere with them. The authors have shown that the particle aspect-ratio is an important particle characteristic in the transport of this type of particles when the flow is turbulent. Additionally, how a particle rotates is influenced by the local flow field. Rosén *et al.*, (2015a, 2015b) have simulated the flow of a single spheroidal particle. They concluded that the particles aspect-ratio is a parameter that determines rotational orientation distributions and can be related to different rheological characteristics. Mortensen *et al.* (2008) simulated the turbulent flow of non-spherical particles and they concluded that the slip velocity has a tendency to increase with particle aspect-ratio for the flow of ellipsoidal particles. Lundell (2015) concluded that the orientation distribution of fibers in turbulent flow is different depending on the fibers aspect-ratio. Fibers with higher aspect-ratio align with the flow, and in contrast fibers with lower aspect-ratio tend to align in the spanwise direction (Kvick, 2014; Lundell, 2015).

IV.2.4 – NUMERICAL SIMULATION

The present mathematical model used to describe the pulp flow cases to be simulated is composed of Equations (III.2) to (III.4), (III.7) and (IV.4). In order to describe the effects of fibers in the flow and their influence on turbulence modelling, different LRN *k*-*ε* turbulence models were tested. The same methodology as previously presented in Chapter III was applied in this chapter.

The complete system of differential equations representing the conservation of mass, momentum in *x* and *r* directions, turbulent kinetic energy and its dissipation rate can be expressed by the same general differential equation as presented in Chapter III:

$$\frac{\rho}{r}\left[\frac{\partial}{\partial x}(ru\phi)+\frac{\partial}{\partial r}(rv\phi)\right]=\frac{1}{r}\left[\frac{\partial}{\partial x}\left(r\Gamma_\phi\frac{\partial\phi}{\partial x}\right)+\frac{\partial}{\partial r}\left(r\Gamma_\phi\frac{\partial\phi}{\partial r}\right)\right]+S_\phi \qquad \text{(III.10)}$$

The dependent variable ϕ, the diffusion coefficient Γ_ϕ and the source-term S_ϕ are presented in Table IV.7. It should be noted that these quantities are expressed in the same way as in the previous chapter; however, turbulent viscosity in LRN *k*-*ε* turbulence models is expressed assuming that it is affected by a damping function in μ_t. Also, two additional damping functions f_1 and f_2 are considered in the LRN *k*-*ε* turbulence models.

Table IV.7 – Model parameters ϕ, Γ_ϕ and S_ϕ – LRN *k*-*ε* turbulence models.

Equation	***Transported property***	ϕ	Γ_ϕ	S_ϕ
Continuity (Equation III.2)	Mass	1	0	0
Navier-Stokes – *x*-component (Equation III.3)	Momentum in *x*-direction	u	μ_{eff}	$-\frac{\partial p}{\partial x}+\frac{\partial}{\partial x}\left(\mu_{\text{eff}}\frac{\partial u}{\partial x}\right)+\frac{1}{r}\frac{\partial}{\partial r}\left(r\mu_{\text{eff}}\frac{\partial v}{\partial x}\right)$
Navier-Stokes – *r*-component (Equation III.4)	Momentum in *r*-direction	v	μ_{eff}	$-\frac{\partial p}{\partial r}+\frac{\partial}{\partial x}\left(\mu_{\text{eff}}\frac{\partial u}{\partial r}\right)+\frac{1}{r}\frac{\partial}{\partial r}\left(r\mu_{\text{eff}}\frac{\partial v}{\partial r}\right)$ $-2\mu_{\text{eff}}\frac{v}{r^2}$
Turbulent kinetic energy (t.k.e.) (Equation III.7)	Turbulent kinetic energy	k	$\mu+\frac{\mu_t}{\sigma_k}$	P_k - $\rho\varepsilon$
Dissipation rate of turbulent kinetic energy (t.d.r.) (Equation IV.4)	Dissipation rate of k	ε	$\mu+\frac{\mu_t}{\sigma_\varepsilon}$	$\left(C_{\varepsilon1}f_1P_k-C_{\varepsilon2}f_2\rho\varepsilon\right)\frac{\varepsilon}{k}$

To summarize, the constants C_μ, $C_{\varepsilon 1}$, $C_{\varepsilon 2}$, σ_k and σ_ε are presented in Table IV.8 for the different formulations of LRN *k*-ε turbulence models. The damping functions f_μ, f_1 and f_2 are defined in Table IV.9.

Table IV.8 – Model constants C_μ, $C_{\varepsilon 1}$, $C_{\varepsilon 2}$, σ_k and σ_ε.

Model	C_μ	$C_{\varepsilon 1}$	$C_{\varepsilon 2}$	σ_k	σ_ε
AKN Malin (AM)	0.09	1.50	1.90	1.4	1.4
AKN Bartosik I (ABI)	0.09	1.50	1.90	1.4	1.4
AKN Bartosik II (ABII)	0.09	1.50	1.90	1.4	1.4
CHC Malin (CM)	0.09	1.44	1.92	1.0	1.3
CHC Bartosik I (CBI)	0.09	1.44	1.92	1.0	1.3
new CHC Bartosik I (CBI.1)	0.09	1.44	1.92	1.0	1.3
CHC Bartosik II (CBII)	0.09	1.44	1.92	1.0	1.3
new CHC Bartosik II (CBII.1)	0.09	1.44	1.92	1.0	1.3

Table IV.9 – Different damping functions tested.

Model	f_μ
AKN Malin (AM) CHC Malin (CM)	$f_\mu = \left[1-\exp\left(-\frac{0.0165Re_k}{n^{1/4}}\right)\right]^2\left(1+\frac{20.5}{Re_t}\right)$
AKN Bartosik I (ABI) CHC Bartosik I (CBI)	$f_\mu = \exp\left[-3.4\left(1+\frac{\tau_y}{\tau_w}\right)\Big/\left(1+\frac{Re_t}{50}\right)^2\right]$
new CHC Bartosik I (CBI.1)	$f_\mu = \exp\left\{-\left[3.4\left(1+\frac{\tau_y}{\tau_w}\right)+r^{1/4}\left(1+\frac{Re_t}{50}\right)^2\right]\Big/\left(1+\frac{Re_t}{50}\right)^2\right\}$
AKN Bartosik II (ABII) CHC Bartosik II (CBII)	$f_\mu = \exp\left\{-3.4\left[1+A_S^3 d^2\left(8-88A_S d\right)c_v^{0.5}\right]\Big/\left(1+\frac{Re_t}{50}\right)^2\right\}$
new CHC Bartosik II (CBII.1)	$f_\mu = \exp\left\{-\left[3.4\left[1+A_S^3 d^2\left(8-88A_S d\right)c_v^{0.5}\right]+r^{1/4}\left(1+\frac{Re_t}{50}\right)^2\right]\Big/\left(1+\frac{Re_t}{50}\right)^2\right\}$
AKN Malin, AKN Bartosik I, AKN Bartosik II: $f_2 = \left[1-\exp\left(-\frac{Re_\varepsilon}{3.1}\right)\right]^2 \times\left\{1-0.3\exp\left[-\left(\frac{Re_t}{6.5}\right)^2\right]\right\}$ CHC Malin, CHC Bartosik I, *new* CHC Bartosik I, CHC Bartosik II, *new* CHC Bartosik II: $f_2 = \left[1-0.01\exp\left(-Re_t^2\right)\right]\times\left[1-\exp\left(-0.0631Re_k\right)\right]$	

$Re_t = \frac{k^2}{\varepsilon\nu}$; $Re_k = \frac{y k^{1/2}}{\nu}$; $Re_\varepsilon = \frac{y\left(\frac{\mu\varepsilon}{\rho}\right)^{1/4}}{\nu}$; f_1=1.0

IV.2.4.1 – NUMERICAL METHODOLOGY

The numerical methodology applied is based on the control-volume-based technique previously described in Chapter III, Section III.3.3.1. It includes the integration, discretization and linearization of the transport equations in a numerical domain divided into control volumes. Afterwards, the system composed of linear equations is solved with an appropriate algorithm. The complete system of differential equation represented in the general form Equation (III.10) is integrated for each control volume resulting in the complete set of algebraic equations expressed by Equation (III.13) for each dependent variable:

$$a_{\mathrm{P}}\phi_{\mathrm{P}} = \sum_{\mathrm{nb}} a_{\mathrm{nb}}\phi_{\mathrm{nb}} + b \tag{III.13}$$

An upwind scheme, first-order upwind scheme, is applied assuming that the face value is the same as the quantity in the cell upstream centre. This is extremely important for velocity components since their values are stored in cell centres although they are calculated at cell interfaces. The pressure-velocity SIMPLE (Semi-Implicit Method for Pressure-Linked Equations) coupling algorithm is used to link the continuity equation and Navier-Stokes equations. This process is briefly discussed here, considering only the discretized momentum equation in the *x*-direction:

$$a_{\mathrm{P}}u_{\mathrm{P}} = \sum_{\mathrm{nb}} a_{\mathrm{nb}}u_{\mathrm{nb}} + b + A_{\mathrm{w}}\left(p_{\mathrm{W}} - p_{\mathrm{P}}\right) \tag{III.16}$$

where the pressure field is needed to be known. That pressure field is obtained with the SIMPLE coupling algorithm in which an initial field for pressure, *p**, should be given to start the numerical calculations. This initial pressure field leads to a velocity field expressed as:

$$a_{\mathrm{P}}u^{*}_{\mathrm{P}} = \sum_{\mathrm{nb}} a_{\mathrm{nb}}u^{*}_{\mathrm{nb}} + b + A_{\mathrm{w}}\left(p^{*}_{\mathrm{W}} - p^{*}_{\mathrm{P}}\right) \tag{III.18}$$

However, this initial pressure field guess can lead to a velocity field where continuity condition is not satisfied. To guarantee that continuity condition is satisfied ($\sum_{\mathrm{f}}^{\mathrm{nf}} J_{\mathrm{f}} A_{\mathrm{f}} = 0$) it is introduced a correction for pressure and in this way a correction in the velocity field:

$$p = p^{*} + p' \tag{III.21}$$

$$u = u^* + u' \tag{III.22}$$

Subtracting Equation (III.18) from Equation (III.16) and taking into account the definition for u' in Equation (III.22) it can be obtained a correction for the velocity component in x-direction:

$$a_P u'_P = \sum_{nb} a_{nb} u'_{nb} + A_w \left(p'_W - p'_P \right) \tag{III.24}$$

assuming that the term $\sum_{nb} a_{nb} u'_{nb}$ is considered of flow relative importance

$$a_P u'_P = A_w \left(p'_W - p'_P \right) \tag{III.26}$$

$$u'_P = d_w \left(p'_W - p'_P \right) \tag{III.27}$$

in this way the complexity in Equation (III.24) resulting from the fact that it requires the information from the neighbour cells on the numerical domain, is avoided.

The final equation for velocity correction is given by:

$$u_P = u_P^* + d_w \left(p'_W - p'_P \right) \tag{III.30}$$

The discretized equation for pressure correction can be expressed by:

$$a_P p'_P = \sum_{nb} a_{nb} p'_{nb} + b \tag{III.32}$$

considering that the final equation for velocity correction is included in the discrete continuity equation through mass flux of the control volume in the x-direction (ρu) or in the r-direction (ρv).

The complete system of linear equations to be solved (Equations (III.13) and (III.32)) is solved with a point implicit linear equation solver through the Gauss-Seidel technique in algebraic multigrid (AMG) scheme. To avoid convergence problems resulting from high or low amplitude in the solution of the dependent variables between the actual and previous iteration step, it is used a sub-relaxation strategy as described in Chapter III, Section III.3.3.1. The initial field for variables, required in the commercial software ANSYS Fluent, to initialize the numerical calculation was considered equal to zero, except k and ε which were

initialized with 1 m^2 s^{-2} and 1 m^2 s^{-3}, respectively. The solution was considered converged when the scaled residuals (Equations (III.37) and (III.38)) were less than 1×10^{-5}.

Boundary conditions

The different LRN *k-ε* turbulence models considered in the present study are represented by a complete system of differential equations corresponding to the complete transport equation expressed in its general form by Equation (III.10), with the supplementary information of Tables IV.7 to IV.9. As indicated in Chapter III, Section III.3.3.2, there is not a single solution for this complete system of differential equations. In order to obtain the most accurate solution for the different pulp flow conditions tested in this work, it is necessary to specify the proper boundary conditions for each dependent variable. These boundary conditions are required at the (*1*) inlet and (*2*) outlet of the flow domain, (*3*) pipe axis, and (*4*) pipe wall (see Figure III.6 and Table IV.10). Also, as mentioned in in Chapter III, Section III.3.3.2, inlet and outlet of flow domain are linked as periodic boundary condition. At the pipe axis it is considered pipe symmetry axis, and a wall boundary condition at the pipe wall.

Table IV.10 – Boundary conditions.

Boundary	***Boundary condition type***
(1) inlet	Periodic boundary
(2) outlet	
(3) pipe axis	Symmetry axis
(4) pipe wall	Wall boundary

(1) (2) Inlet and outlet of the flow domain: It was verified in Chapter III that to consider inlet and outlet boundaries linked as periodic boundaries is suitable for the pulp flow characteristics subject of study in the present work. This type of boundary condition in ANSYS Fluent allows to specify the mass flow rate for an unknown pressure gradient which is calculated in an iterative process, or it can be specified the pressure gradient. For the problem under study it was specified the mass flow rate for each pulp and flow conditions tested. The output data was the pressure drop, main control variable to validate the numerical results, by comparing it with the experimental data. The calculation procedure implemented internally in the commercial CFD software was reported in Chapter III, Section III.3.3.2.

(3) Pipe axis: This boundary condition was specified at the centreline of the 2D axisymmetric geometry. It is internally implemented in ANSYS Fluent where no additional specifications are required.

(4) Pipe wall: This type of boundary condition was selected to include the effect of the presence of a solid wall in the flow field. It is in the near wall region that the larger gradients are present, as can be seen in the results presented in Chapter III, Section III.4. This observation together with the fact that the problem under study involves simulating the flow of complex fluids with highly non-Newtonian behaviour, lead to apply a modelling strategy in which the differential equations are resolved all the way down to the wall (LRN *k*-*ε* turbulence models) with the proper mesh constructed till very near the wall (y^+ first mesh node ≈ 1). In this way, and contrarily to that reported in Chapter III, Section III.3.3.2, the complete system of differential transport equations is solved numerically also in the viscous sublayer besides being solved in the fully turbulent wall layer, without applying standard wall functions to link momentum quantities at the solid boundary with the fluid flow domain. At the pipe wall, the no-slip velocity condition was selected for the velocity boundary condition:

$$u_{\text{wall}} = v_{\text{wall}} = 0 \tag{III.42}$$

The wall boundary conditions for the turbulent quantities, turbulent kinetic energy and its dissipation rate, for the different LRN *k*-*ε* turbulence models tested are presented in Table IV.11.

Table IV.11 – Wall boundary conditions for k and ε – LRN k-ε turbulence models.

Model	k_w **– B.C.**	ε_w **– B.C.**
AKN	0	$2\nu\left(\frac{\partial\sqrt{k}}{\partial y}\right)^2$
AKN Malin (AM)	0	$2\nu\left(\frac{\partial\sqrt{k}}{\partial y}\right)^2$
AKN Bartosik I (ABI)	0	$2\nu\left(\frac{\partial\sqrt{k}}{\partial y}\right)^2$
AKN Bartosik II (ABII)	0	$2\nu\left(\frac{\partial\sqrt{k}}{\partial y}\right)^2$
CHC	0	$\nu\frac{\partial^2 k}{\partial y^2}$
CHC Malin (CM)	0	$\nu\frac{\partial^2 k}{\partial y^2}$
CHC Bartosik I (CBI)	0	$\nu\frac{\partial^2 k}{\partial y^2}$
new CHC Bartosik I (CBI.1)	0	$\nu\frac{\partial^2 k}{\partial y^2}$
CHC Bartosik II (CBII)	0	$\nu\frac{\partial^2 k}{\partial y^2}$
new CHC Bartosik II (CBII.1)	0	$\nu\frac{\partial^2 k}{\partial y^2}$

There are two main modifications proposed in this chapter: (*i*) to consider the non-Newtonian molecular viscosity expressed as a function of shear rate and pulp consistency and, (*ii*) to apply different LRN k-ε turbulence models, standard and modified versions. These modifications were included in ANSYS Fluent solver through User-Defined Functions (UDFs) which are source code files written in C programming language. These source files can be interpreted or compiled in ANSYS Fluent. After the compiling process, it is possible to turn on the respective function name in the dialog box of the commercial CFD solver.

Implementation of LRN k-ε turbulence models – UDFs

The different own-developed LRN k-ε turbulence models (standard and modified versions) were implemented into the commercial CFD solver, ANSYS Fluent 13.0, using UDFs source code. In ANSYS Fluent, the different standard LRN k-ε turbulence models cited in the beginning of Section IV.2.2 can be selected by default, for numerical simulations. However, modifying them is a hard task, with the commercial CFD solver being quite closed

in terms of applying an UDF code only to perform modifications to the damping function f_μ. In this way it was decided to turn off the equations for turbulence, and to develop own UDF source codes to be loaded into ANSYS Fluent with all the specifications needed to supply the turbulent equations that had been turned off. In Appendix A, the UDF coded to incorporate the turbulent kinetic energy and its dissipation rate equations for the AKN turbulence model is presented, as an example, since it was one of the models chosen to be modified with new damping functions. The AKN turbulence model was also used to validate the developed UDF, by comparing numerical results obtained with the default ANSYS Fluent model with those obtained with the own-developed AKN model.

In the CFD solver, the standard *k*-*ε* turbulence model with enhanced wall treatment was chosen, in which the differential transport equations are solved all the way down to the wall. The built-in turbulence equations for *k* and *ε* were turned off as mentioned before. Two scalar quantities were added to represent turbulent variables which are solved with the momentum equations. For each scalar equation representing turbulent quantities, the source terms are supplied as User Defined Scalar (UDS) Source. The diffusion coefficients for turbulent scalar variables are added as User Defined Scalar Diffusivity in material properties. The turbulent viscosity defined by default in the CFD solver for momentum equations was modified (Equation (IV.3)) by including the new formulation for turbulent viscosity in the model dialog box (Appendix A).

IV.2.5 – MESH OPTIMIZATION

The accuracy of simulations is highly influenced by the mesh used to discretize the numerical domain into control volumes. When using LRN *k*-*ε* turbulence models it is required that the mesh quality is high near the pipe wall, allowing the numerical solution of the transport equations in the viscous sublayer. This means that mesh must be appropriate to ensure sufficient resolution of the system of equations in this region. Usually, the first near wall mesh node should be placed at $y^+ \approx 1.0$ (Ansys Inc., 2010).

In the present study it was chosen to discretize the numerical domain with a structured non-uniform mesh, more refined in the near wall region (cells thickness is smaller) – Figure IV.4. The meshing commercial program GAMBIT 2.4.6 (Fluent Inc., 2007) was used to make all meshes tested. The type of mesh chosen is appropriate for the simple geometry considered and since larger variations of flow properties are expected to be encountered in the near wall

region. Also, special attention was given to spatial distribution and to the number of mesh nodes in the *r* direction, i.e. it was avoided to have a mesh too refined in the near wall region losing accuracy in the core region where strong non-Newtonian behaviour is present.

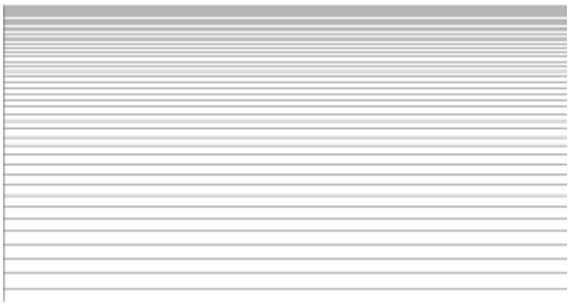

Figure IV.4 – Sample views of the mesh in the near wall region, at the inlet to the domain.

As mentioned before, the construction of the mesh used in all simulations with parameters specifications required by GAMBIT 2.4.6, was made assuming that the first mesh node should be placed at a distance to the pipe wall for which $y^+ \approx 1.0$. As presented in the previous chapter, y^+ can be calculated from:

$$y^+ = \frac{\rho u_\tau y}{\mu_w} \tag{III.45}$$

and,

$$u_\tau = \sqrt{\frac{\tau_w}{\rho}} \tag{III.47}$$

assuming, here, Newtonian viscosity, water viscosity μ_w (T = 293 K), and the wall shear stress, τ_w, calculated from the experimental pressure drop – Equation (IV.8). Different calculations with the previous equation were made for the different experimental conditions to be simulated, in order to obtain a single y_p value to be used in all the calculations. The lower y_p value obtained from all the tests was accepted as the reference cell thickness to place the first interior node.

One of the parameters required in the meshing commercial program is the interval length ratio, *R*, corresponding to the ratio of two successive interval lengths (Fluent Inc., 2007):

$$R = \frac{l_{i+1}}{l_i} \tag{IV.14}$$

where l_i and l_{i+1} stand for length of intervals i and i+1, respectively. Assuming, that the mesh to be created must be fine enough near the pipe wall, but at the same time it should be not so refined but not too coarse in the central part of the radial pipe geometry, as mentioned before, interval length ratios of 1.05, 1.10 and 1.15 were considered. For these R values, different total number of intervals (54, 68, 72, 118, 126 and 140) was tested to obtain the length of the first interval to compare with that obtained from Equation (III.45). When the value of the length of the first interval, l_1, matches with y_P it was assumed that the total number of nodes to be specified in GAMBIT 2.4.6 was obtained. Additionally, the optimal total number of nodes in x direction was also investigated. After obtaining the optimized parameters of the mesh in radial direction, different total number of nodes in x direction (10, 15, 20, 25, 30, 35 and 40) were considered. The appropriate mesh was determined by comparing different simulation results with different interval length ratio and different total number of nodes. The optimized mesh parameters used in all simulations are summarized in Table IV.12.

Table IV.12 – Mesh parameters used in the simulations.

Parameter	**Value**
Mesh (1 m of pipe)	20 (axial) × 118 (radial) nodes
Total number of quadrilateral cells	2223
Total number of nodes	2360
Total number of interfaces	4465
Interval length ratio, R	1.05

It should be noted that the position of the first node of the mesh in the domain was confirmed in the post-processing for all simulations performed and it has been found that effectively it was placed at $y^+ \approx 1.0$.

IV.3 – RESULTS AND DISCUSSION

The model was validated with flow experiments of both refined *Eucalyptus* bleached (hard fibers) and *Pine* unbleached pulp (soft fibers) suspensions. The fibers characteristic properties are presented in Table IV.13. The *Eucalyptus* fibers have the same characteristic properties as the fibers studied in Chapter III. Again, pulp flow simulations were validated with experimental data from Ventura *et al.* (2008a, 2008b, 2011), where the main control variable is the pressure drop. Also, a qualitative analysis was made comparing the expected shape of dimensionless velocity profiles with those reported in Jäsberg (2007). In addition, the profiles of turbulent quantities and viscosity are also presented.

Table IV.13 – *Eucalyptus* and *Pine* fibers characteristic properties (Ventura *et al.*, 2007, 2008b).

	Eucalyptus	***Pine***
Average fiber length, L_{fiber} [mm]	0.706	2.564
Average fiber diameter, d_{fiber} [mm]	0.016	0.016
Fiber aspect-ratio, r	44	160
Freeness, ºSR	33	-

Therefore, the experimental data to be replicated in this part of the work correspond to the data presented in Tables IV.14 and IV.15. In spite of experimental information being accessible for different pulp flow regimes, the mean flow velocity was chosen in such a way that the flow regime corresponded as close as possible to fully developed turbulent flow, since the flow of pulp suspensions with a *drag reduction* effect presents industrial importance.

The CFD conditions for all simulation tests performed are presented in Table IV.16. The standard LRN *k-ε* turbulence models implemented with UDFs were validated by comparing the main results with those obtained with the default models from ANSYS Fluent. This is discussed in the next section.

Table IV.14 – Experimental data – *Eucalyptus* pulp (Ventura *et al.*, 2008b, 2011).

Flow case	***c*** **[%]**	***N crowding factor***	U_b **[m s^{-1}]**	$\dot{m}_b$ **[kg s^{-1}]**	$\Delta p/L_{water}$ **[Pa m^{-1}]**	$\Delta p/L_{pulp}$ **[Pa m^{-1}]**
G	0.91	1181	4.2	19	1522	861
H	0.91	1181	4.5	21	1744	1019
I	0.91	1181	5.0	23	2141	1260
J	0.91	1181	5.5	25	2524	1537
K	0.91	1181	5.9	27	2850	1754
L	0.91	1181	6.1	28	3056	1896
A	1.50	1947	4.5	20	1744	829
M	1.50	1947	5.1	23	2183	972
N	1.50	1947	5.5	25	2524	1014
O	1.50	1947	6.1	28	3056	1269
B	1.50	1947	6.2	28	3184	1289
P	2.20	2856	4.4	20	1683	976
Q	2.20	2856	5.1	23	2162	1128
R	2.20	2856	5.5	25	2524	1235
S	2.20	2856	6.0	27	2936	1356
T	2.20	2856	6.2	28	3184	1385
E	2.50	3245	4.9	22	2046	1579
U	2.50	3245	5.3	24	2391	1702
F	2.50	3245	5.6	25	2582	1754
V	2.50	3245	5.9	27	2850	1839
W	2.50	3245	6.0	27	2936	1878

Table IV.15 – Experimental data – *Pine* pulp (Ventura *et al.*, 2008b, 2011).

Flow case	***c*** **[%]**	***N crowding factor***	U_b **[m s^{-1}]**	$\dot{m}_b$ **[kg s^{-1}]**	$\Delta p/L_{water}$ **[Pa m^{-1}]**	$\Delta p/L_{pulp}$ **[Pa m^{-1}]**
a	0.80	13696	4.1	19	1466	661
b	0.80	13696	4.4	20	1683	715
c	0.80	13696	4.8	22	2001	818
d	0.80	13696	5.4	24	2414	996
e	0.80	13696	5.9	27	2850	1247
f	1.50	25680	4.2	19	1522	981
g	1.50	25680	4.6	21	1825	778
h	1.50	25680	5.1	23	2183	885
i	1.50	25680	5.5	25	2524	984
j	1.50	25680	5.8	26	2755	1079
k	1.50	25680	6.2	28	3184	1169
l	2.30	39376	4.3	19	1575	1080
m	2.30	39376	4.6	21	1825	1164
n	2.30	39376	5.1	23	2183	1330
o	2.30	39376	5.6	25	2582	1451
p	2.30	39376	6.2	28	3184	1648

Table IV.16 – Numerical parameters.

Parameter	Value
Iterations – Periodic boundary	2
Relaxation factor – Periodic boundary	0.5
Turbulence model	Standard low-Reynolds-number *k-ε* models: AKN and CHC Standard low-Reynolds-number *k-ε* models (User-Defined Functions): AKN and CHC Modified low-Reynolds-number *k-ε* models (User-Defined Functions): AKN and CHC
Under-relaxation parameters	0.3 (pressure), 0.7 (momentum), 0.8 (t.k.e. or corresponding User defined scalar), 0.8 (t.d.r. or corresponding User defined scalar)
Pulp viscosity and pulp consistency	Table (IV.2)
Pulp density	Water density (293K)

It should be highlighted that the modifications proposed in this chapter were not always applied to simulate all the *Eucalyptus* and *Pine* flow cases presented in Tables IV.14 and IV.15. Nevertheless, each step applied during the modification process from the initial Newtonian homogeneous single-phase fluid model until the final model, was validated for the flow of *Eucalyptus* pulp suspensions at least to two distinct pulp consistencies and two velocities for each consistency (c = 1.50 % (medium consistency) U_b = 4.5 and 6.2 m s^{-1}, and 2.50 % (high consistency) U_b = 4.9 and 5.6 m s^{-1}). Also, for the flow of *Pine* pulp suspensions, two distinct pulp consistencies and two velocities for each consistency were considered (c = 0.80 % (medium consistency) U_b = 4.1 and 5.9 m s^{-1}, and 2.30 % (high consistency) U_b = 4.3 and 6.2 m s^{-1}). However, the most relevant model modifications will be presented for all pulp flow conditions mentioned above (see Tables IV.14 and IV.15). The cases tested are described with the code of the general form IV.C.MD.FN, where IV denotes tested model in Chapter IV, C stands for consistency profile considered in the lubrication layer (NF represents the pure water annulus and F corresponds to the existence of fibers in lubrication layer), M corresponds to the standard LRN *k-ε* turbulence models and D is the damping function tested (see code MD presented in Tables IV.8 and IV.9, MD represented by A means standard AKN model and C represents standard CHC model), F represents the flow case (see Tables IV.14 and IV.15), and N is related to the identification of test cases where new constant values in the damping function were tried (0 stands for the standard LRN *k-ε* turbulence models tested).

IV.3.1 – STANDARD LOW-REYNOLDS-NUMBER *k-ε* MODELS

In this section the numerical results used to validate the implementation of LRN *k-ε* turbulence models using own-developed models applying User-Defined Functions, will be presented. Additionally, simulation results are discussed in order to evaluate the applicability of standard low-Reynolds-number *k-ε* turbulence models to reproduce the *drag reduction* effect observed in the flow of pulp suspensions.

IV.3.1.1 – VALIDATION OF THE LRN *k-ε* TURBULENCE MODELS IMPLEMENTED WITH UDFs

In this section the pressure drop values predicted with the default LRN *k-ε* turbulence models (AKN and CHC) from ANSYS Fluent as well as with the LRN *k-ε* turbulence models own-developed, implemented through UDFs, are presented.

Two mean flow velocities for two different consistencies were chosen to validate the own-developed UDFs. The UDFs models were validated by comparing the numerical results with those obtained with the LRN *k-ε* turbulence models implemented in ANSYS Fluent. It was chosen to present the results for the two most concentrated *Eucalyptus* pulp suspensions tested. A pure water annulus was assumed to surround the core region. It was taken into account the non-Newtonian behaviour of the pulp suspension described by Equation (IV.1). In Table IV.17, the pressure drop values obtained with built-in and UDF models are presented. As can be seen, the pressure drop values obtained with the LRN *k-ε* turbulence models implemented with UDFs agree well with the results from the built-in models.

Table IV.17 – Numerical pressure drop values, built-in and UDFs models – *Eucalyptus* pulp.

Flow case	***c*** **[%]**	U_b **[m s^{-1}]**	$\Delta p/L_{water}$ **[Pa m^{-1}]**	$\Delta p/L_{exp}$ **[Pa m^{-1}]**	**AKN model**		**CHC model**	
					$\Delta p/L_{built\text{-}in}$ **[Pa m^{-1}]**	$\Delta p/L_{UDF}$ **[Pa m^{-1}]**	$\Delta p/L_{built\text{-}in}$ **[Pa m^{-1}]**	$\Delta p/L_{UDF}$ **[Pa m^{-1}]**
P	2.20	4.4	1683	976	1161	1200	1184	1178
T	2.20	6.2	3184	1385	1565	1489	1592	1590
E	2.50	4.9	2046	1579	1917	1861	1845	1843
F	2.50	5.6	2582	1754	2102	2046	2029	2022

Next, comparison of the radial profiles is made for the dependent variables, namely, profiles of turbulent quantities. These profiles are presented in Figures IV.5 and IV.6 for the

two different LRN *k*-*ε* turbulence models evaluated. The profiles predicted with the built-in models from ANSYS Fluent and those predicted using UDFs agree well, only minor differences being observable.

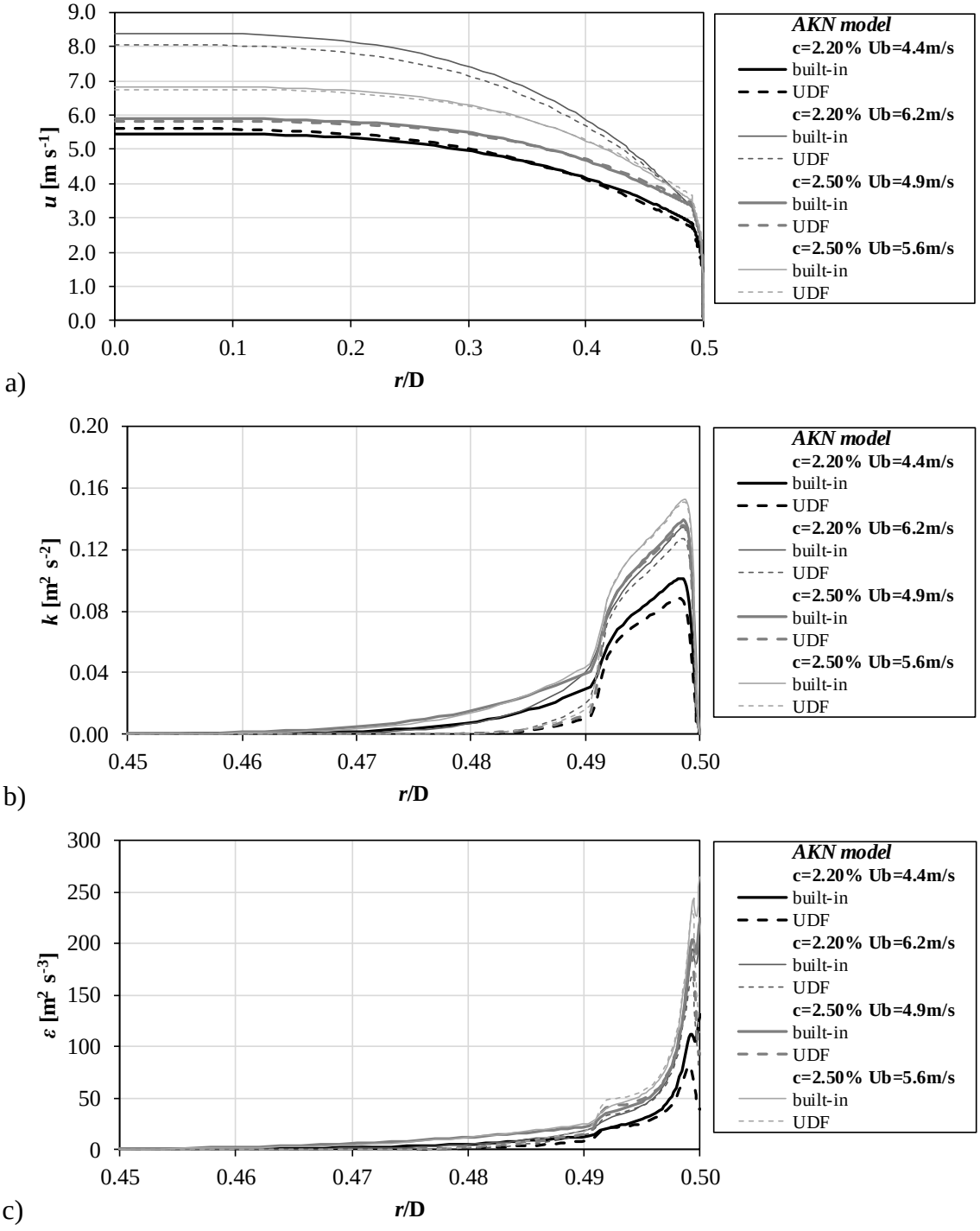

Figure IV.5 – Comparison of AKN built-in and UDF models, radial profiles of (a) velocity, (b) turbulent kinetic energy, and, (c) its dissipation rate.

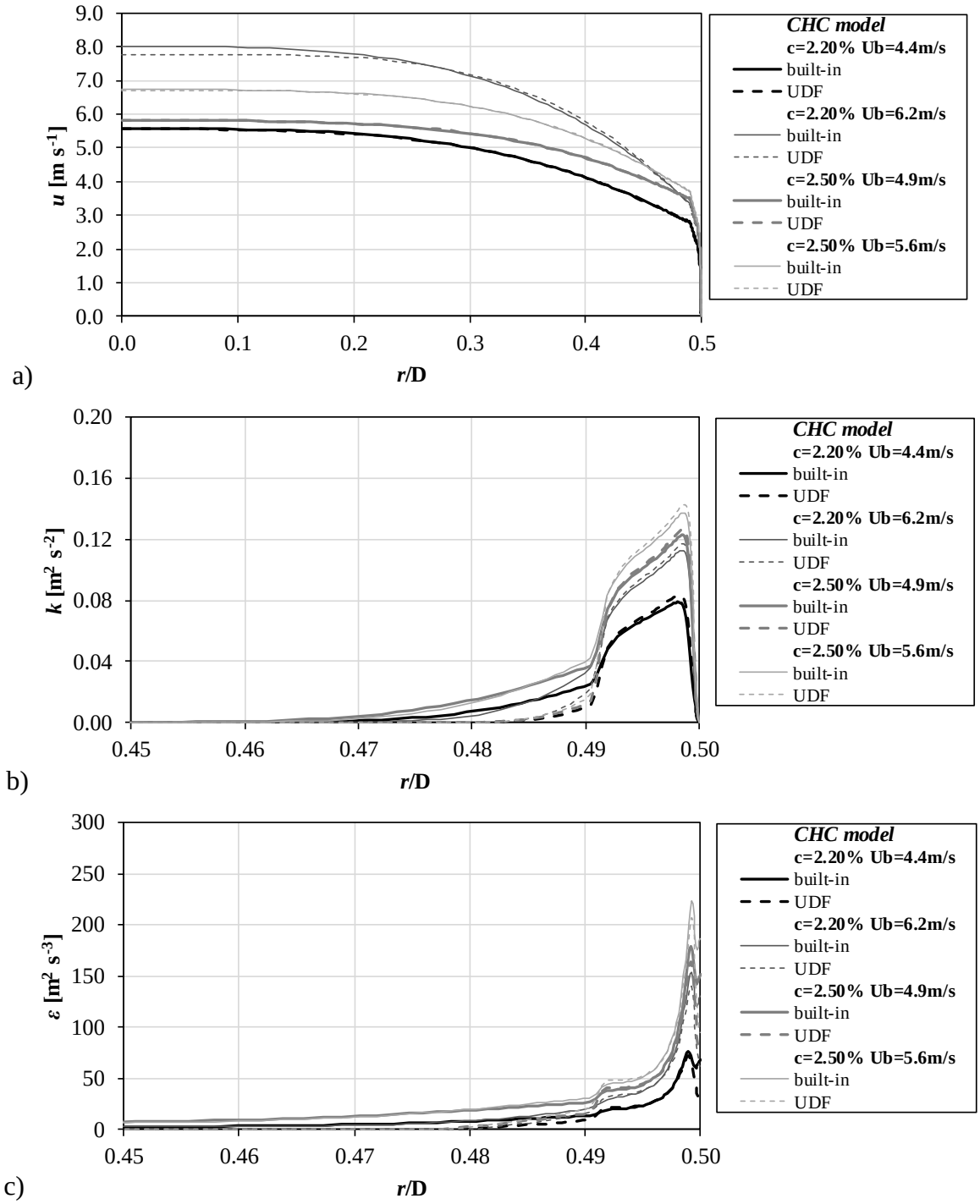

Figure IV.6 – Comparison of CHC built-in and UDF models, radial profiles of (a) velocity, (b) turbulent kinetic energy, and, (c) its dissipation rate.

Mathur and He (2013) have discussed the implementation of the LS *k*-*ε* turbulence model in ANSYS Fluent. They compared the results obtained from UDFs with results from the built-in model and, additionally, with results from other CFD codes. Also, some discrepancies are noticed between the built-in model and the model implemented with UDF. The authors have attributed that to a possible different formulations used. This supports that the developed UDF and procedure followed is able to reproduce the LRN *k*-*ε* turbulence

models, namely the AKN and CHC low-Reynolds-number *k-ε* turbulence models. After this test, the formulation of LRN *k-ε* turbulence models (standard and modified versions) was implemented in this way in the commercial CFD code.

IV.3.1.2 – SIMULATION WITH STANDARD AKN/ CHC MODELS

In order to evaluate the modifications to be implemented during the different stages of the model development to simulate pulp suspensions flow, the standard AKN and CHC models assuming only the non-Newtonian behaviour of pulps were investigated. The following control cases were used to validate the modifications implemented (*Eucalyptus* pulp Table IV.14): (*1*) A – c = 1.50 %, U_b = 4.5 m s^{-1}; (*2*) B – c = 1.50 %, U_b = 6.2 m s^{-1}; (*3*) E – c = 2.50 %, U_b = 4.9 m s^{-1}; and, (*4*) F – c = 2.50 %, U_b = 5.6 m s^{-1}.

Pressure drop values are presented in Table IV.18 for both the AKN and CHC UDFs models. Also, the relative error:

$$\delta = \frac{\left| \Delta p/L_{\text{exp}} - \Delta p/L_{\text{num}} \right|}{\Delta p/L_{\text{exp}}} \times 100\% \qquad \text{(IV.15)}$$

is presented in Table IV.18. In spite of simulation results for c = 2.50 % (pure water annulus) having been presented previously in Section IV.3.1.1, it was decided to show them again here for the reader's convenience. In spite of the *drag reduction* being reproduced in most of the cases tested, the pressure drop values calculated still do not fit adequately the experimental values, especially for the lower consistency (i.e. 1.50 %).

Table IV.18 – Numerical pressure drop values, AKN and CHC UDFs models – *Eucalyptus* pulp.

c [%]	U_b [m s^{-1}]	$\Delta p/L_{water}$ [Pa m^{-1}]	$\Delta p/L_{exp}$ [Pa m^{-1}]	AKN model			CHC model		
				Case	$\Delta p/L_{num}$ [Pa m^{-1}]	δ [%]	*Case*	$\Delta p/L_{num}$ [Pa m^{-1}]	δ [%]
1.50	4.5	1744	829	IV.NF.A.A0	1560	88	IV.NF.C.A0	1763	116
1.50	6.2	3184	1289	IV.NF.A.B0	3094	140	IV.NF.C.B0	3164	146
1.50	4.5	1744	829	IV.F.A.A0	1963	137	IV.F.C.A0	1660	100
1.50	6.2	3184	1289	IV.F.A.B0	3389	163	IV.F.C.B0	3212	149
2.50	4.9	2046	1579	IV.NF.A.E0	1861	18	IV.NF.C.E0	1843	17
2.50	5.6	2582	1754	IV.NF.A.F0	2046	17	IV.NF.C.F0	2022	16
2.50	4.9	2046	1579	IV.F.A.E0	1727	9	IV.F.C.E0	1823	15
2.50	5.6	2582	1754	IV.F.A.F0	1915	9	IV.F.C.F0	1999	14

Viscosity, velocity and profiles of turbulent quantities will be presented next for the tests performed, to enable comparison with the further modifications which will be

implemented in the coming sections. Viscosity profiles are presented in Figure IV.7. Dynamic viscosity increases from the pipe wall up to the pipe centre where lower shear rates are present. This shape reflects also the higher consistency values in the core region. Flow resistance will then be greater in the central region. The orders of magnitude of viscosity values for the two consistencies tested are in accordance with the tendency observed for lower shear rate values in the rheograms (see Figures III.3 and IV.1), even if there is a lack of rheological information for very low shear rate range due to limitations of data acquisition from the rheometer.

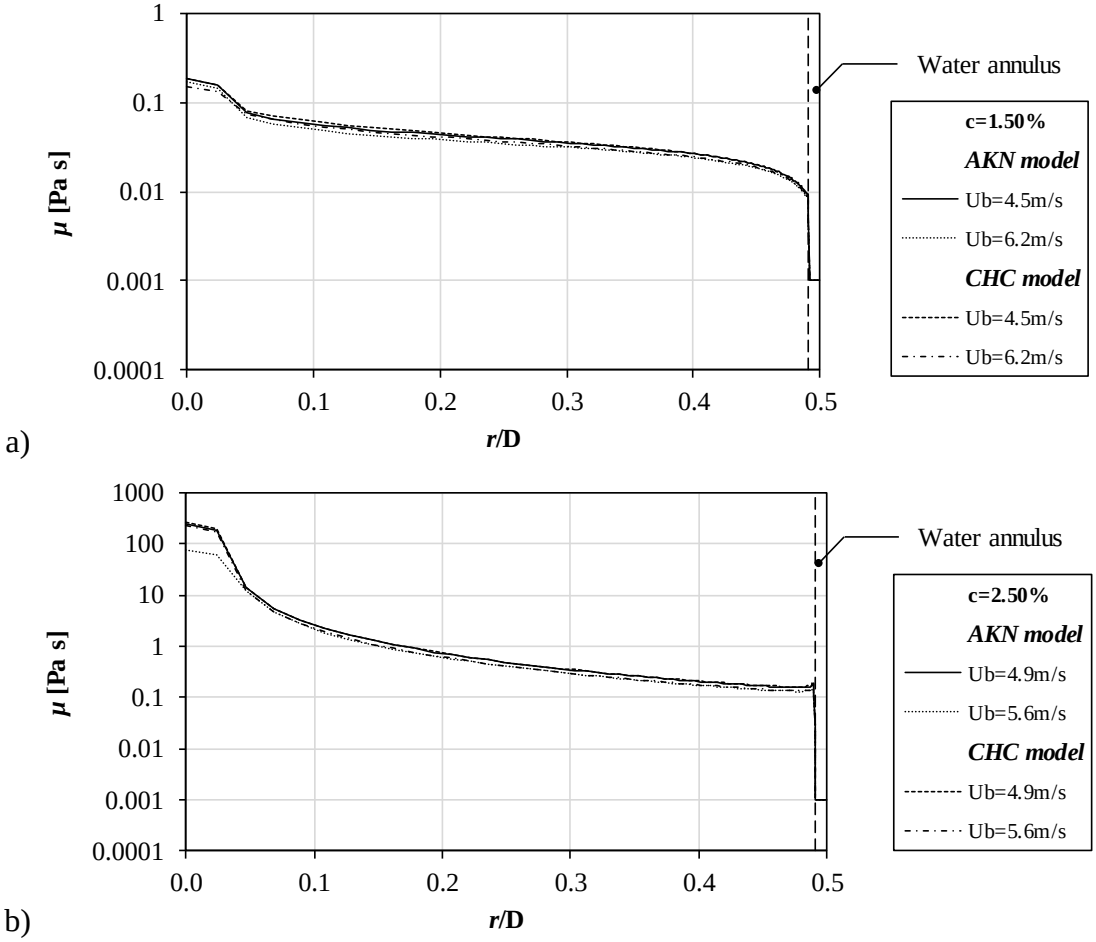

Figure IV.7 – Radial profiles of viscosity, AKN and CHC models (a) lubrication layer without fibers, *c*=1.50 %, (b) lubrication layer without fibers, *c* = 2.50 %, (c) lubrication layer with fibers, *c* = 1.50 %, and, (d) lubrication layer with fibers, *c* = 2.50 %.

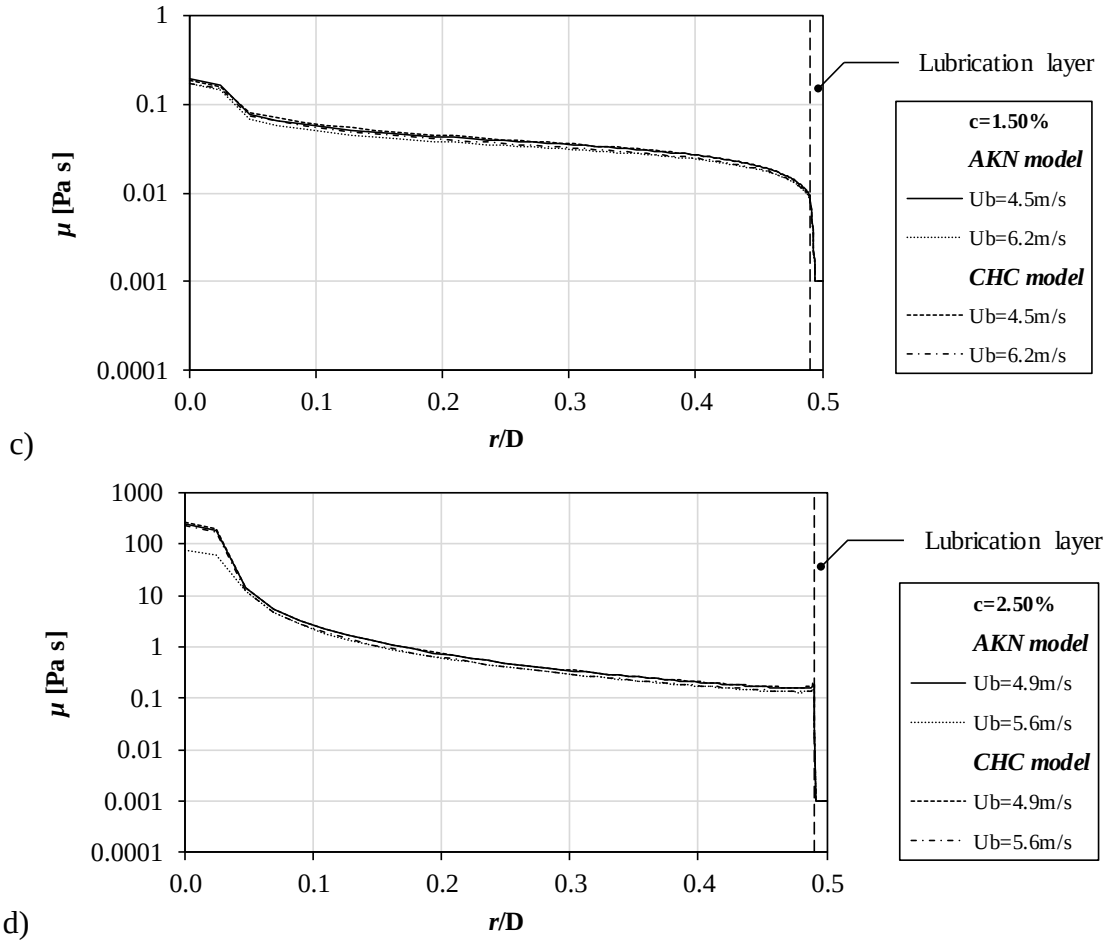

Figure IV.7 – Radial profiles of viscosity, AKN and CHC models (a) lubrication layer without fibers, *c*=1.50 %, (b) lubrication layer without fibers, *c* = 2.50 %, (c) lubrication layer with fibers, *c* = 1.50 %, and, (d) lubrication layer with fibers, *c* = 2.50 % (continued).

In Figures IV.8 and IV.9 the velocity and dimensionless velocity profiles are presented. One may easily notice a sudden transition between the core region and the lubrication layer which is more obvious for the simulation test of higher pulp consistency (i.e. *c* = 2.50 %, Figures IV.8b), IV.8d), IV.9b) and IV.9d)). This is more remarkable in the dimensionless velocity profiles, where the profiles clearly do not coincide with the Newtonian logarithmic law, having a tendency to follow an S-shaped profile similar to those reported in Jäsberg (2007), mainly for the higher consistency tests. The better fit of numerical pressure drop values with the experimental ones obtained for the higher consistency case (see pressure drop values in Table IV.18, Cases IV.NF.A.E0, IV.NF.A.F0, IV.F.A.E0 and IV.F.A.F0/ IV.NF.C.E0, IV.NF.C.F0, IV.F.C.E0 and IV.F.C.F0) is in line with the fact that the dimensionless velocity profile does qualitatively agree with the peculiar envelope curve described by Jäsberg (2007) for the flow of *Birch* pulp (*c* = 2 %) (see Figures IV.9b) and IV.9d)).

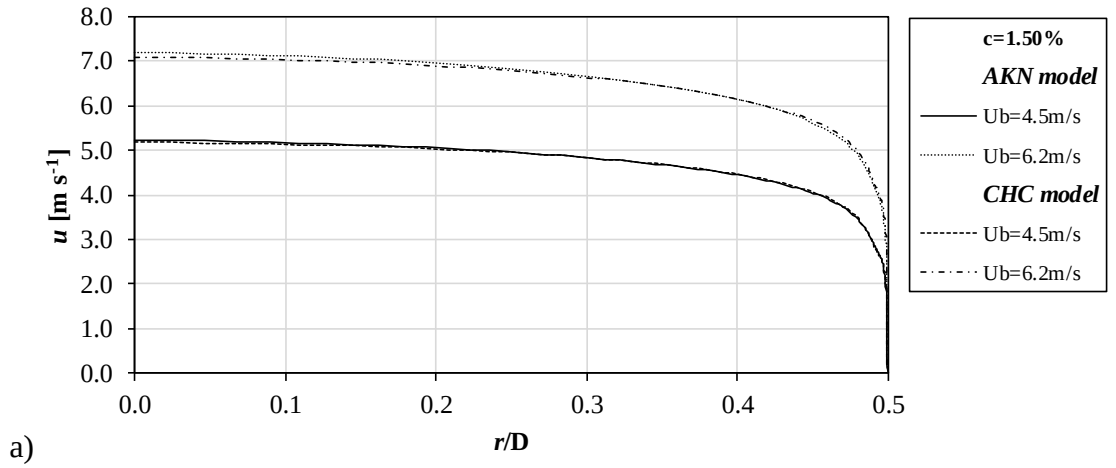

a)

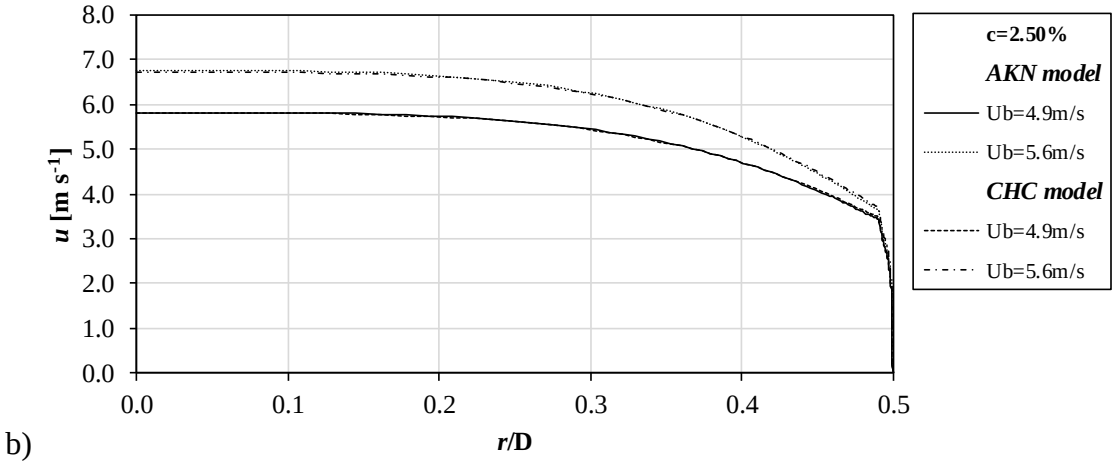

b)

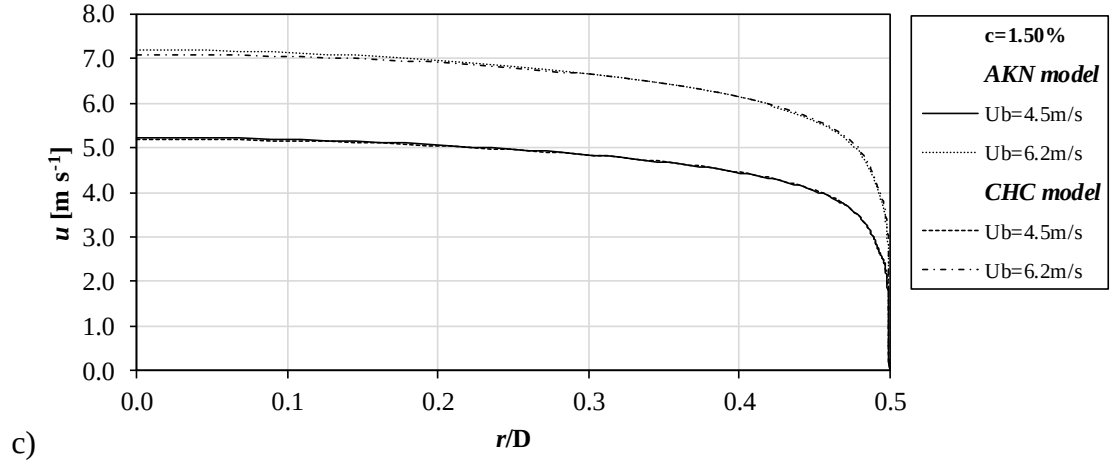

c)

Figure IV.8 – Radial profiles of velocity, AKN and CHC models (a) lubrication layer without fibers, c = 1.50 %, (b) lubrication layer without fibers, c = 2.50 %, (c) lubrication layer with fibers, c = 1.50 %, and, (d) lubrication layer with fibers, c = 2.50 %.

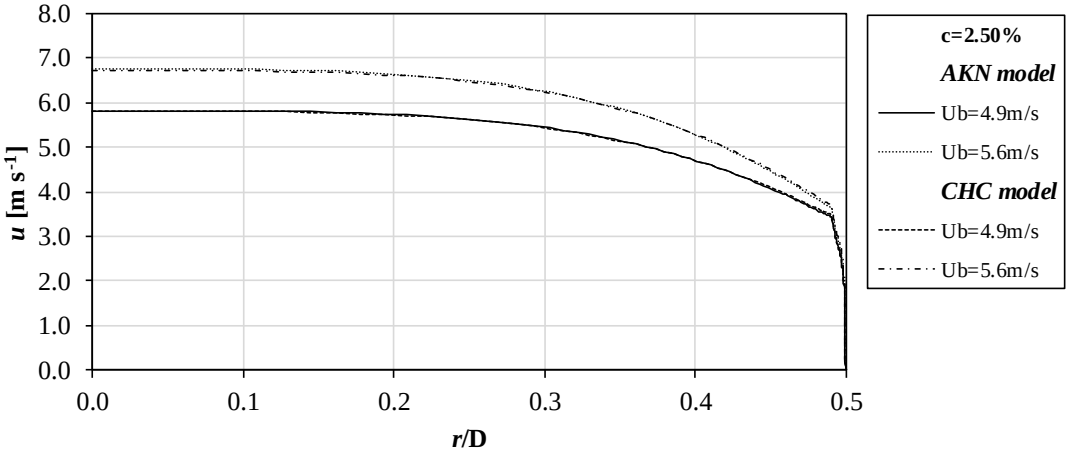

d)

Figure IV.8 – Radial profiles of velocity, AKN and CHC models (a) lubrication layer without fibers, c = 1.50 %, (b) lubrication layer without fibers, c = 2.50 %, (c) lubrication layer with fibers, c = 1.50 %, and, (d) lubrication layer with fibers, c = 2.50 % (continued).

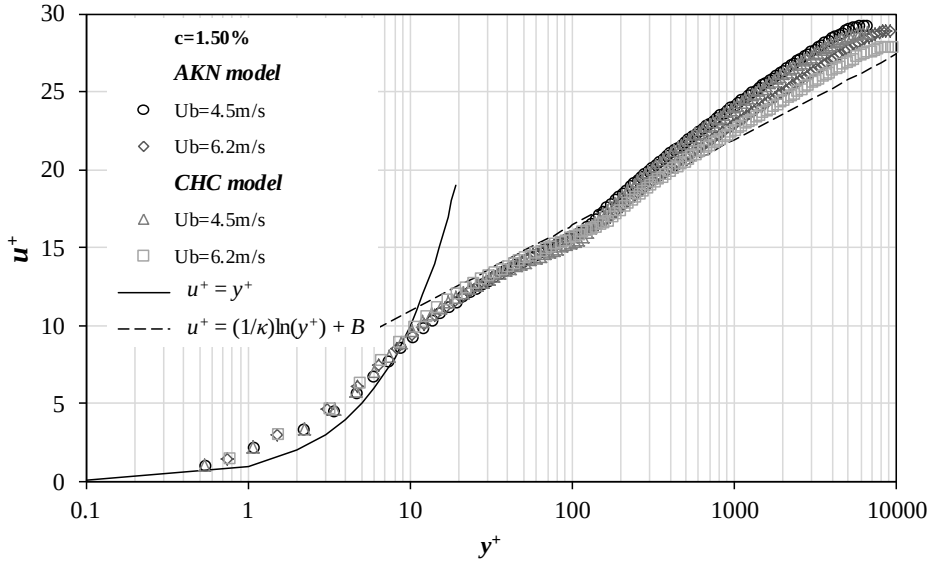

a)

Figure IV.9 – Dimensionless velocity profiles, AKN and CHC models (a) lubrication layer without fibers, c = 1.50 %, (b) lubrication layer without fibers, c = 2.50 %, (c) lubrication layer with fibers, c = 1.50 %, and, (d) lubrication layer with fibers, c = 2.50 %.

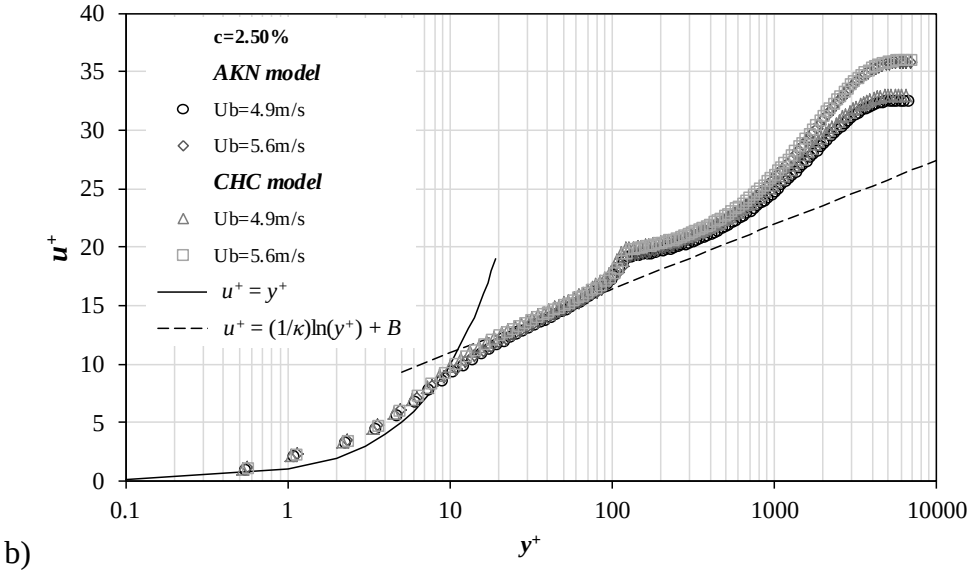

b)

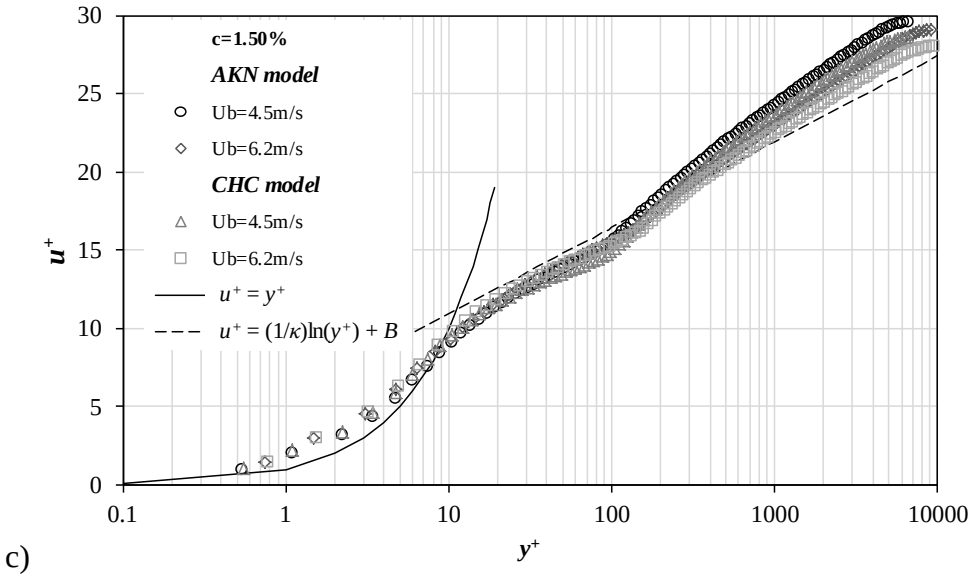

c)

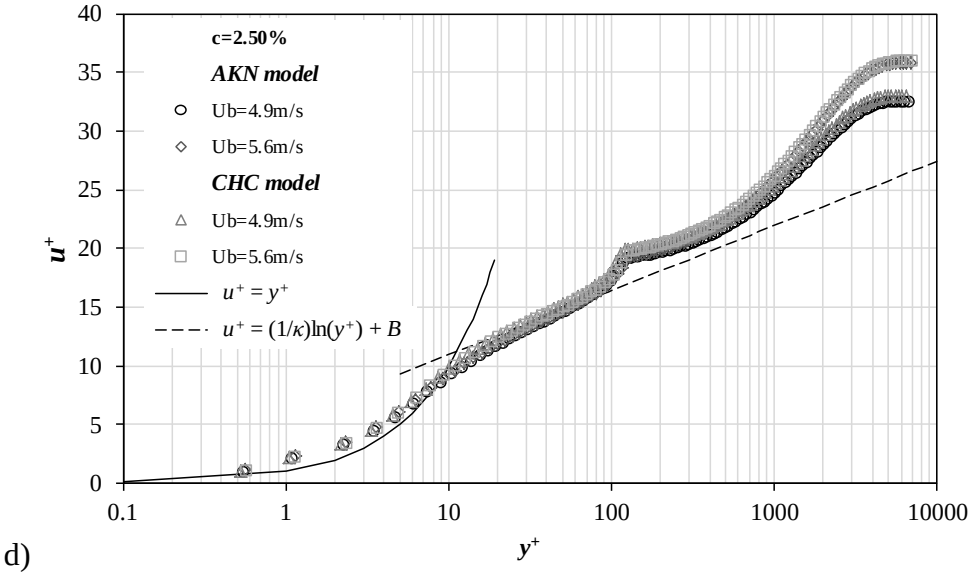

d)

Figure IV.9 – Dimensionless velocity profiles, AKN and CHC models (a) lubrication layer without fibers, c = 1.50 %, (b) lubrication layer without fibers, c = 2.50 %, (c) lubrication layer with fibers, c = 1.50 %, and, (d) lubrication layer with fibers, c = 2.50 % (continued).

The radial profiles of turbulent kinetic energy and its dissipation rate are shown in Figure IV.10 and Figure IV.11, respectively. The *r*/D axis in the graphs of turbulent kinetic energy and its dissipation rate is limited to the region closer to the wall for the higher consistency cases (i.e. 2.50 %), in order to show the variation of k and ε near the pipe wall. The higher turbulent quantities values are observed for c = 1.50 % and U_b = 6.2 m s^{-1}. For the higher consistency case (i.e. c = 2.50 %), turbulence plays an important role mainly near the pipe wall, which is in accordance with the better fit to the experimental pressure drop data observed for the two cases tested for the higher pulp consistency (Cases IV.NF.A.E0, IV.NF.A.F0, IV.F.A.E0 and IV.F.A.F0/ IV.NF.C.E0, IV.NF.C.F0, IV.F.C.E0 and IV.F.C.F0 – Table IV.18). As observed in Figures IV.10b), IV.10d), IV.11b) and IV.11d), for the higher pulp consistency (i.e. 2.50 %), the turbulent kinetic energy and its dissipation rate are lower than for the lower consistency case (i.e. 1.50 %) which corresponds to a higher *drag reduction* effect. For the lower consistency, it seems that mainly a good compromise between viscous forces and turbulence must be achieved. For the higher consistency the strong non-Newtonian behaviour of pulp dampens the turbulent structures leading to a more uniform velocity distribution in the core region (see Figures IV.8b) and IV.8d)) where higher viscosity values are observed (radial momentum transfer is reduced) and turbulence intensity is reduced when comparing with viscosity effects.

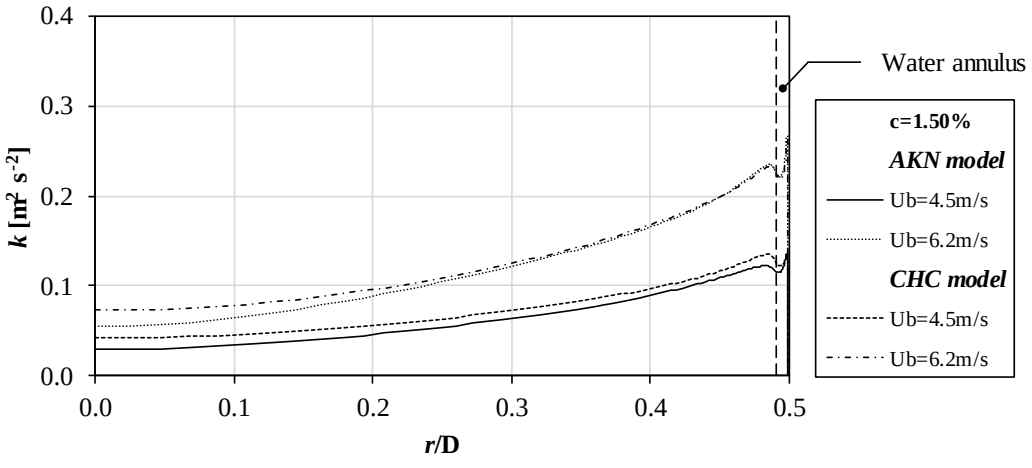

a)

Figure IV.10 – Radial profiles of turbulent kinetic energy, AKN and CHC models (a) lubrication layer without fibers, c = 1.50 %, (b) lubrication layer without fibers, c = 2.50 %, (c) lubrication layer with fibers, c = 1.50 %, and, (d) lubrication layer with fibers, c = 2.50 %.

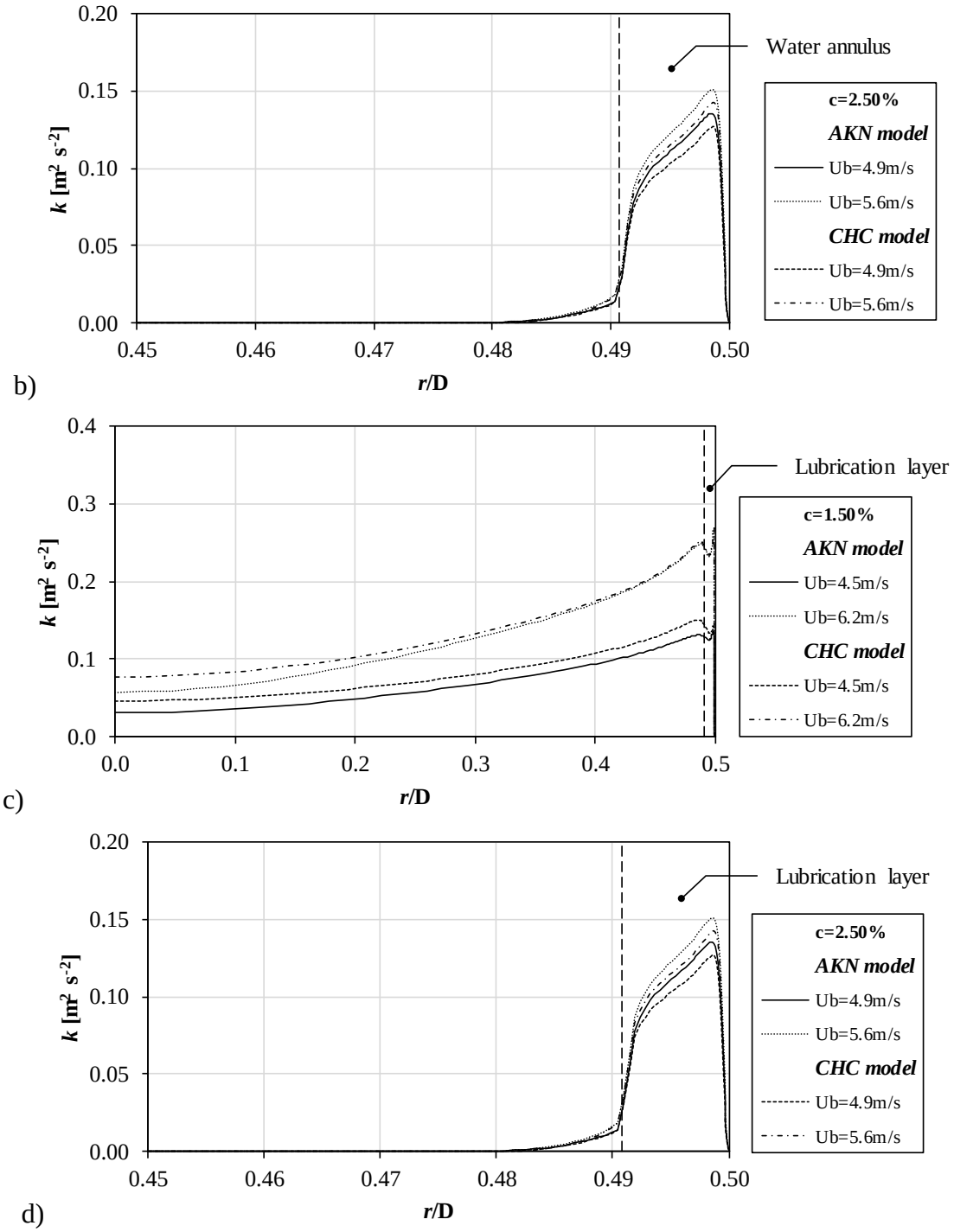

Figure IV.10 – Radial profiles of turbulent kinetic energy, AKN and CHC models (a) lubrication layer without fibers, c = 1.50 %, (b) lubrication layer without fibers, c = 2.50 %, (c) lubrication layer with fibers, c = 1.50 %, and, (d) lubrication layer with fibers, c = 2.50 % (continued).

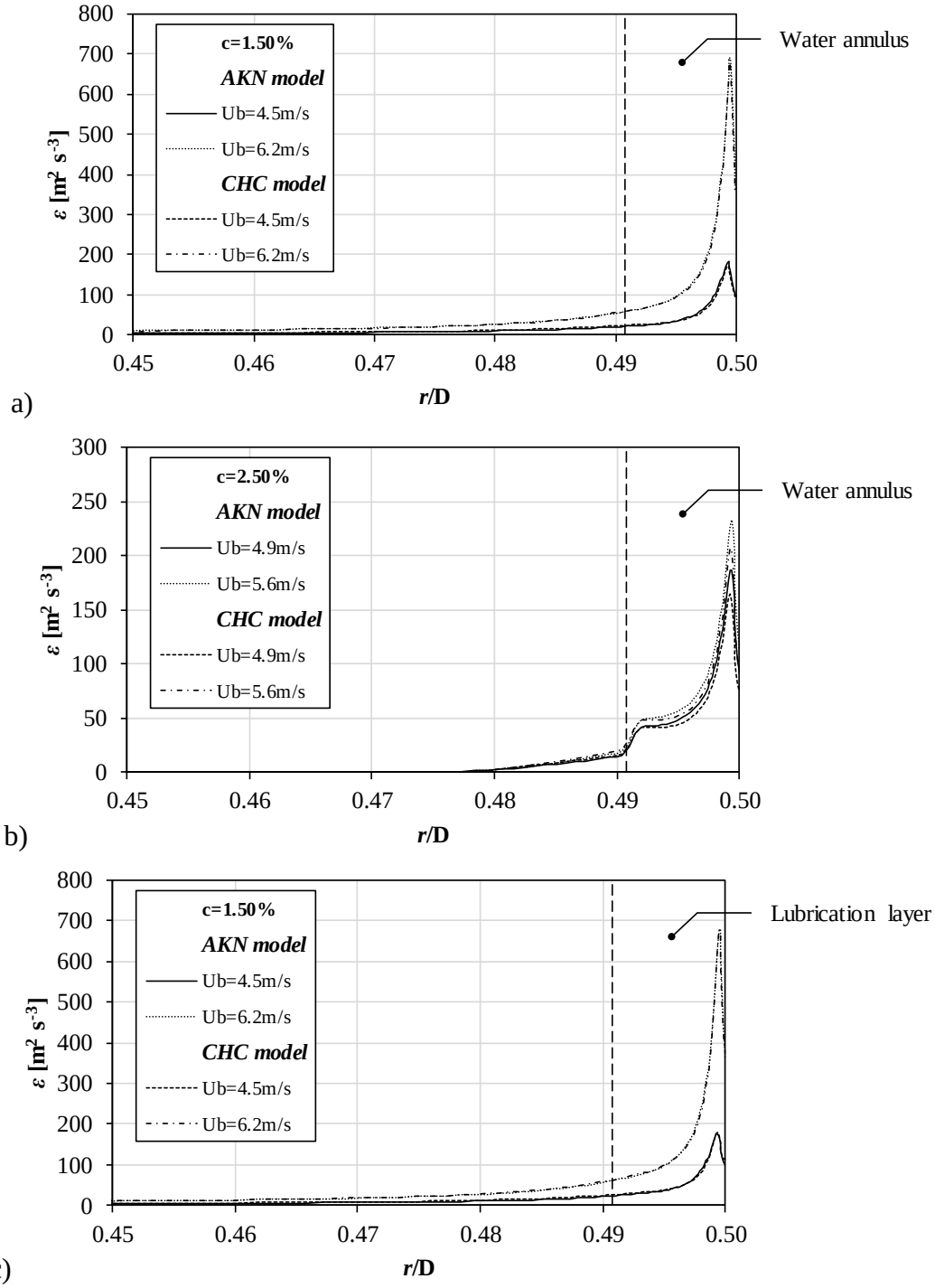

Figure IV.11 – Radial profiles of dissipation rate of turbulent kinetic energy, AKN and CHC models (a) lubrication layer without fibers, c = 1.50 %, (b) lubrication layer without fibers, c = 2.50 %, (c) lubrication layer with fibers, c = 1.50 %, and, (d) lubrication layer with fibers, c = 2.50 %.

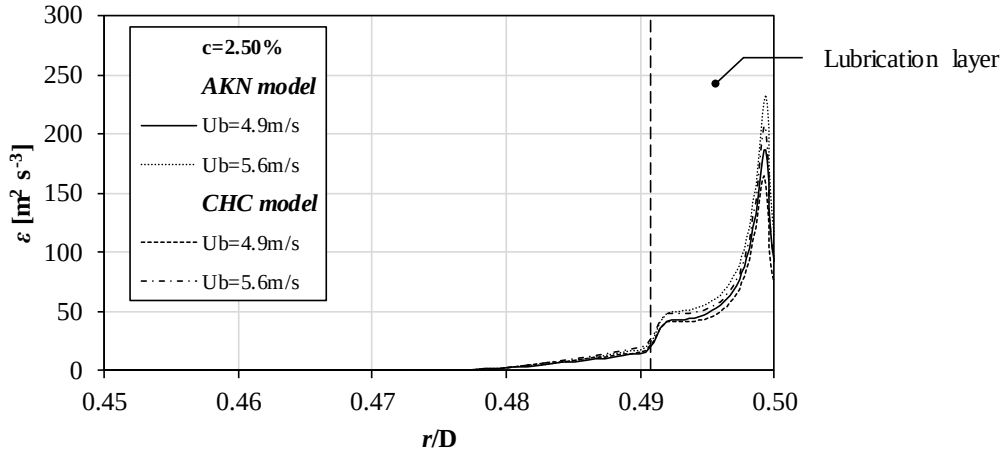

d)

Figure IV.11 – Radial profiles of dissipation rate of turbulent kinetic energy, AKN and CHC models (a) lubrication layer without fibers, c = 1.50 %, (b) lubrication layer without fibers, c = 2.50 %, (c) lubrication layer with fibers, c = 1.50 %, and, (d) lubrication layer with fibers, c = 2.50 % (continued).

All the results presented in Figures IV.7 to IV.11 suggest that the inclusion of fibers in the lubrication layer is not the main question in this study. However, it is important that the CFD model takes into account the existence of fibers in the lubrication layer in order to provide a more realistic description of reality. Thus, in Tables IV.19 and IV.20 the numerical pressure drop values obtained with the standard AKN and CHC models are presented, for all the flow conditions presented in Tables IV.14 and IV.15, assuming the presence of fibers in the lubrication layer. As can be seen from Tables IV.19 and IV.20, the test cases A, B, E and F for the *Eucalyptus* pulp suspension, and *a*, *e*, *l* and *p* for the *Pine* pulp suspensions are adequate to evaluate the modifications to be implemented in the numerical model. The numerical predictions for the cases selected show that they represent cases where the standard LRN k-ε turbulence models are not able to reproduce the numerical pressure drop, revealing high relative errors (Cases IV.F.A.A0 and IV.F.A.B0/ IV.F.C.A0 and IV.F.C.B0; IV.F.A.*a*0 and IV.F.A.*e*0/ IV.F.C.*a*0 and IV.F.C.*e*0 - Tables IV.19 and IV.20). Also, cases where the numerical predictions with the standard LRN k-ε turbulence models are more similar to the experimental pressure drop values were chosen (Cases IV.F.A.E0 and IV.F.A.F0/ IV.F.C.E0 and IV.F.C.F0 – Tables IV.19 and IV.20), corresponding to a higher consistency situation. For the *Pine* pulp, the cases IV.F.A.*l*0 and IV.F.A.*p*0/ IV.F.C.*l*0 and IV.F.C.*p*0 were selected in order to evaluate the LRN k-ε turbulence models for the higher pulp consistency (i.e. 2.30%). The AKN model was not tested for all the pulp flow conditions because as shown by Hsieh and Chang (1996), the CHC model is more universal than the AKN model since the model constants are the same as in the standard high Reynolds k-ε turbulence model. Additionally, as presented previously in this section, the profiles predicted for viscosity,

velocity, turbulent kinetic energy and its dissipation rate were very similar for both AKN and CHC models, and therefore test cases were selected in order to optimize the sets of simulations to run.

Table IV.19 – Numerical pressure drop values, AKN and CHC UDFs models – *Eucalyptus* pulp.

c [%]	U_b [m s^{-1}]	$\Delta p/L_{water}$ [Pa m^{-1}]	$\Delta p/L_{exp}$ [Pa m^{-1}]	AKN model			CHC model		
				Case	$\Delta p/L_{num}$ [Pa m^{-1}]	δ [%]	*Case*	$\Delta p/L_{num}$ [Pa m^{-1}]	δ [%]
0.91	4.2	1522	861	IV.F.A.G0	-	-	IV.F.C.G0	1721	100
0.91	4.5	1744	1019	IV.F.A.H0	-	-	IV.F.C.H0	1975	94
0.91	5.0	2141	1260	IV.F.A.I0	-	-	IV.F.C.I0	2424	92
0.91	5.5	2524	1537	IV.F.A.J0	-	-	IV.F.C.J0	2861	86
0.91	5.9	2850	1754	IV.F.A.K0	-	-	IV.F.C.K0	3237	85
0.91	6.1	3056	1896	IV.F.A.L0	-	-	IV.F.C.L0	3458	82
1.50	4.5	1744	829	IV.F.A.A0	1963	137	IV.F.C.A0	1660	100
1.50	5.1	2183	972	IV.F.A.M0	-	-	IV.F.C.M0	2288	135
1.50	5.5	2524	1014	IV.F.A.N0	-	-	IV.F.C.N0	2577	154
1.50	6.1	3056	1269	IV.F.A.O0	-	-	IV.F.C.O0	3249	156
1.50	6.2	3184	1289	IV.F.A.B0	3389	163	IV.F.C.B0	3212	149
2.20	4.4	1683	976	IV.F.A.P0	-	-	IV.F.C.P0	1013	4
2.20	5.1	2183	1128	IV.F.A.Q0	-	-	IV.F.C.Q0	1266	12
2.20	5.5	2524	1235	IV.F.A.R0	-	-	IV.F.C.R0	1352	10
2.20	6.0	2936	1356	IV.F.A.S0	-	-	IV.F.C.S0	1427	5
2.20	6.2	3184	1385	IV.F.A.T0	-	-	IV.F.C.T0	1481	7
2.50	4.9	2046	1579	IV.F.A.E0	1727	9	IV.F.C.E0	1823	15
2.50	5.3	2391	1702	IV.F.A.U0	-	-	IV.F.C.U0	1854	9
2.50	5.6	2582	1754	IV.F.A.F0	1915	9	IV.F.C.F0	1999	14
2.50	5.9	2850	1839	IV.F.A.V0	-	-	IV.F.C.V0	1915	9
2.50	6.0	2936	1878	IV.F.A.W0	-	-	IV.F.C.W0	2045	9

Table IV.20 – Numerical pressure drop values, AKN and CHC UDFs models – *Pine* pulp.

c [%]	U_b [m s^{-1}]	$\Delta p/L_{water}$ [Pa m^{-1}]	$\Delta p/L_{exp}$ [Pa m^{-1}]	AKN model			CHC model		
				Case	$\Delta p/L_{num}$ [Pa m^{-1}]	δ [%]	*Case*	$\Delta p/L_{num}$ [Pa m^{-1}]	δ [%]
0.80	4.1	1466	661	IV.F.A.*a*0	1543	133	IV.F.C.*a*0	1666	152
0.80	4.4	1683	715	IV.F.A.*b*0	-	-	IV.F.C.*b*0	1885	164
0.80	4.8	2001	818	IV.F.A.*c*0	-	-	IV.F.C.*c*0	2251	175
0.80	5.4	2414	996	IV.F.A.*d*0	-	-	IV.F.C.*d*0	2748	176
0.80	5.9	2850	1247	IV.F.A.*e*0	3091	148	IV.F.C.*e*0	3206	157
1.50	4.2	1522	981	IV.F.A.*f*0	-	-	IV.F.C.*f*0	984	44
1.50	4.6	1825	778	IV.F.A.*g*0	-	-	IV.F.C.*g*0	1033	33
1.50	5.1	2183	885	IV.F.A.*h*0	-	-	IV.F.C.*h*0	1124	27
1.50	5.5	2524	984	IV.F.A.*i*0	-	-	IV.F.C.*i*0	1216	24
1.50	5.8	2755	1079	IV.F.A.*j*0	-	-	IV.F.C.*j*0	1282	19
1.50	6.2	3184	1169	IV.F.A.*k*0	-	-	IV.F.C.*k*0	1383	18
2.30	4.3	1575	1080	IV.F.A.*l*0	1655	53	IV.F.C.*l*0	1997	85
2.30	4.6	1825	1164	IV.F.A.*m*0	-	-	IV.F.C.*m*0	2181	87
2.30	5.1	2183	1330	IV.F.A.*n*0	-	-	IV.F.C.*n*0	2483	87
2.30	5.6	2582	1451	IV.F.A.*o*0	-	-	IV.F.C.*o*0	2739	89
2.30	6.2	3184	1648	IV.F.A.*p*0	3337	103	IV.F.C.*p*0	3085	87

Although both the AKN and the CHC models were able to reproduce the *drag reduction* effect observed experimentally, mainly for the higher consistency case (i.e. *Eucalyptus* pulp c = 2.50 %, and *Pine* pulp c = 2.30 %), the numerical results are still not acceptable. Next, further modifications considering proposals from literature where the *drag reduction* effect is present, are evaluated.

IV.3.2 – SIMULATIONS WITH MODIFIED AKN/ CHC LOW-REYNOLDS-NUMBER *k-ε* MODELS

In this section the application of different damping functions in the standard AKN and CHC low-Reynolds-number *k-ε* turbulence models is evaluated. The simulations were performed for these two LRN *k-ε* turbulence models employing the damping functions applied successfully to study the turbulent flow of power-law fluids (Malin, 1997b), and spherical particles (Bartosik, 2010, 2011a; Bartosik, 2011b). A detailed investigation of the damping function's parameters is addressed; the purpose was to evaluate their variation on the numerical predictions of the new system.

In order to compare the results presented in this section with those obtained with the standard AKN and CHC *k-ε* turbulence models, the same control cases were used: (*i*) flow cases for *Eucalyptus* pulp of Table IV.14: (*1*) A – c = 1.50 %, U_b = 4.5 m s^{-1}; (*2*) B – c = 1.50 %, U_b = 6.2 m s^{-1}; (*3*) E – c = 2.50 %, U_b = 4.9 m s^{-1}; and, (*4*) F – c = 2.50 %, U_b = 5.6 m s^{-1}; (*ii*) flow cases for *Pine* pulp of Table IV.15: (*1*) *a* – c = 0.80 %, U_b = 4.1 m s^{-1}; (*2*) *e* – c = 0.80 %, U_b = 5.9 m s^{-1}; (*3*) *l* – c = 2.30 %, U_b = 4.3 m s^{-1}; and, (*4*) *p* – c = 2.30 %, U_b = 6.2 m s^{-1}.

IV.3.2.1 – MALIN DAMPING FUNCTION

The applicability of Malin damping function (Malin, 1997b) as originally presented was tested. Also, it was decided to adapt the Malin damping function to the present flow system testing new Malin constants C_{M1}, C_{M2} and C_{M3} in Equation (IV.6). Radial profiles of viscosity, dimensionless velocity and turbulent quantities are presented only for the AKN/CHC models modified with the standard Malin damping function and for the better case

considering the Malin damping function modified with the best set of Malin constants C_{M1}, C_{M2} and C_{M3} that allows a best fitting to the experimental data.

Standard version

The predicted values of pressure drop AKN/CHC modified with the standard Malin damping function are presented in Table IV.21. The results clearly showed that applying the Malin damping function without further modifications does not allow to improve the numerical calculations for *Eucalyptus* pulp suspension (compare results presented in Tables IV.18 and IV.21) and *Pine* pulp suspension (compare pressure drop values presented in Tables IV.20 and IV.22). Thus, it is of interest to study the influence that Malin constants represented by C_{M1}, C_{M2} and C_{M3} in Equation (IV.6) have on the numerical calculations.

Table IV.21 – Numerical pressure drop values, AKN and CHC models, f_μ Malin (1997b) – *Eucalyptus* pulp.

c [%]	U_b [m s^{-1}]	$\Delta p/L_{water}$ [Pa m^{-1}]	$\Delta p/L_{exp}$ [Pa m^{-1}]	AKN Malin model			CHC Malin model		
				Case	$\Delta p/L_{num}$ [Pa m^{-1}]	δ [%]	*Case*	$\Delta p/L_{num}$ [Pa m^{-1}]	δ [%]
1.50	4.5	1744	829	IV.NF.AM.A0	1773	114	IV.NF.CM.A0	1739	110
1.50	6.2	3184	1289	IV.NF.AM.B0	3257	153	IV.NF.CM.B0	3151	145
1.50	4.5	1744	829	IV.F.AM.A0	1717	107	IV.F.CM.A0	1859	124
1.50	6.2	3184	1289	IV.F.AM.B0	3293	156	IV.F.CM.B0	3382	162
2.50	4.9	2046	1579	IV.NF.AM.E0	1891	20	IV.NF.CM.E0	1843	17
2.50	5.6	2582	1754	IV.NF.AM.F0	2067	18	IV.NF.CM.F0	1994	14
2.50	4.9	2046	1579	IV.F.AM.E0	1829	16	IV.F.CM.E0	1726	10
2.50	5.6	2582	1754	IV.F.AM.F0	2004	14	IV.F.CM.F0	1945	11

Table IV.22 – Numerical pressure drop values, AKN and CHC models, f_μ Malin (1997b) – *Pine* pulp.

c [%]	U_b [m s^{-1}]	$\Delta p/L_{water}$ [Pa m^{-1}]	$\Delta p/L_{exp}$ [Pa m^{-1}]	AKN Malin model			CHC Malin model		
				Case	$\Delta p/L_{num}$ [Pa m^{-1}]	δ [%]	*Case*	$\Delta p/L_{num}$ [Pa m^{-1}]	δ [%]
0.80	4.1	1466	661	IV.NF.AM.*a*0	1623	92	IV.NF.CM.*a*0	1164	152
0.80	5.9	2850	1247	IV.NF.AM.*e*0	3176	155	IV.NF.CM.*e*0	3268	162
0.80	4.1	1466	661	IV.F.AM.*a*0	1617	144	IV.F.CM.*a*0	1667	152
0.80	5.9	2850	1247	IV.F.AM.*e*0	3163	154	IV.F.CM.*e*0	3224	158
2.30	4.3	1575	1080	IV.NF.AM.*l*0	2136	98	IV.NF.CM.*l*0	2052	90
2.30	6.2	3184	1648	IV.NF.AM.*p*0	3450	109	IV.NF.CM.*p*0	3383	105
2.30	4.3	1575	1080	IV.F.AM.*l*0	2051	90	IV.F.CM.*l*0	2035	89
2.30	6.2	3184	1648	IV.F.AM.*p*0	3176	93	IV.F.CM.*p*0	3103	88

Modified version of Malin damping function

The constants C_{M1}, C_{M2} and C_{M3} proposed in Malin (1997b) were optimized for the flow of power-law fluids with different characteristics, namely power-law indices which were different from those for the pulps studied in the present work. As observed from pressure drop results presented in Tables IV.21 and IV.22, turbulence is still overpredicted mainly for the lower consistency cases (i.e. *Eucalyptus* pulp c = 1.50 %, and *Pine* pulp c = 0.80 %). In this way several tests were performed to investigate whether and how Malin constants affect the numerical predictions. As can be seen in Equation (IV.6), modifying C_{M1} and C_{M2} influences the term including Re_k, while changing C_{M3} affects the term with Re_t. Assuming that Re_k and Re_t are unchanged, a decrease of C_{M1} or C_{M3} or an increase of C_{M2} leads to a decrease of f_μ. As shown in Mohseni and Bazargan (2012), it is expected that better predictions of the flow of Newtonian fluids are obtained when f_μ increases from 0 (value at the wall) up to 1, in a closer distance to pipe wall. The following constant values were evaluated: C_{M1} range from 0.01 to 0.0195; C_{M2} range from 0.1 to 4.0 and C_{M3} range from 10.25 to 30.75. Due to the large number of tests executed it was chosen to present here only pressure drop results obtained for the most representative sets of parameters. It should be noted that to save computational time and to avoid waste of time doing simulations where the results are expected not to have notorious differences, it was chosen to show the pressure drop results for *Eucalyptus* pulp when fibers are considered in lubrication layer only for the best set of Malin constants. The differences between considering just a pure water annulus or fibers in the lubrication layer are insignificant (see pressure drop values in Tables IV.21 and IV.22). Additionally, it was decided to present only the most representative sets of tests for *Pine* pulp for the cases where fibers are considered in lubrication layer.

The selected new Malin constants values tested and respective identification of test cases (N in the general code IV.C.MD.FN) are presented in Table IV.23. As can be seen from Table IV.23 when one parameter was modified the remaining ones were kept equal to the standard values of Malin (1997b). The calculated values of pressure drop for AKN/CHC with Malin modified damping function are presented in Table IV.24 (AKN/CHC Malin modified) for the *Eucalyptus* pulp suspension and in Table IV.25 (CHC Malin modified) for the *Pine* pulp suspension. The numerical results presented in Table IV.24 show that the predictions with the AKN or CHC with Malin modified damping function are very similar. Thus, for the

Pine pulp suspension, it was decided to present the numerical pressure drop only for the CHC Malin modified model. It should be noted that the test case designation in Table IV.23 for the different values of C_{M2} is not organised in accordance with the sequential decrease of the values of C_{M2} since test case 9 was only presented for the *Pine* pulp suspension, the lower pulp consistency (i.e. 0.80 %), and it was not the optimum value for any case of *Eucalyptus* pulp suspension. The effect of C_{M2} on the calculated pressure drop can be clearly seen (Table IV.24: Cases IV.NF.AM.A5, IV.NF.AM.B5, IV.NF.AM.E6 and IV.NF.AM.F6/ IV.NF.CM.A5, IV.NF.CM.B5, IV.NF.CM.E6 and IV.NF.CM.F6, and Table IV.25: Cases IV.F.CM.*a*9, IV.F.CM *e*9, IV.F.CM *l*7 and IV.F.CM *p*7). This parameter must likely be different for each pulp consistency tested and should even be different depending on the LRN *k-ε* turbulence model selected. This suggests that C_{M2} should be related to both flow and pulp characteristics. A more detailed investigation of the dependence of C_{M2} on the flow and pulp characteristics is not addressed in this thesis, since pressure drop values for the lower consistency case are still not acceptable. The remaining parameters tested, C_{M1} and C_{M3}, have no significant effect on the predicted pressure drop.

Table IV.23 – Tested values of Malin damping function constants C_{M1}, C_{M2} and C_{M3}.

Damping function constant	***AKN Malin model***	***AKN Malin modified***								
		Test case								
		1	**2**	**3**	**4**	**5**	**6**	**7**		
C_{M1}	0.0165	0.0195	0.0125	0.0165	0.0165	0.0165	0.0165	0.0165		
C_{M2}	0.25	0.25	0.25	0.25	0.25	3.5	3.0	2.0		
C_{M3}	20.5	20.5	20.5	30.75	10.25	20.5	20.5	20.5		
Damping function constant	***CHC Malin model***	***CHC Malin modified***								
		Test case								
		1	**2**	**3**	**4**	**5**	**6**	**7**	**8**	**9**
C_{M1}	0.0165	0.0195	0.0125	0.0165	0.0165	0.0165	0.0165	0.0165	0.0165	0.0165
C_{M2}	0.25	0.25	0.25	0.25	0.25	3.0	2.0	1.5	0.5	2.5
C_{M3}	20.5	20.5	20.5	30.75	10.25	20.5	20.5	20.5	20.5	20.5

Table IV.24 – Numerical pressure drop values, AKN and CHC models, f_μ Malin (1997b) modified – *Eucalyptus* pulp.

c [%]	U_b [m s^{-1}]	$\Delta p/L_{water}$ [Pa m^{-1}]	$\Delta p/L_{exp}$ [Pa m^{-1}]	AKN Malin modified			CHC Malin modified		
				Case	$\Delta p/L_{num}$ [Pa m^{-1}]	δ [%]	*Case*	$\Delta p/L_{num}$ [Pa m^{-1}]	δ [%]
1.50	4.5	1744	829	IV.NF.AM.A1	1846	123	IV.NF.CM.A1	1859	124
				IV.NF.AM.A2	1634	97	IV.NF.CM.A2	1663	101
				IV.NF.AM.A3	1826	120	IV.NF.CM.A3	1803	117
				IV.NF.AM.A4	1791	116	IV.NF.CM.A4	1809	118
				IV.NF.AM.A5	1551	87	IV.NF.CM.A5	1475	78
	6.2	3184	1289	IV.NF.AM.B1	3369	162	IV.NF.CM.B1	3136	143
				IV.NF.AM.B2	3065	138	IV.NF.CM.B2	3055	137
				IV.NF.AM.B3	3250	152	IV.NF.CM.B3	3087	139
				IV.NF.AM.B4	3183	147	IV.NF.CM.B4	3132	143
				IV.NF.AM.B5	2790	117	IV.NF.CM.B5	1477	15
1.50	4.5	1744	829	IV.F.AM.A5	1696	105	IV.F.CM.A7	1428	72
1.50	6.2	3184	1289	IV.F.AM.B5	3161	145	IV.F.CM.B7	2827	119
2.50	4.9	2046	1579	IV.NF.AM.E1	1845	17	IV.NF.CM.E1	1841	17
				IV.NF.AM.E2	1868	18	IV.NF.CM.E2	1834	16
				IV.NF.AM.E3	1892	20	IV.NF.CM.E3	1835	16
				IV.NF.AM.E4	1883	19	IV.NF.CM.E4	1846	17
				IV.NF.AM.E6	1641	4	IV.NF.CM.E6	1508	5
	5.6	2582	1754	IV.NF.AM.F1	2081	19	IV.NF.CM.F1	2020	15
				IV.NF.AM.F2	2045	17	IV.NF.CM.F2	2016	15
				IV.NF.AM.F3	2071	18	IV.NF.CM.F3	2019	15
				IV.NF.AM.F4	2063	18	IV.NF.CM.F4	2028	16
				IV.NF.AM.F6	1831	1	IV.NF.CM.F6	1720	2
2.50	4.9	2046	1579	IV.F.AM.E7	1623	3	IV.F.CM.E8	1640	4
	5.6	2582	1754	IV.F.AM.F7	1844	5	IV.F.CM.F8	1844	5

Table IV.25 – Numerical pressure drop values, CHC model, f_μ Malin (1997b) modified – *Pine* pulp.

c [%]	U_b [m s^{-1}]	$\Delta p/L_{water}$ [Pa m^{-1}]	$\Delta p/L_{exp}$ [Pa m^{-1}]	CHC Malin modified		
				Case	$\Delta p/L_{num}$ [Pa m^{-1}]	δ [%]
0.80	4.1	1466	661	IV.F.CM.*a*1	1671	153
				IV.F.CM.*a*2	1622	145
				IV.F.CM.*a*3	1653	150
				IV.F.CM.*a*4	1685	155
				IV.F.CM.*a*9	1013	53
	5.9	2850	1247	IV.F.CM.*e*1	3240	160
				IV.F.CM.*e*2	3193	156
				IV.F.CM.*e*3	3222	158
				IV.F.CM.*e*4	3258	161
				IV.F.CM.*e*9	1989	60
2.30	4.3	1575	1080	IV.F.CM.*l*1	1859	72
				IV.F.CM.*l*2	1824	69
				IV.F.CM.*l*3	1839	70
				IV.F.CM.*l*4	1853	72
				IV.F.CM.*l*7	1118	4
	6.2	3184	1648	IV.F.CM.*p*1	2993	82
				IV.F.CM.*p*2	2945	79
				IV.F.CM.*p*3	2984	81
				IV.F.CM.*p*4	2990	81
				IV.F.CM.*p*7	1829	11

The different techniques and devices used to monitor the flow of pulp suspensions have certain limitations, mainly related to low resolution near the pipe wall where there is less information concerning the flow variables even if the higher gradients occur there. Aiming to access some information which can be valuable for experimentalists, the profiles of viscosity, velocity and turbulent properties for the pipe cross section are presented. According to the previous simulations done with AKN/CHC models, the predictions obtained with both models, in their standard and modified versions, are very similar. Still, since the CHC model is more universal than the AKN model (Hsieh and Chang, 1996) only the radial profiles obtained for the flow of *Eucalyptus* pulp with the standard version of the CHC model, the CHC Malin model and the best cases of the CHC Malin modified model are compared. Additionally, the profiles here presented are for cases where fibers are assumed to be present in the lubrication layer.

In Figure IV.12 the radial viscosity profiles obtained with the CHC turbulence model as base model are presented. An increase of viscosity is observed in the central region, near the pipe axis, for the modified Malin model. This is more pronounced for the higher consistency case. The main reason for these differences is the lower shear rates values predicted with the modified models mostly for the pulp with higher consistency (i.e. 2.50 %), where it is expected to obtain flatter velocity profiles in the central part of pipe when applying the modified CHC models tested (see velocity profiles in Figure IV.13).

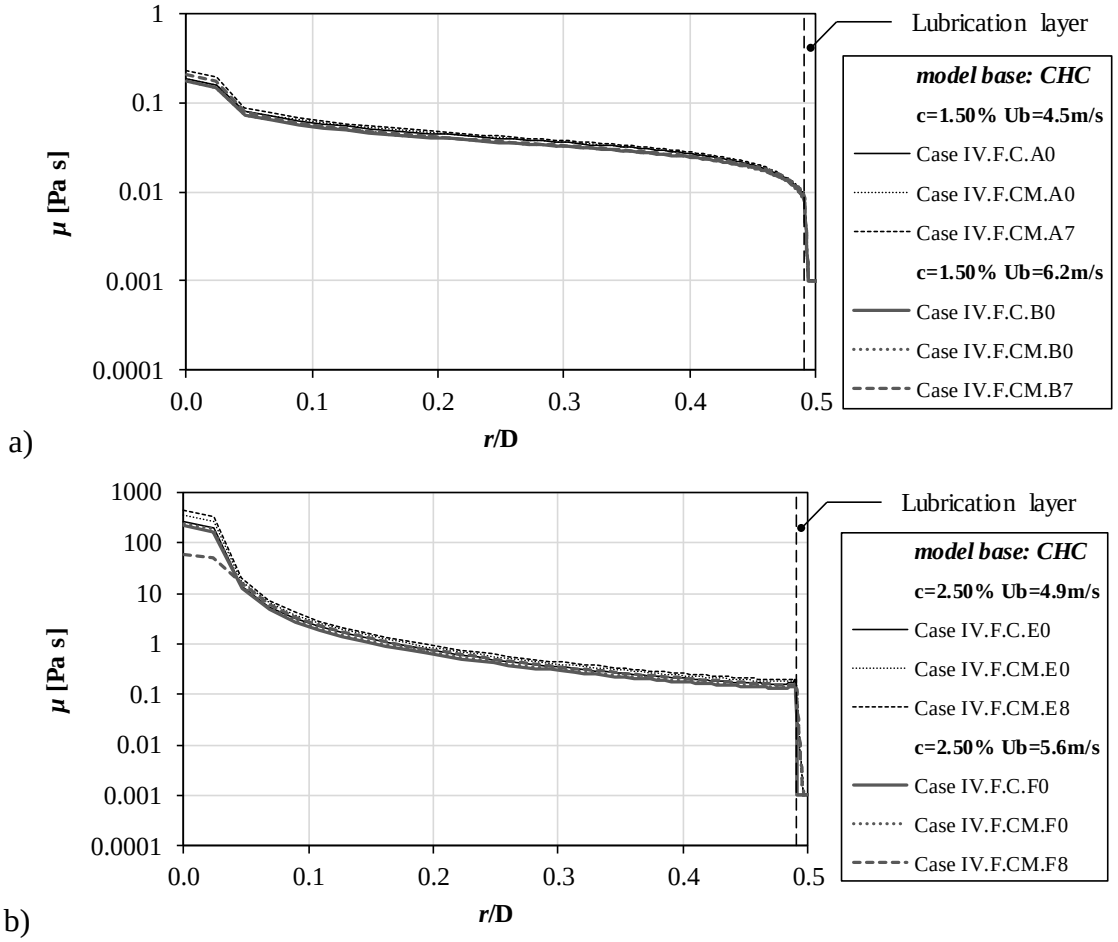

Figure IV.12 – Radial profiles of viscosity, CHC based models (a) c = 1.50 %, and, (b) c = 2.50 %.

The corresponding velocity and dimensionless velocity profiles are shown in Figures IV.13 and IV.14. For the lower consistency case (i.e. 1.50 %), as expected from viscosity results, the differences of predicted velocity between the standard CHC model and model modified with the versions of the Malin damping function tested are not notorious. For the higher consistency case (i.e. 2.50 %), the differences observed in the viscosity profiles are mainly due to the prediction of wider lower shear rates zones when the CHC model is modified with Malin damping function (standard and modified versions) resulting from the flatter velocity profile (see Figure IV.13b)). Comparing the dimensionless velocity profiles obtained from calculations (Figure IV.14) with what is described in Jäsberg (2007) (see Figure III.8, Chapter III, Section III.3.3.2), one can identify the different zones (*near wall*, *yield* and *core* region) I, II and III. For the lower consistency cases, it seems that the *core* region is almost inexistent. This can be explained with the different location of the test conditions on the pressure drop curve for pulp flow (see Figure I.4, Chapter I, Section I.1.1), i.e. for the lower consistency case (i.e. 1.50 %) the data simulated are in the fully turbulent flow regime. However, due to experimental limitations, the data measured for the higher

consistency case (i.e. 2.50 %) do not correspond to a so pronounced turbulent regime. Also, for the lower consistency cases (i.e. 1.50 %) the slope in the fully turbulent wall layer ($y^+ > 11.225$) tends to be similar to that for turbulent Newtonian fluids, standard logarithmic law, resulting from a more even distribution of the fibers in the flow which is taken into account by the viscosity model. Moreover, for this consistency, fiber aggregates are minimized, especially for the higher velocity.

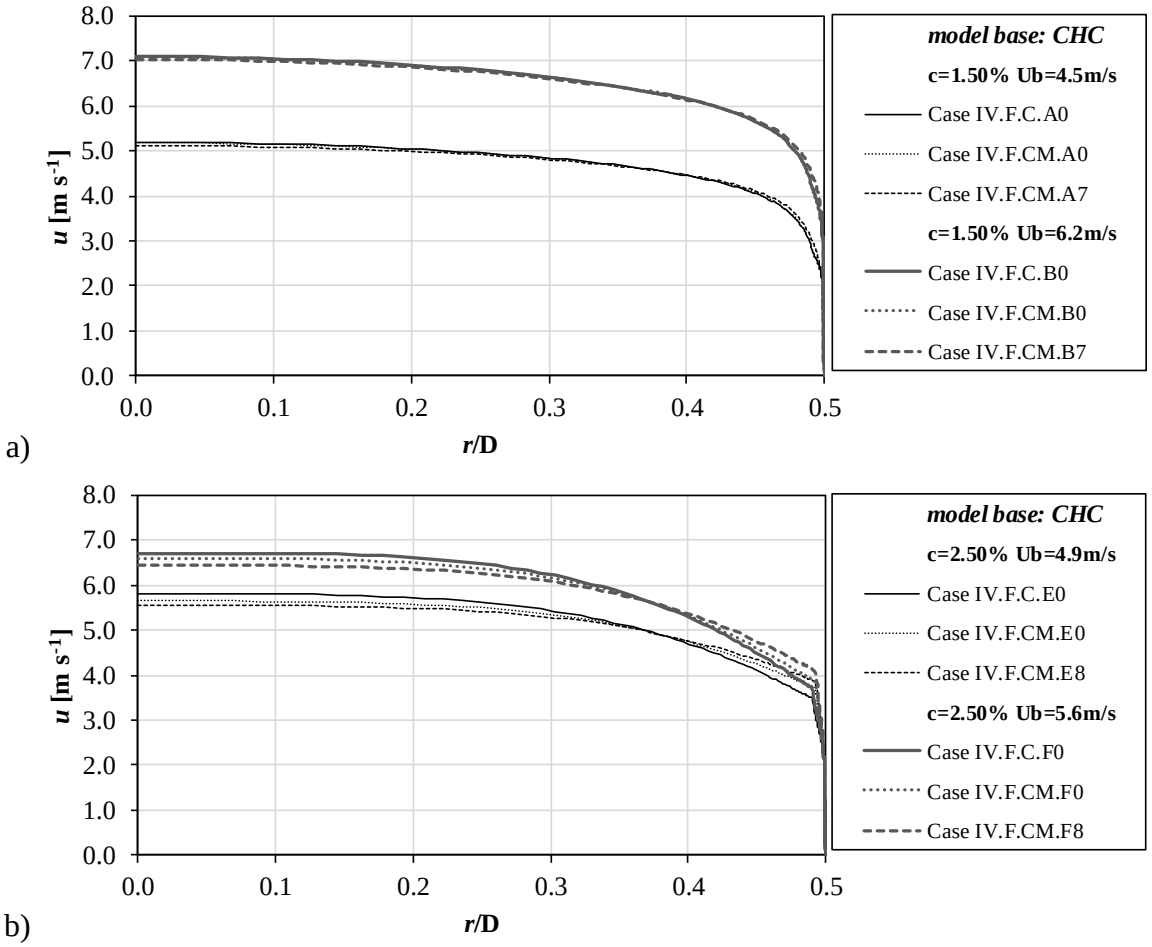

Figure IV.13 – Radial profiles of velocity, CHC based models (a) c = 1.50 %, and, (b) c = 2.50 %.

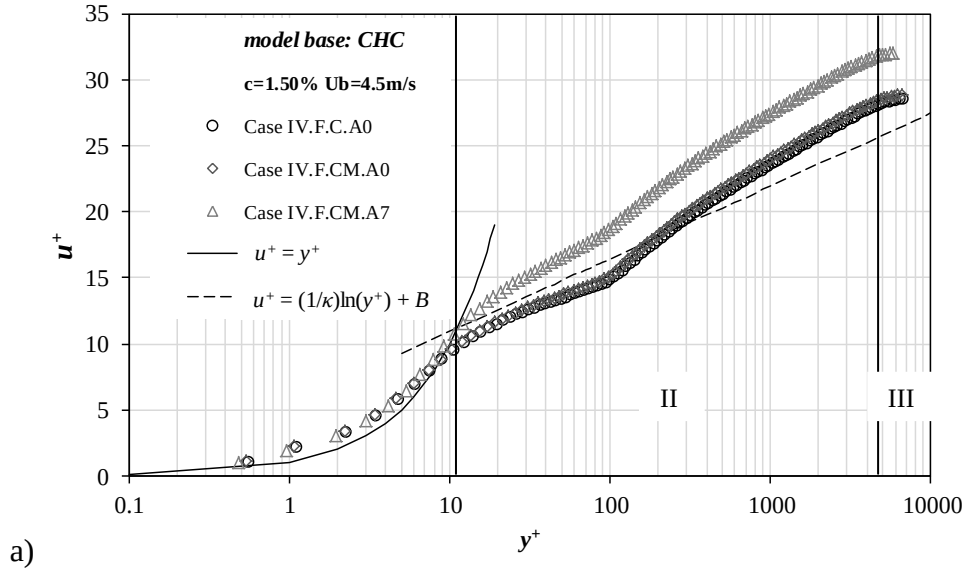

a)

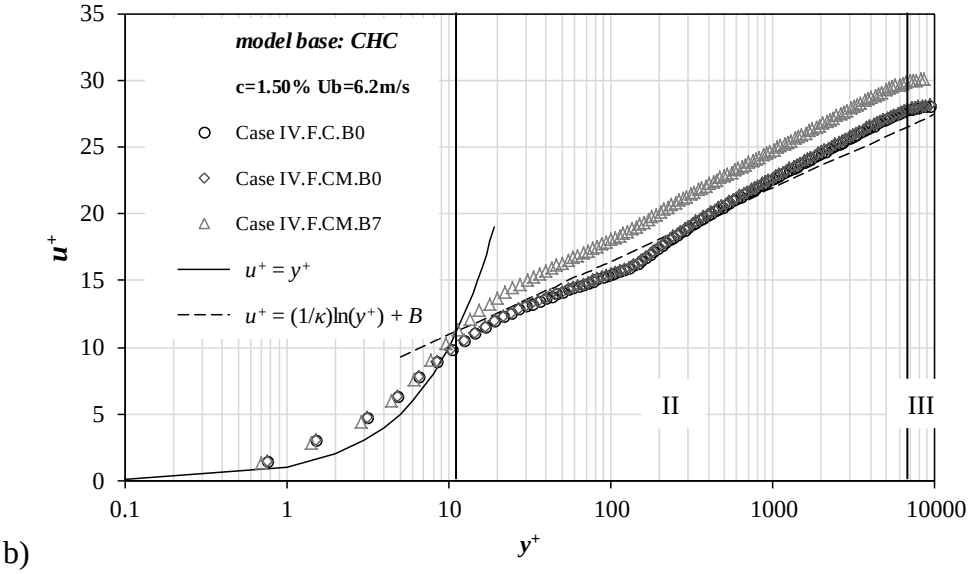

b)

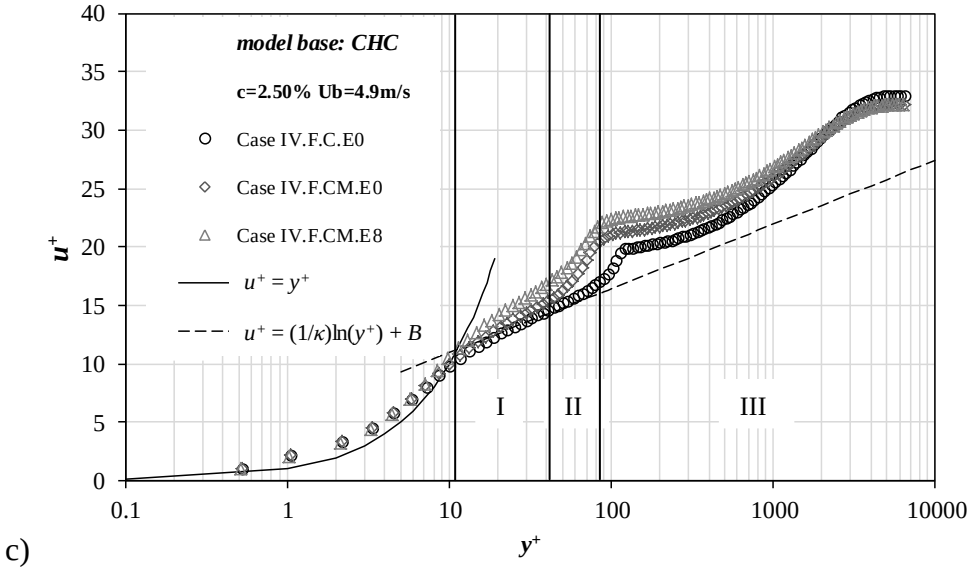

c)

Figure IV.14 – Dimensionless velocity profiles, CHC based models (a) c = 1.50 % U_b = 4.5 m s^{-1}, (b) c = 1.50 % U_b = 6.2 m s^{-1}, (c) c = 2.50 % U_b = 4.9 m s^{-1}, and, c = 1.50 % U_b = 5.6 m s^{-1}.

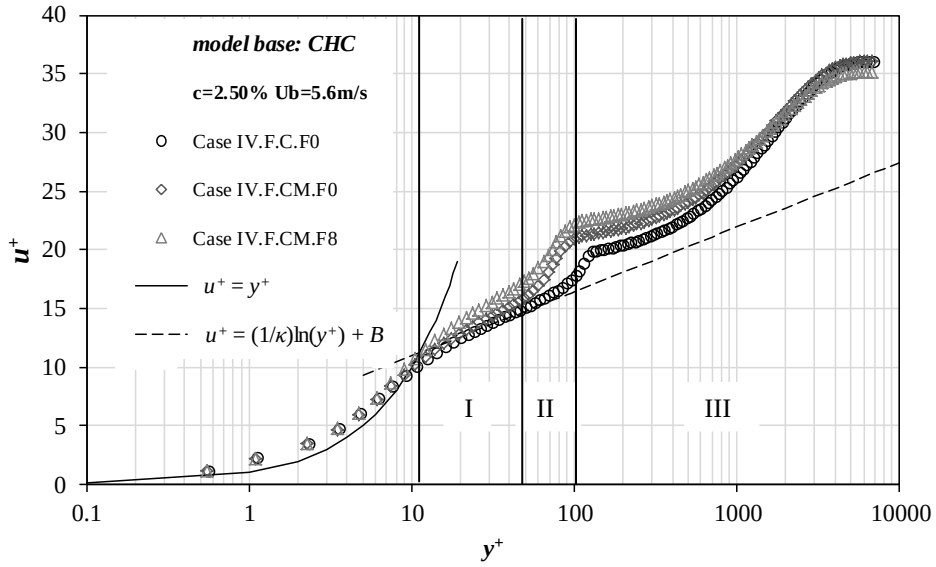

d)

Figure IV.14 – Dimensionless velocity profiles, CHC based models (a) c = 1.50 % U_b = 4.5 m s^{-1}, (b) c = 1.50 % U_b = 6.2 m s^{-1}, (c) c = 2.50 % U_b = 4.9 m s^{-1}, and, c = 1.50 % U_b = 5.6 m s^{-1} (continued).

In order to evaluate the effect of damping function f_μ modification on turbulent quantities, the k and ε radial profiles are presented in Figures IV.15 and IV.16. For the lower consistency case (Figures IV.15a) and IV.16a)), modifying the damping function according to Malin (1997b) leads to similar profiles of μ, u and u^+ to that reported for the standard CHC k-ε turbulence model. The better numerical pressure drop values obtained for that consistency case with the Malin damping function modified (see pressure drop values in Table IV.24) is mainly caused by better turbulence prediction with that function: turbulence is dampened when the Malin damping function is modified. For the higher pulp consistency (Figures IV.15b) and IV.16b)), the stronger variations of turbulence occur in the near wall region while in the pipe centre molecular viscosity is more important. Still, there is a slightly larger damping of turbulence, also for the higher consistency, when the Malin damping function is introduced.

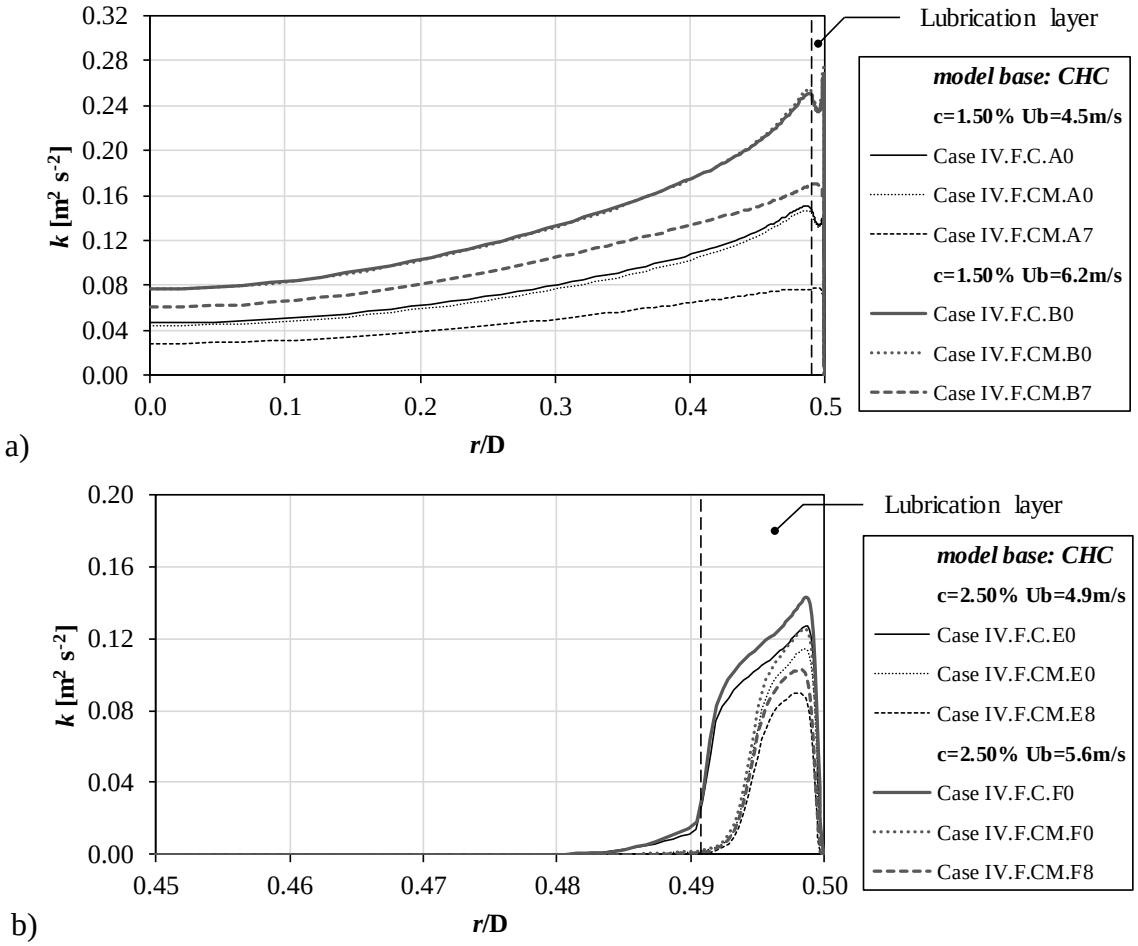

Figure IV.15 – Radial profiles of turbulent kinetic energy, CHC based models (a) c = 1.50 %, and, (b) c = 2.50 %.

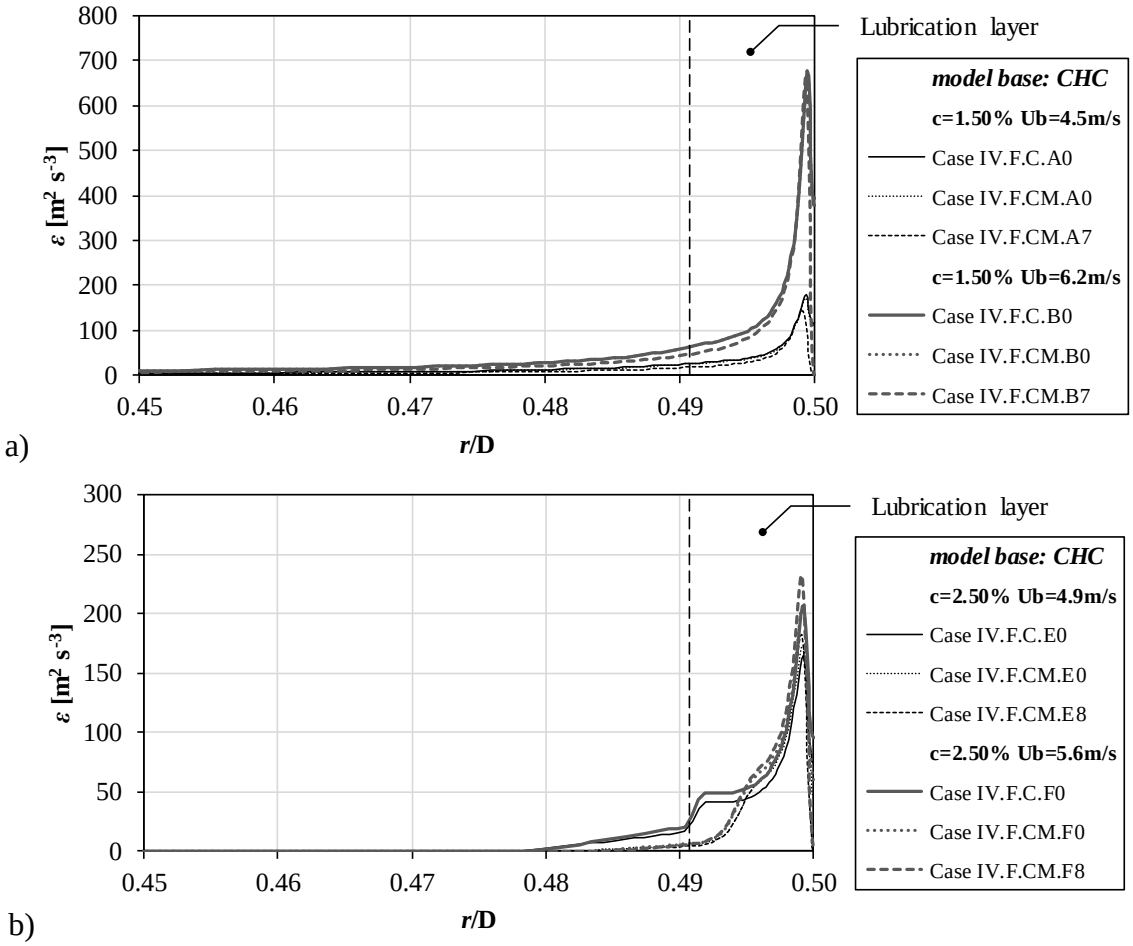

Figure IV.16 – Radial profiles of dissipation rate of turbulent kinetic energy, CHC based models (a) c = 1.50 %, and, (b) c = 2.50 %.

The results presented in this section have shown that: AKN or CHC models, standard or adapted with the standard Malin or Malin modified damping functions, are still not able to reproduce the experimental pressure drop data for the flow of *Pine* pulp suspensions and for the flow of *Eucalyptus* pulp suspensions, mainly for the lower consistency cases tested (i.e. *Eucalyptus* pulp c = 1.50 %, and *Pine* pulp c = 0.80 %). This can be due to the fact that the flow phenomena corresponding to pulp and power-law fluids are different and the Malin damping function does not manage to describe the *drag reduction* as well as for the power-law fluids, since the flow phenomena involved in pulp flow can be caused by different mechanisms than that of power-law fluids. In this way, it was decided not to present the numerical pressure drop values obtained with the AKN and CHC models adapted with the Malin modified damping function for all the flow conditions presented in Tables IV.14 and IV.15.

IV.3.2.2 – BARTOSIK DAMPING FUNCTIONS

In this section the applicability of two different damping functions proposed by Bartosik (2010, 2011a) and Bartosik (2011b) to simulate fully developed turbulent flow of *Eucalyptus* pulp is discussed.

Standard Bartosik I damping function

In Table IV.26 the pressure drop values obtained with the AKN/CHC models modified with the Bartosik I damping function (Bartosik, 2010, 2011a) are presented. As one can conclude, modifying the AKN or the CHC turbulence model with the damping function of Bartosik (2010, 2011a) does not lead to better predictions of pressure drop values (see pressure drop values in Tables IV.18, IV.19 and IV.26), especially for the lower consistencies (i.e. 0.91 and 1.50 %). Again, the effect of considering fibers in the lubrication layer is not influential in numerical simulations. These conclusions are in agreement with that achieved with the Malin damping function, i.e. further modifications need to be implemented. In order to optimize the damping function for the flow of pulp suspensions, a Bartosik I damping function optimized to predict flows of different fluid systems exhibiting *drag reduction* effect was tested in Section IV.3.3. The strategy to consider will require including in the damping function additional terms related to fibers characteristics. This subject is addressed later in Section IV.3.3. For this reason, it was decided not to present in this section the profiles of scalar variables as well as molecular viscosity, instead it was decided to present them in a further section, where the standard LRN k-ε turbulence model, modified damping function based on Bartosik studies and a new damping function is proposed, in order to facilitate the comparison between the models. However, the numerical pressure drop values are presented in Table IV.26 for all pulp flow conditions specified in Table IV.14 in order to compare with the optimized damping function which will be discussed in Section IV.3.3.

Table IV.26 – Numerical pressure drop values, AKN and CHC models, f_μ Bartosik (2010, 2011a) – *Eucalyptus* pulp.

c [%]	U_b [m s^{-1}]	$\Delta p/L_{water}$ [Pa m^{-1}]	$\Delta p/L_{exp}$ [Pa m^{-1}]	AKN Bartosik I model			CHC Bartosik I model		
				Case	$\Delta p/L_{num}$ [Pa m^{-1}]	δ [%]	*Case*	$\Delta p/L_{num}$ [Pa m^{-1}]	δ [%]
0.91	4.2	1522	861	IV.NF.ABI.G0	1969	129	IV.NF.CBI.G0	1820	111
0.91	4.5	1744	1019	IV.NF.ABI.H0	2270	123	IV.NF.CBI.H0	2094	106
0.91	5.0	2141	1260	IV.NF.ABI.I0	2732	117	IV.NF.CBI.I0	2516	100
0.91	5.5	2524	1537	IV.NF.ABI.J0	3222	110	IV.NF.CBI.J0	2962	93
0.91	5.9	2850	1754	IV.NF.ABI.K0	3607	106	IV.NF.CBI.K0	3320	89
0.91	6.1	3056	1896	IV.NF.ABI.L0	3813	101	IV.NF.CBI.L0	3523	86
1.50	4.5	1744	829	IV.NF.ABI.A0	2069	150	IV.NF.CBI.A0	1651	99
1.50	5.1	2183	972	IV.NF.ABI.M0	2586	166	IV.NF.CBI.M0	2470	154
1.50	5.5	2524	1014	IV.NF.ABI.N0	2961	192	IV.NF.CBI.N0	2800	176
1.50	6.1	3056	1269	IV.NF.ABI.O0	3632	186	IV.NF.CBI.O0	3413	169
1.50	6.2	3184	1289	IV.NF.ABI.B0	3778	193	IV.NF.CBI.B0	2990	132
2.20	4.4	1683	976	IV.NF.ABI.P0	1225	26	IV.NF.CBI.P0	1190	22
2.20	5.1	2183	1128	IV.NF.ABI.Q0	1335	18	IV.NF.CBI.Q0	1322	17
2.20	5.5	2524	1235	IV.NF.ABI.R0	1403	14	IV.NF.CBI.R0	1387	12
2.20	6.0	2936	1356	IV.NF.ABI.S0	1481	9	IV.NF.CBI.S0	1446	7
2.20	6.2	3184	1385	IV.NF.ABI.T0	1517	10	IV.NF.CBI.T0	1473	6
2.50	4.9	2046	1579	IV.NF.ABI.E0	1912	21	IV.NF.CBI.E0	1854	17
2.50	5.3	2391	1702	IV.NF.ABI.U0	1961	15	IV.NF.CBI.U0	1974	16
2.50	5.6	2582	1754	IV.NF.ABI.F0	2092	19	IV.NF.CBI.F0	2033	16
2.50	5.9	2850	1839	IV.NF.ABI.V0	2227	21	IV.NF.CBI.V0	2110	15
2.50	6.0	2936	1878	IV.NF.ABI.W0	2259	20	IV.NF.CBI.W0	2158	15
0.91	4.2	1522	861	IV.F.ABI.G0	1790	108	IV.F.CBI.G0	1699	97
0.91	4.5	1744	1019	IV.F.ABI.H0	2078	104	IV.F.CBI.H0	1968	93
0.91	5.0	2141	1260	IV.F.ABI.I0	2500	98	IV.F.CBI.I0	2382	89
0.91	5.5	2524	1537	IV.F.ABI.J0	2970	93	IV.F.CBI.J0	2824	84
0.91	5.9	2850	1754	IV.F.ABI.K0	3294	88	IV.F.CBI.K0	3171	81
0.91	6.1	3056	1896	IV.F.ABI.L0	3502	85	IV.F.CBI.L0	3353	77
1.50	4.5	1744	829	IV.F.ABI.A0	2047	147	IV.F.CBI.A0	1950	135
1.50	5.1	2183	972	IV.F.ABI.M0	2555	163	IV.F.CBI.M0	2432	150
1.50	5.5	2524	1014	IV.F.ABI.N0	2921	188	IV.F.CBI.N0	2726	169
1.50	6.1	3056	1269	IV.F.ABI.O0	3594	183	IV.F.CBI.O0	3331	163
1.50	6.2	3184	1289	IV.F.ABI.B0	3753	191	IV.F.CBI.B0	2908	126
2.20	4.4	1683	976	IV.F.ABI.P0	1166	20	IV.F.CBI.P0	1100	13
2.20	5.1	2183	1128	IV.F.ABI.Q0	1295	15	IV.F.CBI.Q0	1237	10
2.20	5.5	2524	1235	IV.F.ABI.R0	1358	10	IV.F.CBI.R0	1310	6
2.20	6.0	2936	1356	IV.F.ABI.S0	1444	7	IV.F.CBI.S0	1383	2
2.20	6.2	3184	1385	IV.F.ABI.T0	1480	7	IV.F.CBI.T0	1420	3
2.50	4.9	2046	1579	IV.F.ABI.E0	1843	17	IV.F.CBI.E0	1747	11
2.50	5.3	2391	1702	IV.F.ABI.U0	1930	13	IV.F.CBI.U0	1869	10
2.50	5.6	2582	1754	IV.F.ABI.F0	2019	15	IV.F.CBI.F0	1929	10
2.50	5.9	2850	1839	IV.F.ABI.V0	2068	12	IV.F.CBI.V0	2007	9
2.50	6.0	2936	1878	IV.F.ABI.W0	2115	13	IV.F.CBI.W0	2055	9

Standard Bartosik II damping function

The pressure drop values obtained with the use of the AKN/CHC models modified with the Bartosik II damping function (Bartosik, 2011b) are shown in Table IV.27. Similarly to the

results obtained with the AKN/CHC models modified with the Bartosik I damping function (Bartosik, 2010, 2011a), improvements of numerical predictions were not achieved also in this case (see pressure drop values in Tables IV.18, IV.19 and IV.27).

Table IV.27 – Numerical pressure drop values, AKN and CHC models, f_{μ} Bartosik (2011b) – *Eucalyptus* pulp.

c [%]	U_b [m s^{-1}]	$\Delta p/L_{water}$ [Pa m^{-1}]	$\Delta p/L_{exp}$ [Pa m^{-1}]	AKN Bartosik II model			CHC Bartosik II model		
				Case	$\Delta p/L_{num}$ [Pa m^{-1}]	δ [%]	*Case*	$\Delta p/L_{num}$ [Pa m^{-1}]	δ [%]
0.91	4.2	1522	861	IV.NF.ABII.G0	1966	128	IV.NF.CBII.G0	1803	109
0.91	4.5	1744	1019	IV.NF.ABII.H0	2264	122	IV.NF.CBII.H0	2077	104
0.91	5.0	2141	1260	IV.NF.ABII.I0	2725	116	IV.NF.CBII.I0	2499	98
0.91	5.5	2524	1537	IV.NF.ABII.J0	3207	109	IV.NF.CBII.J0	2944	92
0.91	5.9	2850	1754	IV.NF.ABII.K0	3598	105	IV.NF.CBII.K0	3302	88
0.91	6.1	3056	1896	IV.NF.ABII.L0	3800	100	IV.NF.CBII.L0	3506	95
1.50	4.5	1744	829	IV.NF.ABII.A0	2026	144	IV.NF.CBII.A0	1566	89
1.50	5.1	2183	972	IV.NF.ABII.M0	2584	166	IV.NF.CBII.M0	2423	149
1.50	5.5	2524	1014	IV.NF.ABII.N0	2960	192	IV.NF.CBII.N0	2744	171
1.50	6.1	3056	1269	IV.NF.ABII.O0	3631	186	IV.NF.CBII.O0	3354	164
1.50	6.2	3184	1289	IV.NF.ABII.B0	3776	193	IV.NF.CBII.B0	2931	127
2.20	4.4	1683	976	IV.NF.ABII.P0	1168	20	IV.NF.CBII.P0	1173	20
2.20	5.1	2183	1128	IV.NF.ABII.Q0	1319	17	IV.NF.CBII.Q0	1292	15
2.20	5.5	2524	1235	IV.NF.ABII.R0	1397	13	IV.NF.CBII.R0	1355	10
2.20	6.0	2936	1356	IV.NF.ABII.S0	1481	9	IV.NF.CBII.S0	1426	5
2.20	6.2	3184	1385	IV.NF.ABII.T0	1518	10	IV.NF.CBII.T0	1461	6
2.50	4.9	2046	1579	IV.NF.ABII.E0	1913	21	IV.NF.CBII.E0	1829	16
2.50	5.3	2391	1702	IV.NF.ABII.U0	2033	20	IV.NF.CBII.U0	1951	15
2.50	5.6	2582	1754	IV.NF.ABII.F0	2092	19	IV.NF.CBII.F0	2011	15
2.50	5.9	2850	1839	IV.NF.ABII.V0	2169	18	IV.NF.CBII.V0	2089	14
2.50	6.0	2936	1878	IV.NF.ABII.W0	2217	18	IV.NF.CBII.W0	2137	14
0.91	4.2	1522	861	IV.F.ABII.G0	1793	108	IV.F.CBII.G0	1702	98
0.91	4.5	1744	1019	IV.F.ABII.H0	2085	105	IV.F.CBII.H0	1973	94
0.91	5.0	2141	1260	IV.F.ABII.I0	2492	98	IV.F.CBII.I0	2377	89
0.91	5.5	2524	1537	IV.F.ABII.J0	2957	92	IV.F.CBII.J0	2815	83
0.91	5.9	2850	1754	IV.F.ABII.K0	3316	89	IV.F.CBII.K0	3168	81
0.91	6.1	3056	1896	IV.F.ABII.L0	3502	85	IV.F.CBII.L0	3350	77
1.50	4.5	1744	829	IV.F.ABII.A0	2108	61	IV.F.CBII.A0	1930	133
1.50	5.1	2183	972	IV.F.ABII.M0	2574	62	IV.F.CBII.M0	2447	152
1.50	5.5	2524	1014	IV.F.ABII.N0	2949	66	IV.F.CBII.N0	2746	171
1.50	6.1	3056	1269	IV.F.ABII.O0	3618	65	IV.F.CBII.O0	3346	164
1.50	6.2	3184	1289	IV.F.ABII.B0	3766	66	IV.F.CBII.B0	3481	170
2.20	4.4	1683	976	IV.F.ABII.P0	1171	20	IV.F.CBII.P0	1103	13
2.20	5.1	2183	1128	IV.F.ABII.Q0	1289	14	IV.F.CBII.Q0	1239	10
2.20	5.5	2524	1235	IV.F.ABII.R0	1363	10	IV.F.CBII.R0	1312	6
2.20	6.0	2936	1356	IV.F.ABII.S0	1448	7	IV.F.CBII.S0	1386	2
2.20	6.2	3184	1385	IV.F.ABII.T0	1484	7	IV.F.CBII.T0	1423	3
2.50	4.9	2046	1579	IV.F.ABII.E0	1825	16	IV.F.CBII.E0	1714	9
2.50	5.3	2391	1702	IV.F.ABII.U0	1935	14	IV.F.CBII.U0	1872	10
2.50	5.6	2582	1754	IV.F.ABII.F0	2023	15	IV.F.CBII.F0	1931	10
2.50	5.9	2850	1839	IV.F.ABII.V0	2073	13	IV.F.CBII.V0	2010	9
2.50	6.0	2936	1878	IV.F.ABII.W0	2121	13	IV.F.CBII.W0	2058	10

Modified Bartosik II damping function

In order to determine the influence, on the results, of modifying the empirical constant A_S, and, of representing the parameter *d* by other fiber characteristics than the fiber diameter, new values of constants C_{B1} and C_{B2} in Equation (IV.11) were tested (see Table IV.28). However, due to the large number of pulp flow conditions it was decided to show how numerical predictions are influenced by variation of C_{B1} and C_{B2} values only for the control cases of *Eucalyptus* pulp: A, B, E and F. The parameter C_{B2} originally representing the particles diameter was assumed to be equal to fiber length in these new tests. Additionally, the parameter C_{B1} was tested in the range 50 to 150. As can be seen from data collected in Table IV.28 when changing one parameter the other was kept constant and equal to the standard value tested in Bartosik II damping function. However, the numerical calculations were not improved considerably with the new values tested (compare flow cases A, B, E and F presented in Tables IV.27 and IV.29).

Table IV.28 – Tested values of Bartosik II damping function C_{B1} and C_{B2}.

Damping function constant	***AKN Bartosik II model***	***AKN Bartosik II modified***		
		Test case		
		1	**2**	**3**
C_{B1}	100	100	150	50
C_{B2}	0.000016	0.00706	0.000016	0.000016
Damping function constant	***CHC Bartosik II model***	***CHC Bartosik II modified***		
		Test case		
		1	**2**	**3**
C_{B1}	100	100	150	50
C_{B2}	0.000016	0.00706	0.000016	0.000016

Table IV.29 – Numerical pressure drop values, AKN and CHC models, f_{μ} Bartosik (2011b) modified – *Eucalyptus* pulp.

c [%]	U_b [m s^{-1}]	$\Delta p/L_{water}$ [Pa m^{-1}]	$\Delta p/L_{exp}$ [Pa m^{-1}]	AKN Bartosik II modified			CHC Bartosik II modified		
				Case	$\Delta p/L_{num}$ [Pa m^{-1}]	δ [%]	*Case*	$\Delta p/L_{num}$ [Pa m^{-1}]	δ [%]
1.50	4.5	1744	829	IV.NF.ABII.A1	2000	141	IV.NF.CBII.A1	2082	151
				IV.NF.ABII.A2	2063	149	IV.NF.CBII.A2	1572	90
				IV.NF.ABII.A3	2063	149	IV.NF.CBII.A3	1567	89
	6.2	3184	1289	IV.NF.ABII.B1	3393	163	IV.NF.CBII.B1	3427	127
				IV.NF.ABII.B2	3777	193	IV.NF.CBII.B2	2184	69
				IV.NF.ABII.B3	3776	193	IV.NF.CBII.B3	2931	166
1.50	4.5	1744	829	IV.F.ABII.A1	1980	139	IV.F.CBII.A1	2191	164
				IV.F.ABII.A2	2059	148	IV.F.CBII.A2	1926	132
				IV.F.ABII.A3	2059	148	IV.F.CBII.A3	1932	133
	6.2	3184	1289	IV.F.ABII.B1	3318	158	IV.F.CBII.B1	3232	151
				IV.F.ABII.B2	3764	192	IV.F.CBII.B2	3764	192
				IV.F.ABII.B3	3766	192	IV.F.CBII.B3	3480	170
2.50	4.9	2046	1579	IV.NF.ABII.E1	1845	17	IV.NF.CBII.E1	1877	19
				IV.NF.ABII.E2	1912	21	IV.NF.CBII.E2	1830	16
				IV.NF.ABII.E3	1913	21	IV.NF.CBII.E3	1829	16
	5.6	2582	1754	IV.NF.ABII.F1	2089	19	IV.NF.CBII.F1	2057	17
				IV.NF.ABII.F2	2092	19	IV.NF.CBII.F2	2011	15
				IV.NF.ABII.F3	2092	19	IV.NF.CBII.F3	2010	15
2.50	4.9	2046	1579	IV.F.ABII.E1	1780	13	IV.F.CBII.E1	1748	11
				IV.F.ABII.E2	1824	16	IV.F.CBII.E2	1714	9
				IV.F.ABII.E3	1825	16	IV.F.CBII.E3	1714	9
	5.6	2582	1754	IV.F.ABII.F1	1960	12	IV.F.CBII.F1	1960	12
				IV.F.ABII.F2	2023	15	IV.F.CBII.F2	1932	10
				IV.F.ABII.F3	2024	15	IV.F.CBII.F3	2006	14

In Section IV.3.3 the Bartosik I and II damping functions will be further modified by including a new term related to fibers characteristics.

IV.3.3 – ADAPTATION OF BARTOSIK I AND II DAMPING FUNCTIONS FOR THE DESCRIPTION OF PULP SUSPENSIONS FLOW

A detailed investigation to simulate the turbulent flow of pulp suspensions assuming the new damping functions based on Bartosik (2010, 2011a), Equation (IV.12), and Bartosik (2010b), Equation (IV.13), is addressed in this section. Study of the influence of the proposed Bartosik I and II new damping functions on viscosity, velocity and profiles of turbulent quantities, for the control test cases (*Eucalyptus* pulp: A, B, E and F; *Pine* pulp: *a*, *e*, *l* and *p*), used in the previous studies, is presented. In order to validate the complete CFD model and to show its generality, it was applied to simulate all the flow data presented in Tables IV.14 and

IV.15 (different consistencies and flow rates) for two different pulps: *Eucalyptus* and *Pine* pulp suspensions.

According to the preliminary results previously presented in Section IV.3.2, using either the AKN or the CHC models is not the main question. As shown in Hsieh and Chang (1996), the CHC model reveals to be more universal than the AKN model. Thus, the CFD model discussed in the present section is evaluated only considering the CHC model as LRN *k-ε* turbulence base model.

Tables IV.30 and IV.31 show numerical pressure drops predicted when using the CHC *k-ε* turbulence model modified with the new Bartosik I damping function as well as when adapted with the new Bartosik II damping function, for all pulp flow conditions specified in Table IV.14 (*Eucalyptus* pulp) and in Table IV.15 (*Pine* pulp). From Section IV.3.2.2 (Tables IV.26 and IV.27, *Eucalyptus* pulp), it is obvious that the additional term $r^{1/4}$ does produce similar results when applied to the Bartosik I damping function as well as when applied to the Bartosik II damping function. This fact was verified with the numerical predictions presented in Tables IV.30 and IV.31. Also, it is almost impossible to distinguish between profiles obtained when applying these two damping functions with the CHC *k-ε* turbulence model. Thus, the choice of the most suitable damping function base, between these two, to describe the pulp suspension flow cases is not obvious. Furthermore, it is noticeable the improvements obtained with the new damping functions tested. However, it seems that the new Bartosik I damping function is the most appropriate to be employed in the CHC *k-ε* turbulence model since it presents a more realistic meaning by including fiber aspect-ratio as well as the yield stress. Additionally, the numerical results presented in Section IV.3.2 have shown that to consider only pure water annulus or the existence of fibers in the lubrication layer does not have a preponderate effect on the numerical calculations. However, the CFD model is more complete, i.e. able to describe the turbulent flow of pulp suspensions, and closer to reality, if the existence of fibers in the lubrication layer is taken into account. The predicted pressure drop values fit well the experimental data (see pressure drop values in Tables IV.30 and IV.31). In spite of the quantitative agreement obtained for pressure drop, it was investigated the qualitative agreement between predicted velocity and dimensionless velocity profiles with those described by Jäsberg (2007). Additionally, the trend in turbulent quantities and viscosity was investigated. Radial profiles of molecular viscosity, velocity and non-dimensional velocity and turbulent quantities are presented for the CHC model with the new Bartosik I damping function assuming the existence of fibers in the lubrication layer, for *Eucalyptus*

pulp suspension (control cases: A, B, E and F), and *Pine* pulp suspension (control cases: *a*, *e*, *l* and *p*).

Table IV.30 – Numerical pressure drop values, CHC base model, f_μ new Bartosik I and II damping functions – *Eucalyptus* pulp.

c [%]	U_b [m s^{-1}]	$\Delta p/L_{water}$ [Pa m^{-1}]	$\Delta p/L_{exp}$ [Pa m^{-1}]	*new* CHC Bartosik I model			*new* CHC Bartosik II model		
				Case	$\Delta p/L_{num}$ [Pa m^{-1}]	δ [%]	*Case*	$\Delta p/L_{num}$ [Pa m^{-1}]	δ [%]
0.91	4.2	1522	861	IV.NF.CBI.1.G0	1034	21	IV.NF.CBII.1.G0	1049	22
0.91	4.5	1744	1019	IV.NF.CBI.1.H0	1200	18	IV.NF.CBII.1.H0	1301	28
0.91	5.0	2141	1260	IV.NF.CBI.1.I0	1444	15	IV.NF.CBII.1.I0	1445	15
0.91	5.5	2524	1537	IV.NF.CBI.1.J0	1685	10	IV.NF.CBII.1.J0	1683	10
0.91	5.9	2850	1754	IV.NF.CBI.1.K0	1890	8	IV.NF.CBII.1.K0	1893	8
0.91	6.1	3056	1896	IV.NF.CBI.1.L0	2018	7	IV.NF.CBII.1.L0	2014	6
1.50	4.5	1744	829	IV.NF.CBI.1.A0	970	17	IV.NF.CBII.1.A0	967	17
1.50	5.1	2183	972	IV.NF.CBI.1.M0	1273	31	IV.NF.CBII.1.M0	1268	30
1.50	5.5	2524	1014	IV.NF.CBI.1.N0	1481	46	IV.NF.CBII.1.N0	1474	45
1.50	6.1	3056	1269	IV.NF.CBI.1.O0	1842	45	IV.NF.CBII.1.O0	1833	45
1.50	6.2	3184	1289	IV.NF.CBI.1.B0	1920	49	IV.NF.CBII.1.B0	1910	48
2.20	4.4	1683	976	IV.NF.CBI.1.P0	1048	7	IV.NF.CBII.1.P0	1045	7
2.20	5.1	2183	1128	IV.NF.CBI.1.Q0	1179	5	IV.NF.CBII.1.P0	1177	4
2.20	5.5	2524	1235	IV.NF.CBI.1.R0	1265	2	IV.NF.CBII.1.R0	1263	2
2.20	6.0	2936	1356	IV.NF.CBI.1.S0	1341	1	IV.NF.CBII.1.S0	1338	1
2.20	6.2	3184	1385	IV.NF.CBI.1.T0	1370	1	IV.NF.CBII.1.T0	1368	1
2.50	4.9	2046	1579	IV.NF.CBI.1.E0	1611	2	IV.NF.CBII.1.E0	1608	2
2.50	5.3	2391	1702	IV.NF.CBI.1.U0	1724	1	IV.NF.CBII.1.U0	1720	1
2.50	5.6	2582	1754	IV.NF.CBI.1.F0	1787	2	IV.NF.CBII.1.F0	1784	2
2.50	5.9	2850	1839	IV.NF.CBI.1.V0	1865	1	IV.NF.CBII.1.V0	1862	1
2.50	6.0	2936	1878	IV.NF.CBI.1.W0	1913	2	IV.NF.CBII.1.W0	1910	2
0.91	4.2	1522	861	IV.F.CBI.1.G0	1032	20	IV.F.CBII.1.G0	1032	20
0.91	4.5	1744	1019	IV.F.CBI.1.H0	1188	17	IV.F.CBII.1.H0	1188	17
0.91	5.0	2141	1260	IV.F.CBI.1.I0	1428	13	IV.F.CBII.1.I0	1427	13
0.91	5.5	2524	1537	IV.F.CBI.1.J0	1682	9	IV.F.CBII.1.J0	1680	9
0.91	5.9	2850	1754	IV.F.CBI.1.K0	1883	7	IV.F.CBII.1.K0	1882	7
0.91	6.1	3056	1896	IV.F.CBI.1.L0	1995	5	IV.F.CBII.1.L0	1996	5
1.50	4.5	1744	829	IV.F.CBI.1.A0	946	14	IV.F.CBII.1.A0	949	15
1.50	5.1	2183	972	IV.F.CBI.1.M0	1252	29	IV.F.CBII.1.M0	1255	29
1.50	5.5	2524	1014	IV.F.CBI.1.N0	1460	44	IV.F.CBII.1.N0	1464	44
1.50	6.1	3056	1269	IV.F.CBI.1.O0	1822	44	IV.F.CBII.1.O0	1828	44
1.50	6.2	3184	1289	IV.F.CBI.1.B0	1899	47	IV.F.CBII.1.B0	1905	48
2.20	4.4	1683	976	IV.F.CBI.1.P0	1030	6	IV.F.CBII.1.P0	1031	6
2.20	5.1	2183	1128	IV.F.CBI.1.Q0	1165	3	IV.F.CBII.1.Q0	1166	3
2.20	5.5	2524	1235	IV.F.CBI.1.R0	1252	1	IV.F.CBII.1.R0	1253	1
2.20	6.0	2936	1356	IV.F.CBI.1.S0	1337	1	IV.F.CBII.1.S0	1338	1
2.20	6.2	3184	1385	IV.F.CBI.1.T0	1366	1	IV.F.CBII.1.T0	1365	2
2.50	4.9	2046	1579	IV.F.CBI.1.E0	1577	0.1	IV.F.CBII.1.E0	1584	0.3
2.50	5.3	2391	1702	IV.F.CBI.1.U0	1751	3	IV.F.CBII.1.U0	1752	3
2.50	5.6	2582	1754	IV.F.CBI.1.F0	1809	3	IV.F.CBII.1.F0	1810	3
2.50	5.9	2850	1839	IV.F.CBI.1.V0	1886	3	IV.F.CBII.1.V0	1887	3
2.50	6.0	2936	1878	IV.F.CBI.1.W0	1935	3	IV.F.CBII.1.W0	1936	3

Table IV.31 – Numerical pressure drop values, CHC base model, f_μ new Bartosik I and II damping functions – *Pine* pulp.

c [%]	U_b [m s^{-1}]	$\Delta p/L_{water}$ [Pa m^{-1}]	$\Delta p/L_{exp}$ [Pa m^{-1}]	*new* CHC Bartosik I model			*new* CHC Bartosik II model		
				Case	$\Delta p/L_{num}$ [Pa m^{-1}]	δ [%]	*Case*	$\Delta p/L_{num}$ [Pa m^{-1}]	δ [%]
0.80	4.1	1466	661	IV.NF.CBI.1.*a*0	724	10	IV.NF.CBII.1.*a*0	723	9
0.80	4.4	1683	715	IV.NF.CBI.1.*b*0	813	14	IV.NF.CBII.1.*b*0	811	14
0.80	4.8	2001	818	IV.NF.CBI.1.*c*0	1040	27	IV.NF.CBII.1.*c*0	973	19
0.80	5.4	2414	996	IV.NF.CBI.1.*d*0	1161	17	IV.NF.CBII.1.*d*0	1158	16
0.80	5.9	2850	1247	IV.NF.CBI.1.*e*0	1372	10	IV.NF.CBII.1.*e*0	1365	10
1.50	4.2	1522	981	IV.NF.CBI.1.*f*0	722	6	IV.NF.CBII.1.*f*0	715	5
1.50	4.6	1825	778	IV.NF.CBI.1.*g*0	803	3	IV.NF.CBII.1.*g*0	815	5
1.50	5.1	2183	885	IV.NF.CBI.1.*h*0	889	0.4	IV.NF.CBII.1.*h*0	882	0.4
1.50	5.5	2524	984	IV.NF.CBI.1.*i*0	953	3	IV.NF.CBII.1.*i*0	946	4
1.50	5.8	2755	1079	IV.NF.CBI.1.*j*0	998	8	IV.NF.CBII.1.*j*0	994	8
1.50	6.2	3184	1169	IV.NF.CBI.1.*k*0	1071	8	IV.NF.CBII.1.*k*0	1112	5
2.30	4.3	1575	1080	IV.NF.CBI.1.*l*0	1092	1	IV.NF.CBII.1.*l*0	1094	1
2.30	4.6	1825	1164	IV.NF.CBI.1.*m*0	1253	8	IV.NF.CBII.1.*m*0	1255	8
2.30	5.1	2183	1330	IV.NF.CBI.1.*n*0	1475	11	IV.NF.CBII.1.*n*0	1470	11
2.30	5.6	2582	1451	IV.NF.CBI.1.*o*0	1647	14	IV.NF.CBII.1.*o*0	1639	13
2.30	6.2	3184	1648	IV.NF.CBI.1.*p*0	1907	16	IV.NF.CBII.1.*p*0	1893	15
0.80	4.1	1466	661	IV.F.CBI.1.*a*0	718	9	IV.F.CBII.1.*a*0	718	9
0.80	4.4	1683	715	IV.F.CBI.1.*b*0	807	13	IV.F.CBII.1.*b*0	806	13
0.80	4.8	2001	818	IV.F.CBI.1.*c*0	816	0.1	IV.F.CBII.1.*c*0	964	18
0.80	5.4	2414	996	IV.F.CBI.1.*d*0	1154	16	IV.F.CBII.1.*d*0	1154	16
0.80	5.9	2850	1247	IV.F.CBI.1.*e*0	1392	12	IV.F.CBII.1.*e*0	1362	9
1.50	4.2	1522	981	IV.F.CBI.1.*f*0	720	6	IV.F.CBII.1.*f*0	722	6
1.50	4.6	1825	778	IV.F.CBI.1.*g*0	817	5	IV.F.CBII.1.*g*0	817	5
1.50	5.1	2183	885	IV.F.CBI.1.*h*0	899	2	IV.F.CBII.1.*h*0	897	1
1.50	5.5	2524	984	IV.F.CBI.1.*i*0	956	3	IV.F.CBII.1.*i*0	954	3
1.50	5.8	2755	1079	IV.F.CBI.1.*j*0	997	8	IV.F.CBII.1.*j*0	995	8
1.50	6.2	3184	1169	IV.F.CBI.1.*k*0	1059	9	IV.F.CBII.1.*k*0	1059	9
2.30	4.3	1575	1080	IV.F.CBI.1.*l*0	1464	36	IV.F.CBII.1.*l*0	1460	35
2.30	4.6	1825	1164	IV.F.CBI.1.*m*0	1583	36	IV.F.CBII.1.*m*0	1581	36
2.30	5.1	2183	1330	IV.F.CBI.1.*n*0	1764	33	IV.F.CBII.1.*n*0	1763	33
2.30	5.6	2582	1451	IV.F.CBI.1.*o*0	1930	33	IV.F.CBII.1.*o*0	1930	33
2.30	6.2	3184	1648	IV.F.CBI.1.*p*0	2158	31	IV.F.CBII.1.*p*0	2158	31

Molecular viscosity profiles for control cases of *Eucalyptus* pulp (A – c = 1.50 %, U_b = 4.5 m s^{-1}; B – c = 1.50 %, U_b = 6.2 m s^{-1}; E – c = 2.50 %, U_b = 4.9 m s^{-1}; and, F – c = 2.50 %, U_b = 5.6 m s^{-1}) are presented in Figure IV.17. The new formulation predicts slightly larger values of molecular viscosity near the pipe axis. It was expected that a viscosity increase leads to growing flow resistance and higher pressure drop values were expected; however, turbulent viscosity was modified to take into account the presence of fibers in the flow. In this way, resistance to the flow and turbulence are better described in this new model formulation, since a better approach to the experimental data was obtained when applying the new viscosity expression as well as the new Bartosik I and II damping functions.

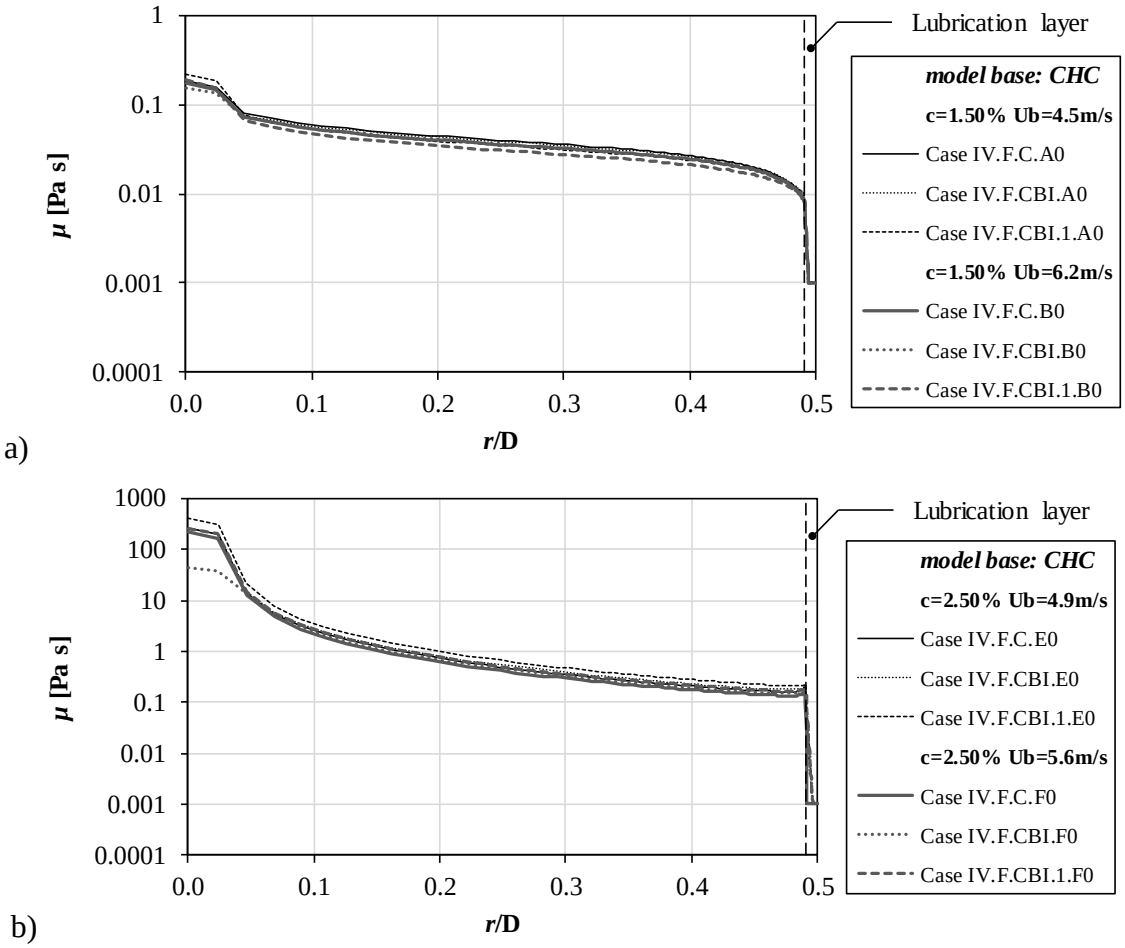

Figure IV.17 – Radial profiles of viscosity, CHC model, CHC Bartosik I model and new CHC Bartosik I model, for *Eucalyptus* pulp: (a) c = 1.50 %, and, (b) c = 2.50 %.

Figure IV.18 shows the molecular viscosity profiles for control cases of *Pine* pulp (*a* – c = 0.80 %, U_b = 4.1 m s^{-1}; *e* – c = 0.80 %, U_b = 5.9 m s^{-1}; *l* – c = 2.30 %, U_b = 4.3 m s^{-1}; and, *p* – c = 2.30 %, U_b = 6.2 m s^{-1}). It was decided not to include here the results of the CHC model with Bartosik I damping function, as well as in all the profiles presented in this section, concerning the control cases for *Pine* pulp. This choice was made because it was expected to observe similar profile to that reported for the cases of *Eucalyptus* pulp when comparing the three different versions of the CHC model tested (standard CHC, CHC model with Bartosik I damping function, and CHC model with new Bartosik I damping function). The lubrication layer has larger thickness for *Pine* pulp cases due to the fact that *Pine* fibers are longer than the *Eucalyptus* fibers. It is clearly observable in Figure IV.18a) the variation of viscosity since for the lower consistency (i.e. 0.80 %) the viscosity of pulp is almost Newtonian. The presence of less fiber in the flow close to the wall is replicated through a consistency profile in the lubrication layer more uniform when comparing with the more concentrated pulp. Additionally, viscosity values obtained for the range of shear rates and pulp consistency in the

lubrication layer for the *Pine* pulp with consistency of 0.80 % indicate that a layer free of fibers exists near the pipe wall. This is consistent with less fibers in the flow leading to free water space which can be present near the pipe wall due to the presence of turbulent lubrication layer. Again, as for the *Eucalyptus* pulp, the CHC model with the new Bartosik I damping function leads to slightly larger values of molecular viscosity near the pipe axis.

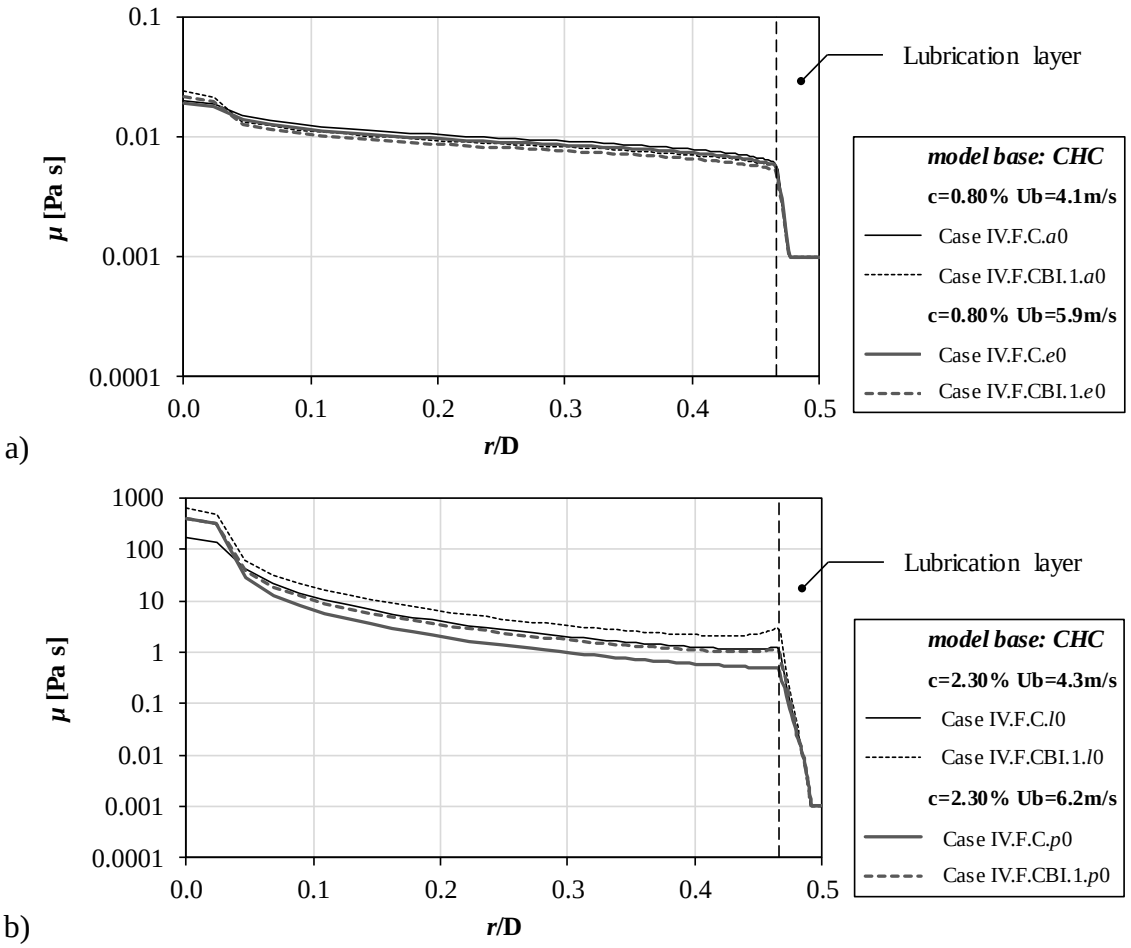

Figure IV.18 – Radial profiles of viscosity, CHC model and new CHC Bartosik I model, for *Pine* pulp: (a) c = 0.80 %, and, (b) c = 2.30 %.

In Figures IV.19 and IV.20 the velocity and non-dimensional velocity profiles (*Eucalyptus* pulp) are presented. As expected, for the lower consistency pulp (i.e. 1.50 %), the flow data to be simulated correspond to a regime where turbulence is more developed than in the higher consistency case (i.e. 2.50 %) where the proximity to transition regime is closer. For these cases, the model predicts only two different regions in the fully turbulent wall layer: *yield* (II) and *core* (III) regions (see Figures IV.20a) and IV.20b)). The thickness of the *core* region is very small as the turbulent regime was better approached experimentally for lower consistency cases. The existence of only two zones in the fully turbulent wall layer was not

observable in the dimensionless velocity profiles presented in the study of Jäsberg (2007) for the *Pine* pulp flow (c = 1 %). There are no dimensionless velocity profiles for the *Birch* pulp flow (c = 2%) presented in Jäsberg (2007). However, it can be presumed from Jäsberg (2007) measurements (*Pine* case) that the trend is to have a fully turbulent wall layer without distinguish *near wall*, *yield* and *core* regions, when flow rate is increased. It should be noted that these conclusions are achieved by looking at Jäsberg (2007) dimensionless velocity data for different pulp type, even if different flow rates from those simulated in the present work are presented and, also, smaller pipe diameter. For the higher consistency case (c = 2.50 %), the three distinct regions: *near wall*, *yield* and *core* were observed (see Figures IV.20c) and IV.20d)). The results for the higher consistency represent well the dimensionless velocity profiles expected from observations of Jäsberg (2007) and, pressure drop values are in good agreement with the experimental data (see pressure drop values in Table IV.30). Moreover, Haavisto *et al.* (2015) presented experimental data, namely velocity profile for the flow of MFC (micro fibrillated cellulose) in a pipe. The authors measured the velocity information using OCT (optical coherent tomography) and UVP techniques. It should be noted that using OCT provided velocity information also in zones very close to the pipe wall. Three distinct regions are observed: *wall layer*, *yielded* region and *plug* flow (Haavisto *et al.*, 2015) which can be assumed to the *near wall*, *yield* and *core* regions (pulp case). Thus even if Haavisto *et al.* (2015) results refer MFC fibers (smaller than pulp fibers) tested in a pipe with smaller diameter, they can be qualitatively compared with the velocity profiles predicted in this work, especially since the experimental data for these systems is very scarce and, as far as author's known, inexistent, so far, for the region very close to the pipe wall. In this way, the velocity profiles for the pulp consistency cases c = 2.50 % (see Figure IV.19b)) are in agreement with the results presented by Haavisto *et al.* (2015). Moreover, the higher velocity variation described in Haavisto *et al.* (2015) occurs in the *wall layer* which agrees with the sudden transition in the velocity profile observed in Figure IV.19b).

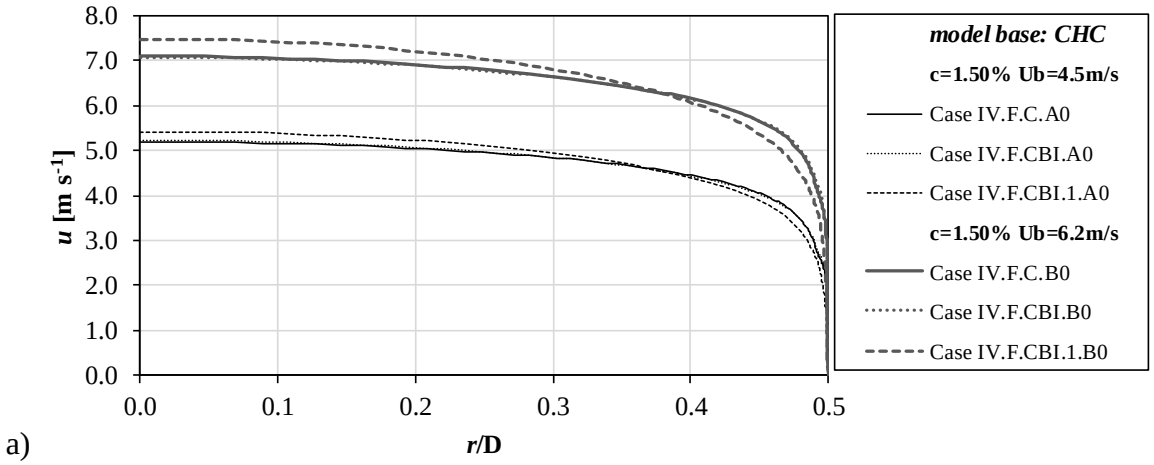

a)

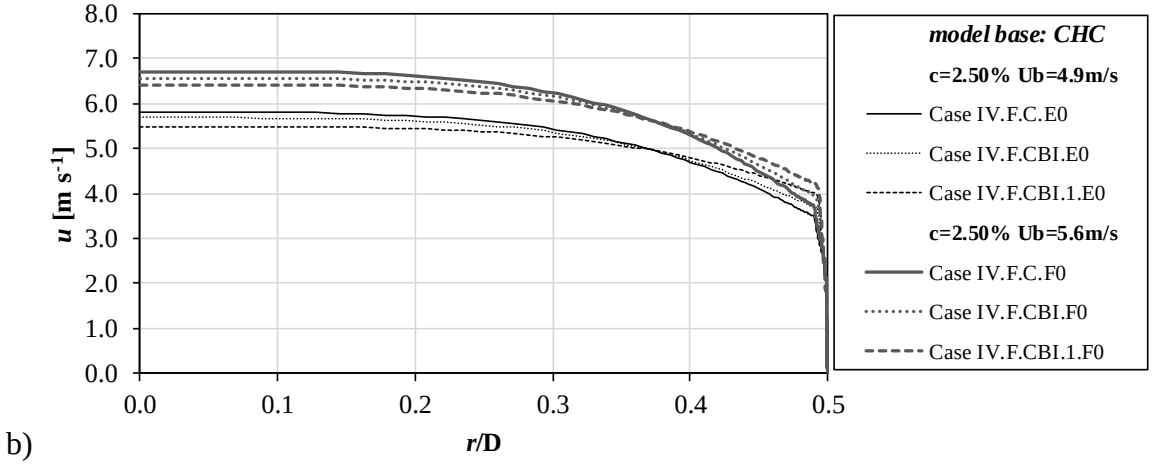

b)

Figure IV.19 – Radial profiles of velocity, CHC model, CHC Bartosik I model and new CHC Bartosik I model, for *Eucalyptus* pulp: (a) c = 1.50 %, and, (b) c = 2.50 %.

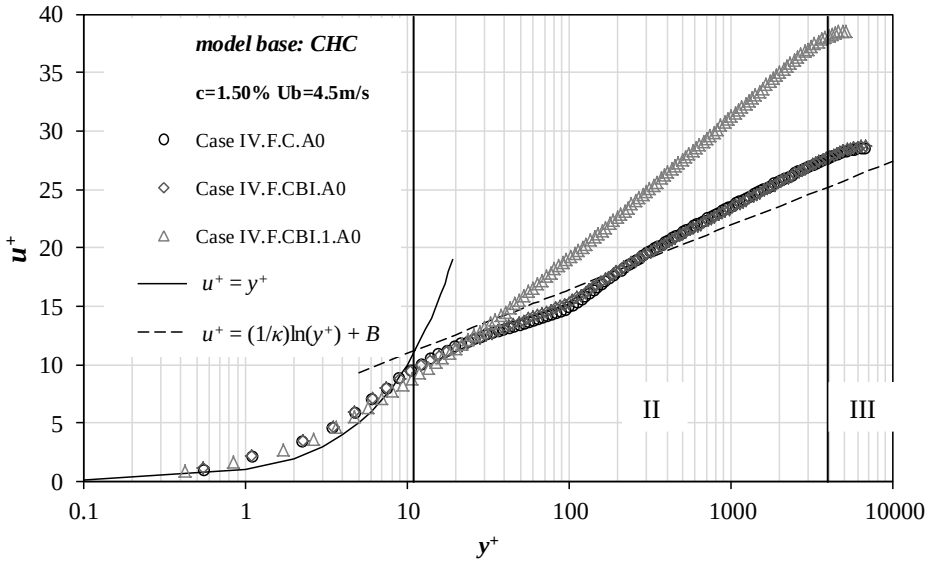

a)

Figure IV.20 – Dimensionless velocity profiles, CHC model, CHC Bartosik I model and new CHC Bartosik I model, for *Eucalyptus* pulp: (a) c = 1.50 % U_b = 4.5 m s^{-1}, (b) c = 1.50 % U_b = 6.2 m s^{-1}, (c) c = 2.50 % U_b = 4.9 m s^{-1}, and, (d) c = 2.50 % U_b = 5.6 m s^{-1}.

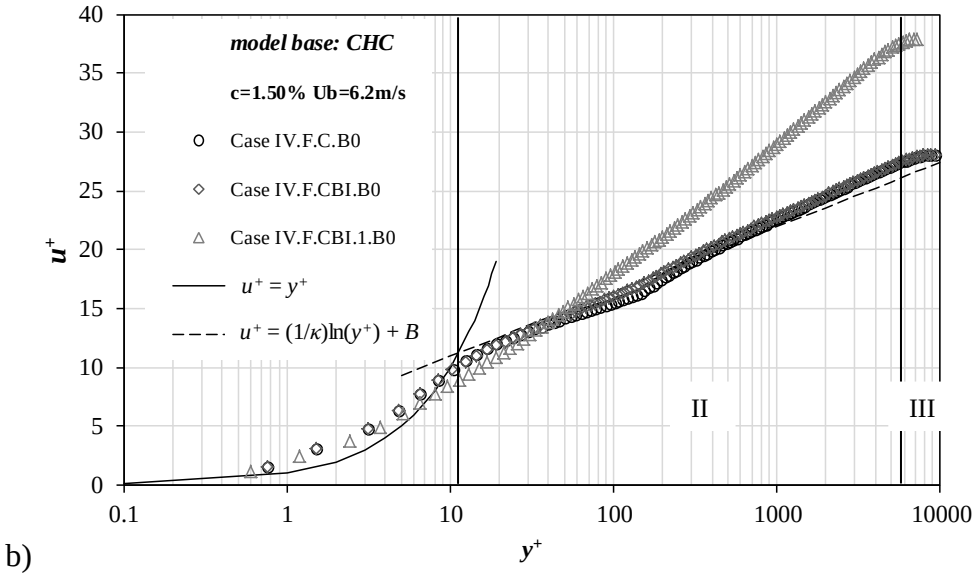

b)

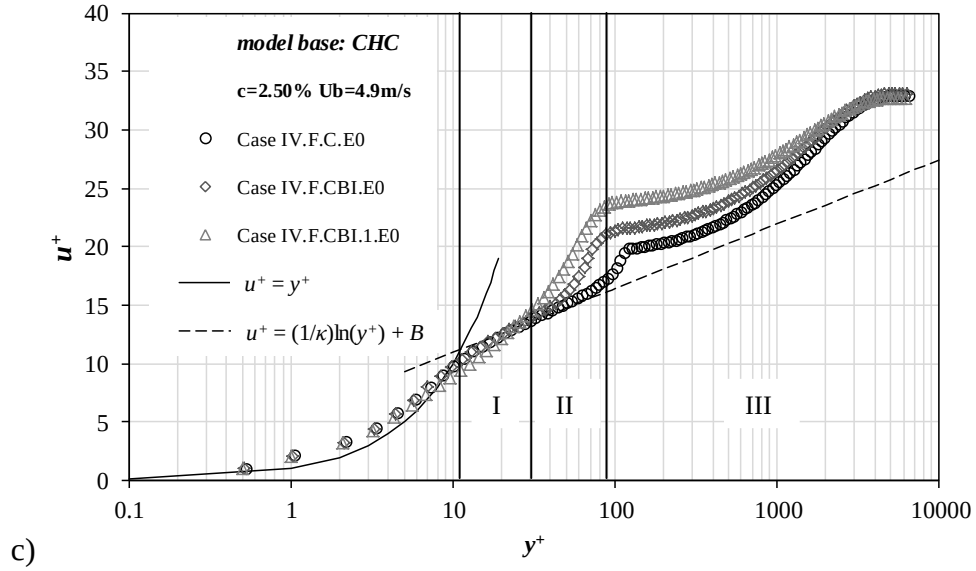

c)

Figure IV.20 – Dimensionless velocity profiles, CHC model, CHC Bartosik I model and new CHC Bartosik I model, for *Eucalyptus* pulp: (a) c = 1.50 % U_b = 4.5 m s^{-1}, (b) c = 1.50 % U_b = 6.2 m s^{-1}, (c) c = 2.50 % U_b = 4.9 m s^{-1}, and, (d) c = 2.50 % U_b = 5.6 m s^{-1} (continued).

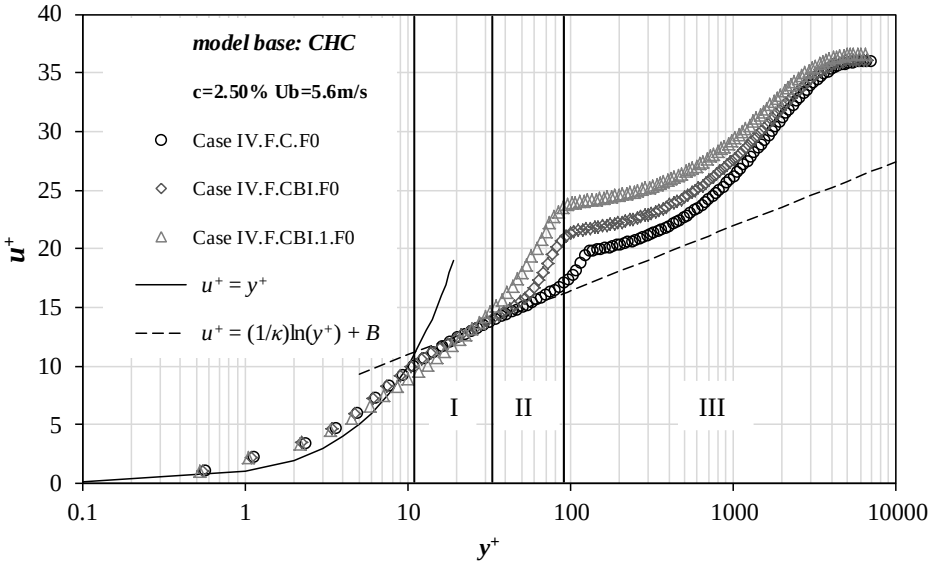

d)

Figure IV.20 – Dimensionless velocity profiles, CHC model, CHC Bartosik I model and new CHC Bartosik I model, for *Eucalyptus* pulp: (a) c = 1.50 % U_b = 4.5 m s^{-1}, (b) c = 1.50 % U_b = 6.2 m s^{-1}, (c) c = 2.50 % U_b = 4.9 m s^{-1}, and, (d) c = 2.50 % U_b = 5.6 m s^{-1} (continued).

Velocity and dimensionless velocity profiles for *Pine* pulp are presented in Figures IV.21 and IV.22. As can be seen from these data, turbulent pulp flow regime was achieved mainly for the cases of the lower consistency pulp (i.e. 0.80 %) where well defined *yield* (II) and *core* (III) regions can be identified (see Figures IV.22a) and IV.22b)). The thickness of the *core* region is very small, corresponding to a better approximation to the turbulent pulp flow regime where the homogeneity of fibers in the flow is high. Also, as in the calculations for the *Eucalyptus* pulp (c = 1.50 %), the velocity profiles are flatter in the flow core region which is in accordance with the expected velocity shape for this consistency and flow conditions (turbulent pulp flow regime). For the higher consistency (i.e. 2.30 %), even if the velocity and dimensionless velocity profiles presented by Jäsberg (2007) are for the *Pine* pulp flow assuming a lower pulp consistency (i.e. 1 %), different mean flow velocities, and smaller pipe diameter, it can be concluded that the CFD model developed in this work is able to reproduce the peculiar S-shaped profile of dimensionless velocity. When comparing with the results of Jäsberg (2007), two main factors should be taken into account: (*i*) the results of Jäsberg (2007) were obtained for a pipe with smaller diameter, and (*ii*) Jäsberg (2007) only presented dimensionless velocity profiles for *Pine* suspension consistency of 1 %, even if different flow rates were tested. In this way, it can be assumed that the velocity and dimensionless velocity profiles, for the higher pulp consistency, are in accordance with those reported in the work of Jäsberg (2007). Moreover, the distinct three regions (*near wall*, *yield* and *core* region) are observed (see Figures IV.22c) and IV.22d)). Also, the approach for the

dimensionless velocity profile described in Chapter III, Section III.3.3.2 (Modified momentum wall functions) and presented in Figure III.8, Jäsberg (2007), is well reproduced for the control cases of *Pine* pulp: $l - c$ = 2.30 % U_b = 4.3 m s^{-1}, and $p - c$ = 2.30 % U_b = 6.2 m s^{-1}. Again, the velocity profiles presented in Figure IV.21b) are in agreement with that reported in Haavisto *et al*. (2015) even if MFC was tested in a pipe with smaller diameter. The high values of relative error obtained for pressure drop values (see Cases IV.F.CBI.1.*l*0 and IV.F.CBI.1.*p*0, Table IV.31) when comparing with the remaining tests (Cases IV.F.CBI.1.) of Table IV.31, can result from the lack of information on the viscosity adjustment for lower shear rate ranges. In this way, the dimensionless velocity profiles indicate a larger *core* region than expected.

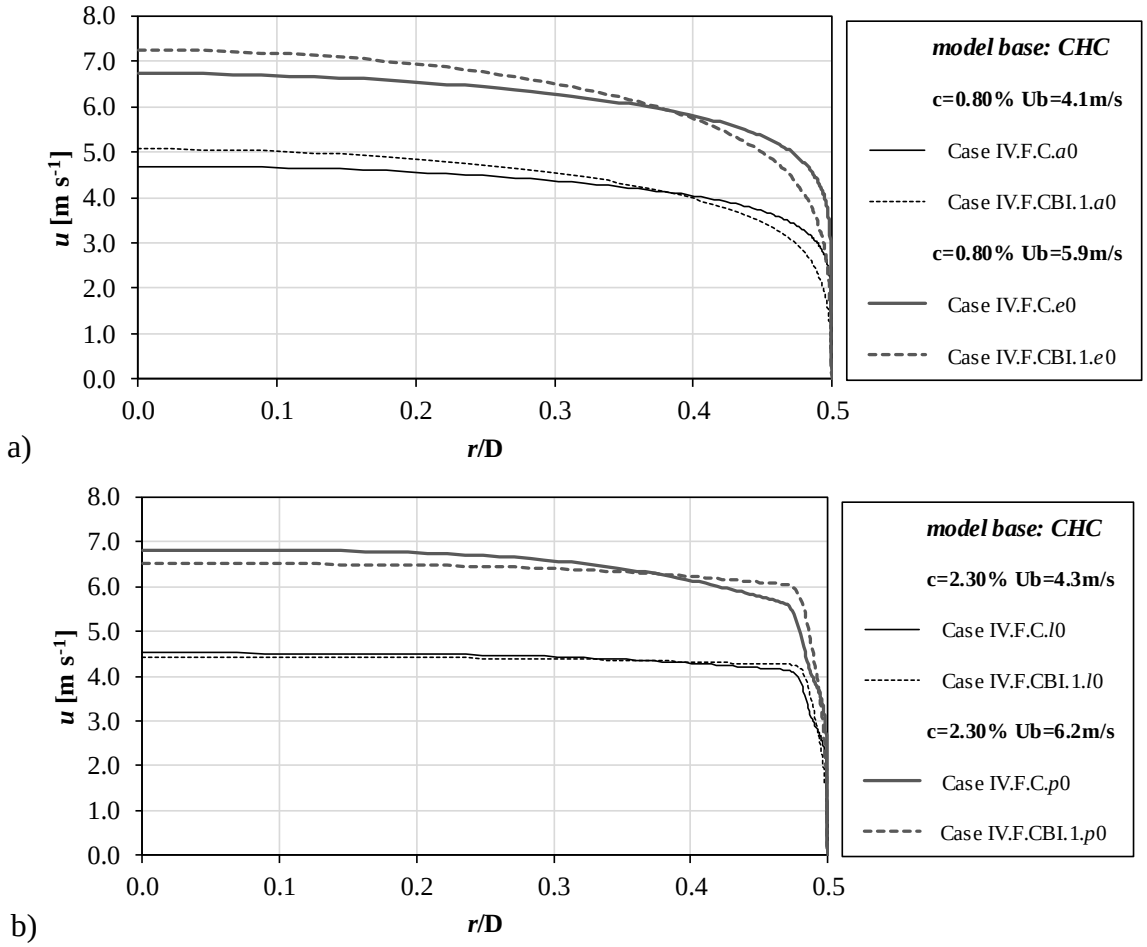

Figure IV.21 – Radial profiles of velocity, CHC model and new CHC Bartosik I model, for *Pine* pulp: (a) c = 0.80 %, and, (b) c = 2.30 %.

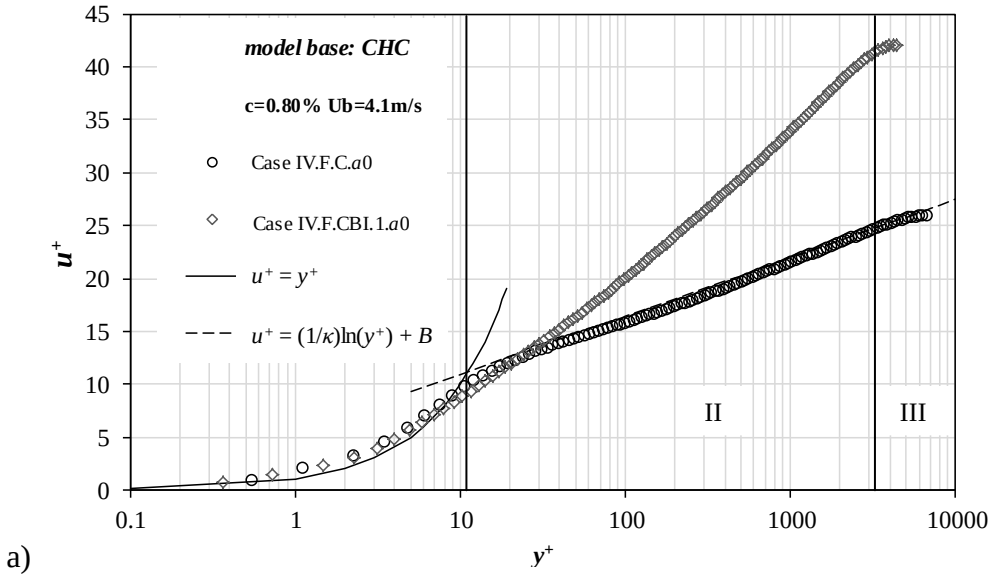

a)

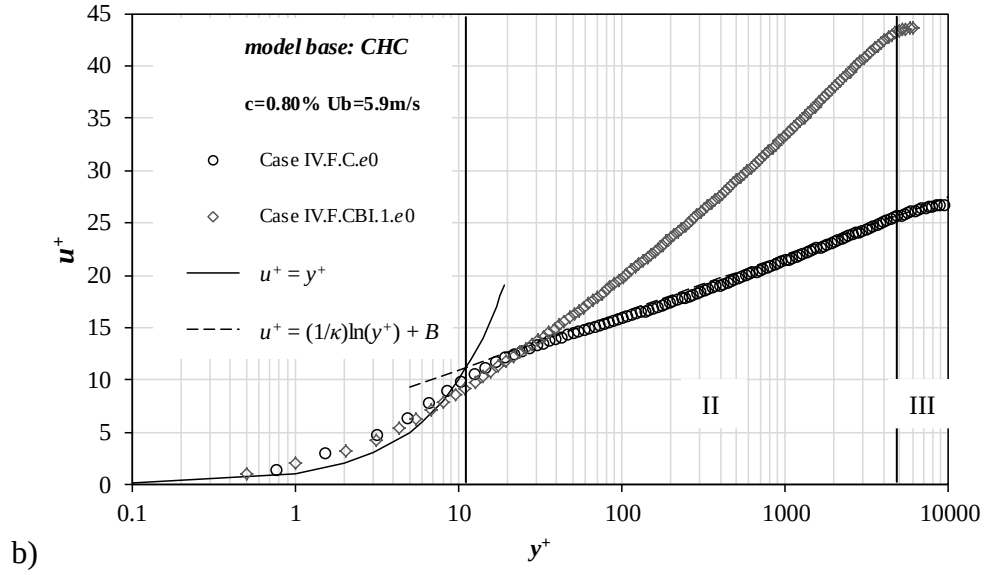

b)

Figure IV.22 – Dimensionless velocity profiles, CHC model and new CHC Bartosik I model, for *Pine* pulp: (a) c = 0.80 % U_b = 4.1 m s^{-1}, (b) c = 0.80 % U_b = 5.9 m s^{-1}, (c) c = 2.30 % U_b = 4.3 m s^{-1}, and, (d) c = 2.30 % U_b = 6.2 m s^{-1}.

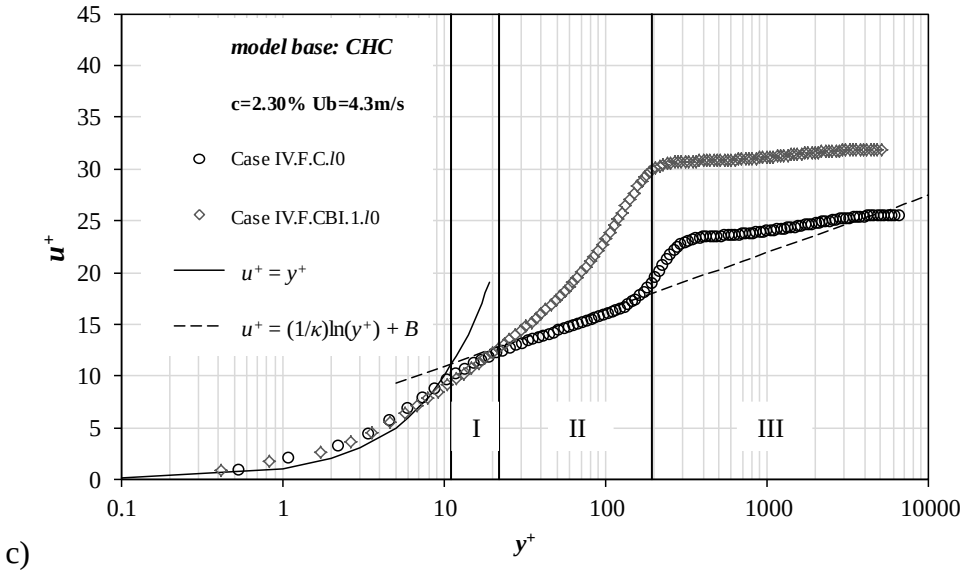

c)

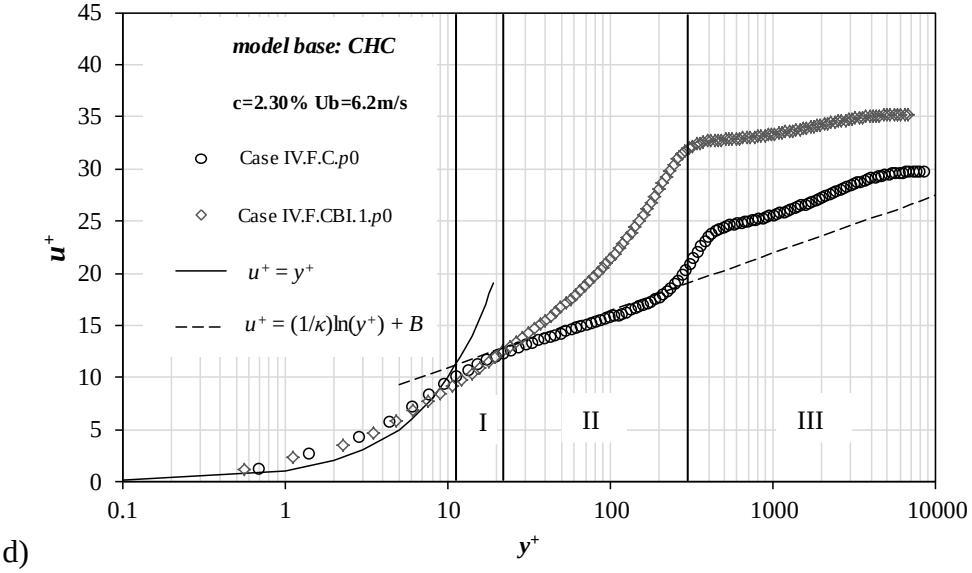

d)

Figure IV.22 – Dimensionless velocity profiles, CHC model and new CHC Bartosik I model, for *Pine* pulp: (a) c = 0.80 % U_b = 4.1 m s^{-1}, (b) c = 0.80 % U_b = 5.9 m s^{-1}, (c) c = 2.30 % U_b = 4.3 m s^{-1}, and, (d) c = 2.30 % U_b = 6.2 m s^{-1} (continued).

Turbulent kinetic energy and its dissipation rate are presented in Figures IV.23 and IV.24 (*Eucalyptus* pulp). The turbulent kinetic energy is increased in the near wall region whereas its dissipation is diminished. Mainly, for the higher consistency case (c = 2.50 %) the variations near the pipe wall are observed to be confined to a region closer to the wall when applying the new CFD model.

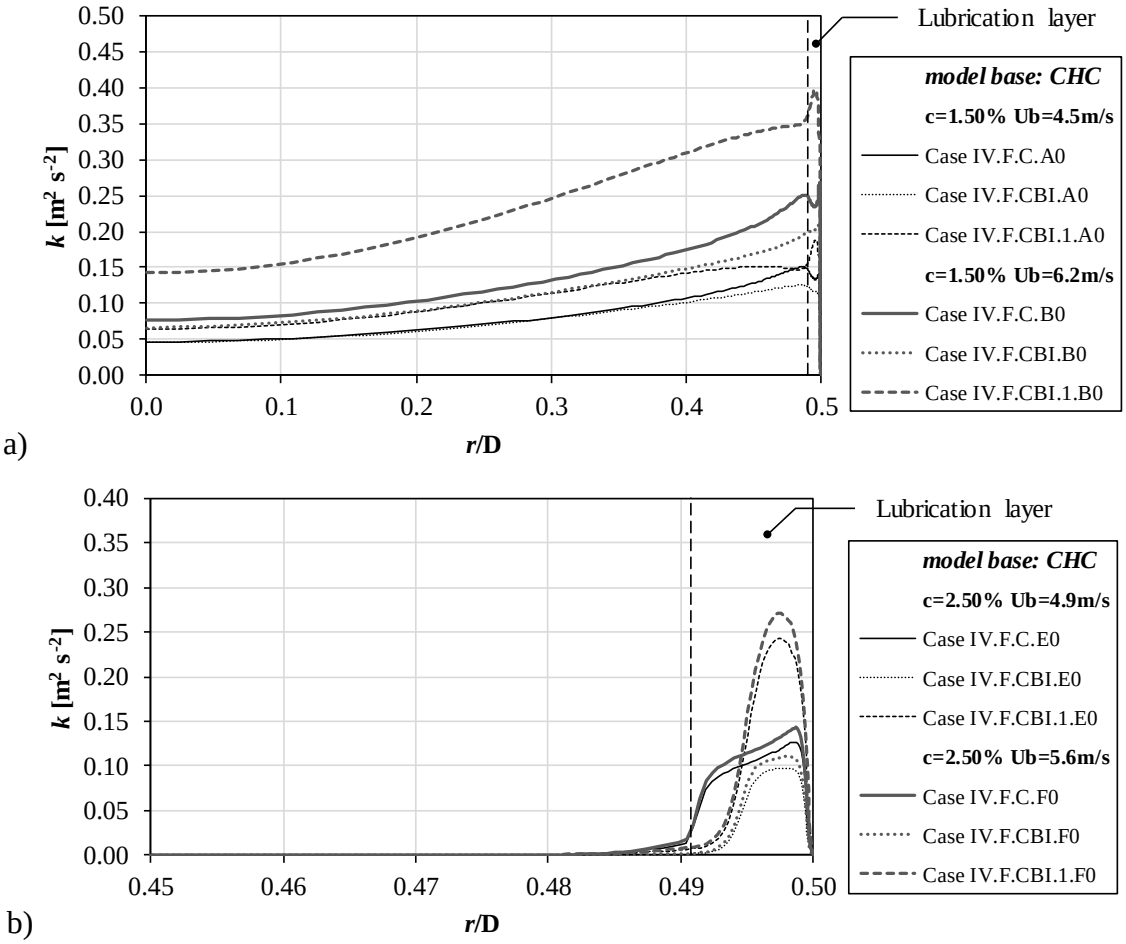

Figure IV.23 – Radial profiles of turbulent kinetic energy, CHC model, CHC Bartosik I model and new CHC Bartosik I model, for *Eucalyptus* pulp: (a) c = 1.50 %, and, (b) c = 2.50 %.

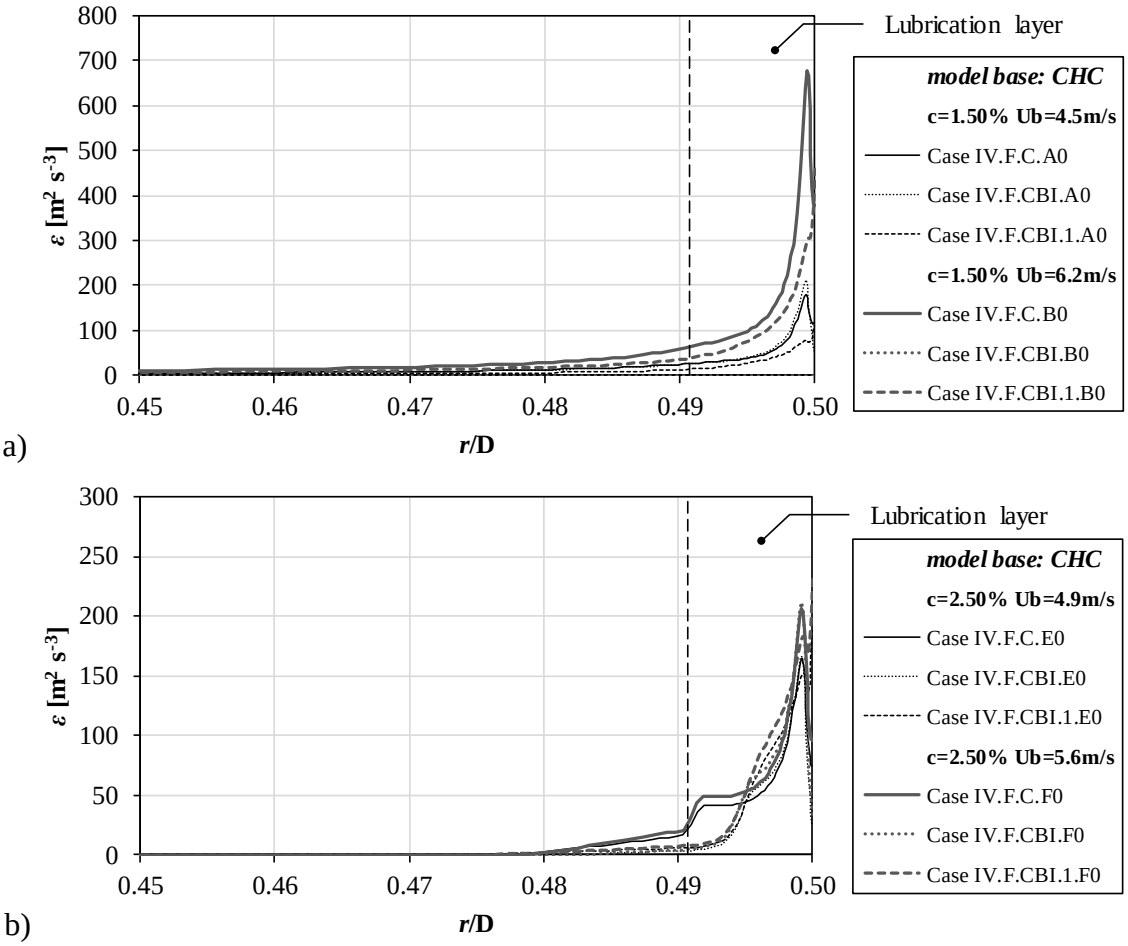

Figure IV.24 – Radial profiles of dissipation rate of turbulent kinetic energy, CHC model, CHC Bartosik I model and new CHC Bartosik I model, for *Eucalyptus* pulp: (a) c = 1.50 %, and, (b) c = 2.50 %.

In Figures IV.25 and IV.26 the turbulent kinetic energy and its dissipation rate for *Pine* pulp are shown. For the *Pine* pulp suspension as well for the *Eucalyptus* pulp suspension, the larger variations of turbulent kinetic energy and its dissipation rate are closer to pipe wall where only the presence of less fibers is assumed. In that region turbulent quantities are not as dampened as observed in the flow core due to the presence of a turbulent lubrication layer. Also, the new Bartosik I damping function lead to lower values of dissipation rate of turbulent kinetic energy even in the near wall region.

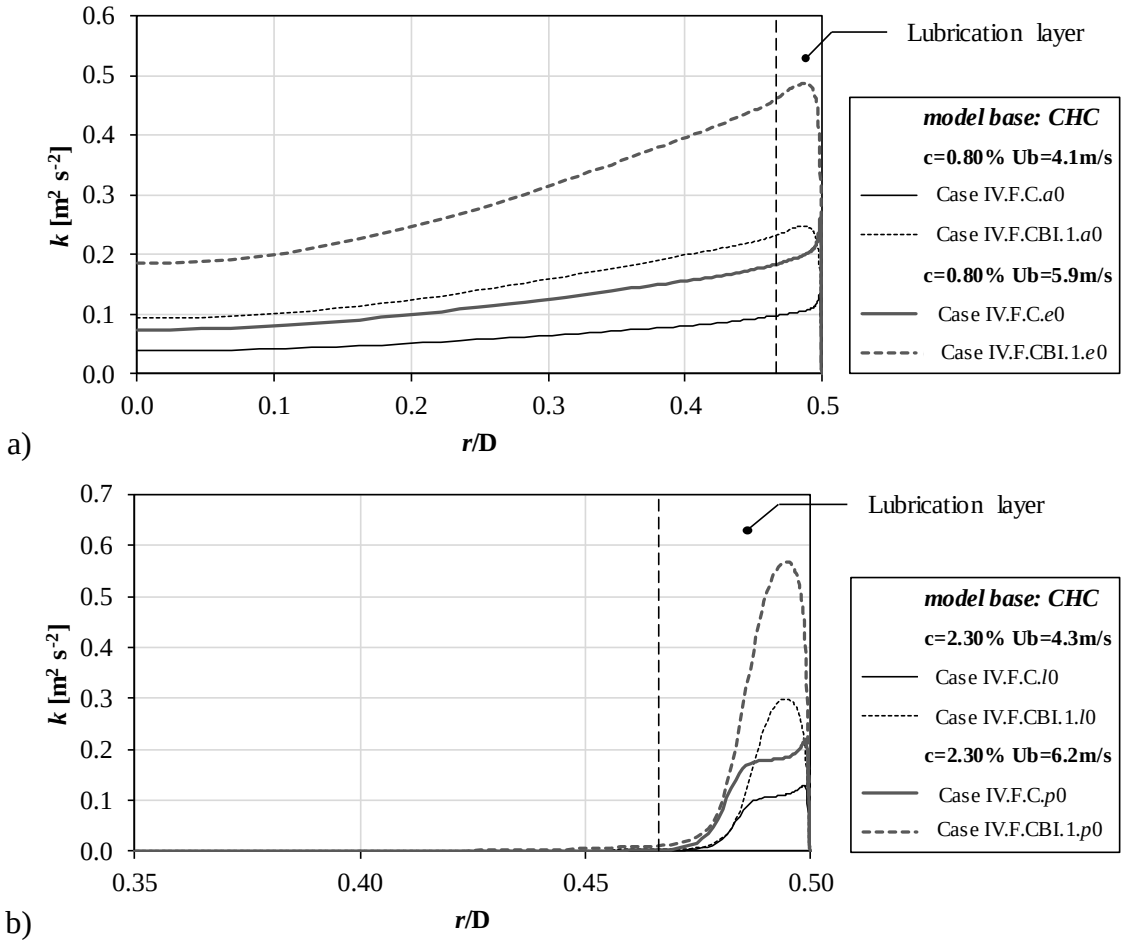

Figure IV.25 – Radial profiles of turbulent kinetic energy, CHC model and new CHC Bartosik I model, for *Pine* pulp: (a) c = 0.80 %, and, (b) c = 2.30 %.

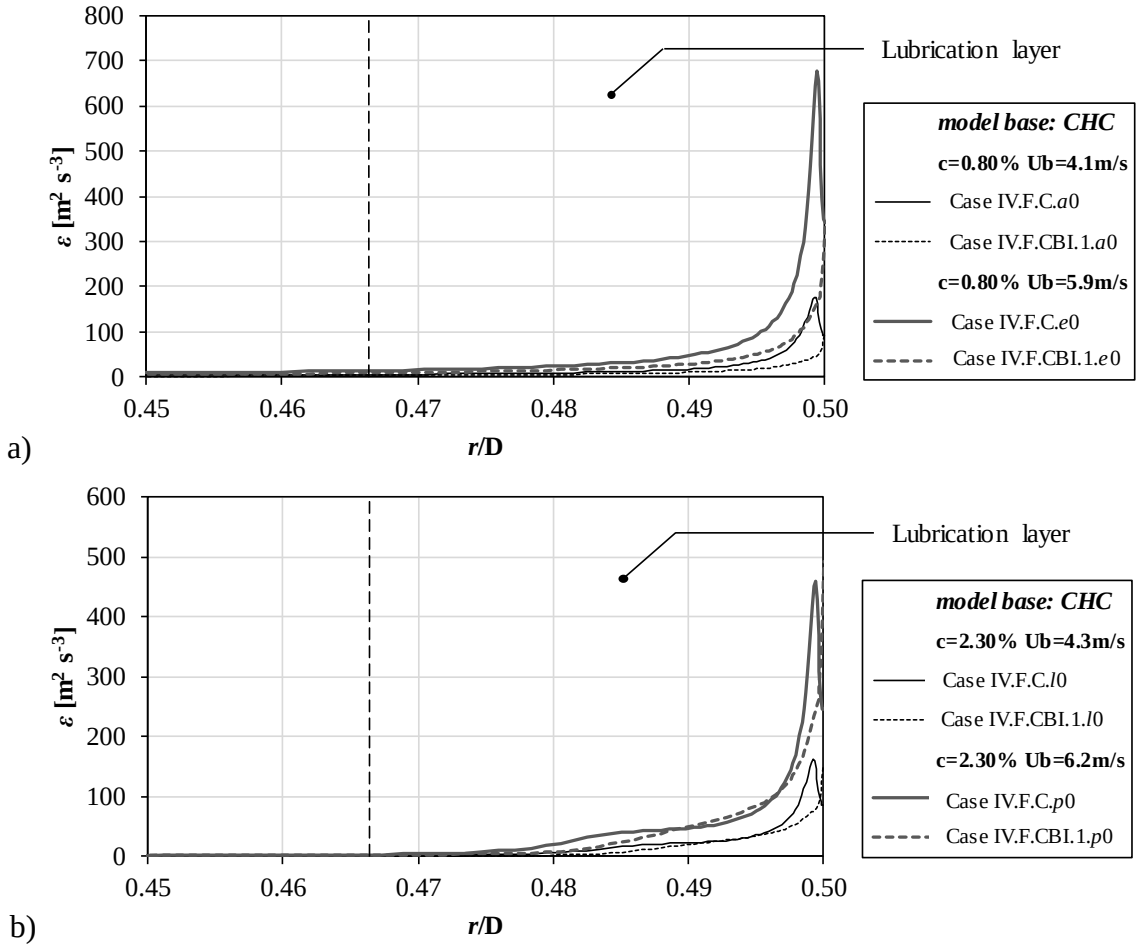

Figure IV.26 – Radial profiles of dissipation rate of turbulent kinetic energy, CHC model and new CHC Bartosik I model, for *Pine* pulp: (a) c = 0.80 %, and, (b) c = 2.30 %.

Root mean square (RSM) velocity can be used to investigate turbulence. Claesson *et al.* (2012) have presented an experimental study where the authors investigated velocity profiles and RMS profiles obtained from experimental measurements using LDA technique for the flow of bleached softwood *kraft* pulp in a channel. In order to infer qualitatively the trends of turbulence obtained from simulations, it was decided to calculate also RMS profiles. The RMS velocity was calculated by (Mandø *et al.*, 2009):

$$u_{RMS} = \sqrt{\frac{2}{3}k} \tag{IV.16}$$

The RMS velocity profiles for *Eucalyptus* pulp are shown in Figure IV.27. Obviously the same trend of the turbulent kinetic energy is observed for RMS velocity results. The results obtained through numerical simulations are in agreement with those reported by Claesson *et al.* (2012) even if pulp flow was evaluated for a different configuration. Root mean square velocities tend to increase towards the pipe wall with high values being

observable along the *r* coordinate for lower consistency cases with even higher values near the wall. The presence of fibers damps turbulence and for higher consistency, this dampening effect is stronger as a consequence of a stronger network of fibers that can be formed. Turbulence is attenuated which is reflected in turbulent kinetic energy and RMS velocity profiles corresponding to lower values with increasing pulp consistency, especially in the central region of the pipe cross section where fiber structures are stronger. Also, the shape of the RMS velocity near the pipe wall, where higher variations occurs, is in agreement with that reported in Claesson *et al.* (2012).

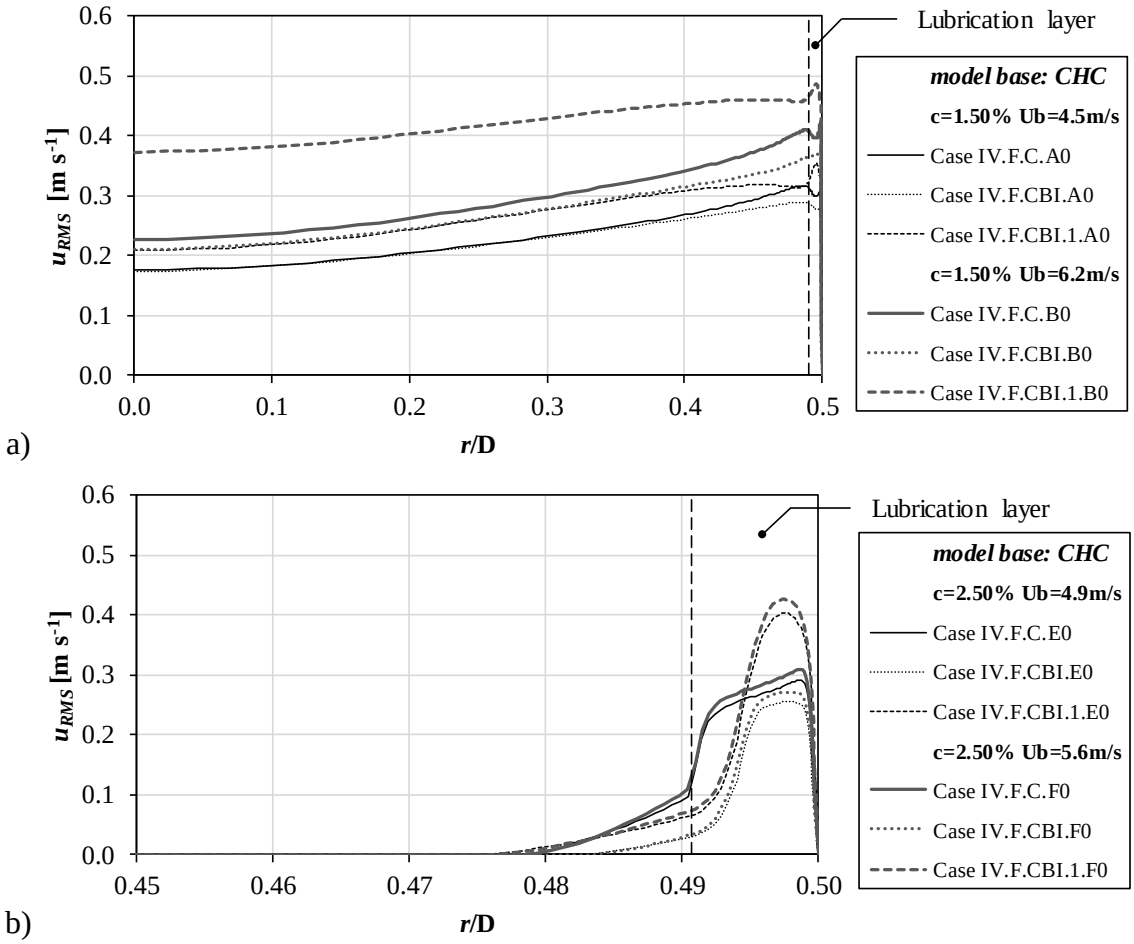

Figure IV.27 – Radial profiles of u_{RMS}, CHC model, CHC Bartosik I model and new CHC Bartosik I model, for *Eucalyptus* pulp: (a) c = 1.50 %, and, (b) c = 2.50 %.

Figure IV.28 shows the RMS velocity profiles for *Pine* pulp. The calculations are in accordance with the observations for *Eucalyptus* pulp (see Figure IV.27). RMS velocity tends to decrease towards the pipe centre. Also, high values are predicted for the lower consistency cases (i.e. 0.80 %). Turbulence is dampened due to the presence of fibers in the flow as discussed for the *Eucalyptus* pulp. In this way, higher values of turbulent quantities and RMS

velocity are obtained with decreasing pulp consistency, especially in the central zone of the pipe. Again, the RMS velocity profiles are in accordance with those profiles described in Claesson *et al.* (2012) even if a different configuration was evaluated.

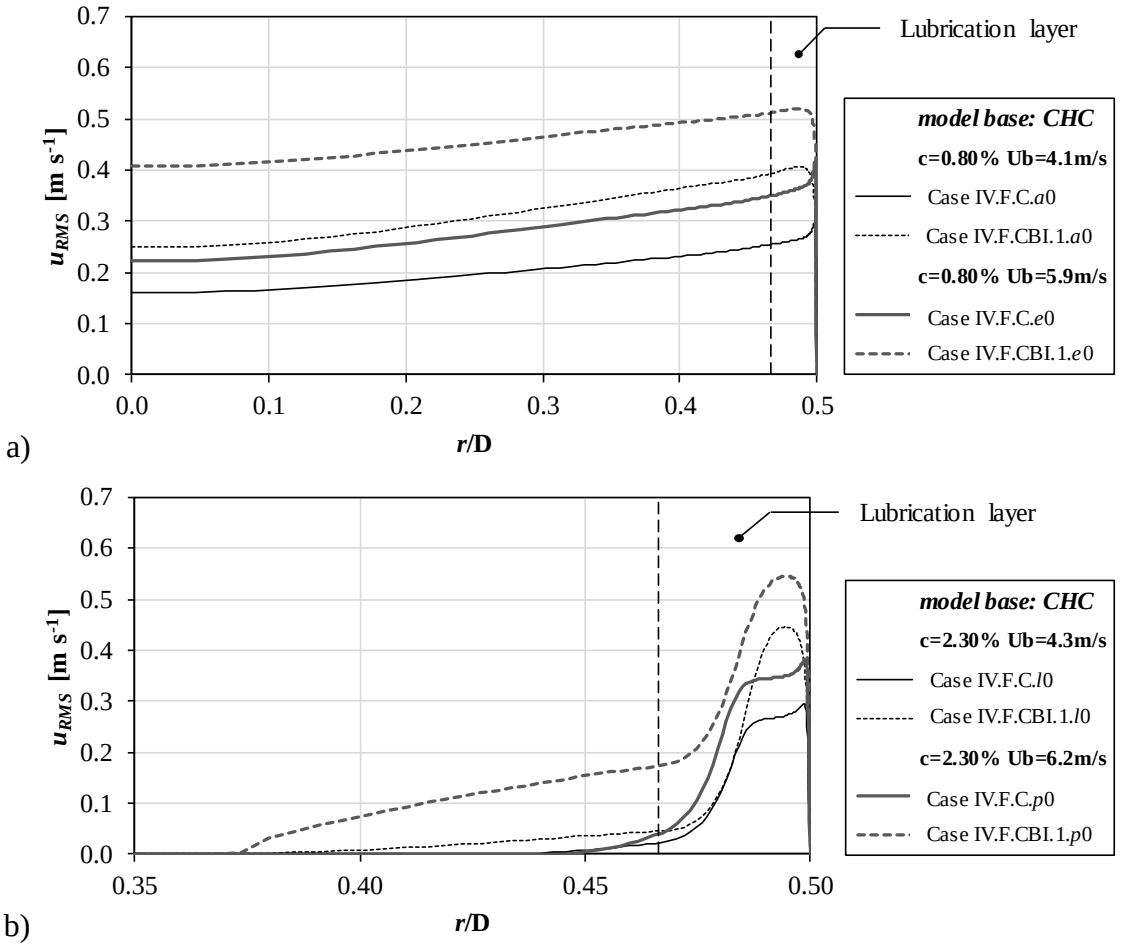

Figure IV.28 – Radial profiles of u_{RMS}, CHC model and new CHC Bartosik I model, for *Pine* pulp: (a) c = 0.80%, and, (b) c = 2.30 %.

In order to understand the effect of the additional term $r^{1/4}$ on the Bartosik I damping function, as well as the effect on the calculations of modifying the standard CHC model with the standard Bartosik I damping function, the profiles of f_μ along the pipe radius were compared for *Eucalyptus* pulp (see Figure IV.29) and *Pine* pulp (see Figure IV.30). Additionally, turbulent Reynolds number, Re_t, and turbulent viscosity are presented in Figures IV.31 and IV.33 (*Eucalyptus* pulp), and Figures IV.32 and IV.34 (*Pine* pulp).

From Figure IV.29 it can be seen that the inclusion of fiber aspect-ratio in the damping function of Bartosik (2010, 2011b) leads to its decrease. This decrease was expected since the inclusion of fibers in the flow leads to higher *drag reduction* effect than when considering the presence of spherical particles. For turbulent flow of Newtonian fluids it is reported for

example in Patel *et al.* (1984) that f_μ varies from 0 at the wall, to 1 at $60 < y^+ < 300$, depending on the LRN *k-ε* turbulence model. For the CHC model and CHC Bartosik I model, that trend is observable albeit a sudden transition is noticeable at the interface between lubrication layer and flow core region. The drop in the damping function at the pipe centre, for the standard CHC model and when using the Bartosik I damping function, is due to high variations of molecular viscosity observed in that region. For the higher consistency cases, the *drag reduction* effect is greater and lower values of the damping function are predicted.

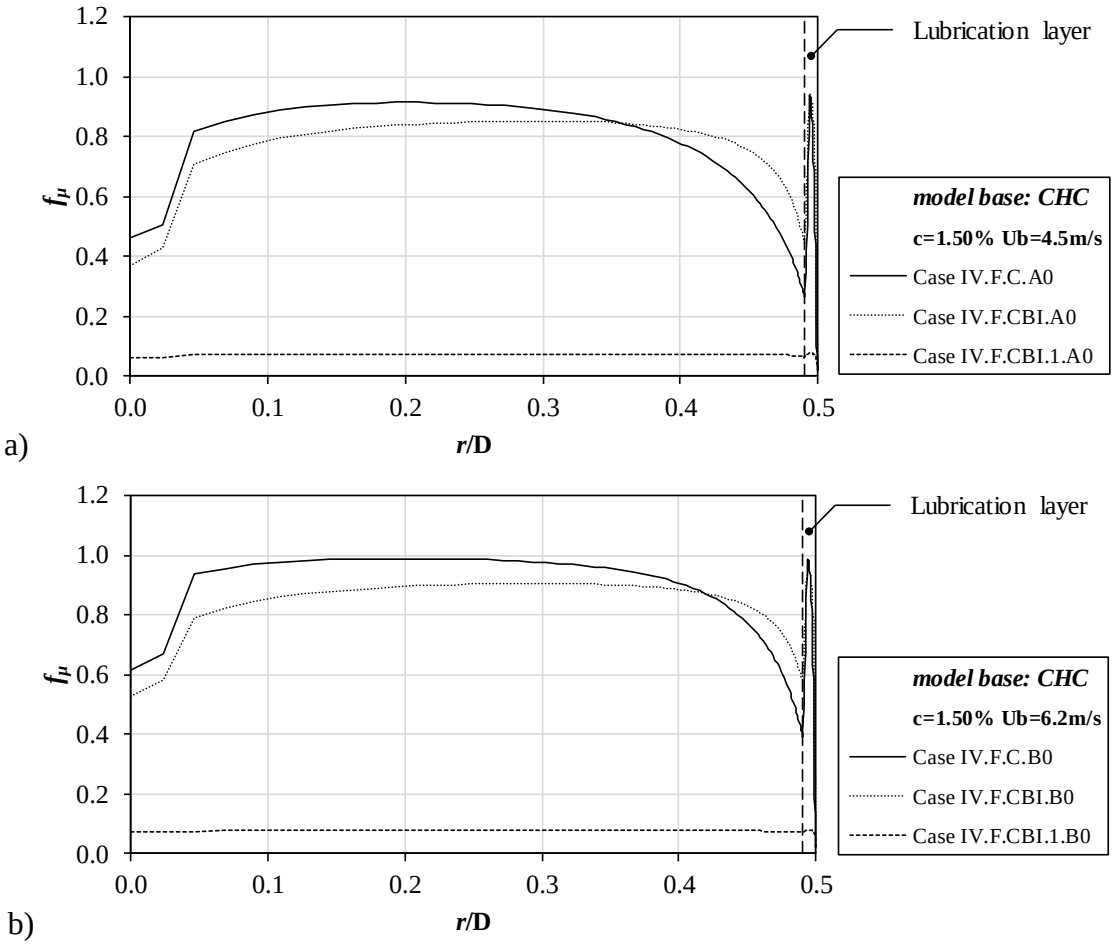

Figure IV.29 – Variation of the damping function f_μ, CHC model, CHC Bartosik I model and new CHC Bartosik I model, for *Eucalyptus* pulp: (a) c = 1.50 % U_b = 4.5 m s^{-1}, (b) c = 1.50 % U_b = 6.2 m s^{-1}, (c) c = 2.50 % U_b = 4.9 m s^{-1}, and, (d) c = 2.50 % U_b = 5.6 m s^{-1}.

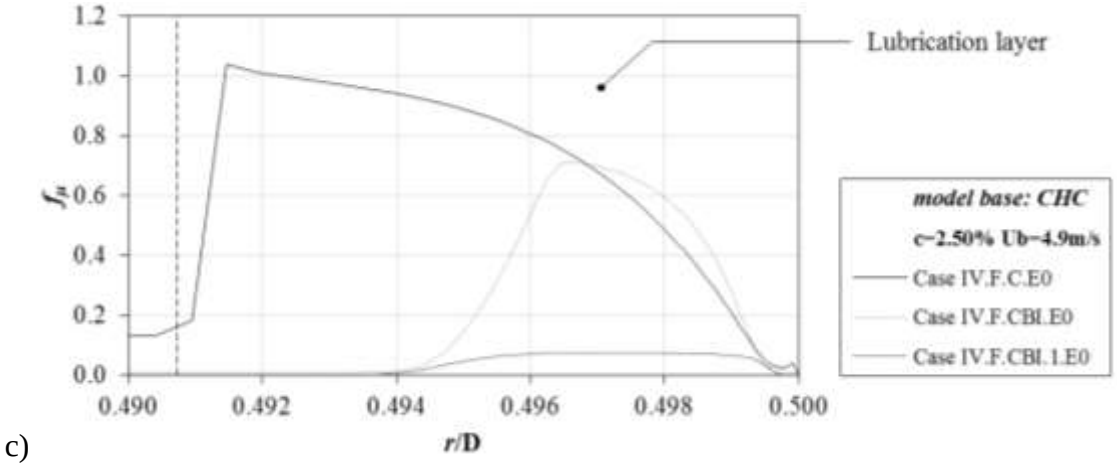

c)

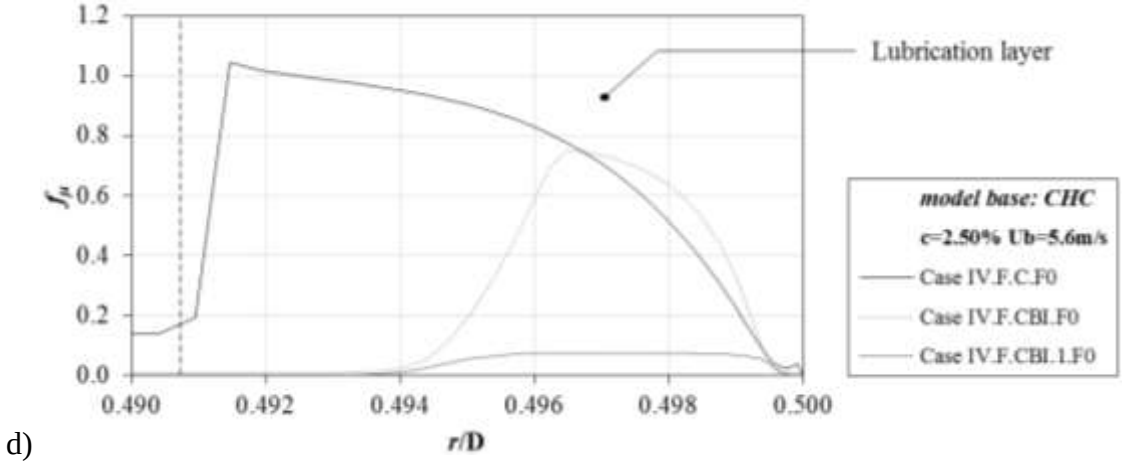

d)

Figure IV.29 – Variation of the damping function f_μ, CHC model, CHC Bartosik I model and new CHC Bartosik I model, for *Eucalyptus* pulp: (a) c = 1.50 % U_b = 4.5 m s^{-1}, (b) c = 1.50 % U_b = 6.2 m s^{-1}, (c) c = 2.50 % U_b = 4.9 m s^{-1}, and, (d) c = 2.50 % U_b = 5.6 m s^{-1} (continued).

In Figure IV.30 the profiles of f_μ for the control cases of *Pine* pulp suspension are presented. The same trend observed for *Eucalyptus* pulp suspension is detected for *Pine* pulp suspension. For the lower consistency cases (see Figures IV.30a) and IV.30b)), the profile of f_μ for the standard CHC turbulence model is in accordance with the expected for the flow of a Newtonian fluid as reported for example in Patel *et al.* (1984). The slight drop on f_μ observed near the pipe wall is due to the interface between lubrication layer and flow core. As expected, the increase of mean flow velocity leads to increase of turbulence with pulp flow showing a fluid-like behaviour. In this way, the homogeneity of pulp is higher, and also as observed in Figure IV.21a) the velocity profile is flatter, without pronounced transition between lubrication layer and flow core, contrary to what happens for the higher pulp consistency cases (i.e. 2.30 %). However, the presence of fibers in the flow leads to turbulence attenuation which is predicted when fiber aspect-ratio is included in the damping function. The inclusion of fiber aspect-ratio in the damping function is even more important in

the case of the flow of *Pine* suspensions, since *Pine* fibers are longer than the *Eucalyptus* fibers. The turbulence is more attenuated in the flow of *Pine* suspension and thus, to assume only in the model the influence of viscosity, through the different adjustment parameters, *K'*, α and β in Equation (IV.1), is not sufficient to reproduce the experimental data.

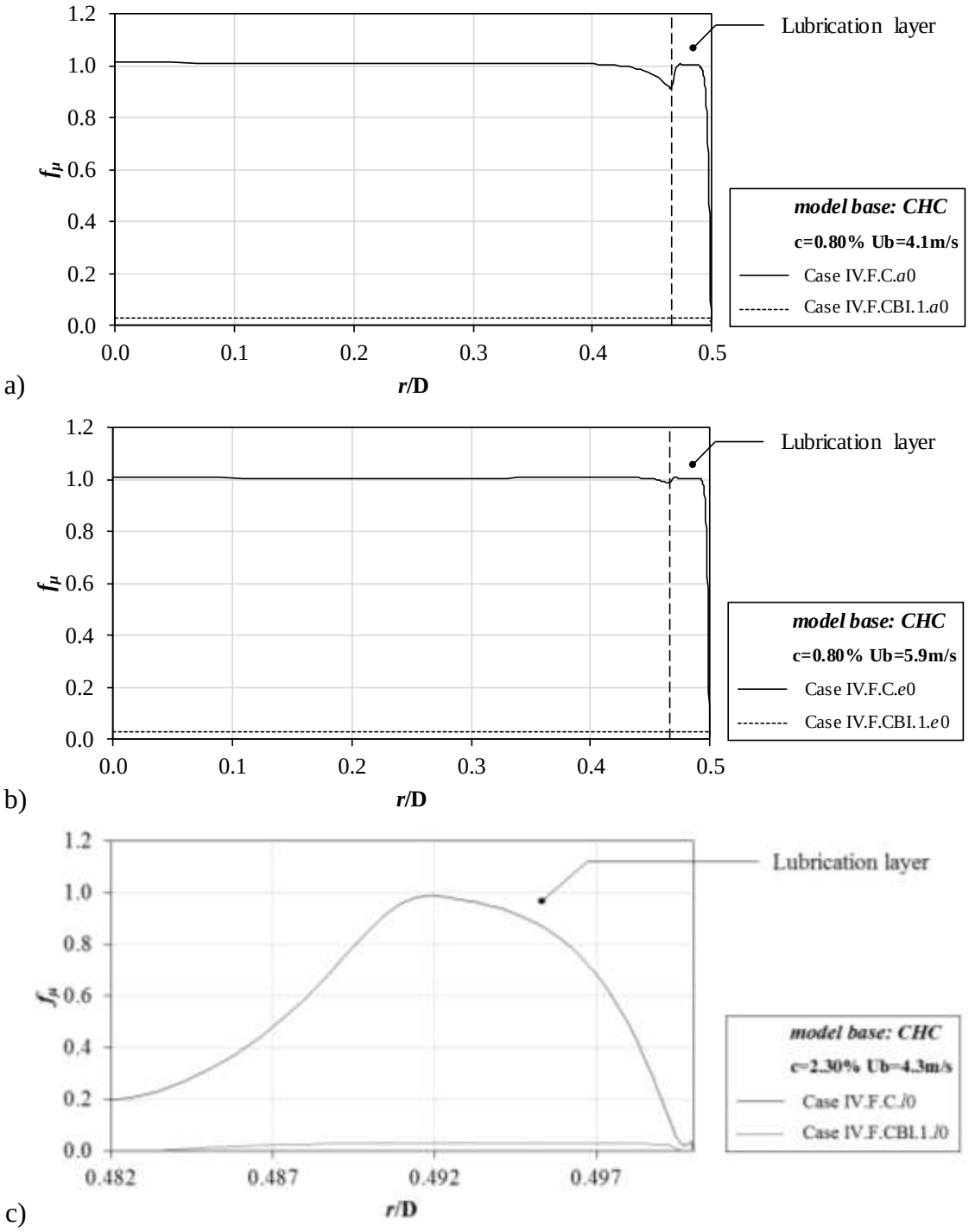

Figure IV.30 – Variation of the damping function f_μ, CHC model and new CHC Bartosik I model, for *Pine* pulp: (a) c = 0.80 % U_b = 4.1 m s^{-1}, (b) c = 0.80 % U_b = 5.9 m s^{-1}, (c) c = 2.30 % U_b = 4.3 m s^{-1}, and, (d) c = 2.30 % U_b = 6.2 m s^{-1}.

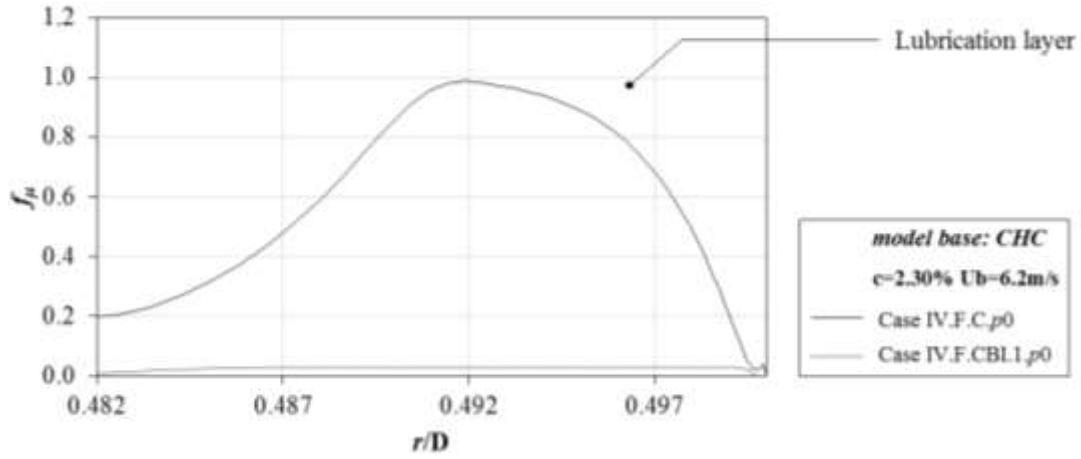

d)

Figure IV.30 – Variation of the damping function f_μ, CHC model and new CHC Bartosik I model, for *Pine* pulp: (a) c = 0.80 % U_b = 4.1 m s^{-1}, (b) c = 0.80 % U_b = 5.9 m s^{-1}, (c) c = 2.30 % U_b = 4.3 m s^{-1}, and, (d) c = 2.30 % U_b = 6.2 m s^{-1} (continued).

As can be seen from Figure IV.31 (*Eucalyptus* pulp), larger variations of turbulent Reynolds number are observable near the pipe wall, where fiber consistency is lower and turbulent quantities are higher. For the higher consistency cases (c = 2.50 %), the strongest non-Newtonian behaviour of pulp is a predominant factor leading to lower turbulent Reynolds number in the flow core region.

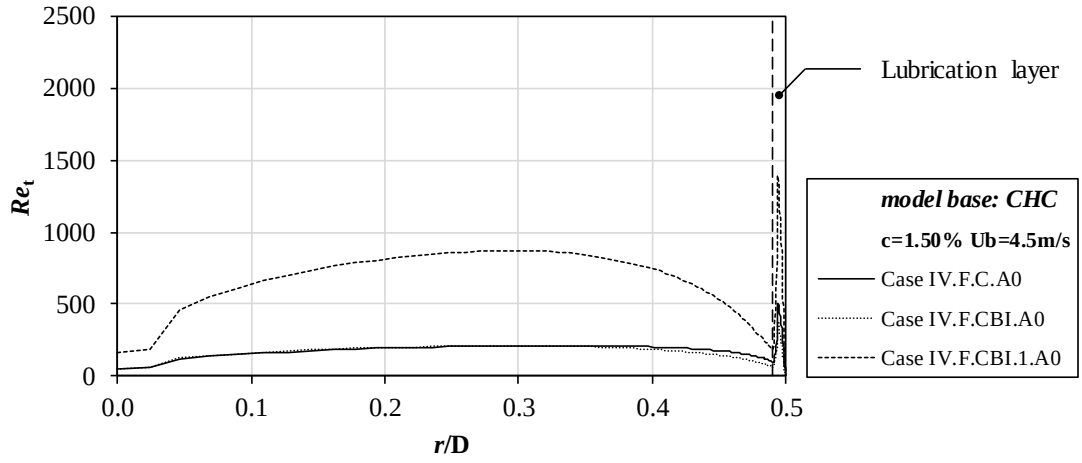

a)

Figure IV.31 – Variation of the turbulent Reynolds number Re_t, CHC model, CHC Bartosik I model and new CHC Bartosik I model, for *Eucalyptus* pulp: (a) (a) c = 1.50 % U_b = 4.5 m s^{-1}, (b) c = 1.50 % U_b = 6.2 m s^{-1}, (c) c = 2.50 % U_b = 4.9 m s^{-1}, and, (d) c = 2.50 % U_b = 5.6 m s^{-1}.

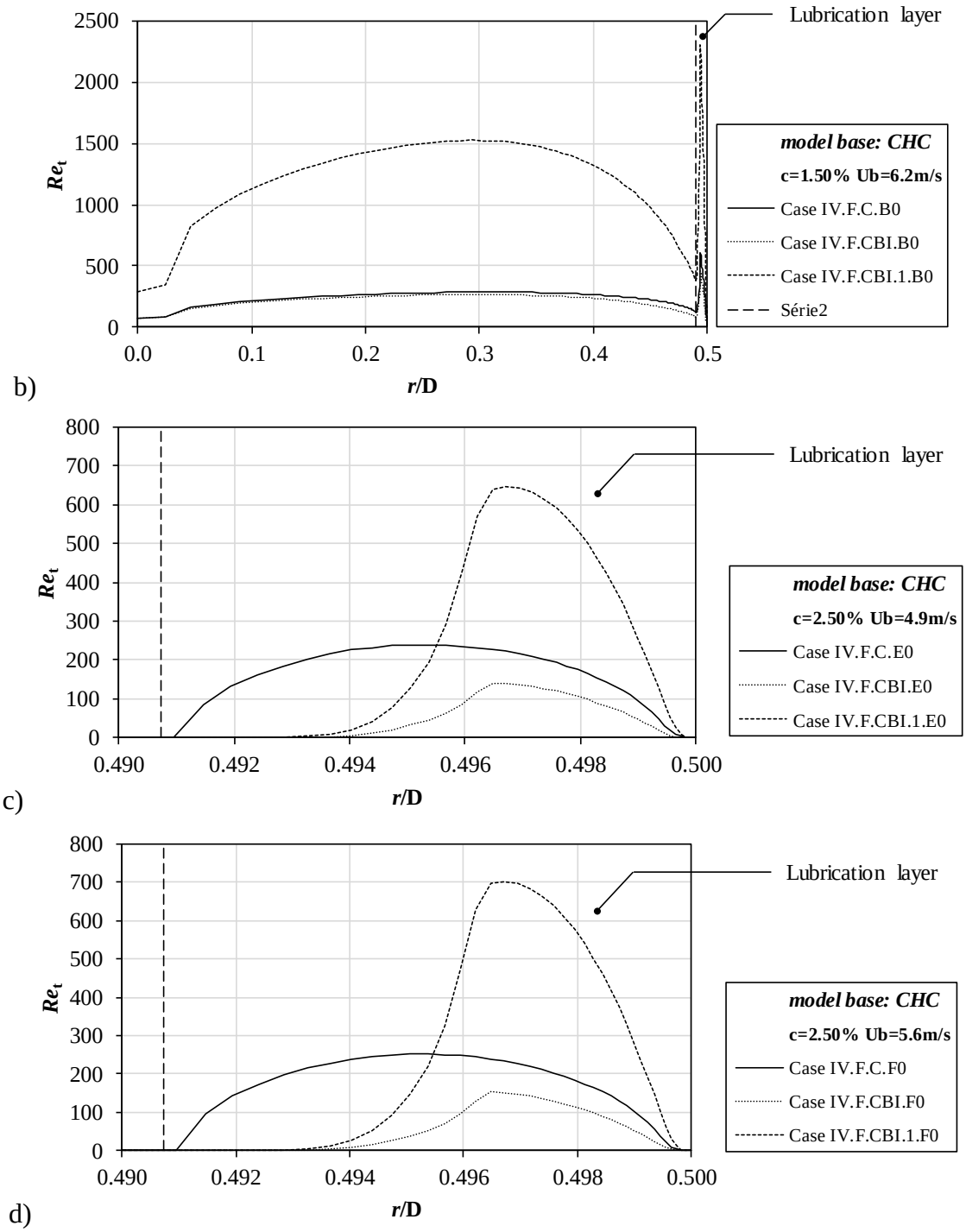

Figure IV.31 – Variation of the turbulent Reynolds number Re_t, CHC model, CHC Bartosik I model and new CHC Bartosik I model, for *Eucalyptus* pulp: (a) (a) c = 1.50 % U_b = 4.5 m s^{-1}, (b) c = 1.50 % U_b = 6.2 m s^{-1}, (c) c = 2.50 % U_b = 4.9 m s^{-1}, and, (d) c = 2.50 % U_b = 5.6 m s^{-1} (continued).

Figure IV.32 shows the radial variation of turbulent Reynolds number for *Pine* pulp. As observed for the *Eucalyptus* pulp case (see Figure IV.31), higher variations of Re_t occur near the pipe wall where less fiber is present and turbulent lubrication layer is better approached. For the lower pulp consistency (i.e. 0.80 %), the higher values of turbulent Reynolds number

are in agreement with lower turbulence attenuation (less pronounced non-Newtonian behaviour) where turbulence is not as dampened as for the higher consistency case (*c* = 2.30%).

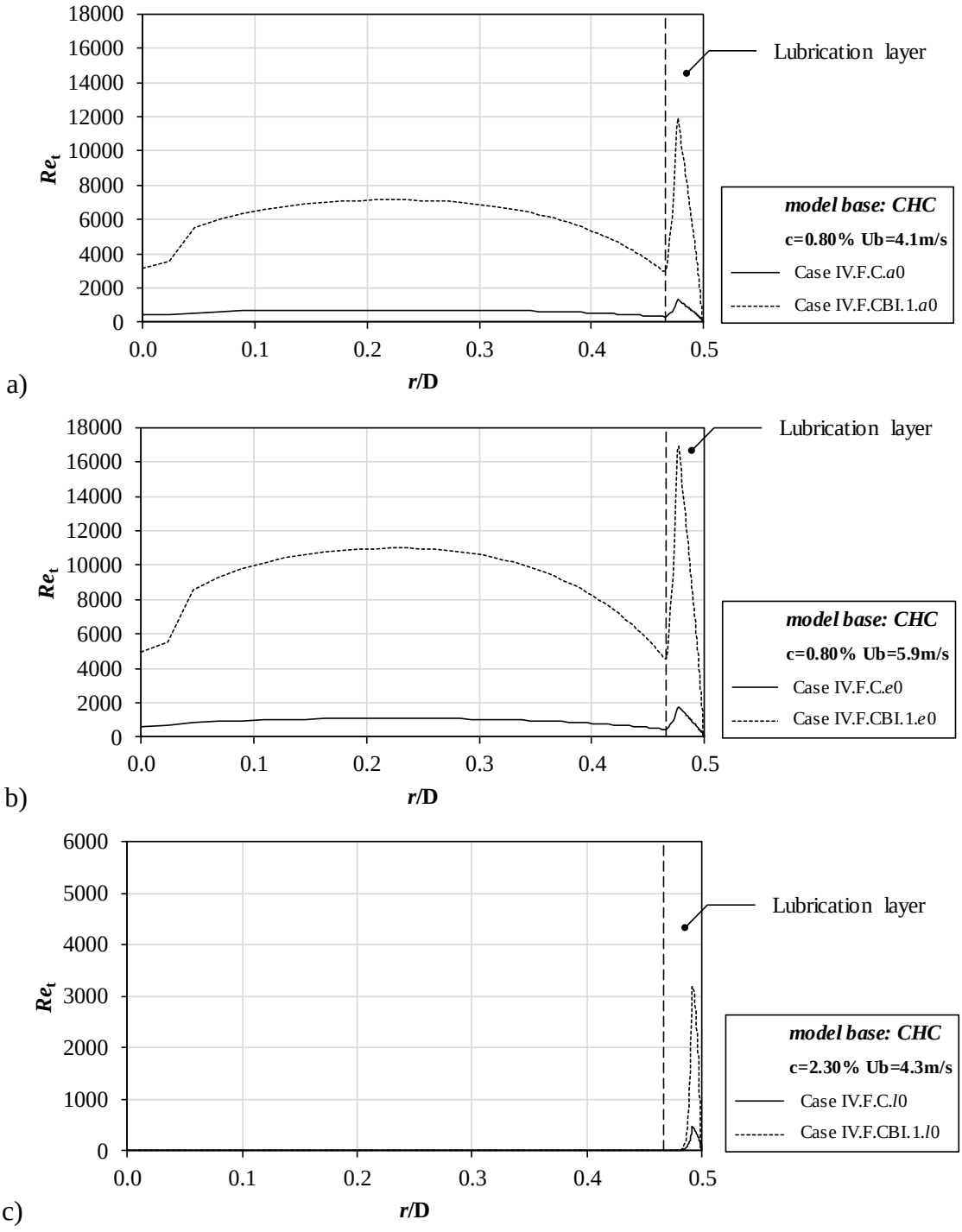

Figure IV.32 – Variation of the turbulent Reynolds number Re_t, CHC model and new CHC Bartosik I model, for *Pine* pulp: (a) c = 0.80 % U_b = 4.1 m s^{-1}, (b) c = 0.80 % U_b = 5.9 m s^{-1}, (c) c = 2.30 % U_b = 4.3 m s^{-1}, and, (d) c = 2.30 % U_b = 6.2 m s^{-1}.

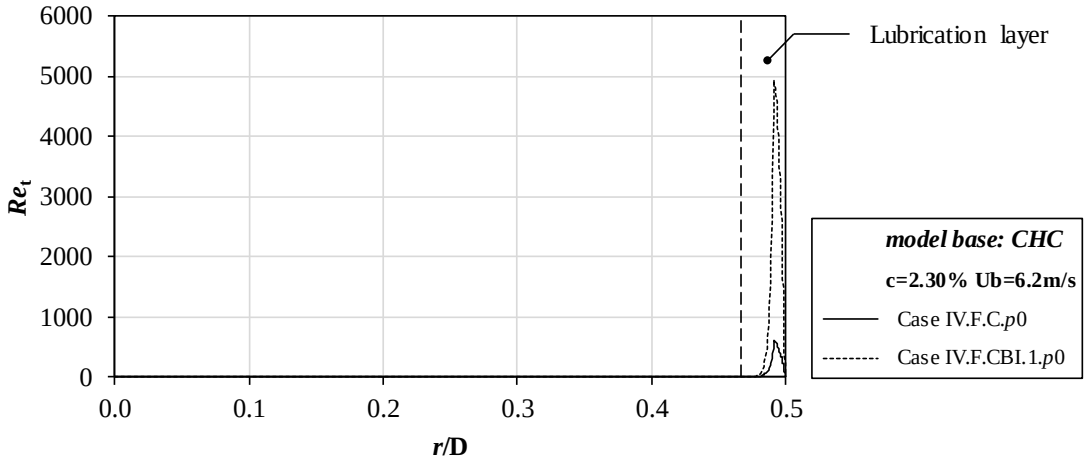

d)

Figure IV.32 – Variation of the turbulent Reynolds number Re_t, CHC model and new CHC Bartosik I model, for *Pine* pulp: (a) c = 0.80 % U_b = 4.1 m s^{-1}, (b) c = 0.80 % U_b = 5.9 m s^{-1}, (c) c = 2.30 % U_b = 4.3 m s^{-1}, and, (d) c = 2.30 % U_b = 6.2 m s^{-1} (continued).

As expected, turbulent viscosity (Figure IV.33 – *Eucalyptus* pulp) has larger values for the lower consistency cases (i.e. 1.50 %) where the turbulent regime is better approached and the non-Newtonian behaviour of the pulp is not so noticeable. Additionally, for the higher consistency case (i.e. 2.50 %), in the core region, turbulence is more attenuated due to larger amount of fibers in the flow and also because viscous effects are stronger with a higher contribution from molecular viscosity in the CFD model, if damping functions are used in the model.

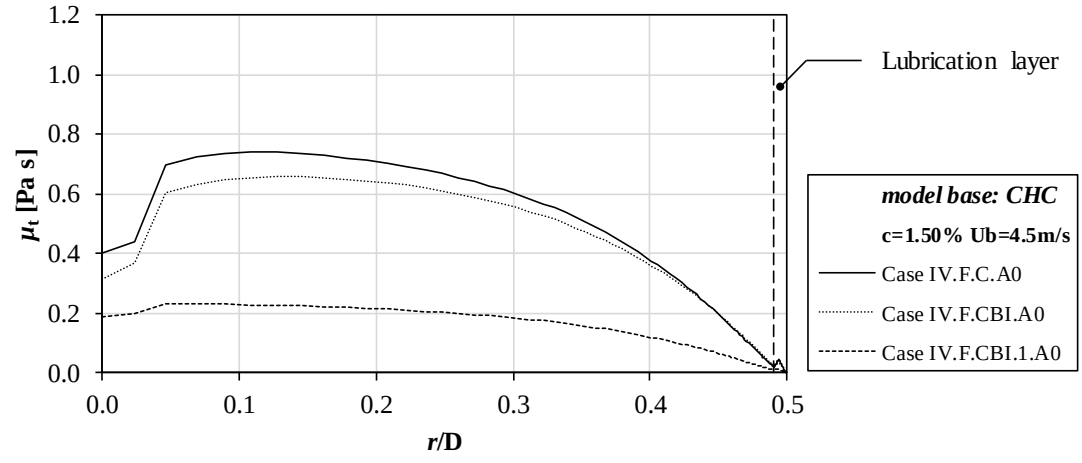

a)

Figure IV.33 – Variation of turbulent viscosity, CHC model, CHC Bartosik I model and new CHC Bartosik I model, for *Eucalyptus* pulp: (a) c = 1.50 % U_b = 4.5 m s^{-1}, (b) c = 1.50 % U_b = 6.2 m s^{-1}, (c) c = 2.50 % U_b = 4.9 m s^{-1}, and, (d) c = 2.50 % U_b = 5.6 m s^{-1}.

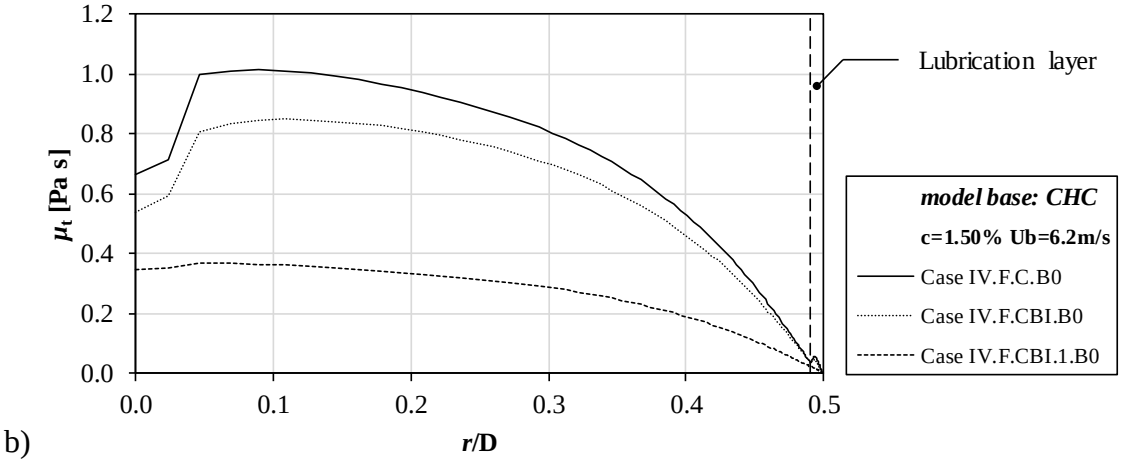

b)

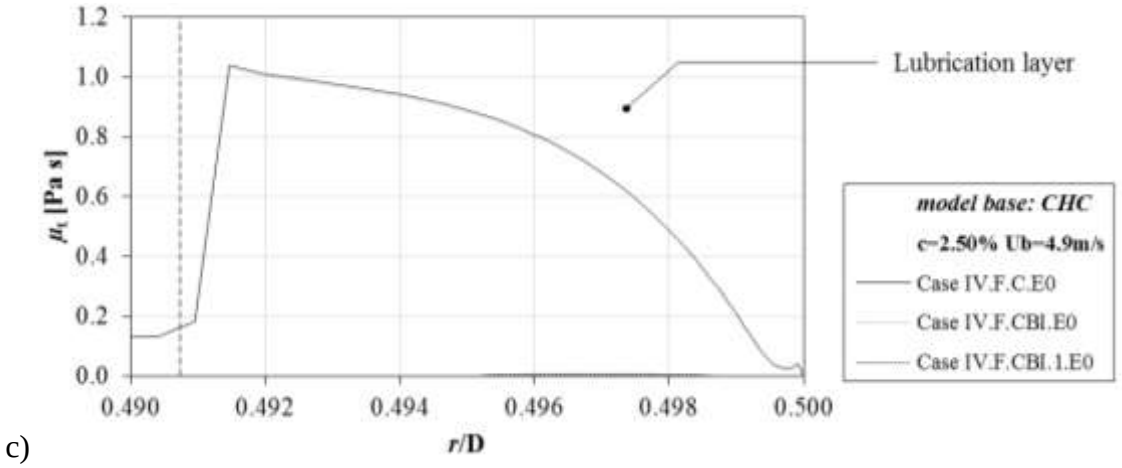

c)

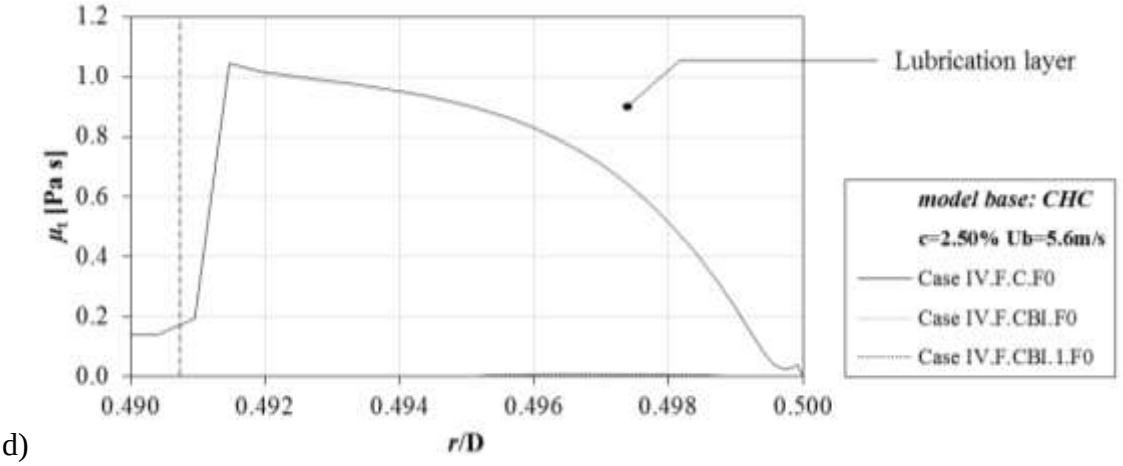

d)

Figure IV.33 – Variation of turbulent viscosity, CHC model, CHC Bartosik I model and new CHC Bartosik I model, for *Eucalyptus* pulp: (a) c = 1.50 % U_b = 4.5 m s^{-1}, (b) c = 1.50 % U_b = 6.2 m s^{-1}, (c) c = 2.50 % U_b = 4.9 m s^{-1}, and, (d) c = 2.50 % U_b = 5.6 m s^{-1} (continued).

The trend observed in Figure IV.33 (*Eucalyptus* pulp) is also predicted for the *Pine* pulp suspension (Figure IV.34). For the lower consistency (i.e. 0.80%), turbulent viscosity and molecular viscosity are two important factors that the CFD model must adequately account for. For the higher pulp consistency (c = 2.30 %), turbulent viscosity indicates stronger variation in the near wall region (see Figures IV.34c) and IV.34d)), mainly in the turbulent

lubrication layer where, due to the presence of fibers in that region, turbulence is more adequately predicted. In the flow core region, the stronger non-Newtonian behaviour of pulp is replicated by higher values of molecular viscosity. As turbulence is further dampened, the inclusion of the new Bartosik I damping function leads to a reduction of the turbulent viscosity, i.e. reduction of turbulent effects.

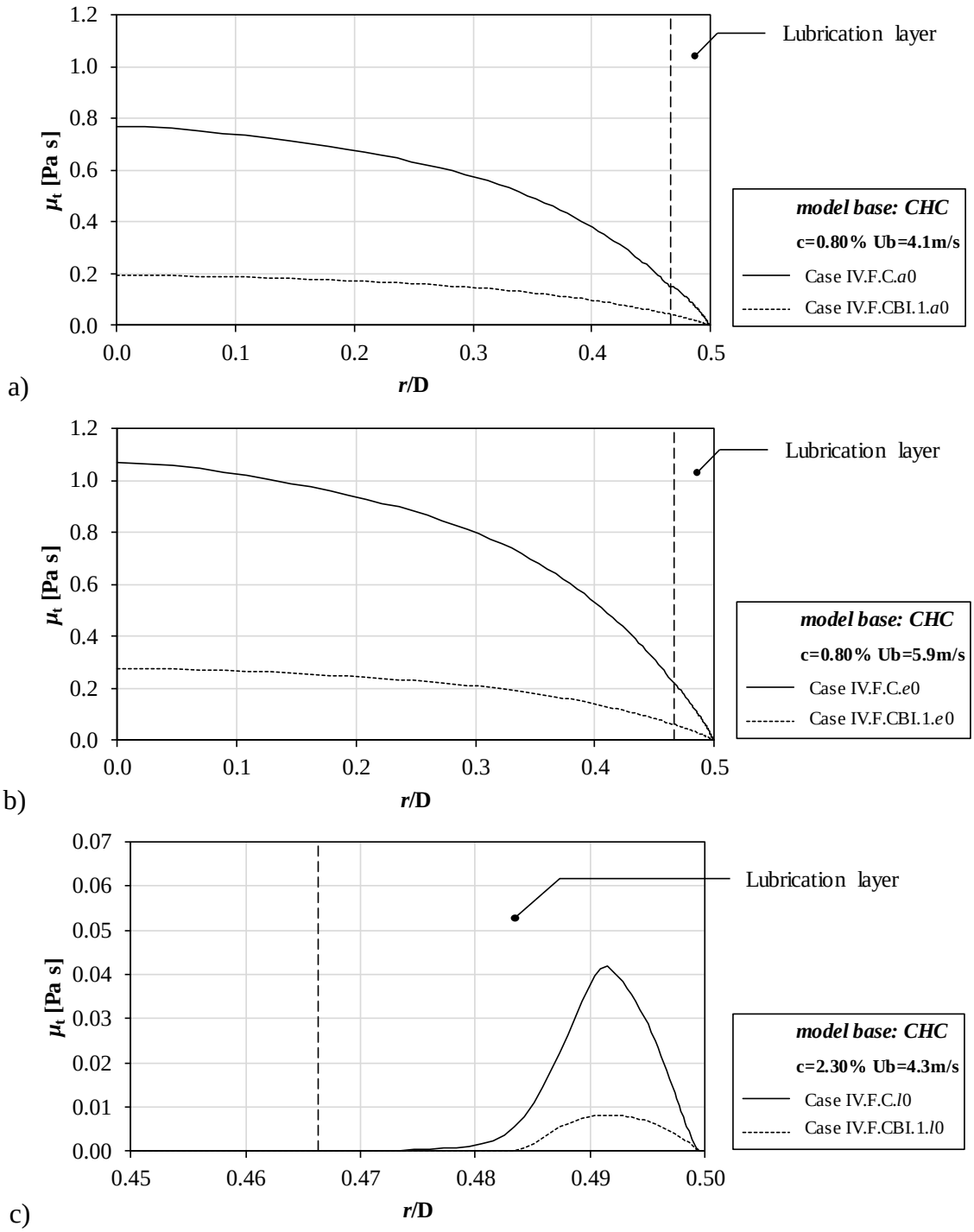

Figure IV.34 – Variation of turbulent viscosity, CHC model and new CHC Bartosik I model, for *Pine* pulp: (a) c = 0.80 % U_b = 4.1 m s^{-1}, (b) c = 0.80 % U_b = 5.9 m s^{-1}, (c) c = 2.30 % U_b = 4.3 m s^{-1}, and, (d) c = 2.30 % U_b = 6.2 m s^{-1}.

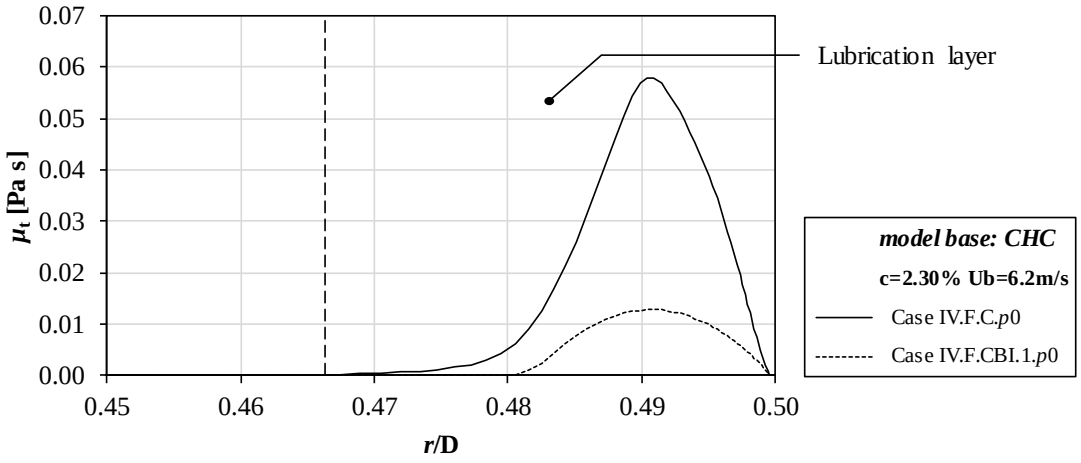

d)

Figure IV.34 – Variation of turbulent viscosity, CHC model and new CHC Bartosik I model, for *Pine* pulp: (a) c = 0.80 % U_b = 4.1 m s^{-1}, (b) c = 0.80 % U_b = 5.9 m s^{-1}, (c) c = 2.30 % U_b = 4.3 m s^{-1}, and, (d) c = 2.30 % U_b = 6.2 m s^{-1} (continued).

From the results presented in this section, one may conclude that, for the lower consistency cases (i.e. *Eucalyptus* pulp c = 1.50 %, and *Pine* pulp c = 0.80 %), turbulence is fully developed with turbulent eddies not suffering from a very high attenuation due to the presence of fibers. Thus, a fluid-like behaviour is more evident for those cases. On the other hand, for the higher consistency (i.e. *Eucalyptus* pulp c = 2.50 %, and *Pine* pulp c = 2.30 %), the presence of three distinct zones in the dimensionless velocity profiles indicates that in the flow core region there is a high attenuation of turbulence, which is manifested by the underestimation of the damping function, turbulent Reynolds number and turbulent viscosity values near the pipe axis.

IV.3.3.1 – SUMMARY OF CFD PREDICTIONS: *EUCALYPTUS* AND *PINE* FLOW DATA

The CFD model proposed in this work for pulp suspension flow is composed of Equations III.2 to III.4, III.7 and IV.4. The molecular viscosity is calculated by Equation IV.1, assuming the effect of fibers in the lubrication layer. The modulation of turbulence is derived from the presence of fibers in the flow by taking into account the yield stress and fiber characteristics described by the aspect-ratio: *new* Bartosik I damping function. The model was applied to simulate all the pulp flow conditions for the *Eucalyptus* and *Pine* pulps presented in Tables IV.14 and IV.15 (see pressure drop values in Tables IV.30 and IV.31).

In Figure IV.35 the predicted and experimental pressure drop values for the flow *Eucalyptus* pulp are presented. Is was chosen to compare in Figure IV.35 the results obtained

with the CFD model proposed in this work, CHC model with new Bartosik I damping function, as well as the results obtained with the standard CHC model and model modified with the Bartosik I damping function. A good fit to the experimental data is observed for all consistencies when the new modified Bartosik I damping function was implemented. The trend in the numerical predictions for c = 1.50 % (see Figure IV.35b)) is to slightly overestimate obtained experimentally pressure drop values. This can be due to the fact that for this pulp consistency the rheological adjustment is less reliable for lower shear rates values. However, it seems that the numerical predictions for that pulp consistency lead to pressure drop values with a trend parallel to those for turbulent water flow in the same test rig, which is expected to occur in turbulent pulp flow regime.

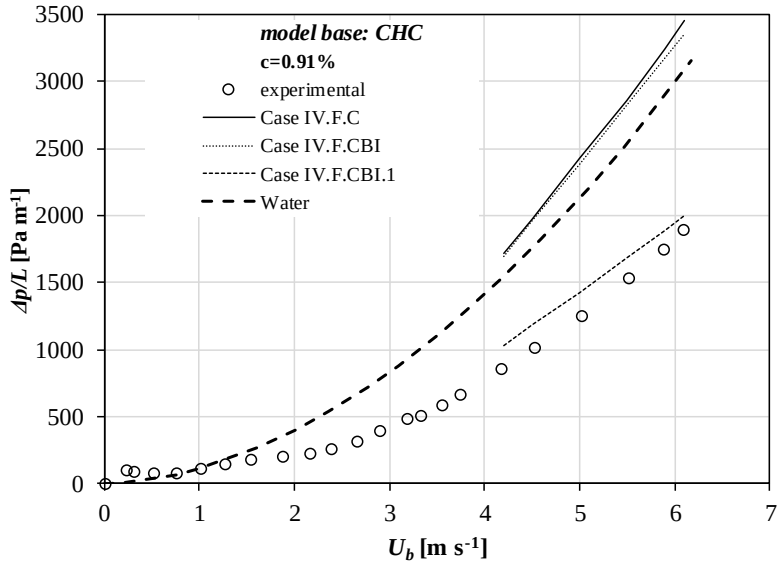

a)

Figure IV.35 – Experimental and numerical pressure drop predicted with CHC model, CHC Bartosik I model and new CHC Bartosik I model, plotted in linear scales, for *Eucalyptus* pulp: (a) c = 0.91 %, (b) c = 1.50 %, (c) c = 2.20 %, and, c = 2.50 %.

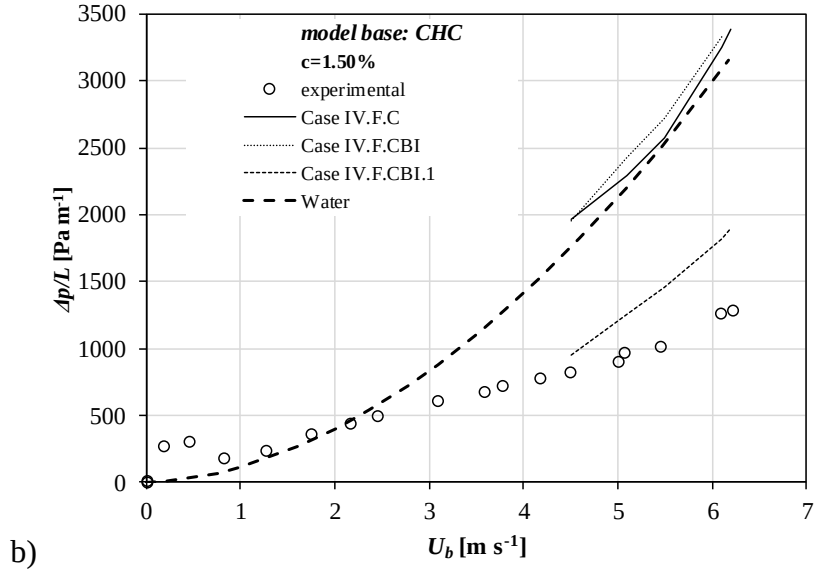

b)

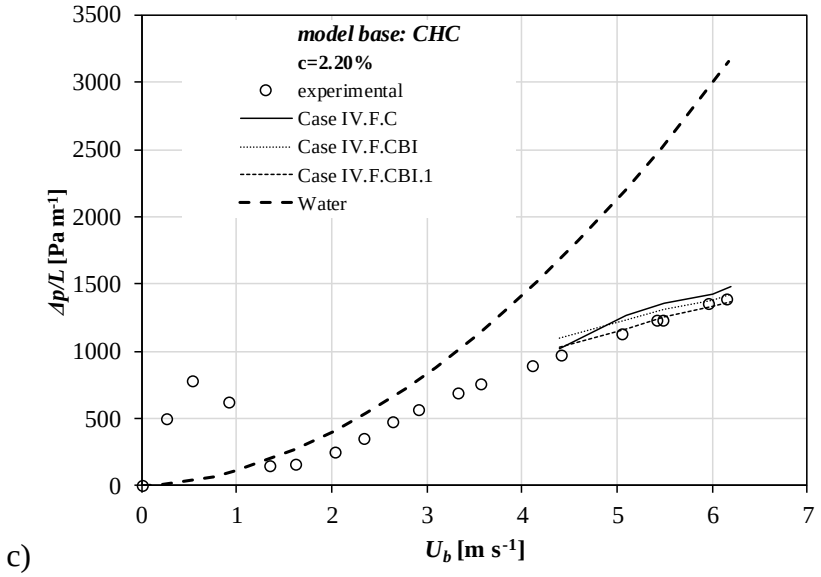

c)

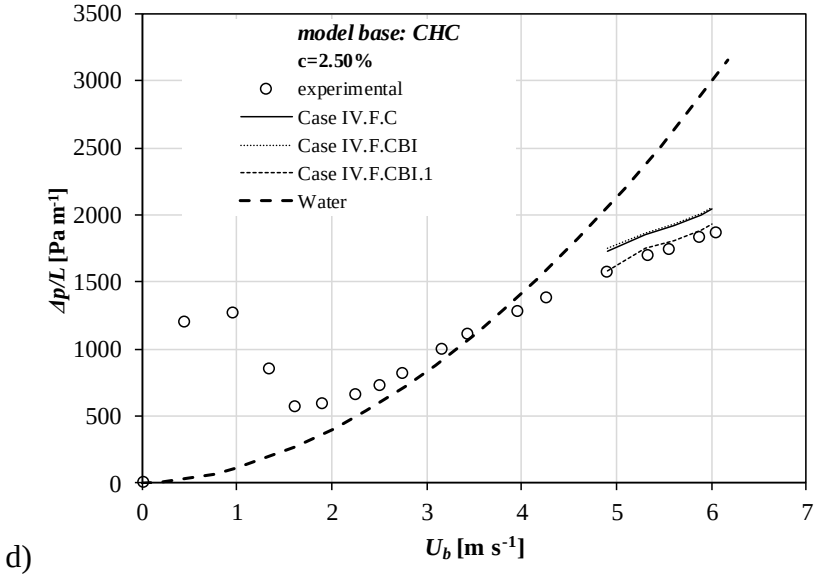

d)

Figure IV.35 – Experimental and numerical pressure drop predicted with CHC model, CHC Bartosik I model and new CHC Bartosik I model, plotted in linear scales, for *Eucalyptus* pulp: (a) c = 0.91 %, (b) c = 1.50 %, (c) c = 2.20 %, and, c = 2.50 % (continued).

Experimental and numerical pressure drop values are presented in Figure IV.36, for the flow of *Pine* pulp suspension. According to the results presented, the numerical predictions are consistent with the experimental measurements. Looking at Figure IV.36c) it seems that the fully turbulent pulp flow regime was not fully reached experimentally for c = 2.30 %, i.e. probably the data collected experimentally correspond to a regime closer to the transition regime instead of fully turbulent with fluid-like behaviour, due to experimental difficulties. This may justify the larger deviations between experimental and calculated pressure drops for this consistency (i.e. 2.30 %). Also, it is expected that for higher consistencies the velocity curves will present a flatter profiles in the flow core than those of lower consistencies (see velocity curves for *Pine* pulp flow – Figure IV.21). This fact leads to low shear rates in the flow core region. However, the lack of information for lower shear rates could have led to less reliable viscosity values in that region and, in this way, less accurate pressure drop values are also predicted. Additionally, the differences observed in Table IV.31, for the higher consistency (i.e. 2.30 %), where better results are obtained when considering pure water annulus can indicate as well that the fully develop turbulent regime has not been reached and the plug of fibers is not totally disrupted.

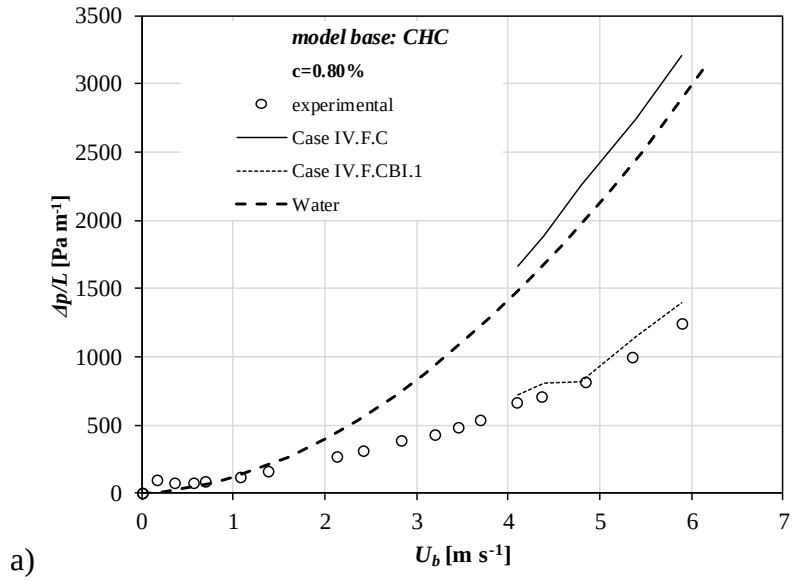

a)

Figure IV.36 – Experimental and numerical pressure drop predicted with CHC model and new CHC Bartosik I model, plotted in linear scales, for *Pine* pulp: (a) c = 0.80 %, (b) c = 1.50 %, and, (c) c = 2.30 %.

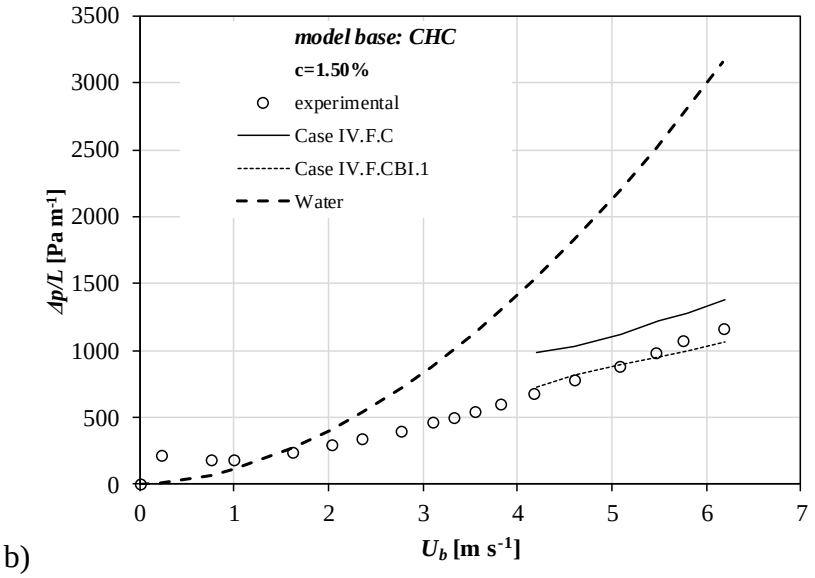

b)

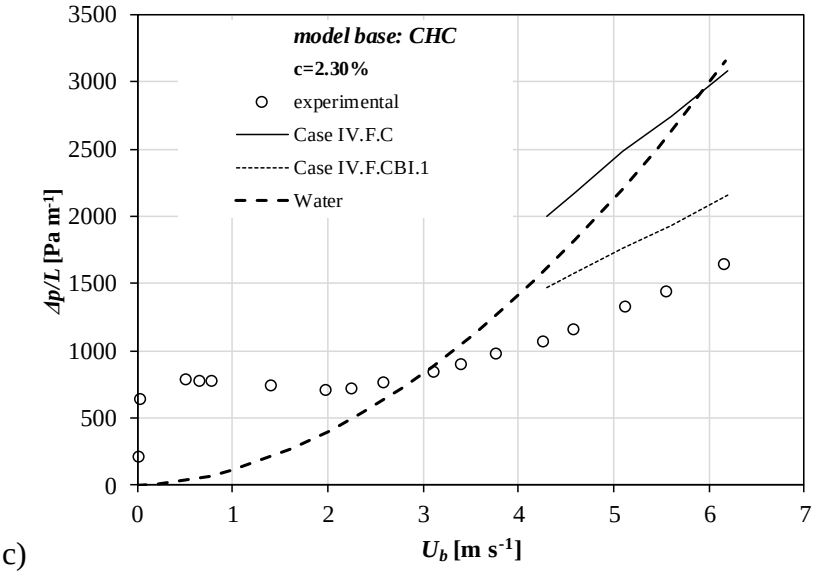

c)

Figure IV.36 – Experimental and numerical pressure drop predicted with CHC model and new CHC Bartosik I model, plotted in linear scales, for *Pine* pulp: (a) c = 0.80 %, (b) c = 1.50 %, and, (c) c = 2.30 % (continued).

Therefore, the good agreement between the calculated pressure drops with those obtained experimentally (*Eucalyptus* and *Pine* pulp suspensions) constitutes a good validation of the CFD model proposed here to simulate pulp suspensions turbulent flow. Additionally, the prediction of the unique S-shaped profile for the dimensionless velocity, following the observations from Jäsberg (2007), shows that the turbulent pulp flow is adequately predicted. Moreover, the RMS velocity profiles are in accordance with the trend found in Claesson *et al.* (2012).

IV.4 – CONCLUSIONS

The research conducted in this work aims to propose a CFD model able to simulate the turbulent flow of *Eucalyptus* and *Pine* pulp suspensions. In this way, a strategy based on applying different low-Reynolds-number (LRN) *k-ε* turbulence models was employed. The successful application of this type of models to simulate flows where a *drag reduction* effect is present motivated this approach.

Molecular viscosity was expressed as a function of pulp consistency and shear rate. In this way, the consistency gradient could be taken into account in the CFD model. It was decided to test the influence that the presence of a certain number of fibers in the lubrication layer has on the numerical calculations. The inclusion of fibers in the lubrication layer was achieved by imposing a consistency gradient in the lubrication layer, considering consistency as a linear function of distance to the pipe wall.

Several computational tests were made in order to study the applicability of LRN *k-ε* turbulence models to simulate the turbulent flow of pulp suspensions. It was found that these types of models could be applied to simulate the flow of pulp suspensions; however, it was also concluded that without further modifications those models were not able to resolve the flow accurately for the cases under present study, more so for the medium consistency situations. Different strategies applied successfully in simulations of turbulent flows of other systems where *drag reduction* effects were present, were investigated. After a careful analysis of different strategies suggested in literature, it was decided to modify the damping function f_μ of the most suitable LRN *k-ε* turbulence models according to information from literature for power-law fluids and particulate flows of spherical particles. Preliminary results have shown that the AKN and CHC models were the most appropriate models to be modified in order to implement new damping functions. Since the flow of pulp suspensions is qualitatively different from those of power-law fluids and spherical particles suspensions, the new damping functions tested were not able to lead a CFD model to good enough predictions of pressure drop. A set of new tests was performed in order to investigate the influence that different constants values in modified damping functions had on the numerical predictions. Modifying those constants allowed to get better numerical predictions. It was found that better predictions of pressure drop were obtained when varying C_{M2} in the modified version of Malin damping function. This parameter is related to Re_k and should have a higher value than

the standard value from Malin (1997b). In the modified Bartosik II damping function new values of constants C_{B1} and C_{B2} were tested. The parameter C_{B2} was assumed equal to the fiber length since this parameter represents fiber diameter when applying the standard Bartosik II damping function. The parameter C_{B1}, representing the empirical constant A_S, was modified assuming that it could have a higher and a lower value than that of the standard Bartosik II damping function. However, the numerical pressure drops obtained were still not acceptable for all flow cases. To develop a model suitable to deal with the turbulent flow of pulp suspensions it was found that the damping function must have a term related to fiber characteristics and fiber aspect-ratio was chosen to describe the anisotropic nature of fibers. For this modified damping function, the experimental pressure drops agree well with the experimental values. Also, dimensionless velocity profiles are in qualitatively good agreement with those reported in literature, as well as the RMS velocity profiles are consistent with the trends reported by other authors. Additionally, it was found that the accuracy of the numerical calculations is slightly dependent on the inclusion of fibers in the lubrication layer. However, it seems that it is mainly dependent on the correctness of the rheological information for low shear rates ranges. Still, for the sake of better presentations, of what must happen in the lubrication layer, it is recommended to consider that some fibers must also be present in that layer.

The numerical results obtained with the CFD model proposed shows that the near wall region is important since the main variations of scalar variables occur in that region, and needs to have a proper treatment. For higher consistencies, the strong non-Newtonian behaviour dominates in the flow core region with lower values of turbulent viscosity. For lower consistencies, contribution from molecular viscosity and turbulence must be both taken into account.

It must be pointed out that the damping function is like a correction function and the development of different reliable functions is possible. In this work, a model that can be effective to predict the *Eucalyptus* and *Pine* pulp suspensions flow is presented.

Finally, the CFD model proposed is able to simulate well the turbulent flow of *Eucalyptus* and *Pine* pulp suspensions for different flow conditions and pulp consistencies (medium and high sub-ranges of consistencies). Most obviously a good compromise between the viscosity model and turbulence modulation needs to be achieved in order to develop a suitable model to deal with the turbulent flow of pulp suspensions.

PART C. EUCALYPTUS PIPE FLOW: CFD AND EXPERIMENTAL STUDIES

In this part of the work, the pseudo-homogeneous model proposed in Chapter IV is investigated to simulate the flow of *Eucalyptus* pulp suspensions in a test section equipped with an imaging technique, electrical impedance tomography system existing at University of Coimbra (UC) facilities. In the CFD model, molecular viscosity depends on pulp consistency and shear rate. The presence of fibers is considered in the lubrication layer, surrounding the flow core, with pulp consistency related to the distance to the pipe wall. The low-Reynolds-number k-ε turbulence model, Chang-Hsieh-Chen, is used to model turbulence. The damping function of turbulent viscosity is modified by its extension with an additional term related to fiber aspect-ratio, as described in Chapter IV, Section IV.2.3.2.

Electrical impedance tomography technique is used to inspect the pulp flow regime. Experimental information is intended to obtain qualitative information on the transition and turbulent regimes, namely, evolution of plug core. Subsequently, the flow of *Eucalyptus* pulp suspensions is simulated for different mean pulp consistencies and flow data. The CFD predictions of pressure drop are compared with experimental values acquired in the pilot plant.

V – FURTHER ASSESSMENT OF THE CFD PSEUDO-HOMOGENEOUS MODEL OF TURBULENT PULP FLOW

Electrical Impedance Tomography (EIT) is a powerful tool to infer velocity and concentration distributions of multiphase flows where electrical impedance differences occur between two different phases. Therefore, the main objective of this chapter is to investigate the applicability of the EIT technique to get information about the flow of refined *Eucalyptus* bleached pulp in a pipe (pulp characteristics are presented in Tables III.1 and IV.13). The EIT system used to characterise pulp suspensions behaviour was developed by Faia *et al.* (2015b) under the project PTDC/EQU-EQU/112388/2009. The pulp flow in a pipe with different dimensions from those simulated in Chapters III and IV was evaluated. The cases studied were modelled using a pseudo-homogeneous CFD model. The numerical predictions were quantitatively validated with experimental data of pressure drop. Additionally, the pulp flow regime was qualitatively evaluated with tomographic data. The CFD results are in accordance with experimental data, mainly for transition regime. The model was able to reproduce data for turbulent flow. The accuracy of the model tends to decrease when plug or transition flow regimes exist. Nevertheless, the CFD model was found to give the expected compromise between turbulence predictions and the calculated pressure drop values for the different flow regimes considered.

V.1 – INTRODUCTION

The validation of CFD tools to predict the flow of pulp suspensions depends on the accuracy of the experimental techniques used to obtain flow data, as well as on the experimental strategies applied to measure rheological properties. Nowadays, as presented in Chapter II, most of the experimental devices for velocity measurements have limitations to get data near solid walls, and are not suitable to work with flows of high pulp consistencies. Additionally, the lack of experimental information concerning spatial distribution of fibers in circular or square sections during the flow of pulp suspensions, results on CFD validations made basically by comparing numerical pressure drop values with those obtained

experimentally, without proper validation in the near wall region. For these reasons, spatial distribution of fibers, namely plug size evolution in the circular pipe section, was accomplished with an EIT experimental technique. The experimental investigations were used to validate qualitatively the differences in plug evolution for different pulp flow regimes. In this way, the experimental trials were used to validate the applicability of the pseudo-homogeneous model developed for turbulent pulp flow, out of the turbulent pulp flow regime.

Before describing the experiments performed to obtain qualitative information in the pipe circular cross section, the imaging technique, EIT, will be presented, as well as a brief description of the pilot plant will be addressed. In addition, the experimental procedure will be described in detail.

The pseudo-homogeneous CFD model proposed in Chapter IV will be tested to simulate the set of experiments when the test section was equipped with the EIT system. The CFD results and experimental data will be presented for the validation and extension of the numerical model developed for fiber suspension flows.

V.2 – EIT TECHNIQUE

Electrical Impedance Tomography is a powerful tool for imaging multiphase flows, and for mapping velocity and concentration profiles. This technique is based on differences of electrical impedance between different fluids or phases. It was applied successfully for visualization of different multiphase flows such as oil/water flow (Wang *et al.*, 2005), water-in-oil/oil-in-water emulsions in oscillatory bluffed reactor (Vilar *et al.*, 2008), and gas/water two-phase flow (Zhang and Dong, 2010). The review works presented by Tapp *et al.* (2003) and Rasteiro *et al*. (2011) described several applications of electrical tomography techniques to the chemical engineering fields of mixing, separation, transport and flow, and reactors. This technique is useful to identify mixing and stagnant zones in reactors and for phase identification in separation processes as well as phase boundaries in multiphase flows.

A ring composed of electrode sensors is placed around the vessel/pipe (Figure V.1) in such a way that the electrodes surfaces are in contact with the interior domain not disturbing the flow pattern, i.e. they are flush mounted in the pipe wall. The physical principle of EIT is based on injecting a current through a pair of electrodes and measuring the response voltages in the remaining electrodes. All the electrodes must be used for injection in order to complete the process. The electrical field distribution in the domain is conditioned by the dispersion of

the different fluids/phases in the interior domain. At the end, the distribution of conductivity, σ, is obtained.

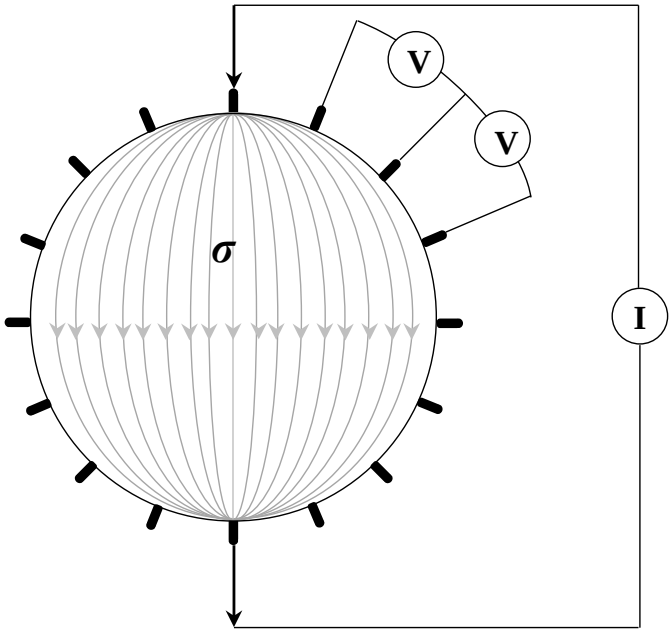

Figure V.1 – Physical principle of electrical impedance tomography process, opposite injection with adjacent measuring (adapted from Zhou and Halttunen (2005) and Bera and Nagaraju (2012)).

Basically, this technique is characterised mathematically through two types of problems: forward problem and inverse problem. In the forward problem, it is needed an initial guess for conductivity distribution in order to find the potential distribution and to calculate the electrical potentials in the boundary, knowing the current injected; the inverse problem is characterized by obtaining the conductivity distribution from the electrical potentials measured in the boundary (Faia *et al.*, 2015b). A non-linear inverse algorithm is then used to obtain the conductivity distribution from the electrical potentials measured. The two different strategies that can be used for the excitation of the tomographic sensors and voltage measurement procedure are: (*i*) opposite injection with adjacent measuring (see Figure V.1), and (*ii*) adjacent injection and measuring. A detailed description of these two strategies can be found in Bera and Nagaraju (2012).

The opposite injection with adjacent measuring is used in the present work based on detailed studies conducted by the team of the project PTDC/EQU-EQU/112388/2009 (Faia *et al.*, 2015b). The opposite current injection protocol is based on current injected through two opposite electrodes. The electrical potentials are measured on the remaining electrodes, having as the reference electrode the electrode adjacent to the current-injecting electrode. The total number of electrodes, *n*, in the ring allows the same number of current projections, *n*,

with differential potentials measured successively from n-3 electrode pairs. A total number of $n\times(n\text{-}3)$ voltage measurements can be done; however, this total number of measurements includes measurements when voltage electrodes are interchanged giving similar voltage measurements. Thus, only $n\times(n\text{-}3)/2$ electrical voltage measurements represents independent data.

In order to get EIT data in the vessel/pipe cross-section, the EIT system must be composed of: constant current injector, signal conditioner, automatic electrode switching module and data acquisition system (Bera and Nagaraju, 2012). The conductivity images are obtained through the complete voltage data set treated with the proper software in a personal computer (PC), as will be described in the next sections.

V.3 – EXPERIMENTAL STUDIES

The *Eucalyptus* pulp flow experiments were performed in the pilot plant schematically presented in Chapter III, Section III.2. The test section was upgraded with a 2D imaging system, electrical impedance tomographic system. The *Eucalyptus* pulp collected from the Portuguese mill Soporcel was squeezed and washed as described in Faia *et al.* (2015b), and the liquid in the suspension was replaced with tap water doped with sodium chloride, NaCl. The conductivity was adjusted to a prescribed value in order to set a better contrast between the two phases. Flow tests were conducted for different consistencies and flow velocities. Pressure drop values as well as mean flow rate values were measured. Additionally, EIT images were obtained.

V.3.1 – EQUIPMENT

The flow studies were carried out in a pilot rig (see Figure V.2) existent at the Department of Chemical Engineering (DEQ), Faculty of Sciences and Technology University of Coimbra (FCTUC). The pilot plant presented in Figure V.2 was upgraded with a tomographic system, as mentioned previously, which is illustrated in Figure V.3.

Figure V.2 – Pilot rig existent in DEQ-FCTUC without the EIT system (adapted from Rasteiro (2011)).

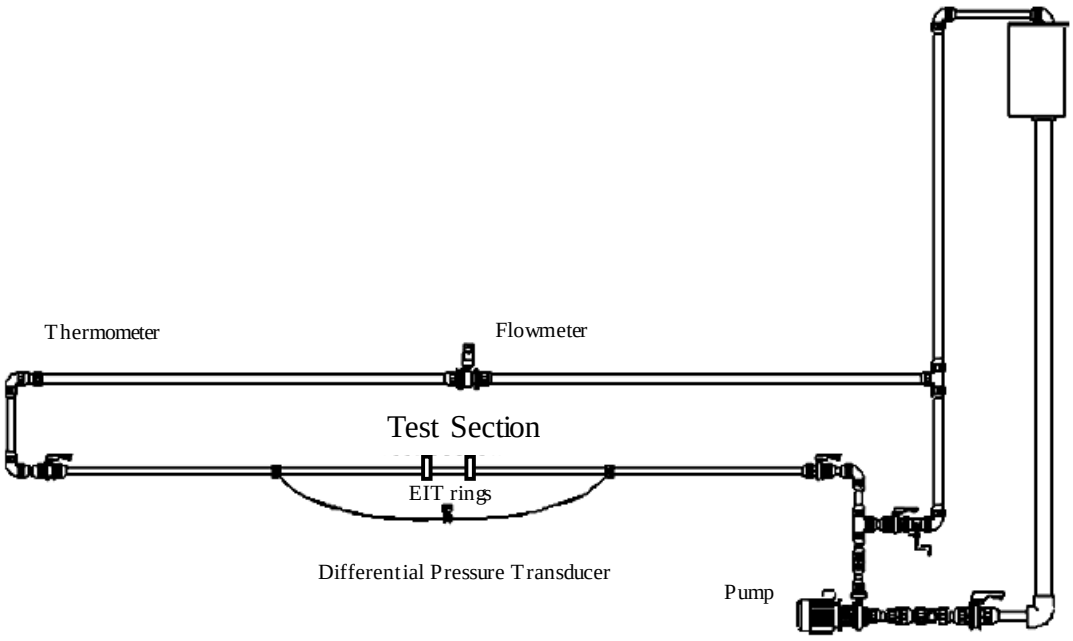

Figure V.3 – Schematic diagram of pilot rig equipped with the EIT system (adapted from Ventura *et al.* (2008b)).

The pilot rig included a test section composed of a horizontal pipe made of polyvinyl chloride (PVC) with 4.45 m in length and 0.10 m of internal diameter (Faia *et al.*, 2015b). This test section was inserted in a horizontal pipe downstream a pipe segment with appropriate length to guarantee fully developed turbulent flow; also, a sufficiently long pipe segment was placed downstream the test section in order to minimize exit effects. The total length of these three pipe segments was 11.5 m.

The EIT system used was composed of an electrode ring including 32 Titanium electrodes of 5 mm each, circumferentially equally spaced (Faia *et al.*, 2015b). EIT rings were placed in a poly(methyl 2-methylpropenoate), Perpex, transparent pipe segment in order to

allow flow visualization. Even if only a tomographic ring was used in the experiments, the tomographic section was composed of three EIT rings placed 0.010 and 0.020 m separately. An additional length resulted from the inclusion of the EIT system, equivalent pipe length of 1.2 m, mainly due to connections between the different pipe segments in the test section.

The tomographic system, developed under the project PTDC/EQU-EQU/112388/2009 to deal with pulp fiber flows, was based on injecting a voltage source instead of a current source. A 10 kHz, $2V_{pp}$ (peak-to-peak electrode voltage) fixed excitation frequency was applied for all tests conducted (Faia *et al.*, 2015b). An opposite current injection method was used. For the forward problem, tap water doped with NaCl with conductivity around 1200 µS cm^{-1} was used for homogeneous data sets, in order to get the electrical potentials in the boundary. For the pulp flow tests, the adjacent voltage differences collected with the different electrodes were fed into the open source software EIDORS (Electrical Impedance and Diffuse Optical Reconstruction Software) (Polydorides and Lionheart, 2002). This software is a MatLab based reconstruction algorithm and gives an EIT image of the domain section. A finite element method (FEM) mesh of the EIDORS algorithm was used: structured mesh composed of 2304 regular triangular elements and 1201 nodes to discretize the domain. The forward problem was solved with the Complete Electrode Model, CEM (Cheng *et al.*, 1989). For the inverse problem, a one-step Gauss-Newton inverse algorithm was used.

The pulp suspension was introduced into the pilot rig through an open tank placed at the pump level. It should be noted that a second tank was placed at a higher level in order to avoid the formation of air bubbles and to guarantee that the flow did not have disturbances, resulted from variations of consistency. The flow rate was measured with a magnetic flowmeter, and it was controlled by two valves placed downstream the pump. The temperature was measured by a metallic thermometer, the data being acquired directly through LabVIEW.

V.3.2 – EXPERIMENTAL PROCEDURE

Before the fiber suspension experiments, a set of tests was performed with only tap water doped with NaCl with conductivity adjusted to around 1200 µS cm^{-1}, for the same flow rates as applied in pulp suspension tests (see Table V.1).

The suspension of *Eucalyptus* pulp was collected from Soporcel, consistency of 3 % and conductivity of 900 µS cm^{-1}, with the same characteristics as presented in Tables III.1 and

IV.13. It was squeezed and washed in order to eliminate the liquid in the suspension. As described in Faia *et al.* (2015b), the liquid in the suspension from industrial pulp contained ions are able to be absorbed by fibers giving low conductivity differences between fibers and carrying medium. The liquid in the suspension was replaced with tap water doped with sodium chloride, NaCl. The suspension conductivity was regulated to the values presented in Table V.1. Pulp flow rate was kept constant for each case tested and monitored by means of a flowmeter. The differences between pressure at inlet and outlet of test section (4.45 m long) were measured with a differential pressure meter. The suspension temperature was monitored by means of a metal thermometer. All flow tests were performed at room temperature. The EIT process was initialized from PC through commands. The tomographic images were obtained in a PC, reconstructed from the read electrical potentials, with the use of the open source software EIDORS.

Table V.1 – Experimental data – *Eucalyptus* pulp.

c [%]	N *crowding factor*	σ *conductivity* [µS cm^{-1}]	U_b [m s^{-1}]	Q_b [m^3 s^{-1}]	$\dot{m}_b$ [kg s^{-1}]	$\Delta p/L_{water}$ [Pa m^{-1}]	$\Delta p/L_{pulp}$ [Pa m^{-1}]
1.01	1311	1440	2.0	56	16	298	316
1.01	1311	1440	3.0	84	24	625	554
1.50	1947	1435	2.0	56	16	298	463
1.50	1947	1435	3.0	84	24	625	679

In order to investigate experimentally the flow of *Eucalyptus* pulp suspensions, data of mean flow rate, pressure drop, and EIT images were obtained for different pulp consistencies as described in the current section. These data were then integrated in the pseudo-homogeneous CFD model of turbulent pulp suspensions described in Sections V.4 and V.5.

V.4 – SIMULATION SET-UP

Simulations carried out in Chapters III and IV have only been validated with pressure drop measurements. The present investigation aims at complement the numerical study with additional 2D tomographic images in order to validate the pulp flow regime. Furthermore, this study intends to obtain qualitative information concerning the fibers radial distribution.

V.4.1 – TRANSPORT EQUATIONS, DISCRETIZATION SCHEME AND BOUNDARY CONDITIONS

The pseudo-homogeneous approach employed in this thesis, including the continuity, momentum and closure equations for turbulent quantities, i.e. turbulent kinetic energy and its dissipation rate, was developed in Chapter IV. The complete system of differential equations is given by Equations (III.2) to (III.4), (III.7) and (IV.4). Additionally, the model can be expressed by the general differential equation in the form of Equation (III.10) with the model parameters indicated in Table IV.7. According to Chapter IV, a new damping function f_μ could be used to take into account the presence of fibers in the flow and its turbulence attenuation effect. In this way, the damping function of turbulent viscosity, μ_t, was expressed according to Equation (IV.12). Pulp consistency and local shear rate values were used to calculate pulp viscosity, Equation (IV.1). Additionally, the model took into account the existence of fibers in the lubrication layer (thickness equal to average fiber length) surrounding the flow core, expressed by the consistency gradient given by Equation (IV.2).

In order to solve numerically the complete system of differential equations, the numerical methodology described in Chapters III and IV was applied. The control-volume-based technique was used to discretize the governing equations. The integration, discretization and linearization of the differential equations were already implemented in the ANSYS Fluent solver. It was assumed that the solution was converged when the scaled residuals were less than 1×10^{-5}.

Boundary conditions required for the numerical solution of the complete system of governing equations was specified for the inlet, outlet, pipe axis and pipe wall as indicated in Table IV.10, and described in Chapter IV, Section IV.2.4.1.

The same methodology to implement the LRN k-ε turbulence models tested in Chapter IV was performed here. It was based on turning off the built-in turbulence equations, representing k and ε as two additional scalar quantities and to provide all the required information such the source terms, diffusion coefficients and other data, through the own-developed UDF as described in Chapter IV, Section IV.2.4.1.

In conclusion, the pseudo-homogeneous CFD model tested in this work was composed of:

(*i*) Continuity equation – Equation (III.2)

(*ii*) Momentum equations – Equations (III.3) and (III.4)

(*iii*) Transport equation of turbulent kinetic energy – Equation (III.7)

(*iv*) Transport equation of dissipation rate of turbulent kinetic energy – Equation (IV.4)

with the main features:

(*v*) Viscosity expression – Equation (IV.1)

(*vii*) Consistency profile in lubrication layer – Equation (IV.2)

(*vii*) *New* CHC Bartosik I model – damping function Equation (IV.12)

with computational model parameters given in Table V.2.

Table V.2 – Computational model parameters.

Parameter	Value
Iterations – Periodic boundary	2
Relaxation factor – Periodic boundary	0.5
Turbulence model	*new* CHC Bartosik I model (User-Defined Functions)
Under-relaxation parameters	0.3 (pressure), 0.7 (momentum), 0.8 (t.k.e. or corresponding User defined scalar), 0.8 (t.d.r. or corresponding User defined scalar)
Pulp viscosity and pulp consistency	Table (IV.2) – Consistency case F
Pulp density	Water density (293K)

V.4.2 – GEOMETRY AND COMPUTATIONAL MESH

The test section to be simulated in this chapter was composed of a smooth pipe with larger diameter and larger length than the test section simulated in Chapters III and IV. The pipe diameter is 0.10 m (Faia *et al.*, 2015b) whereas the total length between pressure taps was equal to 4.45 m. An additional length of 1.2 m was taken into account when converting the pressure drop measured (4.45 m of pipe), to account for the equivalent lengths corresponding to the connections between the different sections, for 1 m of pipe. It was assumed a 2D axisymmetric geometry with only 1 m of pipe to be simulated (see Figure III.2), $L \times R$: 1 m × 0.05 m.

The computational mesh was generated by means of the meshing commercial program GAMBIT 2.4.6 (Fluent Inc., 2007). A structured non-uniform mesh more refined near the wall region, where cells thickness is smaller, was constructed (see the view of the mesh presented in Figure IV.4). Special attention was given to the mesh construction in order to

locate the first mesh node at $y^+ \approx 1.0$ (Ansys Inc., 2010). The strategy presented in Chapter IV, Section IV.2.5, was applied, i.e. three distinct interval length ratio (1.05, 1.10 and 1.15) were considered in mesh generation. In order to apply Equation (IV.14), different total numbers of nodes, according to *r* direction, were investigated (54, 94, 100, 112, 124 and 156). In this way, it was possible to calculate the length of the first interval. Thus, this value obtained could be compared with that obtained from Equation (III.48). It was decided that the total number of mesh nodes in *r* direction was found when the length of the first interval had similar value to the distance to the pipe wall calculated from Equation (III.48). Different total number of nodes in *x* direction were also tested (10, 20, 30 and 40). All simulations were run with the mesh created with the parameters specified in Table V.3.

Table V.3 – Structured non-uniform mesh parameters.

Parameter	Value
Mesh (1 m of pipe)	20 (axial) × 94 (radial) nodes
Total number of quadrilateral cells	1767
Total number of nodes	1880
Total number of interfaces	3780
Interval length ratio, *R*	1.05

V.5 – RESULTS AND DISCUSSION

In order to investigate the flow of pulp suspensions, experimental and numerical studies were conducted. The pulp flow regime was evaluated by means of pressure drop values and EIT tomographic images. Additionally, numerical computations were performed with the CFD model proposed in Chapter IV.

V.5.1 – EXPERIMENTAL STUDIES

EIT images and pressure drop curves for *Eucalyptus* pulp suspension with two different consistencies (c = 1.01 and 1.50 %) were obtained in order to get experimental information about the different pulp flow regimes, mainly knowledge about plug fibers evolution. It should be noted that it was decided here to show only EIT images for the flow tests presented in Table V.1. However, in the pressure drop curves (see Figure V.4) additional experimental points for different mean flow velocities are presented.

The transition flow regime was approached for the three higher velocities attained for the lower pulp consistency (i.e. c = 1.01 % and U_b = 2.0, 2.5 and 3.0 m s^{-1}). Due to pump limitations, experiments with higher velocities were not possible to be performed. In this way, fully developed turbulent pulp flow regime could not be reached. For the higher consistency (i.e. 1.50 %) transition regime was only approached. EIT tomographic images are shown in Figure V.5.

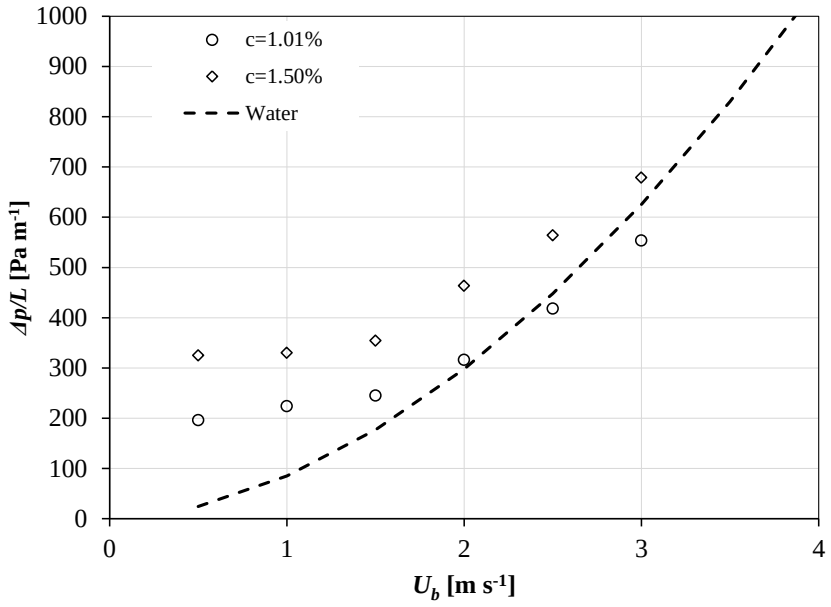

Figure V.4 – Experimental pressure drop profiles plotted in linear scales – *Eucalyptus* pulp.

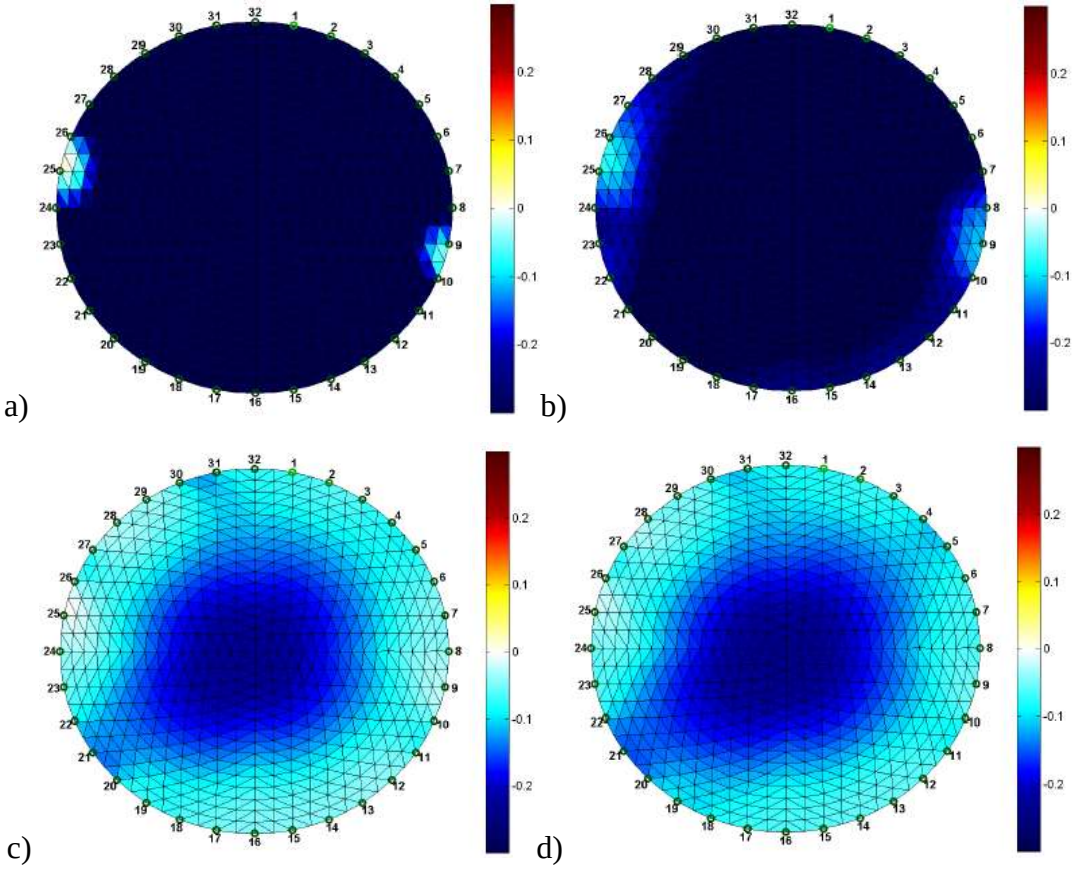

Figure V.5 – EIT images obtained for (a) c = 1.01 % U_b = 2.0 m s^{-1}, (b) c = 1.01 % U_b = 3.0 m s^{-1}, (c) c = 1.50 % U_b = 2.0 m s^{-1}, and, (d) c = 1.50 % U_b = 3.0 m s^{-1}.

In Figure V.5, electrode number 1 indicates the electrode placed at the highest vertical position. A darker colour means a lower conductivity region while, in the opposite, a lighter colour corresponds to higher conductivity regions. Since tap water was doped with NaCl to have higher conductivity than that of fiber suspension, larger values of conductivity were observed for regions where the existence of fibers is lowest.

Comparing EIT images for the two different pulp consistencies tested (i.e. 1.01 and 1.50%), the darker blue colour observed in almost all pipe section for c = 1.01 % indicates high radial homogeneity of fibers, as could be expected in the transition regime, where plug starts to disrupt. However, this data is not completely consistent with what was to be expected, i.e. not so darker blue colours observed until very near the pipe wall. Therefore, a lighter colour region was predictable near the pipe wall even if with lower thickness than that observed in Figures V.5c) and V.5d). Maybe flow instabilities created by plug disruption led to regions with not so well defined differences of conductivity. Also, the tendency of fibers to move towards the pipe wall giving small free water zones, may have led to conductivity represented by a scale of blue colour not so notorious. On the other hand, the global lower

fiber concentration for this consistency could lead to lower signals, lower conductivity differences, which is the signal acquired by the EIT system.

For the higher consistency, c = 1.50 %, fibers were more concentrated near the pipe centre, where from pressure drop curve (Figure V.4) plug flow regime was present. A slightly wider darker blue zone as well as slightly wider intermediate blue zone were observed for the higher mean flow velocity (i.e. U_b = 3.0 m s^{-1} – Figure V.5d)). This profile was in accordance with the tendency of fibers to disperse once flow velocity was increased. Moreover, the intermediate blue colour may indicate that an intermediate zone between the plug and lighter colour zone (water layer) exists. This fact could result from fluctuations in fluid suspension medium due to increasing flow velocity and, consequently, turbulence intensity of suspending medium, which contributed to deform and disintegrate fibers on the plug surface.

EIT tomographic images shown in Figure V.5 corroborated the flow regime expected from pressure drop curves, i.e. only plug and transition regimes where reached in the experiments. Moreover, different pulp flow regimes were obtained for the same flow velocity when pulp consistency changed.

V.5.2 – CFD STUDIES

In this section, simulations were performed for the cases presented in Table V.1 with the CFD model developed in Chapter IV. The model was validated using pressure drop measurements, the parameter commonly available in pulp suspensions flows. CFD pressure drop results are presented in Table V.4. The existence of fibers in the lubrication layer was assumed.

Table V.4 – Numerical pressure drop values – *new* CHC Bartosik I model.

c [%]	U_b [m s^{-1}]	$\dot{m}_b$ [kg s^{-1}]	$\Delta p/L_{water}$ [Pa m^{-1}]	$\Delta p/L_{exp}$ [Pa m^{-1}]	$\Delta p/L_{num}$ [Pa m^{-1}]	δ [%]
1.01	2.0	16	298	316	212	33
1.01	3.0	24	625	554	436	21
1.50	2.0	16	298	463	80	83
1.50	3.0	24	625	679	228	66

It was detected from experiments that the turbulent flow regime of pulp suspensions for which the model was used, was not guaranteed. Observations show that, instead, plug and transition regimes were tested. Nevertheless, as shown in Table V.4, the *new* CHC Bartosik I

model (CHC model with the new Bartosik I damping function, see Chapter IV, Section IV.2.4, for its description) was able to predict the flow of pulp suspensions. However, it should be emphasized that the accuracy of the model was improved when turbulent or transition pulp flow regime was attained (testes for 1.01 % consistency). The two key factors of the CFD model, new viscosity expression and damping function of turbulent viscosity, were able to attenuate turbulence. However, since fully developed turbulent flow regime was not observed, the turbulence reduction was overpredicted, mainly for plug flow regime, numerical pressure drop being always smaller than the experimental one.

In order to evaluate the main scalar variables and the effectiveness in predicting turbulence, the profiles of turbulent quantities, dimensionless velocity and velocity profiles, viscosity and parameters/function related to the LRN k-ε turbulence models are presented next.

As can be seen from viscosity profiles shown in Figure V.6, there were no differences in the viscosity profile when compared with those obtained in Chapters III and IV (see Figures III.10, III.13 and IV.17). Higher flow resistance was observable near the pipe centre whereas lower predicted viscosity values were attained near the pipe wall. As expected, a lower pulp consistency means that fewer fibers are present in the flow leading to lower flow resistance, and in turn to lower viscosity. The viscosity profiles for the higher pulp consistency cases (i.e. 1.50 %, Figure V.6b)) can be compared with those predicted in Chapter IV, Section IV.3.3, for the same pulp consistency (see Figure IV.17a) – Cases IV.F.CBI.1.A0 and IV.F.CBI.1.B0) even if a different pipe diameter and different flow conditions were simulated. According to Figures IV.17a) and V.6b), higher values of pulp viscosity were predicted when the pipe diameter was larger and mean flow velocity was lower (Figure V.6b)). In fact, decreasing mean pulp flow velocity tends to decrease local shear rate and to increase pulp viscosity. For c = 1.50 % U_b = 2.0 m s^{-1} (Figure V.6b)) one can observe a sudden transition in the viscosity profiles between the flow core and the lubrication layer. This fact can be attributed to a more uniform velocity profile predicted near the interface of the flow core region – lubrication layer, which may be related to a more flow homogeneity in this transition region.

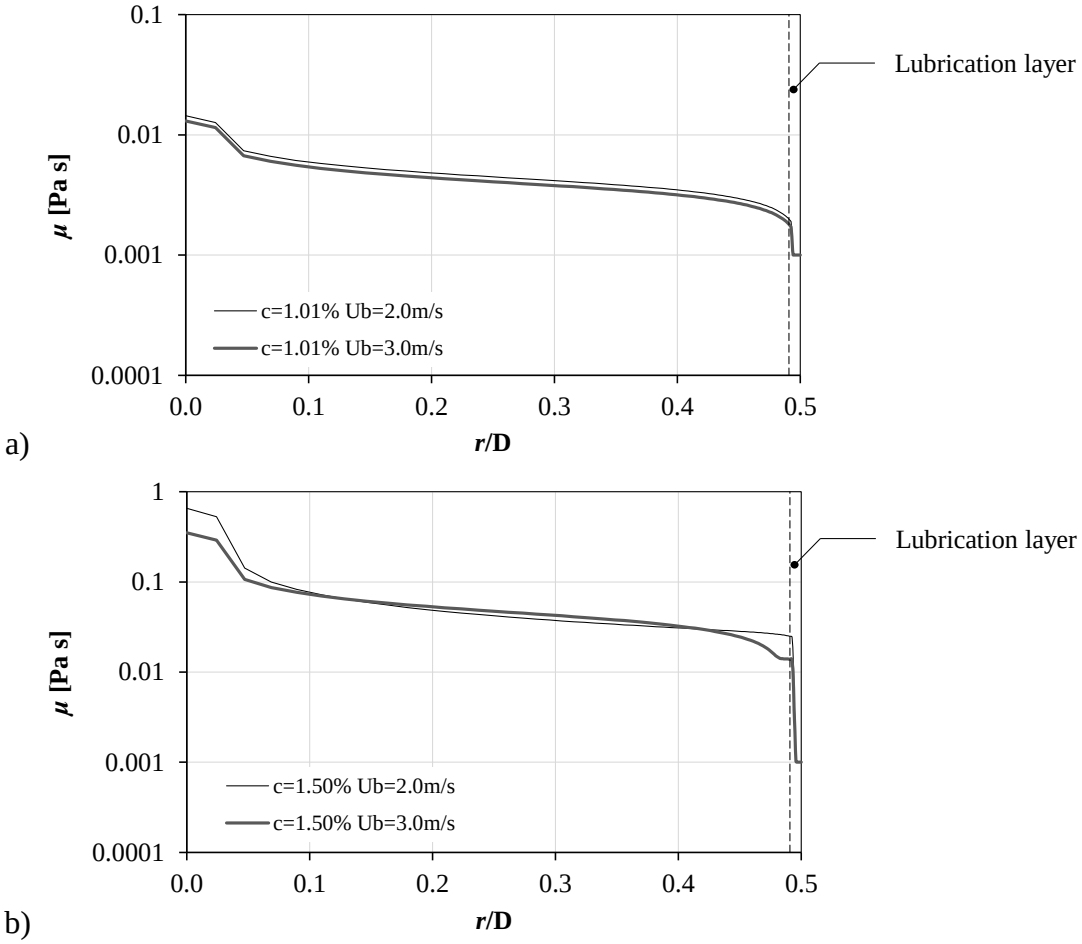

Figure V.6 – Radial viscosity profiles for (a) c = 1.01 %, and, (b) c = 1.50 %.

Figures V.7 and V.8 show the velocity and dimensionless velocity profiles. There is reasonable coherence between those profiles obtained for the different pulp consistencies as well as with those described in Chapter IV, Section IV.3.3 (see Figures IV.19 and IV.20). The profile of u^+ observed in Figure V.8a) (c = 1.01 %) can be explained with the transition pulp flow regime, where the CFD model was able to deal with turbulence and viscosity more adequately. Also, for this pulp consistency a more uniform velocity profile was predicted which is in accordance with the better approach to the transition pulp flow regime. The *yield* region (II) can be easily identified, as well as the *core* region (III) which has small thickness (see Figure V.8a)). Radial velocity and dimensionless velocity profiles for c = 1.50 %, predicted for a smaller pipe diameter and higher flow velocities, are presented in Chapter IV, Section IV.3.3 (see Figures IV.19a), IV.19b), IV.20a) and IV.20b)). However, these data will not be used in this section to compare with profiles presented in Figures V.7b) and IV.8b) since the present results correspond to plug flow regime and, also, upper plug flow regime near to transition pulp flow regime. Two distinct regions can be identified in Figure V.8b): the *yield* region (II), and the *core* region (III). For lower mean flow velocity (i.e. 2.0 m s^{-1}), where

the plug flow regime was better predicted, the thickness of *core* region extends closer to the viscous sublayer than when velocity is higher (i.e. 3.0 m s^{-1}). This fact is in accordance with the wider plug thickness and to a not disrupted plug for this velocity. The increase of mean flow velocity leads to plug deformation as a consequence of increasing turbulence from wall towards the pipe centre, which is observed through the wider *yield* region (see Figure V.8b) c = 1.50 % and U_b = 3.0 m s^{-1}). Additionally, it is not observed the *near wall* region (see Chapter III, Section III.3.3.2, Figure III.8). In the transition pulp flow regime, the plug of fibers starts to disrupt, i.e. the fibers in contact with the lubrication layer tend to separate from the fiber network. In this way, a small fluidized region starts to appear between the plug region and the lubrication layer, which can be identified by a dimensionless velocity profile with the same slope of a Newtonian fluid (*near wall* region).

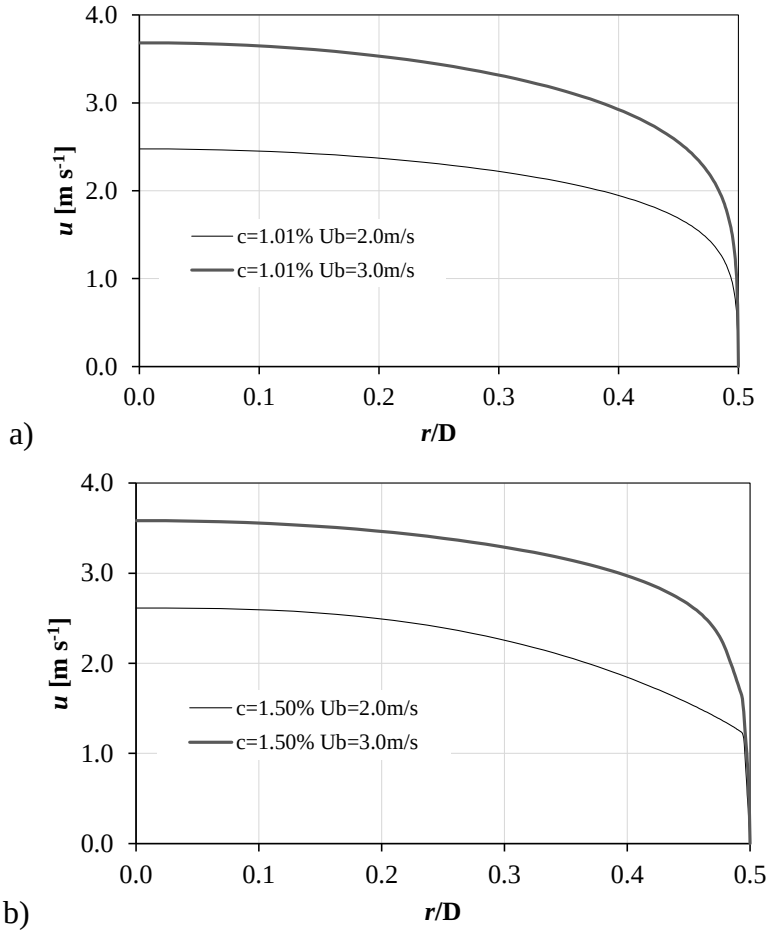

Figure V.7 – Radial profiles of velocity for (a) c = 1.01 %, and, (b) c = 1.50 %.

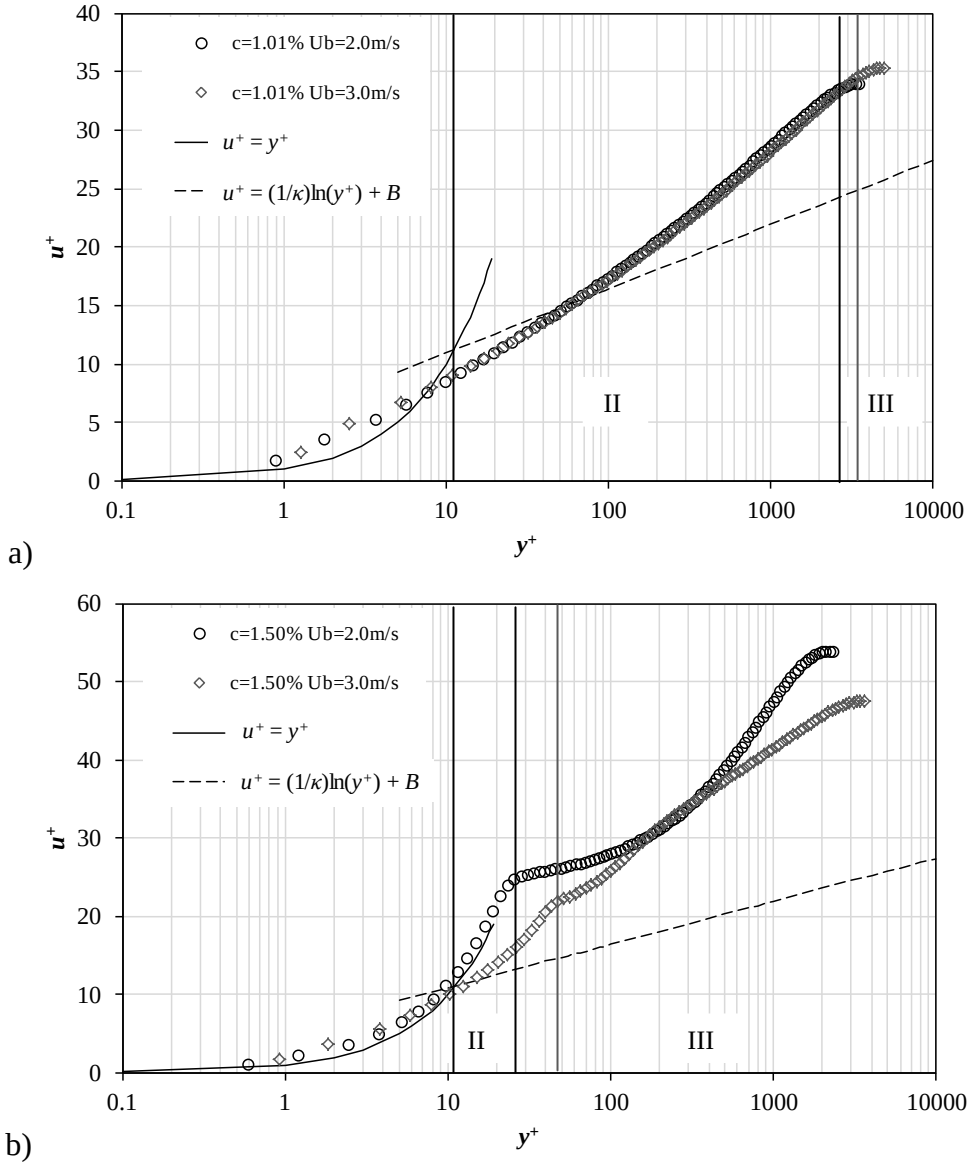

Figure V.8 – Dimensionless velocity profiles for (a) c = 1.01 %, and, (b) c = 1.50 %.

In Figures V.9 and V.10 the turbulent kinetic energy and its dissipation rate are presented. The k and ε profiles for the lower pulp consistency (i.e. 1.01 %) are in accordance with the better approach to the transition pulp flow regime. It should be noted that for c = 1.50%, U_b = 2.0 and 3.0 m s^{-1}, k and ε have very low values, the reason why they could hardly be distinguished if they were represented in the same figure. That is why it was decided to show the k and ε profiles for c = 1.50 %, separately, in Figures V.9b), V.9c), V.10b) and V.10c). These results confirmed that in the transport equation of momentum in r-direction, molecular viscosity preponderated over turbulent viscosity. This fact was in accordance with the absence of turbulence for the higher pulp consistency. That is why turbulence damping was overpredicted for this consistency assuming that the transition regime was barely reached, and thus too low pressure drop values were calculated. The fully turbulent pulp flow regime

simulated in Chapter IV, Section IV.3.3, for c = 1.50 % (see the profiles of k and ε presented in Figures IV.23a) and IV.24a)), was not approached in this chapter, as mentioned previously. This fact can be observed through the lower values of turbulent quantities predicted in this chapter (compare profiles presented in Figure IV.23a) with Figures V.9b) and V.9c), and, Figure IV.24a) with Figures V.10b) and V.10c)).

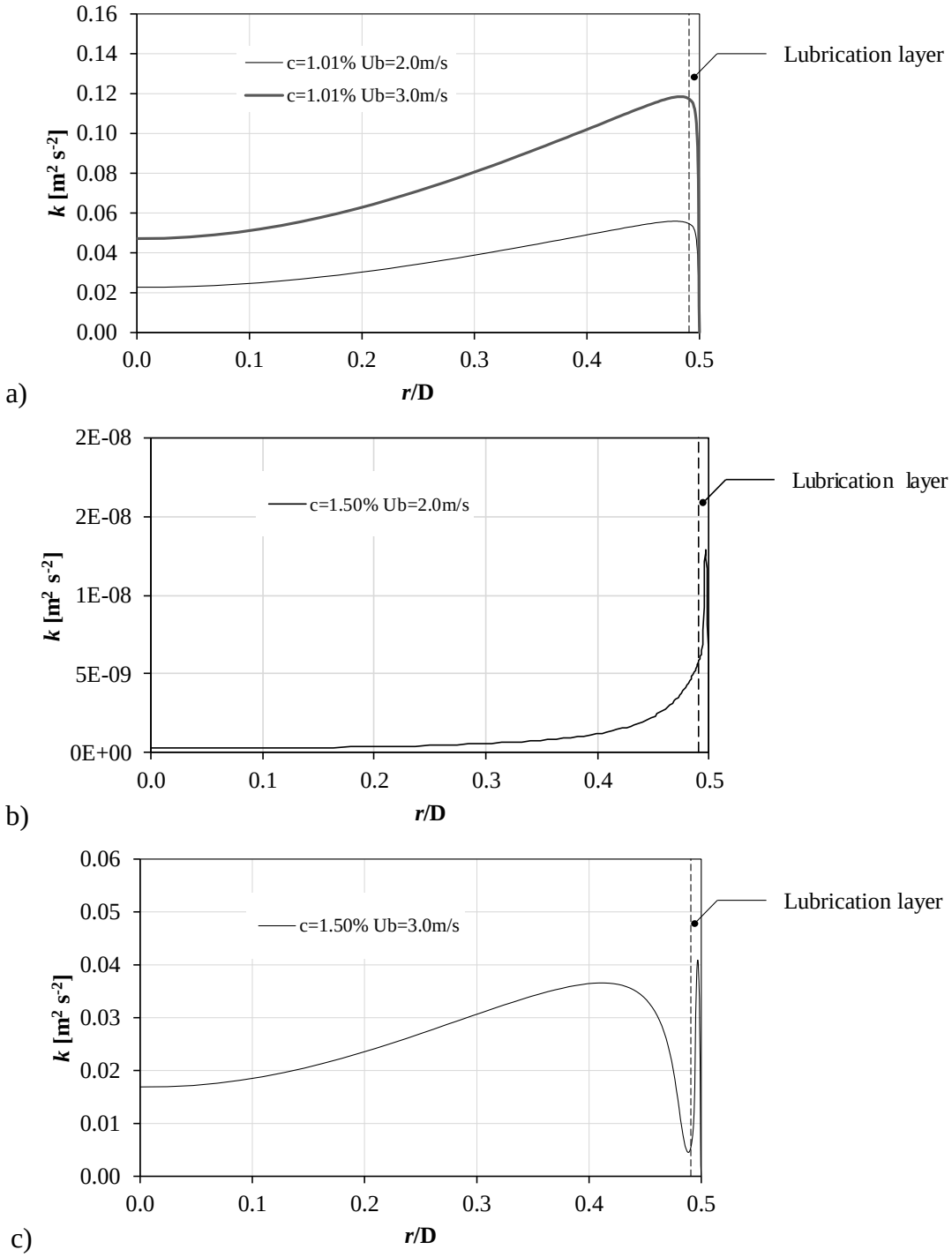

Figure V.9 – Radial profiles of turbulent kinetic energy for (a) c = 1.01 %, (b) c = 1.50 % U_b = 2.0 m s^{-1}, and, (c) c = 1.50 % U_b = 3.0 m s^{-1}.

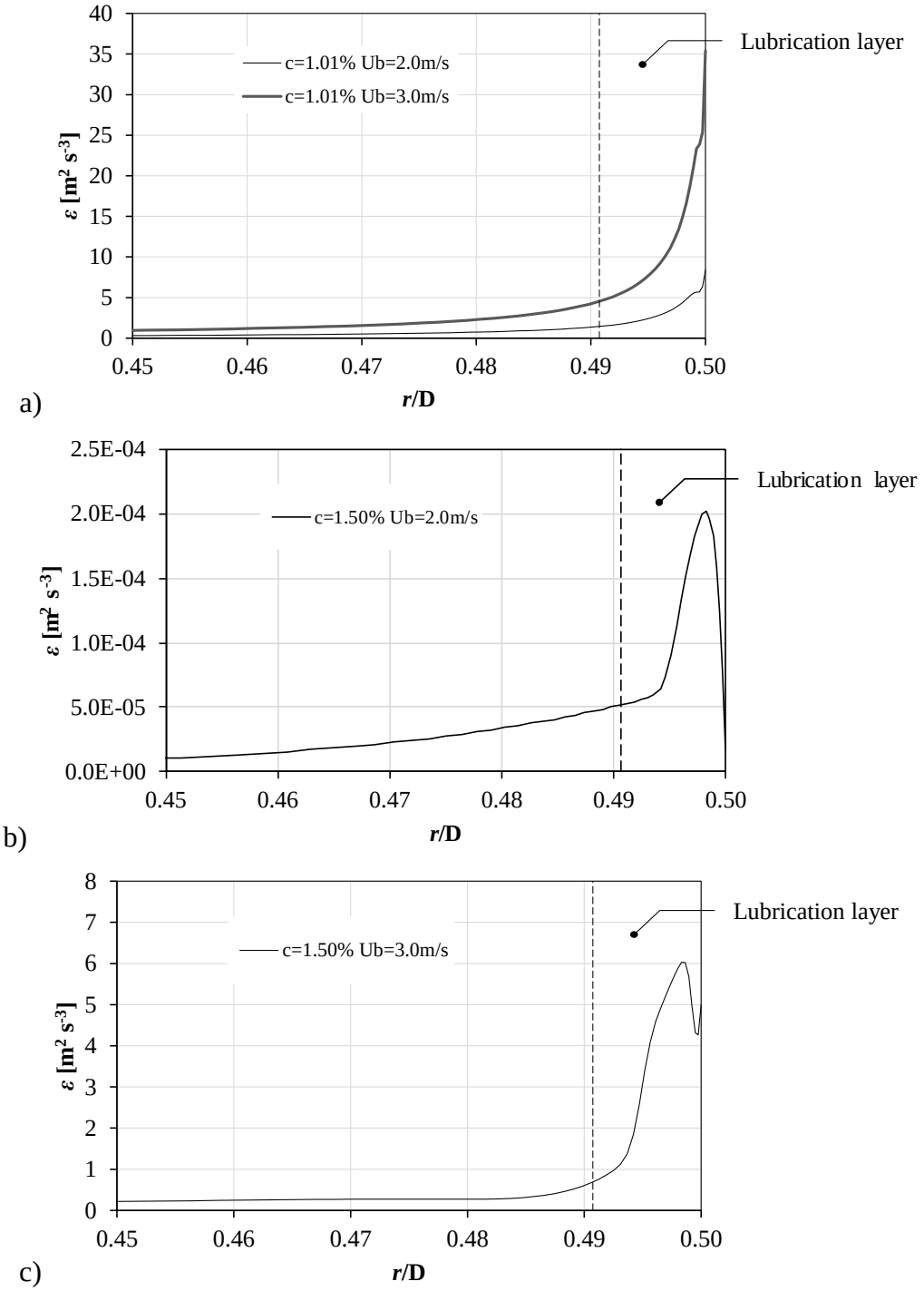

Figure V.10 – Radial profiles of dissipation rate of turbulent kinetic energy for (a) c = 1.01 %, (b) c = 1.50 % U_b = 2.0 m s^{-1}, and, (c) c = 1.50 % U_b = 3.0 m s^{-1}.

After the comparison of turbulent quantities, it is important to compare the radial evolution of f_μ, Re_t and μ_t, since turbulent viscosity is directly related to the damping function which in turn depends on turbulent Reynolds number (see Equation IV.3 and Table IV.9).

Figure V.11 shows the radial variation of the damping function of turbulent viscosity. In fact, the overreduction of turbulent quantities was observed mainly for the higher consistency

cases (especially for U_b = 2.0 m s^{-1}) resulting in lower values of turbulent quantities predicted by using the turbulence damping function (see Figure V.11b)).

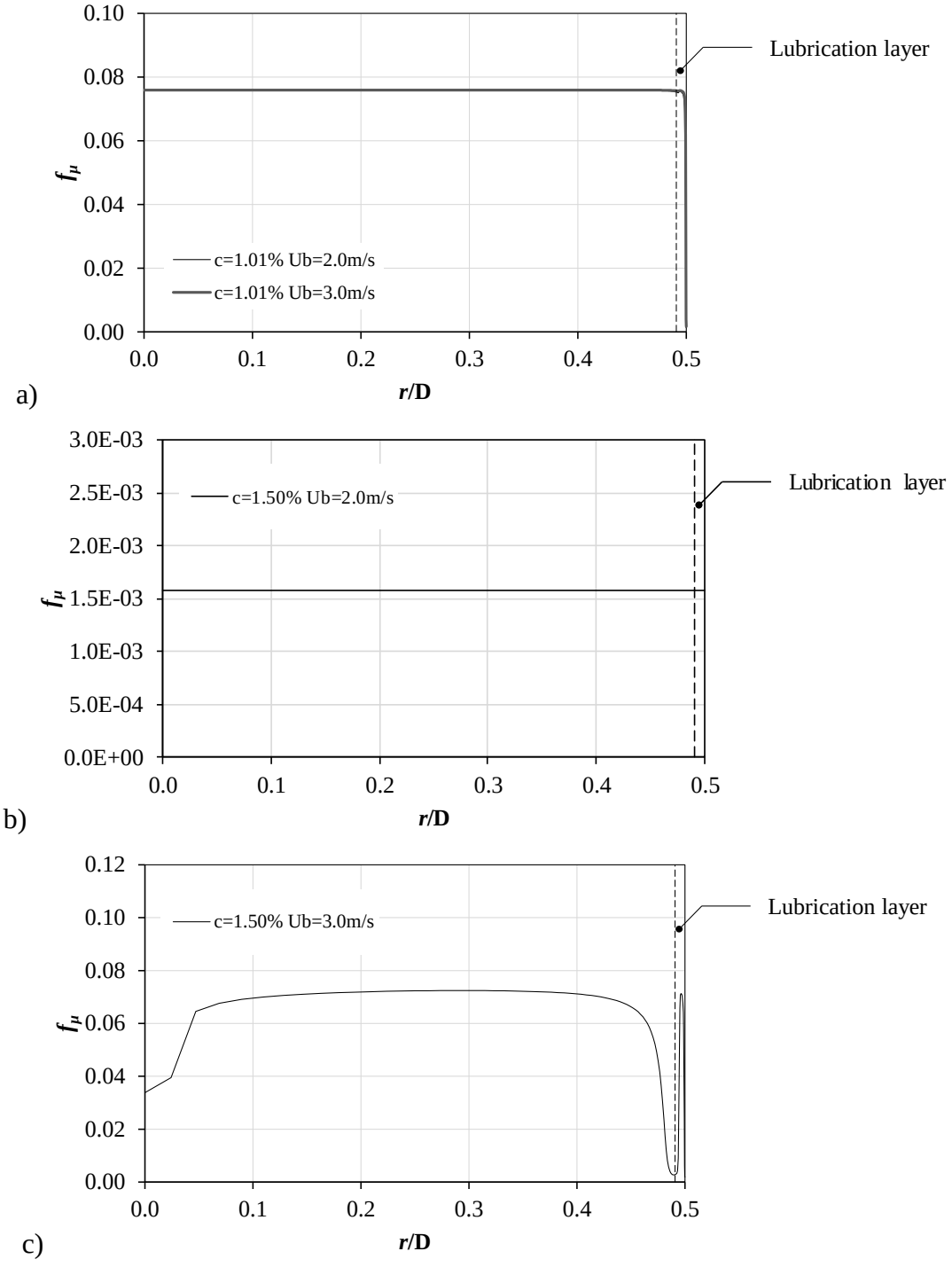

Figure V.11 – Variation of the damping function f_μ for (a) c = 1.01 %, (b) c = 1.50 % U_b = 2.0 m s^{-1}, and, (c) c = 1.50 % U_b = 3.0 m s^{-1}.

The radial profiles of turbulent Reynolds number shown in Figure V.12 complement turbulence characteristics. Also, as happened with turbulent quantities, for c = 1.50 % U_b = 2.0 m s^{-1}, the turbulent Reynolds number reached very low values which cannot be detected if they are represented, in the same figure, with the profile of c = 1.50 % U_b = 3.0 m s^{-1}. The small values near the pipe wall are a consequence of higher values predicted for the dissipation rate of turbulent kinetic energy (see Figure V.10). Also, smaller values than those obtained in Chapter IV, Section IV.3.3 (c = 1.50 %, Figures IV.31a) and IV.31b)) are observed in Figures V.12b) and V.12c).

As can be seen in Figure V.13, turbulent viscosity increases towards to the pipe centre. Additionally, for c = 1.50 % U_b = 2.0 m s^{-1}, turbulence is underpredicted which is a consequence of lower turbulence viscosity values resulted from very high damping effect of the damping function proposed, reflected small values of the function f_μ. Comparing molecular viscosity profiles (Figure V.6) with turbulent viscosity profiles (Figure V.13), one could conclude that for the lower consistency case (i.e. 1.01 %) turbulence was the preponderant factor over viscous effects predicted with the CFD model, whereas for the higher consistency molecular viscosity was the main diffusibility factor resulting from the absence of turbulent flow observed, which was well taken into account by the turbulence model.

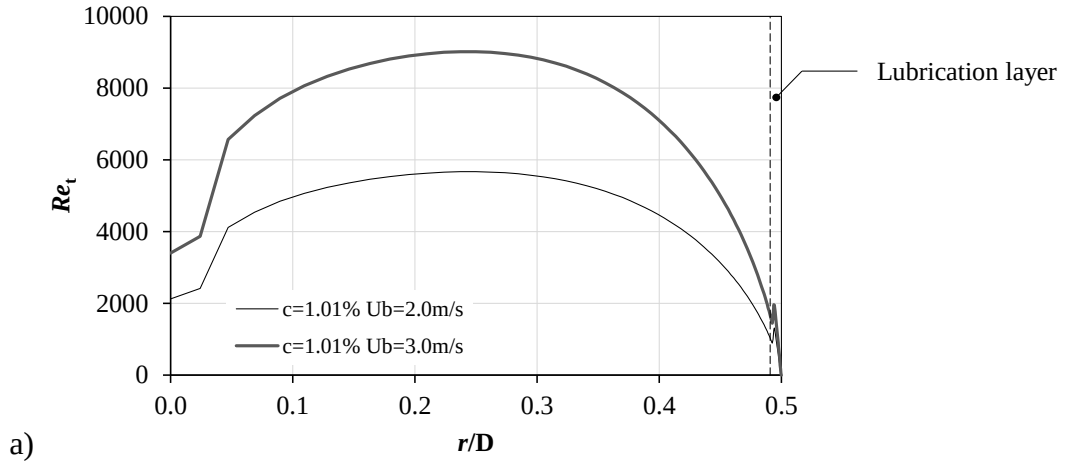

a)

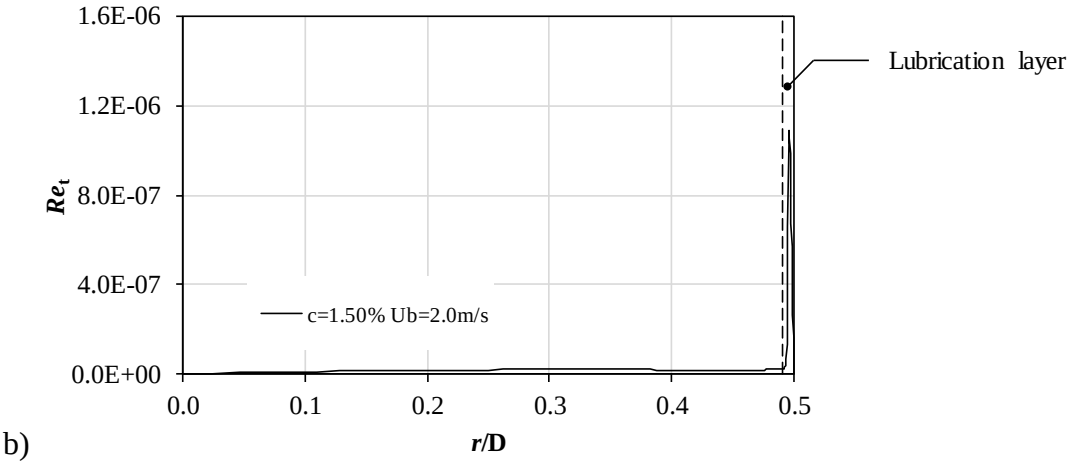

b)

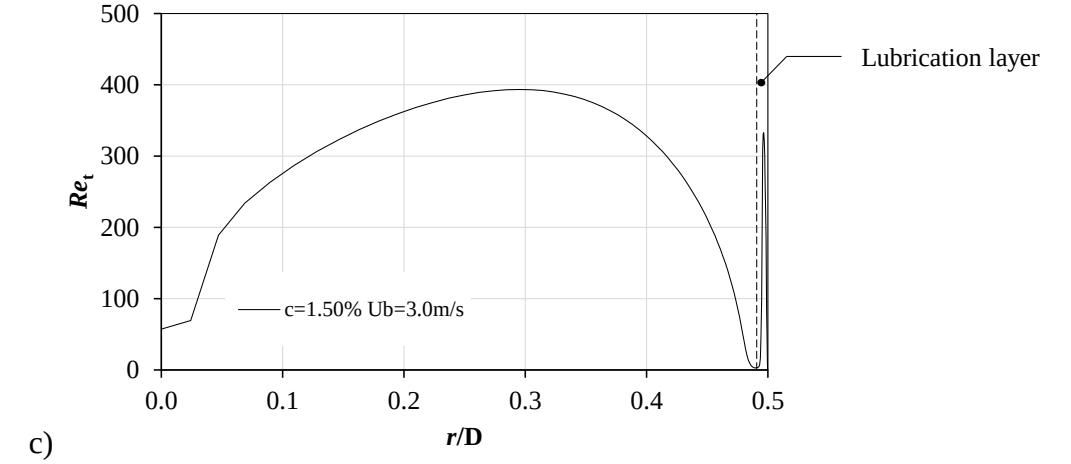

c)

Figure V.12 – Variation of Re_t for (a) c = 1.01 %, (b) c = 1.50 % U_b = 2.0 m s^{-1}, and, (c) c = 1.50 % U_b = 3.0 m s^{-1}.

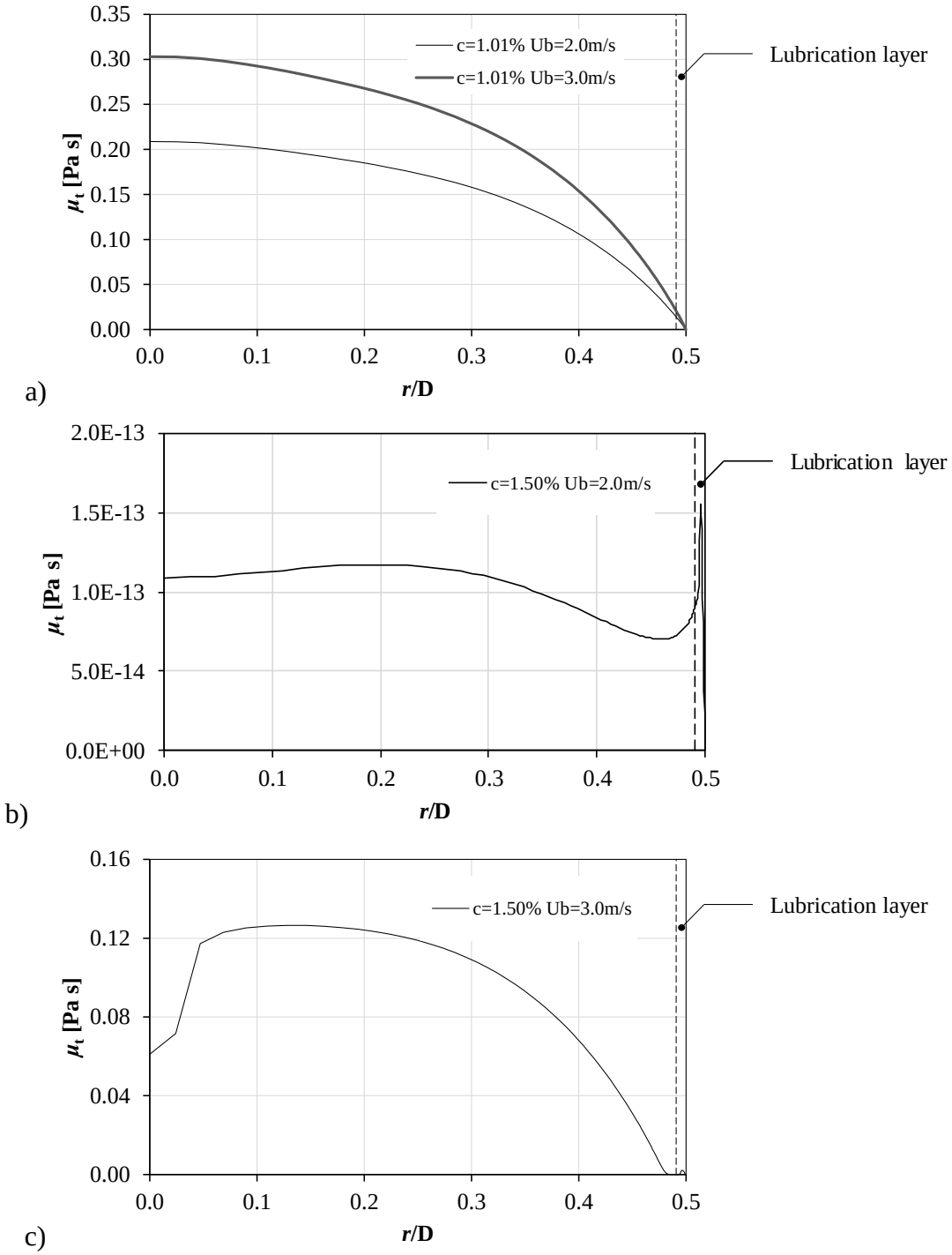

Figure V.13 – Variation of turbulent viscosity for (a) c = 1.01 %, (b) c = 1.50 % U_b = 2.0 m s^{-1}, and, (c) c = 1.50 % U_b = 3.0 m s^{-1}.

The success application of the pseudo-homogeneous CFD modelling of the turbulent pulp flow was dictated by the pulp flow regime. Despite this, its applicability in simulating different pulp flow conditions for different radial pipe dimensions without predicting too deviated pressure drop values and with consistent conclusions, demonstrated that the model proposed is able to reasonably predict the flow of pulp suspensions.

V.6 – CONCLUSIONS

In order to investigate the flow behaviour of *Eucalyptus* fiber suspensions, a CFD pseudo-homogeneous model was applied. The calculated pressure drop values were compared with those obtained from experiments conducted in a pilot rig properly equipped to deal with pulp suspension flows. Additionally, in order to understand the radial distribution of fibers in the flow, an EIT technique was used. Images of conductivity distribution were obtained, which could be interpreted and validated qualitatively by means of expected pulp flow regime.

Flow experiments were performed to obtain data for the validation of the computational model. The EIT technique was used to complement the experimental information (pressure drop), usually used to validate the pulp flow regime. Pressure drop values showed that turbulent pulp flow regime was not reached, instead plug and transition pulp flow regimes were observed. According to EIT images constructed from electrical potential measurements, after a voltage source was injected into the domain, a plug of fibers could be identified, mainly for the highest consistency tested.

A pseudo-homogeneous CFD model of turbulent pulp flow was evaluated. The two key factors of this model were the viscosity model and the damping function specifically developed to deal with the presence of fibers in the flow. Pressure drop values fit well flow data obtained in transition pulp flow regime. However, the accuracy of the CFD model was deteriorated as it was applied to test data of plug flow regime. It was found that the model underpredicts turbulence, mainly when plug flow regime is completely well stablished. In this case, estimated turbulent quantities were significantly reduced. In this way, the calculations could correctly account for the absence of turbulence in the pulp flow. Nevertheless, the CFD solution indicated that the model could be applied to simulate the flow of pulp fiber suspensions even if larger pressure drop differences were encountered for plug flow regime.

PART D. SUMMARY

The last part of this thesis provides a general overview of the work developed on this thesis as well as the main results and conclusions. As a final point, suggestions for future work are proposed.

VI – CONCLUSIONS AND FORTHCOMING WORK

Given the presence of a great number of paper based products in the global market, the research for new, better and optimized technologies to produce high quality products is very important. The process strategy in pulp and paper mills is basically the same, supported in the same process steps. However, different process specifications can lead to different end product properties as well as different applicability of the final product. Important research areas arise from the demand of high quality products, rigorous regulations and economic constraints. The pulp and paper process is expensive, with energy consumption representing a great part of the global costs. Thus, economical optimization without losing end product quality is a challenge. A large part of the global process costs are related to energy costs, some coming from the inadequate design of industrial equipment, usually resulting from the use of empirical correlations out of the range of their applicability, leading to conservative and oversized equipment. A better understanding of pulp suspension flows can help in the design of more correct piping systems with proper process specifications. In this way, economically more favourable industrial processes can be obtained without losing product specifications during the process.

Different strategies have been investigated in this work related to the characterization of the flow of pulp fiber suspensions in order to give better knowledge about this problem. Three main research areas are identified: (*i*) rheological characterization, (*ii*) flow description, and, (*iii*) numerical modelling of pulp flow. Several methods have been proposed to investigate pulp's rheology and to characterise pulp's flow behaviour. Pulp's opacity, flexibility and high flow complexity imposes serious issues in the development of appropriate devices for rheological and flow characterization. Computational strategies are assumed to be a powerful tool to predict reliable data possible to be used in pulp's flow characterization under different flow conditions, as well as for different types of pulp. So far, most of the computational work conducted by several authors was developed considering dilute suspensions due to the high computational resources needed and, also, large number of physical parameters to be included in the modelling. However, in the different pulp and paper process stages, the consistency grade can vary. In this work, research is conducted on the development of a Computational Fluid Dynamics simulation tool for pulp flow modelling considering dilute and high pulp

consistencies (Part B), and of an Electrical Impedance Tomography technique for pulp flow characterization which will be coupled with flow simulation (Part C).

VI.1 – CONCLUSION REMARKS

The development of a CFD based model able to predict the turbulent flow of pulp suspensions in a pipe was investigated in Part B. Aiming to simulate *Eucalyptus* and *Pine* pulp flow under different consistencies and flow conditions, a two-dimensional CFD strategy was followed. A pseudo-homogeneous strategy considering as starting point a homogeneous Newtonian model was tested. Afterwards, in a first stage, the non-Newtonian behaviour of *Eucalyptus* pulp suspension was included in the model by considering variation of pulp's viscosity only with shear rate. A pure water annulus, surrounding the core region, was considered, where the presence of fibers was not included. The standard high Reynolds k-ε turbulence model was used to calculate the pressure loss across 1 m of pipe. It was concluded that to apply only the standard high Reynolds k-ε turbulence model with the inclusion of the non-Newtonian pulp's viscosity behaviour was not enough to replicate experimental information. Pressure drop was considered as the control parameter, due to its importance for design of the complete transport system. Therefore and afterwards, new wall functions were applied and adjusted for the *Eucalyptus* pulp flow cases simulated. Significant improvements on numerical predictions were obtained with the new wall function parameters. In spite of the good fit between numerical and experimental pressure drop data, it was found through the analysis of the numerical profiles that important scalar quantities had too large variations in the near wall region. A different modelling strategy was then investigated.

The flow of *Eucalyptus* and *Pine* pulp suspensions was also investigated with the pseudo-homogeneous model but using different low-Reynolds-number k-ε turbulence models to take into account the damping of turbulence caused by the fibers. A new viscosity model was proposed considering the influence of shear rate as well as the influence of pulp consistency. A very thin layer surrounding the flow core region was again considered. The presence of fibers in the lubrication layer was tested through the inclusion of a gradient of pulp consistency expressed as a linear dependency on distance to pipe wall. It was found that these models could be applied to simulate the flow of pulp suspensions in a pipe leading, however, to an overprediction of pressure drop values. This was attributed to an inadequate modelling of turbulence with underprediction of turbulence attenuation. Also, the effect of

considering only a pure water annulus or a lubrication layer with fibers was not influencing the quality of the numerical solution. Model adaptations were accomplished modifying the damping function of turbulent viscosity. Thereafter, three different damping functions were tested, considering the successfully applicability of those damping functions on the prediction of the flow of power-law fluids and particles flow. Still, fitting to experimental values was not satisfactory enough. Remarkable improvements were observable when adapting the damping function used in the literature for power-law fluids. However, those improvements were mainly attained for the higher consistency tested. Thus, a proper damping function able to improve numerical calculations for both dilute and high concentrated pulps was still needed. Modifications on the two damping functions developed to simulate the flow of particles were proposed. In both damping functions an extra term considering fiber characteristics given by the fibers aspect-ratio was added. The damping function considering the yield stress of pulp suspension possesses more physical meaning, indicating that the final model could capture better the flow of pulp suspensions with that damping function. In general, the new damping function had lower values than those obtained with the LRN k-ε turbulence model base, leading to stronger attenuation of turbulence. Also, a good compromise between molecular viscosity and turbulent viscosity was achieved. For the lower consistency cases, both molecular viscosity and turbulence viscosity are important. Whereas, for the higher consistency case turbulent viscosity was not the main factor in core region where molecular viscosity plays an important role in eddies structure attenuation. Moreover, the CFD pseudo-homogeneous model developed was applied successfully to calculate the flow of two different types of pulp suspensions, *Pine* and *Eucalyptus* suspensions, longer and shorter fibers. Pulp consistencies in dilute and high concentration range as well as different mean flow velocities for each consistency were simulated. The accuracy of the CFD model was dependent on the rheological information for lower shear rates range. The rheological information available for the problem under study might have led to some discrepancies between numerical and experimental data. The final model presented two key features, the molecular viscosity where the presence of fibers on the flow was included in the model, and a new damping function where the turbulence attenuation resulting from the presence of fibers was considered.

In Part C of this thesis, flow of *Eucalyptus* pulp suspensions was characterised by an imaging technique, EIT – Electrical Impedance Tomography method, and simulated with the CFD pseudo-homogeneous model proposed in Part B. Pressure drop measurements were used to anticipate the pulp flow regime from pressure drop curve observations. Following, EIT images were used to corroborate the pulp flow regime predicted. From conductivity

measurements it was concluded about fibers homogeneity and plug evolution. In the plug flow regime, it was observed a well-defined zone of lower conductivity in the central part of the pipe indicating a strong plug of fibers. In spite of this well distinct region, when transition flow regime was detected from the pressure drop curve a higher homogeneity of the fibers was noticed, as expected, even if it was not predictable very low conductivity differences until so very near the pipe wall as observed experimentally. CFD simulations were performed with the model developed for fully turbulent pulp flow. The accuracy of the CFD model was lost for the plug flow regime where turbulence attenuation was over predicted with turbulence quantities under evaluated. This fact was in agreement with the lack of turbulence in the flow domain. Nevertheless, the model was able to be applied to simulate experimental data of transition flow regime.

The validation of the CFD pseudo-homogeneous model proposed in this thesis was done for two different pulp suspensions, different pulp consistencies and flow conditions and, also, for two different pipe diameters. Additionally, it was evaluated if turbulence (or lack of turbulence) was well captured for different pulp flow regimes. Furthermore, the model gave promising results in pulp suspension flows calculations also for the transition flow regime.

VI.2 – SUGGESTIONS FOR FUTURE WORK

CFD tools are able to be used in pulp suspension flows calculations. The numerical results showed that the CFD model could predict fairly well the non-Newtonian behaviour of pulp suspension as well as the attenuation of turbulence due to the presence of fibers in the flow. Both numerical and experimental investigations should continue in order to obtain a better and complete understanding of pulp flow mechanisms for the different pulp flow regimes.

Rheological experiments and modelling strategies should be accomplished for lower shear rates range. Most of the experimental devices give highly uncertain values in low shear rate zones. The present work showed that the rheological model should be as most accurate as possible, mainly, for low shear rate zones where the trend is to have higher variations of pulp's viscosity.

The experimental information of pulp's flow can be further investigated by using Electrical Impedance Tomography (EIT) technology complemented with other techniques such as the Optical Coherence Tomography (OCT) technique. Mainly because experimental

techniques do not supply complete information such as velocity profile until very near the pipe wall, coupling more than one technique is necessary. Thus, using these two imaging techniques, information concerning velocity profiles in all radial domain can be obtained in order to validate the CFD results. Additionally, OCT can provide information about fibers distribution very near the wall. Therefore, that information can represent substantial improvement for a better description of pulp's consistency variation in the lubrication layer, to be included in the CFD model.

The effect of pulp consistency was examined experimentally in both rheological and flow tests. However, the experimental flow tests were not always performed for the same pulp consistency rheologically tested. Therefore, the same pulp consistency should be used in the flow tests and rheological studies. In order to contribute to a better and complete knowledge of the flow of fiber suspensions a wide range of pulp consistencies should be tested, mainly for *Pine* pulp suspensions. Additionally, experimental flow data for concentrated pulp suspensions should be obtained for higher mean flow velocities in order to guarantee turbulent pulp flow regime.

Another important field is related to the development of strategies to obtain information about turbulence intensity in fibrous systems. The pulsed ultrasonic Doppler velocimetry can be used to obtain turbulent fluctuation intensity and turbulence attenuation. Thus, information related with turbulent quantities can be obtained in order to verify the turbulent kinetic energy predicted with the CFD model.

The present results showed that the CFD model developed can give good predictions for both transition and turbulence pulp flow regimes. Thus, it has been proved that the LRN k-ε turbulence model proposed for the liquid phase is a useful tool to predict multiphase flows if adequately adapted. Further experimental research is suggested to investigate the possibility of inclusion in the damping function of an additional term related with the percentage of drag reduction.

Further investigation with rigid fibers can be done in order to validate the model for different types of fibers, flexible and rigid fibers. In this case, it is possible that maybe the rigidity of fibers has to be taken into consideration. Thus, it is suggested that the research developed in this work should continue to study the flow of other types of multiphase systems with industrial relevance.

Finally, the application of the CFD model proposed, for industrial conditions, should be addressed. The presence of a suspending liquid different from pure water can influence the successful application of the CFD model. Still, research efforts should continue in order to

contribute for the better knowledge of the flow of pulp fiber suspensions, and it is suggested to start studying complex pulp fiber suspensions corresponding to real pulp flow conditions.

REFERENCES

Abe, K.; Kondoh, T.; Nagano, Y. (1994) – "*A new turbulence model for predicting fluid flow and heat transfer in separating and reattaching flows – I. Flow field calculations*" – International Journal of Heat and Mass Transfer, 37(1): 139-151.

Abid, R. (1993) – "*Evaluation of two-equation turbulence models for predicting transitional flows*" – International Journal of Engineering Science, 31(6): 831-840.

Ansys Inc. (2010) – *ANSYS FLUENT Documentation*, Release 13.0.

Arola, D.F.; Powell, R.L.; McCarthy, M.J.; Li, T.-Q.; Ödberg, L. (1998) – "*NMR Imaging of pulp suspension flowing through an abrupt pipe expansion*" – AIChE Journal, 44(12): 2597-2606.

Asokan, K.; Kumar, C.V.A.; Dasan, J.; Radhakrishnan, K.; Kumar, K.S.; Ramamohan, T.R. (2005) – "*Review of chaos in the dynamics and rheology of suspensions of orientable particles in simple sjear flow subject to an external periodic force*" – Journal of Non-Newtonian Fluid Mechanics, 129(3): 128-142.

Barbosa, S.E.; Bibbó, M.A. (2000) – "*Fiber motion and rheology of suspensions with uniform fiber orientation*" – Journal of Polymer Science: Part B: Polymer Physics, 38(13): 1788-1799.

Barnes, H.A.; Edwards, M.F.; Woodcock, L.V. (1987) – "*Applications of computer simulations to dense suspension rheology*" – Chemical Engineering Science, 42(4): 591-608.

Bartosik, A. (2010) – "*Application of rheological models in prediction of turbulent slurry flow*" – Flow Turbulence and Combustion, 84(2): 277-293.

Bartosik, A. (2011a) – "*Simulation of the friction factor in a yield-stress slurry flow which exhibits turbulence damping near the pipe wall*" – Journal of Theoretical and Applied Mechanics, 49(2): 283-300.

Bartosik, A. (2011b) – "*Mathematical modelling of slurry flow with medium solid particles*". Mathematical Models and Methods in Modern Science, WSEAS Press, Tenerife, Spain. ISBN 978-1-6-61804-055-8

Bennington, C.P.J.; Kerekes, R.J.; Grace, J.R. (1991) – "*Motion of pulp fibre suspensions in rotary devices*" – The Canadian Journal of Chemical Engineering, 69(1): 251-258.

Bennington, C.P.J.; Kerekes, R.J. (1996) – "*Power requirements for pulp suspension fluidization*" – TAPPI Journal, 79(2): 253-258.

Bera, T.K.; Nagaraju, J. (2012) – "*Studying the resistivity imaging of chicken tissue phantoms with different current patterns in Electrical Impedance Tomography (EIT)*" – Measurement, 45(4): 663-682.

Bird, R.; Stewart, W.; Lightfoot, E. (2002) – "*Transport Phenomena*". Wiley, 2nd Edition, New York.

Björkman, U. (2008a) – "*The nonlinear history of fibre flow research. Part 1: Background and beginning*" – Applied Rheology, 18(2): 23974-23974-11.

Björkman, U. (2008b) – "*The nonlinear history of fibre flow research. Part 2: Continuation, reflections and suggestion*" – Applied Rheology, 18(3): 34694-34694-26.

Blanco, A.; Negro, C.; Fuente, E.; Tijero, J. (2007) – "*Rotor selection for a Searle-type device to study the rheology of paper pulp suspensions*" – Chemical Engineering and Processing, 46(1): 37-44.

Blanco, A.; Dahlquist, E.; Kappen, J.; Manninen, J.; Negro, C.; Ritala, R. (2009) – "*Use of modelling and simulation in the pulp and paper industry*" – Mathematical and Computer Modelling of Dynamical Systems: Methods, Tools and Applications in Engineering and Related Sciences, 15(5): 409-423.

Bousfield, D.W. (2008) – "*Rheological issues in the paper industry*" – Rheology Reviews, 6: 47-70.

Carvalho, M.G.V.S. (1999) – "*Efeito das variáveis de cozimento nas características químicas das pastas KRAFT de Eucalyptus globulus*". Tese de Doutoramento, Faculdade de Ciências e Tecnologia, Universidade de Coimbra, Coimbra, Portugal.

CEPI Sustainability Report (2013) – "*CEPI SUSTAINABILITY REPORT 2013 EUROPEAN PAPER INDUSTRY – ADVANCING THE BIOECONOMY*". www.cepsi-sustainability.eu, accessed 14 December 2014.

Chang, K.C.; Hsieh, W.D.; Chen, C.S. (1995) – "*A modified low-Reynolds-number turbulence model applicable to recirculating flow in pipe expansion*" – Journal of Fluids Engineering, 117(3): 417-423.

Chatterjee, A.; Wu, L.-M. (2008) – "*Predicting rheology of suspensions of spherical and non-spherical particles using dissipative particle dynamics (DPD): methodology and experimental validation*" – Molecular Simulation, 34(3): 243-250.

Chaussy, D.; Martin, C.; Roux, J.-C. (2011) – "*Rheological behavior of cellulose fiber suspensions: application to paper-making processing*" – Industrial & Engineering Chemistry Research, 50(6): 3524-3533.

Cheng, D.C.-H.; Richmond, R.A. (1978) – "*Some observations on the rheological behaviour of dense suspensions*" – Rheologica Acta, 17(4): 446-453.

Cheng, K.-S.; Isaacson, D.; Newell, J.C.; Gisser, D.G. (1989) – "*Electrode models for electric current computed tomography*" – IEEE Transactions on Biomedical Engineering, 36(9): 918-924.

Claesson, J.; Wikström, T.; Rasmuson, A. (2012) – "*An experimental study of the turbulent mixing layer in concentrated fiber suspensions*" – Nordic Pulp and Paper Research Journal, 27(5): 940-946.

Claesson, J.; Rasmuson, A.; Wiklund, J.; Wikström, T. (2013) – "*Measurement and analysis of flow of concentrated fiber suspensions through a 2-D sudden expansion using UVP*" – AIChE Journal, 59(3): 1012-1021.

Costa, J.J. (1996) – "*Estudo do escoamento originado por dois jactos parietais não-isotérmicos num domínio fechado*". Tese de Doutoramento, Faculdade de Ciências e Tecnologia, Universidade de Coimbra, Coimbra, Portugal.

Cotas, C.I.P. (2012) – "*Modelling of fiber suspensions flow in pipes*". Thesis Project, Faculty of Science and Technology, University of Coimbra, Coimbra.

Cotas, C.; Garcia, F.; Ferreira, P.; Faia, P.; Asendrych, D.; Rasteiro, M.G. (2014) – "*Chang-Hsieh-Chen low-Reynolds turbulence model Adaptation to study the flow of concentrated pulp suspensions in pipes*". Proc. 11th World Congress on Computational Mechanics WCCM XI – 5th European Conference on Computational Mechanics ECCM V – 6th European Conference on Computational Fluid Dynamics ECFD VI. Barcelona, Spain, 20-25 July.

Cotas, C.; Silva, R.; Garcia, F.; Faia, P.; Asendrych, D.; Rasteiro, M.G. (2015a) – "*Application of different low-Reynolds k-ε turbulence models to model the flow of concentrated pulp suspensions in pipes*" – Procedia Engineering, 102: 1326-1335.

Cotas, C.; Asendrych, D.; Garcia, F.; Faia, P.; Rasteiro, M.G. (2015b) – "*CFD simulation of a turbulent fiber suspension flow – A modified near-wall treatment*" – Engineering Applications of Computational Fluid Mechanics, 9(1): 233-246.

Cotas, C.; Asendrych, D.; Rasteiro, M.G. (2015c) – "*Numerical simulation of turbulent pulp flow: influence of the non-Newtonian properties of the pulp and of the damping*

function". Proc. The 8th International Conference for Conveying and Handling of Particulate Solids. Tel-Aviv, Israel, 3-7 May.

Cotas, C.; Asendrych, D.; Garcia, F.; Faia, P.; Rasteiro, M.G. (2015d) – "*Turbulent flow of concentrated pulp suspensions in a pipe – numerical study based on a pseudo-homogeneous approach*". Proc. COST Action FP1005 Final Conference. Trondheim, Norway, 9-11 June.

Cruz, D.O.A.; Pinho, F.T. (2003) – "*Turbulent pipe flow predictions with a low Reynolds number k-ε model for drag reducing fluids*" – Journal of non-Newtonian Fluid Mechanics, 114(2-3): 109-148.

Cruz, D.O.A.; Pinho, F.T.; Resende, P.R. (2004) – "*Modelling the new stress for improved drag reduction predictions of viscoelastic pipe flow*" – Journal of non-Newtonian Fluid Mechanics, 121(2-3): 127-141.

Cui, H.; Grace, J.R. (2006) – "*Pneumatic conveying of biomass particles: a review*" – China Particuology, 4(3-4): 183-188.

Cui, H.; Grace, J.R. (2007) – "*Flow of pulp fibre suspension and slurries: A review*" – International Journal of Multiphase Flow, 33(9): 921-934.

Denn, M.M.; Morris, J.F. (2014) – "*Rheology of non-Brownian suspensions*" – Annual Review of Chemical and Biomolecular Engineering, 5: 203-228.

Derakhshandeh, B.; Hatzikiriakos, S.G.; Bennington, C.P.J. (2010) – "*Rheology of pulp suspensions using ultrasonic Doppler velocimetry*" – Rheologica Acta, 49(11-12): 1127-1140.

Derakhshandeh, B.; Kerekes, R.J.; Hatzikiriakos, S.G.; Bennington, C.P.J. (2011) – "*Rheology of pulp fibre suspensions: A critical review*" – Chemical Engineering Science, 66(15): 3460-3470.

Derakhshandeh, B.; Vlassopoulos, D.; Hatzikiriakos, S.G. (2012) – "*Thixotropy, yielding and ultrasonic Doppler velocimetry in pulp fibre suspensions*" – Rheologica Acta, 51(3): 201-214.

Dhotre, M.T.; Ekambara, K.; Joshi, J.B. (2007) – "*CFD simulation of the flow pattern for drag reducing fluids in turbulent pipe flows*" – Journal of Chemical Engineering of Japan, 40(4): 304-311.

Dong, S.; Feng, X.; Salcudean, M.; Gartshore, I. (2003) – "*Concentration of pulp fibers in 3D turbulent channel flow*" – International Journal of Multiphase Flow, 29(1): 1-21.

Duffy, G.G. (1976) – "*A review and evaluation of design methods for calculating friction loss in stock piping systems*" – TAPPI Journal, 59(8): 124-127.

Duffy, G.G. (2003) – "*The significance of mechanistic-based models in fibre suspension flow*" – Nordic Pulp and Paper Research Journal, 18(1): 74-80.

Duffy, G.G. (2006) – "*Measurements, mechanisms and models: Some important insights into the mechanisms of flow of fibre suspensions*" – Annual Transactions of the Nordic Rheology Society, 14: 19-31.

Eberle, A.P.R.; Baird, D.G.; Wapperom, P. (2008) – "*Rheology of non-Newtonian fluids containing glass fibers: a review of experimental literature*" – Industrial & Engineering Chemistry Research, 47(10): 3470-3488.

Faia, P.M.; Krochak, P.; Costa, H.; Lundell, F.; Silva, R.; Garcia, F.A.P.; Rasteiro, M.G. (2015a) – "*A comparative study of magnetic resonance imaging, electrical impedance tomography and ultrasonic Doppler velocimetry for the semi-dilute fibre flow suspension characterisation*". Proc. Multiphase Flow 2015. Valencia, Spain, 20-22 April.

Faia, P.M.; Rasteiro, M.G.; Garcia, F.; Silva, R.; Costa, H.; Branco, B. (2015b) – "*Electrical tomography use for imaging pulp suspensions flow in pipes: restraints and evolution*". Proc. COST Action FP1005 Final Conference. Trondheim, Norway, 9-11 June.

Fan, X.; Phan-Thien, N.; Zheng, R. (1998) – "*A direct simulation of fibre suspensions*" – Journal of non-Newtonian Fluid Mechanics, 74(1-3): 113-135.

Ferziger, J.H.; Perić, M. (2002) – "Computational methods for fluid dynamics". Springer-Verlag Berlin Heidelberg, 3rd Edition, Germany.

Fluent Inc. (2007) – *GAMBIT Documentation*, Release 2.4.

Fock, H.; Wiklund, J.; Rasmuson, A. (2009) – "*Ultrasound Velocity Profile (UVP) measurements of pulp suspension flow near the wall*" – Journal of Pulp and Paper Science, 35(1): 26-33.

Fock, H.; Claesson, J.; Rasmuson, A.; Wikström, T. (2011) – "*Near wall effects in the plug flow of pulp suspensions*" – The Canadian Journal of Chemical Engineering, 89(5): 1207-1216.

Ganani, E.; Powell, R.L. (1985) – "*Suspensions of rodlike particles: literature review and data correlations*" – Journal of Composite Materials, 19(3): 194-215.

Gillissen, J.J.J.; Boersma, B.J.; Mortensen, P.H.; Andersson, H.I. (2007a) – "*On the performance of the moment approximation for the numerical computation of fiber stress in turbulent channel flow*" – Physics of Fluids, 19(3): 035102-035102-9.

Gillissen, J.J.J.; Boersma, B.J.; Mortensen, P.H.; Andersson, H.I. (2007b) – "*The stress generated by non-Brownian fibers in turbulent channel flow simulations*" – Physics of Fluids, 19(11): 115107-115107-8.

Gomez, C.; Derakhshandeh, B.; Hatzikiriakos, S.G.; Bennington, C.P.J. (2010) – "*Carbopol as a model fluid for studying mixing of pulp fibre suspensions*" – Chemical Engineering Science, 65(3): 1288-1295.

Gullichsen, J.; Härkönen, E. (1981) – "*Medium consistency technology I. Fundamental data*" – TAPPI Journal, 64(6): 69-72.

Haavisto, S.; Lille, M.; Liukkonen, J.; Salmela, J. (2010) – "*Laboratory-Scale pipe rheometer: A study of a microfibrillated cellulose suspension*". Proc. 7th International Symposium on Ultrasonic Doppler Methods for Fluid Mechanics and Fluid Engineering ISUD7. Chalmers University, Gothenburg, Sweden, 7-9 April; pp 103-106.

Haavisto, S.; Liukkonen, J.; Jäsberg, A.; Koponen, A.; Lille, M.; Salmela, J. (2011) – "*Laboratory-Scale pipe rheometer: A study of a microfibrillated cellulose suspension*". PaperCon2011. Covington, Kentucky, USA, 1-4 May; pp 704-717.

Haavisto, S.; Koponen, A.I.; Salmela, J. (2014) – "*New insight into rheology and flow properties of complex fluids with Doppler optical coherence tomography*" – Frontiers in Chemistry, 2(27): 1-6.

Haavisto, S.; Salmela, J.; Jäsberg, A.; Saarinen, T.; Karppinen, A.; Koponen, A. (2015) – "*Rheological characterization of microfibrillated cellulose suspension using optical coherence tomography*" – TAPPI Journal, 14(5): 291-302.

Hämäläinen, J.; Eskola, R.; Erkkilä, A.-L.; Leppänen, T. (2011a) – "*Rheology in papermaking- from fibre suspension flows to mechanics of solid paper*" – Korea-Australia Rheology Journal, 23(4): 211-217.

Hämäläinen, J.; Lindström, S.B.; Hämäläinen, T.; Niskanen, H. (2011b) – "*Papermaking fibre-suspension flow simulations at multiple scales*" – Journal of Engineering Mathematics, 71(1): 55-79.

Heikkinen, L.; Kourunen, J.; Paananen, P.; Peltonen, K.; Käyhkö, J.; Vauhkonen, M. (2010) – "*Electrical resistance tomography technique in pulp and paper industry*" – ERCOFTAC Bulletin, 84: 9-11.

Hsieh, W.D.; Chang, K.C. (1996) – "*Calculation of wall heat transfer in pipe-expansion turbulent flows*" – International Journal of Heat and Mass Transfer, 39(18): 3813-3822.

Hsu, T.-J.; Jenkins, J.T.; Liu, P.L.-F. (2003) – "*On two-phase sediment transport: Dilute flow*" – Journal of Geophysical Research, 108(C3): 1978-2012.

Huhtanen, J.-P. (2004) – "*Modeling of fiber suspension flows in refiner and other papermaking processes by combining non-Newtonian fluid dynamics and turbulence*". Doctoral Thesis, Tampere University of Technology, Tampere, Finland.

Huhtanen, J.-P.T.; Karvinen, R.J. (2005) – "*Interaction of non-Newtonian fluid dynamics and turbulence on the behavior of pulp suspension flows*" – Annual Transactions of the Nordic Rheology Society, 13: 177-186.

Huhtanen, J.-P.T.; Karvinen, R.J. (2006) – "Characterization of non-Newtonian fluid models for wood fiber suspensions in laminar and turbulent flows" – Annual Transactions of the Nordic Rheology Society, 14: 51-60.

Inaba, H.; Haruki, N.; Horibe, A. (2000) – "*Flow drag and heat transfer reduction of flowing water containing fibrous material in a straight pipe*" – International Journal of Thermal Sciences, 39(1): 18-29.

Jafari, A.; Zamankhan, P.; Mousavi, S.M. (2007) – "*Computer simulation of flocs interactions: Application in fiber suspension*" – Colloids and Surfaces A: Physicochemical and Engineering Aspects, 292(2-3): 99-109.

Jäsberg, A. (2007) – "*Flow behaviour of fibre suspensions in straight pipes: New experimental techniques and multiphase modeling*". PhD Thesis, Faculty of Mathematics and Science of the University of Jyväskylä, University of Jyväskylä, Finland.

Jeffrey, D.J.; Acrivos, A. (1976) – "*The rheological properties of suspensions of rigid particles*" – AIChE Journal, 22(3): 417-432.

Jha, S.K.; Bomberdelli, F.A. (2009) – "*Two-phase modeling of turbulence in dilute sediment-laden, open-channel flows*" – Environmental Fluid Mechanics, 9(2): 237-266.

Jian-Zhong, L.; Jun, L.; Li, Z.; Olson, J.A. (2005) – "*New equation of turbulent fibre suspensions and its solution and application to the pipe flow*" – Chinese Physics, 14(6): 1185-1192.

Kartushinsky, A.; Michaelides, E.E.; Rudi, Y.; Nathan, G.G. (2010) – "*RANS modeling of a particulate turbulent round jet*" – Chemical Engineering Science, 65(11): 3384-3393.

Kazi, Md.S.N.; Duffy, G.G.; Chen, X.D. (1999) – "*Heat transfer in the drag reducing regime of wood pulp fibre suspensions*" – Chemical Engineering Journal, 73(3): 247-253.

Kazi, S.N.; Duffy, G.G.; Chen, X.D. (2015) – "*The effect of varying fiber characteristics on the simultaneous measurement of heat and momentum transfer of flowing fiber suspensions*" – Journal of Heat Transfer, 137(1): 012601-012601-9.

Kerekes, R.J.; Soszynski, R.M.; Tam Doo, P.A. (1985) – "*The flocculation of pulp fibres*". Papermaking Raw Materials Their Interaction with the Production Process and their effect on Paper Properties, Transactions of the Eighth Fundamental Research Symposium, Mechanical Engineering Publications Limited, London, United Kingdom; pp 265-310.

Kerekes, R.J.; Schell, C.J. (1992) – "*Characterization of fibre flocculation regimes by a crowding factor*" – Journal of Pulp and Paper Science, 18(1): 32-38.

Kerekes, R.J. (2006) – "*Rheology of fibre suspensions in papermaking: An overview of recent research*" – Nordic Pulp and Paper Research Journal, 21(5): 100-114.

Kondora, G.; Asendrych, D. (2013) – "*Modelling the dynamics of flexible and rigid fibres*" – Chemical and Process Engineering, 34(1): 87-100.

Krochak, P.J.; Olson, J.A.; Martinez, D.M. (2009) – "*Fiber suspension flow in a tapered channel: The effect of flow/fiber coupling*" – International Journal of Multiphase Flow, 35(7): 676-688.

Kvick, M. (2014) – "*Transitional and turbulent fibre suspension flow*". PhD Thesis, School of Engineering Science, KTH Royal Institute of Technology, Sweden.

Lam, C.K.G.; Bremhorst, K. (1981) – "*A modified form of the k-ϵ model for predicting wall turbulence*" – Journal of Fluids Engineering, 103(3): 456-460.

Latz, A.; Strautins, U.; Niedziela, D. (2010) – "*Comparative numerical study of two concentrated fiber suspension models*" – Journal of non-Newtonian Fluid Mechanics, 165(13-14): 764-781.

Launder, B.E.; Sharma, B.I. (1974) – "*Application of the energy-dissipation model of turbulence to the calculation of flow near a spinning disc*" – Letters in Heat and Mass Transfer, 1(2): 131-138.

Launder, B.E.; Spalding, D.B. (1974) – "*The numerical computation of turbulent flows*" – Computer Methods in Applied Mechanics and Engineering, 3(2): 269-289.

Li, T.-Q.; Seymour, J.D.; Powell, R.L.; McCarthy, M.J.; McCarthy, K.L.; Ödberg, L. (1994) – "*Visualization of flow patterns of cellulose fiber suspensions by NMR Imaging*" – AIChE Journal, 40(8): 1408-1411.

Li, T.-Q.; Ödberg, L.; Powell, R.L.; Weldon, M.; McCarthy, M.J. (1995a) – "*Flow of pulp suspension through an abrupt contraction studied by flow encoded nuclear magnetic resonance imaging*" – Nordic Pulp & Paper Research Journal, 10(2): 133-138.

Li, T.-Q.; Ödberg, L.; Powell, R.L.; McCarthy, M.J. (1995b) – "*Quantitative measurements of flow acceleration by means of nuclear magnetic resonance imaging*" – Journal of Magnetic Resonance, Series B, 109(2): 213-217.

Li, A.C.; Kerekes, R.J.; Powell, R.L. (2001a) – "*Generalized method for determining the pipe friction loss of flowing pulp suspensions*". TAPPI TIP 0410-14, TAPPI.

Li, A.; Green, S.; Franzen, M. (2001b) – "*Optimum consistency for pumping pulp*". TAPPI TIP 0410-15, TAPPI.

Lin, J.; Zhang, L.; Zang, W. (2006a) – "*Rheological behavior of fiber suspensions in a turbulent channel flow*" – Journal of Colloid and Interface Science, 296(2): 721-728.

Lin, J.Z.; Gao, Z.Y.; Zhou, K.; Chan, T.L. (2006b) – "*Mathematical modeling of turbulent fiber suspension and successive iteration solution in the channel flow*" – Applied Mathematical Modelling, 30(9): 1010-1020.

Lin, J.Z.; Sun, K.; Zhang, W. (2008) – "*Orientation distribution of fibers and rheological property in fiber suspensions flowing in a turbulent boundary layer*" – Acta Mechanica Sinica, 24(3): 243-250.

Lin, J.-Z.; Shen, S.-H. (2010a) – "*A new formula for predicting the velocity distribution in the turbulent fiber suspensions of a channel flow*" – Fibers and Polymers, 11(3): 438-447.

Lin, J.; Shen, S. (2010b) – "*A theoretical model of turbulent fiber suspension and its application to the channel flow*" – Science China Physics, Mechanics & Astronomy, 53(9): 1659-1670.

Lin, J.; Liang, X.; Zhang, S. (2011) – "*Fibre orientation distribution in turbulent fibre suspensions flowing through an axisymmetric contraction*" – The Canadian Journal of Chemical Engineering, 89(6): 1416-1425.

Lin, J.; Shen, S.; Ku, X. (2013) – "*Characteristics of fiber suspension flow in a turbulent boundary layer*" – Journal of Engineered Fibers and Fabrics, 8(1): 17-29.

Lindström, S.B.; Uesaka, T. (2007) – "*Simulation of the motion of flexible fibers in viscous fluid flow*" – Physics of Fluids, 19(11): 113307-113307-16.

Lindström, S.B.; Uesaka, T. (2008) – "*Simulation of semidilute suspensions of non-Brownian fibers in shear flow*" – The Journal of Chemical Physics, 128(2): 024901-024901-14.

Lindström, S.B.; Uesaka, T. (2009) – "*A numerical investigation of the rheology of sheared fiber suspensions*" – Physics of Fluids, 21(8): 083301-083301-18.

Lu, G.; Third, J.R.; Müller, C.R. (2015) – "*Discrete element models for non-spherical particle systems: from theoretical developments to applications*" – Chemical Engineering Science, 127: 425-465.

Lundell, F.; Söderberg, L.D.; Alfredsson, P.H. (2011) – "*Fluid mechanics of papermaking*" – Annual Review of Fluid Mechanics, 43: 195-217.

Lundell, F. (2015) – "*Fibres and fibrils in shear and extension: inertia vs diffusion*". Proc. COST Action FP1005 Final Conference. Trondheim, Norway, 9-11 June.

Mäkipere, K.; Zamankhan, P. (2007) – "*Simulation of fiber suspension – A multiscale approach*" – Transactions of the ASME, 129(4): 446-456.

Malin, M.R. (1997a) – "*The turbulent flow of Bingham plastic fluids in smooth circular tubes*" – International Communications in Heat and Mass Transfer, 24(6): 793-804.

Malin, M.R. (1997b) – "*Turbulent pipe flow of power-law fluids*" – International Communications in Heat and Mass Transfer, 24(7): 977-988.

Malin, M.R. (1998) – "*Turbulent pipe flow of Herschel-Bulkley fluids*" – International Communications in Heat and Mass Transfer, 25(3): 321-330.

Mandø, M.; Lightstone, M.F.; Rosendahl, L.; Yin, C.; Sørensen, H. (2009) – "*Turbulence modulation in dilute particle-laden flow*" – International Journal of Heat and Fluid Flow, 30(2): 331-338.

Marchioli, C.; Fantoni, M.; Soldati, A. (2010) – "*Orientation, distribution, and deposition of elongated, inertial fibers in turbulent channel flow*" – Physics of Fluids, 22(3): 033301-033301-14.

Marchioli, C.; Soldati, A. (2013) – "*Rotation statistics of fibers in wall shear turbulence*" – Acta Mechanica, 224(10): 2311-2329.

Marti, I.; Höfler, O.; Fischer, P.; Windhab, E.J. (2005) – "*Rheology of concentrated suspensions containing mixtures of spheres and fibres*" – Rheologica Acta, 44(5): 502-512.

Mathur, A.; He, S. (2013) – "*Performance and implementation of the Launder-Sharma low-Reynolds number turbulence model*" – Computers & Fluids, 79(25): 134-139.

Mehrabadi, M.A.; Sadeghy, K. (2008) – "*Simulating drag reduction phenomenon in turbulent pipe flows*" – Mechanics Research Communications, 35(8): 609-613.

Melander, O.; Rasmuson, A. (2004) – "*PIV measurements of velocities and concentrations of wood fibres in pneumatic transport*" – Experiments in Fluids, 37(2): 293-300.

Mewis, J. (1996) – "*Flow behaviour of concentrated suspensions: predictions and measurements*" – International Journal of Mineral Processing, 44-45: 17-27.

Mewis, J.; Wagner, N.J. (2009) – "*Current trends in suspension rheology*" – Journal of Non-Newtonian Fluid Mechanics, 157(3): 157-150.

Mohseni, M.; Bazargan, M. (2012) – "*Modification of low Reynolds number k-ε turbulence models for applications in supercritical fluid flows*" – International Journal of Thermal Sciences, 51(1): 51-62.

Möller, K. (1972) – "*The plug flow of paper pulp suspension*". PhD Thesis, University of Auckland, Auckland, New Zeeland.

Morris, J.F. (2009) – "*A review of microstructure in concentrated suspensions and its implications for rheology and bulk flow*" – Rheologica Acta, 48(8): 909-923.

Mortensen, P.H.; Andersson, H.I.; Gillissen, J.J.J.; Boersma, B.J. (2008) – "*Dynamics of prolate ellipsoidal particles in a turbulent channel flow*" – Physics of Fluids, 20(9): 093302-093302-14.

Nikbahkt, A.; Madani, A.; Olson, J.A.; Martinez, D.M. (2014) – "*Fibre suspensions in Hagen-Poiseuille flow: Transition from laminar plug flow to turbulence*" – Journal of Non-Newtonian Fluid Mechanics, 212: 28-35.

Niklas, M.; Asendrych, D. (2006) – "*Modelling of fluid flow with complex rheology*" – Systems, 11(1): 63-72.

Ogawa, K.; Yoshikawa, S.; Ikeda, J.; Ogawa, H. (1990a) – "*Pressure loss and velocity profile of pulp flow in a circular pipe*" – TAPPI Journal, 73(4): 217-221.

Ogawa, K.; Yoshikawa, S.; Suguro, A.; Ikeda, J.; Ogawa, H. (1990b) – "*Flow characteristics and circular pipe flow of pulp-suspension*" – Journal of Chemical Engineering of Japan, 23(1): 1-6.

Oliveira, L.A.; Lopes, A.G. (2010) – "Mecânica dos Fluidos". ETEP – Edições Técnicas e Profissionais, 3ª Edição, Lisboa.

Olson, J.A. (1996) – "*The effect of fiber length on passage through narrow apertures*". PhD Thesis, University of British Columbia, Canada.

Paschkewitz, J.S.; Dubief, Y.; Dimitropoulos, C.D.; Shaqfeh, E.S.G.; Moin, P. (2004) – "*Numerical simulation of turbulent drag reduction using rigid fibres*" – Journal of Fluid Mechanics, 518: 281-317.

Patankar, S.V. (1980) – "*Numerical heat transfer and fluid flow*". Hemisphere Publishing Corporation, 1st Edition, Washington.

Patel, V.C.; Rodi, W.; Scheuerer, G. (1984) – "*Turbulence models for near-wall and low Reynolds number flows: A review*" – AIAA Journal, 23(9): 1308-1319.

Petrie, C.J.S. (1999) – "*The rheology of fibre suspensions*" – Journal of Non-Newtonian Fluid Mechanics, 87(2-3): 369-402.

Pettersson, A.J.; Wikström, T.; Rasmuson, A. (2006) – "*Near wall studies of pulp suspension flow using LDA*" – The Canadian Journal of Chemical Engineering, 84(4): 422-430.

Pinho, F.T.; Li, C.F.; Younis, B.A.; Sureshkumar, R. (2008) – "*A low Reynolds number turbulence closure for viscoelastic fluids*" – Journal of non-Newtonian Fluid Mechanics, 154(2-3): 89-108.

Polydorides, N.; Lionheart, W.R.B. (2002) – "*A Matlab toolkit for three-dimensional electrical impedance tomography: a contribution to the Electrical Impedance and Diffuse Optical Reconstruction Software project*" – Measurement Science and Technology, 13(12): 1871-1883.

Powell, R.L. (1991) – "*Rheology of suspensions of rodlike particles*" – Journal of Statistical Physics, 62(5-6): 1073-1094.

Powell, R.L. (2008) – "*Experimental techniques for multiphase flows*" – Physics of Fluids, 20(4): 040605-040605-22.

Rasteiro, M. (2011) – "*Modelling fiber suspensions flows using rheological data*". COST Action FP1005, 2nd joint MC/WG meeting, Nancy, 13-14 October.

Rasteiro, M.G.; Silva, R.; Garcia, F.A.; Faia, P.M. (2011) – "*Electrical tomography: a review of configurations and applications to particulate processes*" – KONA Powder and Particle Journal, 29(0): 67-80.

Resende, P.R.; Escudier, M.P.; Presti, F.; Pinho, F.T.; Cruz, D.O.A. (2006) – "*Numerical predictions and measurements of Reynolds normal stresses in turbulent pipe flow of polymers*" – International Journal of Heat and Fluid Flow, 27(2): 204-219.

Rosén, T.; Do-Quang, M.; Aidun, C.K.; Lundell, F. (2015a) – "*The dynamical states of a prolate spheroidal particle suspended in shear flow as a consequence of particle and fluid inertia*" – Journal of Fluid Mechanics, 771: 115-158.

Rosén, T.; Do-Quang, M.; Aidun, C.K.; Lundell, F. (2015b) – "*Effect of fluid and particle inertia on the rotation of an oblate spheroidal particle suspended in linear shear flow*" – Physical Review E, 91(5): 053017-053017-15.

Saarikoski, E.; Saarinen, T.; Salmela, J.; Seppälä, J. (2012) – "*Flocculated flow of microfibrillated cellulose water suspensions: an imaging approach for characterization of rheological behaviour*" – Cellulose, 19(3): 647-659.

Sasic, S.; Almstedt, A.-E. (2010) – "*Dynamics of fibres in a turbulent flow field – A particle-level simulation technique*" – International Journal of Heat and Fluid Flow, 31(6): 1058-1064.

Sattari, M.; Tuomela, J.; Niskanen, H.; Hämäläinen, J. (2014) – "*Coupled simulation of the spherical angles of rigid fibres by using a fibre orientation probability distribution model*" – International Journal of Multiphase Flow, 65: 61-67.

Shen, S.; Lin, J. (2010) – "*A new expression for the velocity profile in the turbulent pipe flows of fiber suspension*" – Fibers and Polymers, 11(3): 474-480.

Silveira, M.T.; Ferreira, A.G.M.; Lobo, L.Q. (2002) – "*The viscosity of aqueous suspensions of cellulose fibers Part 1. Influence of consistency and fiber length*" – Silva Lusitana, 10(2): 171-178.

Silveira, M.T.; Ferreira, A.G.M.; Lobo, L.Q. (2003a) – "*The viscosity of aqueous suspensions of cellulose fibres Part 2. Influence of temperature and mix fibres*" – Silva Lusitana, 11(1): 61-66.

Silveira, M.T.; Ferreira, A.G.M.; Lobo, L.Q. (2003b) – "*The viscosity of aqueous suspensions of cellulose fibres Part 3. Influence of pH*" – Silva Lusitana, 11(2): 201-206.

Sorvari, A.; Saarinen, T.; Haavisto, S.; Salmela, J.; Seppälä, J. (2013) – "*Flow behavior and flocculation of MFC suspension measured in rotational rheometer*" – Annual Transactions of the Nordic Rheology Society, 21: 29-34.

Steen, M. (1991) – "*Modeling fiber flocculation in turbulent flow: a numerical study*" – TAPPI Journal, 74(9): 175-182.

Stickel, J.J.; Powell, R.L. (2005) – "*Fluid mechanics and rheology of dense suspensions*" – Annual Review of Fluid Mechanics, 37(1): 129-149.

Swerin, A. (1995) – "*Flocculation and fiber network strength in papermaking suspensions flocculated by retention aid systems*". Doctoral Thesis, Department of Pulp and Paper Chemistry and Technology, Royal Institute of Technology, Stockholm, Sweden.

Switzer III, L.H.; Klingenberg, D.J. (2003) – "*Rheology of sheared flexible fiber suspensions via fiber-level simulations*" – Journal of Rheology, 47(3): 759-778.

Szabó, L.; Soria, A.; Forsström, J.; Keränen. J.T.; Hytönen, E. (2009) – "*A world model of the pulp and paper industry: demand, energy consumption and emission scenarios to 2030*" – Environmental Science & Policy, 12(3): 257-269.

Tapp, H.S.; Peyton, A.J.; Kemsley, E.K.; Wilson, R.H. (2003) – "*Chemical engineering applications of electrical process tomography*" – Sensors and Actuators B, 92(1-2): 17-24.

Tozzi, E.J.; Lavenson, D.M.; McCarthy, M.J.; Powell, R.L. (2013) – "*Effect of fiber length, flow rate, and concentration on velocity profiles of cellulosic fiber suspensions*" – Acta Mechanica, 224(10): 2301-2310.

Underwood, W.M. (1976) – "*Viscometer for slurries and suspensions*" – Review of Scientific Instruments, 47(9): 1079-1082.

Ventura, C.; Blanco, A.; Negro, C.; Ferreira, P.; Garcia, F.; Rasteiro, M. (2007) – "*Modeling pulp fiber suspension rheology*" – TAPPI Journal, 6(7): 17-23.

Ventura, C., Garcia, F.; Ferreira, P.; Rasteiro, M. (2008a) – "*CFD simulation of the turbulent flow of pulp fibre suspensions*". Proc. 2008 AIChE Annual Meeting. Philadelphia, USA, 16-21 November.

Ventura, C.; Garcia, F.; Ferreira, P.; Rasteiro, M. (2008b) – "*Flow dynamics of pulp fiber suspensions*" – TAPPI Journal, 7(8): 20-26.

Ventura, C.A.F.; Garcia, F.A.P.; Ferreira, P.J.; Rasteiro, M.G. (2011) – "*Modeling the turbulent flow of pulp suspensions*" – Industrial & Engineering Chemistry Research, 50(16): 9735-9742.

Vilar, G.; Williams, R.A.; Wang, M.; Tweedie, R.J. (2008) – "*On line analysis of structure of dispersions in an oscillatory baffled reactor using electrical impedance tomography*" – Chemical Engineering Journal, 141(1-3): 58-66.

Wang, M.; Ma, Y.; Holliday, N.; Dai, Y.; Williams, R.A.; Lucas, G. (2005) – "*A high-performance EIT system*" – IEEE Sensors Journal, 5(2): 289-299.

Wiklund, J.A.; Stading, M.; Pettersson, A.J.; Rasmuson, A. (2006) – "*A comparative study of UVP and LDA techniques for pulp suspensions in pipe flow*" – AIChE Journal, 52(2): 484-495.

Wiklund, J.A.; Shahram, I.; Stading, M. (2007) – "*Methodology for in-line rheology by ultrasound Doppler velocity profiling and pressure difference techniques*" – Chemical Engineering Science, 62(16): 4277-4293.

Wiklund, J.; Stading, M. (2008) – "*Application of in-line ultrasound Doppler-based UVP-PD rheometry method to concentrated model and industrial suspensions*" – Flow Measurement and Instrumentation, 19(3): 171-179.

Wikström, T.; Rasmuson, A. (2002) – "*Transition modelling of pulp suspensions applied to a pressure screen*" – Journal of Pulp and Paper Science, 28(11): 374-378.

Xu, H.J.; Aidun, C.K. (2005) – "*Characteristics of fiber suspension flow in a rectangular channel*" – International Journal of Multiphase Flow, 31(3): 318-336.

Yamamoto, S.; Matsuoka, T. (1993) – "*A method for dynamic simulation of rigid and flexible fibers in a flow field*" – The Journal of Chemical Physics, 98(1): 644-650.

Yamanoi, M; Maia, J.M. (2010) – "*Analysis of rheological properties of fibre suspensions in a Newtonian fluid by direct fibre simulation. Part 1: Rigid fibre suspensions*" – Journal of Non-Newtonian Fluid Mechanics, 165(19-20): 1055-1063.

Yamanoi, M.; Maia, J.; Kwak, T. (2010) – "*Analysis of rheological properties of fibre suspensions in a Newtonian fluid by direct fibre simulation. Part 2: Flexible fibre suspensions*" – Journal of Non-Newtonian Fluid Mechanics, 165(19-20): 1064-1071.

Yang, Z.; Shih, T.H. (1993) – "*New time scale based k-ϵ model for near-wall turbulence*" – AIAA Journal, 31(7): 1101-1198.

Yang, W.; Shen, S.; Ku, X. (2013) – "*A new model of turbulent fibre suspension and its application in the pipe flow*" – The Canadian Journal of Chemical Engineering, 91(5): 992-999.

Yenjaichon, W.; Pageau, G.; Bhole, M.; Bennington, C.P.J.; Grace, J.R. (2011) – "*Assessment of mixing quality for an industrial pulp mixer using electrical resistance tomography*" – The Canadian Journal of Chemical Engineering, 89(5): 996-1004.

Yenjaichon, W.; Grace, J.R.; Lim, C.J.; Bennington, C.P.J. (2012) – "*In-line jet mixing of liquid-pulp-fibre suspensions: Effect of concentration and velocities*" – Chemical Engineering Science, 75: 167-176.

Yenjaichon, W.; Grace, J.R.; Lim, C.J.; Bennington, C.P.J. (2013a) – "*Gas dispersion in horizontal pulp-fibre-suspension flow*" – International Journal of Multiphase Flow, 49: 49-57.

Yenjaichon, W.; Grace, J.R.; Lim, C.J.; Bennington, C.P.J. (2013b) – "*Characterisation of gas mixing in water and pulp-suspension flow based on electrical resistance tomography*" – Chemical Engineering Journal, 214: 285-297.

Yokogawa, A.; Suzuki, M.; Shimizu, T. (1985) – "*A study on flow characteristics of pulp suspension flow – Measurement of turbulence intensity and fiber concentration unevenness*" – Bulletin of JSME, 28(239), 846-853.

Yu, D.; Zeng, J.-S.; Chen, K.-F.; Feng, Y.-C.; Yang, X. (2015) – "*Rheological measurement of concentrated pulp fiber suspensions in oscillatory shear using a novel device*" – BioResources, 10(1): 182-195.

Zhang, H.; Ahmadi, G.; Fan, F.-G.; McLaughlin, J.B. (2001) – "*Ellipsoidal particles transport and deposition in turbulent channel flows*" – International Journal of Multiphase Flow, 27(6): 971-1009.

Zhang, F.; Dong, F. (2010) – "*A measurement method of slug flow velocity of gas-liquid two-phase flow in horizontal pipe*". Proc. IEEE Instrumentation and Measurement Technology Conference (I2MTC). Austin, Texas, USA, 3-6 May.

Zhao, L.H.; Andersson, H.I.; Gillissen, J.J.J. (2013) – "*On inertial effects of long fibers in wall turbulence: fiber orientation and fiber stresses*" – Acta Mechanica, 224(10): 2375-2384.

Zhao, L.; Marchioli, C.; Andersson, H.I. (2014) – "*Slip velocity of rigid fibers in turbulent channel flow*" – Physics of Fluids, 26(6): 063302-063302-26.

Zhou, S.; Halttunen, J. (2005) – "*Impedance tomography*". Multiphase Flows in Process Industry. ProMoni, VTT Research Notes 2286, Espoo 2005, Finland; pp 80-96. ISBN 951-38-6537-1

Zhou, S.; Halttunen, J. (2003) – "*Consistency profile measurement in pulp based on electrical impedance tomography*". Proc. XVII IMEKO World Congress: Metrology in the 3rd Millennium. Dubrovnik, Croatia, 22-27 June.

APPENDIX A. USER-DEFINED FUNCTION FOR THE IMPLEMENTATION OF THE AKN TURBULENCE MODEL

This Appendix describes the User-Defined Function source code linked to the commercial CFD solver, ANSYS Fluent 13.0. The UDF is utilized to execute the CFD portion of the model related to the transport equations of LRN k-ε turbulence models, namely the AKN turbulence model proposed for simulations of pulp suspensions flow. A brief description of the UDF code is presented where it is indicated the respective meaning in the modelling and the calculation process.

A.1 – AKN TURBULENCE MODEL – USER-DEFINED FUNCTIONS

This section contains the User-Defined Functions (UDFs) which allows to specify the AKN turbulence model (Abe *et al.*, 1994) presented in Chapter IV. Section A.1.1 presents the UDF developed to set up scalar equations of turbulent kinetic energy and its dissipation rate.

A.1.1 – "AKN_model.c"

The UDF "AKN_model.c" contains the different parts required to define new scalar transport equations representing turbulent kinetic energy and its dissipation rate in ANSYS Fluent 13.0. These parts are divided in the UDF code in such a way that the terms correspond to code description presented in Section A.1.2. These terms provide the required information to be specified in the corresponding panel in the commercial CFD solver. Information is required for the source terms, boundary conditions and diffusion ceofficients.

```
/*****************************************************************************
UDF for the implementation of the Abe, Kondoh and Nagano (AKN) turbulence model
Carla Cotas
University of Coimbra
Czestochowa University of Technology
October 2015
*****************************************************************************/

#include"udf.h"
#include"mem.h"

#define C_MU 0.09
#define SIG_K 1.4
#define SIG_D 1.4
#define C1_D 1.5
#define C2_D 1.9

/* A.1.2.1 User-Defined Scalars */
enum
{
TKE,
```

```
TDR,
N_REQUIRED_UDS
};

/* A.1.2.2 User Defined Memory */
enum
{
MUT,
RET,
RED,
N_REQUIRED_UDM
};

/* A.1.2.3 Damping Functions */
real f_mu(cell_t c, Thread *t)
{
return SQR(1.-exp(-C_UDMI(c,t,RED)/14))*(1.+5.*exp(-SQR(C_UDMI(c,t,RET)/200)/
(pow(C_UDMI(c,t,RET),0.75)));
}

float f_1(cell_t c,Thread *t)
{
return 1.0;
}

real f_2(cell_t c,Thread *t)
{
return SQR(1.-exp(-C_UDMI(c,t,RED)/3.1))*(1.-0.3*exp(-SQR(C_UDMI(c,t,RET)/6.5)));
}

/* A.1.2.4 Source-Terms */
DEFINE_SOURCE(k_src1,c,t,dS,eqn)
{
dS[eqn]=-2.*C_R(c,t)*C_R(c,t)*C_MU*f_mu(c,t)*C_UDSI(c,t,TKE)/C_UDMI(c,t,MUT);
return
-C_R(c,t)*C_R(c,t)*C_MU*f_mu(c,t)*C_UDSI(c,t,TKE)*C_UDSI(c,t,TKE)/C_UDMI(c,t,MUT);
}

DEFINE_SOURCE(k_src2,c,t,dS,eqn)
{
dS[eqn]=0;
return C_UDMI(c,t,MUT)*SQR(C_STRAIN_RATE_MAG(c,t));

DEFINE_SOURCE(d_src1,c,t,dS,eqn)
{
dS[eqn]=C1_D*f_1(c,t)*C__UDMI(c,t,MUT)*SQR(C_STRAIN_RATE_MAG(c,t))/(C_UDSI(c,t,TKE)
);
```

```
return
C1_D*f_1(c,t)*C_UDMI(c,t,MUT)*SQR(C_STRAIN_RATE_MAG(c,t))*C_UDSI(c,t,TDR)/(C_UDSI(c
,t,TKE));
}

DEFINE_SOURCE(d_src2,c,t,dS,eqn)
{
dS[eqn]=-2.*C2_D*f_2(c,t)*C_R(c,t)*C_UDSI(c,t,TDR)/(C_UDSI(c,t,TKE));
return -C2_D*f_2(c,t)*C_R(c,t)*SQR(C_UDSI(c,t,TDR))/(C_UDSI(c,t,TKE));
}

/* A.1.2.5 Diffusibility-Term */
DEFINE_DIFFUSIVITY(ke_diff,c,t,eqn)
{
Switch(eqn)
 {
 case TKE:
 return C_UDMI(c,t,MUT)/SIG_K+C_MU_L(c,t);
 break;
 case TDR:
 return C_UDMI(c,t,MUT)/SIG_D+C_MU_L(c,t);
 break;
 default:
 return C_UDMI(c,t,MUT)+C_MU_L(c,t);
 }
}

/* A.1.2.6 Turbulent Viscosity */
DEFINE_TURBULENT_VISCOSITY(turb_visc,c,t)
{
return C_UDMI(c,t,MUT);
}

/* A.1.2.7 Update UDM in each iteration */
DEFINE_ADJUST(adj_func,d)
{
Thread *t;
cell_t c;
real yp,xw[ND_ND];
thread_loop_c(t,d)
 {
 Begin_c_loop(c,t)
  {
  C_CENTROID(xw,c,t);
  yp=xw[1];
  C_UDMI(c,t,MUT)=C_R(c,t)*C_MU*f_mu(c,t)*SQR(C_UDSI(c,t,TKE))/C_UDSI(c,t,TDR);
  C_UDMI(c,t,RET)=C_R(c,t)*SQR(c_UDSI(c,t,TKE))/C_MU_L(c,t)/(C_UDSI(c,t,TDR));
```

```
  C_UDMI(c,t,RED)=C_R(c,t)*pow(C_MU_L(c,t)*C_UDSI(c,t,TDR)/C_R(c,t),0.25)*(0.0381-
yp)/C_MU_L(c,t);
   if(C_UDSI(c,t,TKE)<1.e-14)
   {
   C_UDSI(c,t,TKE)=1.e-14;
   }
   if(C_UDSI(c,t,TDR)<1.e-20)
   {
   C_UDSI(c,t,TDR)=1.e-20;
   }
   if(C_UDMI(c,t,MUT)>1.e5)
   {
   C_UDMI(c,t,MUT)=1.e5;
   }
  }
 end_c_loop(c,t)
 }
}
```

/* A.1.2.8 Variables Initialization */

```
DEFINE_INIT(init_func,d)
{
cell_t c;
Thread *t;
real xc[ND_ND];
thread_loop_c(t,d)
{
 begin_c_loop(c,t)
 {
 C_CENTROID(xc,c,t);
 C_UDSI(c,t,TKE)=1.0;
 C_UDSI(c,t,TDR)=1.0;
 C_UDMI(c,t,MUT)=998.2*C_MU*SQR(C_UDSI(c,t,TKE))/C_UDSI(c,t,TDR);
 C_UDMI(c,t,RET)=998.2*SQR(C_UDSI(c,t,TKE))/0.001003/(C_UDSI(c,t,TDR));
 C_UDMI(c,t,RED)=998.2*pow(0.001003*C_UDSI(c,t,TDR)/998.2,0.25)*(0.0381-
xc[1])/0.001003;
 }
 end_c_loop(c,t)
}
}
```

/* A.1.2.9 Wall Boundary Condition for dissipation rate of k */

```
DEFINE_PROFILE(wall_epsilon,t,i)
{
Face_t f;
Cell_t c0;
Thread *t0;
```

```
real xw[ND_ND];
real rw;
real Epswall;
 begin_f_loop(f,t)
 {
 c0=F_C0(f,t);
 t0=Thread_T0(t);
 C_CENTROID(xw,c0,t0);
 rw=xw[1];
 Epswall=2.*C_UDSI(c0,t0,TKE)*C_MU_L(c0,t0)/C_R(c0,t0)/SQR(0.0381-rw);
 F_PROFILE(f,t,i)=Epswall;
 }
 end_f_loop(f,t)
}
```

A.1.2 – DESCRIPTION OF THE UDF "AKN_model.c"

Details about each part contained in the UDF "AKN_model.c" are described in this part of Appendix A.

A.1.2.1 – USER-DEFINED SCALARS

User-Defined Scalar (UDS) transport equations were used to define scalar transport equations of k and ε. N_REQUIRED_UDS allows to set names for each User-Defined Scalars own-defined in the corresponding ANSYS Fluent dialog box; it is required to introduce the turbulence differential equations in the CFD solver.

A.1.2.2 – USER-DEFINED MEMORY

User-Defined Memory (UDM) is a macro to access the number of UDM variables own-specified in the corresponding dialog box of ANSYS Fluent, i.e. this macro allows access to UDM locations allocated prior to usage (Ansys Inc., 2010). N_REQUIRED_UDM allows to set names for each UDM allocated. The space allocated prior to use the UDM was defined to store the values of Re_{ε}, Re_{t} and μ_{t}.

A.1.2.3 – DAMPING FUNCTIONS

This part of the UDF code is related to the specifications of damping functions defined in Table IV.9 using the UDM allocated for Re_{ε}, Re_{t} and μ_{t}. The damping functions are declared in accordance with the C data type variables.

A.1.2.4 – SOURCE TERMS

DEFINE_SOURCE is a macro used to specify the source terms for the different scalar transport equations indicated as UDS. This macro must have defined the source term and its derivative. The derivative term is used in the solver to improve stability and convergence of the iterative process. This is applied because the solver linearizes the source terms.

The source term can be expressed as:

$$S_{\phi} = S_{\mathrm{C}} + S_{\mathrm{P}}\phi \tag{III.11}$$

where S_C is the explicit part and $S_P\phi$ is the implicit part. The commercial solver determines automatically whether the given S_P improves stability or not (Ansys Inc., 2010). If it aids stability, the derivative term is used to compute S_C and S_P:

$$S_C = S_{\phi} - \frac{\partial S_{\phi}}{\partial \phi}\phi \tag{A.1}$$

where

$$S_P = \frac{\partial S_{\phi}}{\partial \phi} \tag{A.2}$$

Source terms of k:

$$S_k = \mu_{\mathrm{t}}\left\{2\left[\left(\frac{\partial u}{\partial x}\right)^2 + \left(\frac{\partial v}{\partial r}\right)^2 + \left(\frac{v}{r}\right)^2\right] + \left(\frac{\partial v}{\partial x} + \frac{\partial u}{\partial r}\right)^2\right\} - \rho\varepsilon \tag{A.3}$$

Source terms of ε:

$$S_{\varepsilon} = \left(C_{\varepsilon 1} f_1 P_k - C_{\varepsilon 2} f_2 \rho \varepsilon\right) \frac{\varepsilon}{k} \tag{A.4}$$

A.1.2.5 – DIFFUSIBILITY-TERM

DEFINE_DIFFUSIVITY is a macro which is used to specify the diffusion coefficients to be associated with each UDS transport equation. However, in the present study it is also used with the transport equations for *u* and *v*, because turbulent viscosity now is defined taking the effect of a damping function f_{μ} into account:

$$\mu_{\mathrm{t}} = \rho C_{\mu} f_{\mu} \frac{k^2}{\varepsilon} \tag{IV.3}$$

Diffusion coefficient for u and v:

$$\Gamma_u, \Gamma_v = \mu + \mu_{\mathrm{t}} \tag{A.5}$$

Diffusion coefficient for k:

$$\Gamma_k = \mu + \frac{\mu_{\mathrm{t}}}{\sigma_k} \tag{A.6}$$

Diffusion coefficient for ε:

$$\Gamma_{\varepsilon} = \mu + \frac{\mu_{\mathrm{t}}}{\sigma_{\varepsilon}} \tag{A.7}$$

A.1.2.6 – TURBULENT VISCOSITY

DEFINE_TURBULENT_VISCOSITY is used to specify the expression for turbulent viscosity used to define the UDS transport equations, as well as to replace turbulence viscosity used in momentum equations since in the selected turbulence model the turbulence equations were turned off. This part of the UDF is available in the corresponding dialog box

of ANSYS Fluent where the user can select a new variable representing the turbulent viscosity defined as “turb_visc”.

A.1.2.7 – UPDATE UDM IN EACH ITERATION

DEFINE_ADJUST is used to adjust the UDM variables during the iterative process. The UDM variables defined were updated at each iteration step supplying new set of values for the next iteration.

A.1.2.8 – VARIABLES INITIALIZATION

DEFINE_INIT is a macro used in the UDF to specify the initial set of values for the UDS scalar variables and UDM variables. This macro is called once in the calculation process after the default initialization by the solver is made.

Initial field of k_0*:* 1.0

Initial field of ε_0*:* 1.0

Initial values of $Re_{t,0}$: $\dfrac{998.2 \times k_0^2}{\varepsilon_0 \times 0.001003}$

Initial values of $Re_{\varepsilon,0}$: $\dfrac{y \times \left(\dfrac{998.2 \times \varepsilon_0}{0.001003}\right)^{1/4} \times 998.2}{0.001003}$

Initial values of $\mu_{t,0}$: $998.2 C_{\mu,0} f_{\mu,0} \dfrac{k_0^2}{\varepsilon_0}$

A.1.2.9 – WALL BOUNDARY CONDITION FOR DISSIPATION RATE OF *k*

DEFINE_PROFILE is used to specify the wall boundary condition profile for UDS equation corresponding to ε. This profile is related to spatial coordinate normal to the wall and k obtained from solving the scalar defined equation.

Wall boundary condition for ε*:* $2\nu\left(\dfrac{\partial\sqrt{k}}{\partial y}\right)^2$